ISBN 978-82-326-1308-3 (printed ver.)
ISBN 978-82-326-1309-0 (electronic ver.)
ISSN 1503-8181

Arun Kamath

Doctoral thesis

Doctoral theses at NTNU, 2015:326

Arun Kamath

CFD based Investigation of Wave-Structure Interaction and Hydrodynamics of an Oscillating Water Column Device

NTNU
Norwegian University of
Science and Technology

Doctoral theses at NTNU, 2015:326

NTNU

NTNU
Norwegian University of
Science and Technology
Thesis for the Degree of
Philosophiae Doctor
Faculty of Engineering Science and Technology
Department of Civil and Transport Engineering

NTNU
Norwegian University of
Science and Technology

Arun Kamath

CFD based Investigation of Wave-Structure Interaction and Hydrodynamics of an Oscillating Water Column Device

Thesis for the Degree of Philosophiae Doctor

Trondheim, December 2015

Norwegian University of Science and Technology
Faculty of Engineering Science and Technology
Department of Civil and Transport Engineering

NTNU
Norwegian University of
Science and Technology

NTNU
Norwegian University of Science and Technology

Thesis for the Degree of Philosophiae Doctor

Faculty of Engineering Science and Technology
Department of Civil and Transport Engineering

ISBN 978-82-326-1308-3 (printed ver.)
ISBN 978-82-326-1309-0 (electronic ver.)
ISSN 1503-8181

Doctoral theses at NTNU, 2015:326

Printed by NTNU Grafisk senter

Abstract

The application of computational fluid dynamics (CFD) methods to various problems in the field of coastal and ocean engineering is gaining importance due to the level of detail and accuracy offered by these methods. With the advances made in the computing power over the last decade and anticipated future increase in computational power, large and complex problems can be handled using CFD modeling.

The PhD study aims at the development of a CFD-based numerical wave tank, validation and testing of the wave tank and application of the model to study the hydrodynamics of an Oscillating Water Column (OWC) device and build a platform for further research on OWC design and deployment in arrays. The development of the numerical model covers incorporation of the best available numerical recipes to produce accurate results in the numerical wave tank, using higher-order discretization schemes to obtain a sharp representation of the free surface and avoiding numerical damping of the waves propagating in the wave tank.

The numerical model is validated by investigating various phenomena in coastal engineering such as interaction of non-breaking waves with cylinders, wave shoaling, breaking, and interaction of breaking waves with vertical cylinders and the numerical results are compared to experimental data with very good agreement. Wave shoaling and decomposition over a submerged bar is simulated with very good representation of the phase and amplitude of the decomposed waves observed in experiments. The model is further validated for wave interaction with an OWC device by investigating a 1:12.5 model scale device; the hydrodynamics of the device is studied and the numerical results compared to experimental data.

Wave interaction with cylinders at low Keulegan-Carpenter (KC) numbers is further investigated to obtain insight into the phenomena associated with large coastal structures such as the OWC device. The investigation into high steepness wave diffraction revealed that the wave forces on a single cylinder are over-predicted by about 32% by the McCamy-Fuchs theory for an incident wave of steepness 0.1, due to the difference in the wave diffraction pattern. The phenomenon of wave near-trapping is investigated for a four cylinder group and it is found that the leading cylinder in the group experiences two times the force on a single cylinder due to wave near-trapping at low incident wave steepness of 0.004, but only 1.2 times the force on a single cylinder at a higher wave steepness of 0.06 due to a break-down of the conditions leading to wave near-trapping at a high incident wave steepness.

Breaking wave forces on a vertical cylinder are known to be sensitive to the location of the cylinder with respect to the breaking point. The maximum breaking wave force is calculated in the scenario where the overturning wave crest impacts the cylinder just below the wave crest level and is 1.5 times the magnitude of the wave force calculated when the wave breaks just behind the cylinder. An impinging jet is seen to form behind the vertical cylinder due to breaking wave impact, which can have consequences on the wave forces on a cylinder placed behind it. It is found that when the wave breaks at or just behind the first cylinder, the wave force on the second cylinder is about 10% higher than the breaking wave force on a single cylinder.

The hydrodynamics of an OWC device is studied, including the interaction with steep incident waves, the effect of power take-off (PTO) damping due to the turbine and the air volume in the chamber is investigated. A linear PTO system corresponding to a bi-directional Wells turbine is assumed in the study. It is found that for incident waves with a high steepness of 0.1, the maximum hydrodynamic efficiency is about 40% compared to the maximum hydrodynamic efficiency of 80% obtained at a lower wave steepness of 0.03 for the same incident wavelength.

The effect of damping from the linear PTO system is investigated and it is found that the hydrodynamic efficiency of the OWC is found to increase from about 10% to about 80% for the resonant wavelength on increasing the PTO damping from 0 to 4×10^8 m^{-2}. On further increase in the PTO damping, the hydrodynamic efficiency of the OWC is reduced to 60%. Similar trend is observed for wavelengths away from resonance and it is concluded that there exists an optimal value for PTO damping for every incident wavelength, which results in the maximum hydrodynamic efficiency of the OWC for that wavelength.

The air chamber volume of a 1:12.5 scale model device is increased by increasing the height of the chamber while maintaining the cross-sectional area to study the effect of air compressibility. This effect is found to be negligible both in the model scale device and in the device with an enlarged air chamber. The pressure developed in the OWC chamber, though, is reduced by about 30% and free surface oscillations increased by about 30% in the device with the enlarged chamber compared to the 1:12.5 scale model device. The differences observed could be attributed to the air velocity distribution in the two configurations of the device, as it is found that the high velocity air stream interacts with the free surface in the model scale device but not in the device with the enlarged chamber.

The results show that the numerical model produces a good representation of the hydrodynamics involved in the different wave transformation and interaction processes encountered in coastal waters and in the specialized case of an OWC device. In future work, the model can be used to further investigate the wave forces on an OWC, interaction with irregular waves, the combination of OWC with detached breakwaters and other device parameters to improve the hydrodynamic characteristics of an OWC.

Acknowledgments

I would like to thank my supervisor, Associate Professor Øivind Arntsen, for the opportunity to work in the exciting field of computational fluid dynamics. This research would have not been possible without the routine of discussion, guidance and feedback on an almost daily basis with my co-supervisor and the developer of REEF3D, Dr. Hans Bihs and I am very grateful for the time spent working along with him. I am also thankful to my second co-supervisor Professor Muk Chen Ong, Department of Mechanical and Structural Engineering and Materials Science, University of Stavanger for his help and guidance.

Nothing great was ever accomplished alone. I would like to thank my colleague and fellow PhD Candidate Mayilvahanan Alagan Chella for all the discussions, where we generally lost track of time. It has also been a joy to work together with PhD Candidates Nadeem Ahmad and Mohammad Saud Afzal and masters student Ankit Aggarwal.

I express my thanks to all my colleagues at the department, academic and administrative for all the help, support and camaraderie over the last three years. Thanks are also due to the support staff at The Norwegian Metacenter for Computational Sciences (NOTUR)-NTNU for all the help with operating on the supercomputer Vilje.

This work was carried out under the project "Oscillating Water Column Wave Energy Converters for Combined Energy and Coastal Protection" funded by the Research Council of Norway in collaboration with international partners Indian Institute of Technology-Madras (IIT-M), India and I thank Professor V. Sundar and Professor S.A. Sannasiraj for their guidance and for hosting me at IIT-M. It was also a pleasure hosting and working with my counterpart PhD candidate from IIT-M, John Ashlin.

I express my heartfelt thanks to all my friends and my family for their care and love during both the good and the hard times.

Contents

List of publications

List of international journal papers appended in the thesis

Paper 1 Bihs H., Kamath A., Alagan Chella M., Aggarwal A. and Arntsen Ø.A. **A New Level Set Numerical Wave Tank with Improved Density Interpolation for Complex Wave Hydrodynamics**. Submitted to *Computers and Fluids* 2015.

Paper 2 Kamath A., Alagan Chella M., Bihs H. and Arntsen Ø.A. (2015) **CFD Investigations of Wave Interaction with a Pair of Large Tandem Cylinders**. *Ocean Engineering* 108, 738-748.

Paper 3 Kamath A., Bihs H., Alagan Chella M., Arntsen Ø.A. **Upstream and Downstream Cylinder Influence on the Hydrodynamics of a Four Cylinder Group**. Submitted to *Journal of Waterway, Port, Coastal, and Ocean Engineering* 2015.

Paper 4 Kamath A., Alagan Chella M., Bihs H. and Arntsen Ø.A. **Shoaling and Decomposition of Breaking and Non-Breaking Waves over a Submerged Bar**. Submitted to *Coastal Engineering Journal* 2015.

Paper 5 Kamath A., Alagan Chella M., Bihs H. and Arntsen Ø.A. **Breaking Wave Interaction with a Vertical Cylinder and the Effect of Breaker Location**. Submitted to *Ocean Engineering* 2015.

Paper 6 Bihs H., Kamath A., Alagan Chella M. and Arntsen Ø.A. **Breaking Wave Interaction with Tandem Cylinders under Different Impact Scenarios**. Submitted to *Journal of Waterway, Port, Coastal, and Ocean Engineering* 2015.

Paper 7 Kamath A., Bihs H. and Arntsen Ø.A. (2015) **Numerical Investigations of the Hydrodynamics of an Oscillating Water Column Device**. *Ocean Engineering* 102, 40-50.

Paper 8 Kamath A., Bihs H. and Arntsen Ø.A. (2015) **Numerical Modeling of Power Take-off Damping in an Oscillating Water Column Device**. *International Journal of Marine Energy* 10, 1-16.

Paper 9 Kamath A., Bihs H. and Arntsen Ø.A. **Study of Air Chamber Volume and Compressibility Effects in an Oscillating Water Column Wave Energy Device**. Submitted to *International Journal of Marine Energy* 2015.

Additional international journal papers during the doctoral research not included in the thesis

1. Kamath A., Alagan Chella M., Bihs H., Arntsen Ø.A. (2015) **Evaluating wave forces on groups of three and nine cylinders using a 3D numerical wave tank**. *Engineering Applications of Computational Fluid Mechanics* 9.1, 343-354.

2. Afzal M.S., Bihs H., Kamath A., Arntsen Ø.A. (2015) **Three dimensional numerical modeling of pier scour under current and waves using the level set method**. *Journal of Offshore Mechanics and Arctic Engineering*, 137(3), DOI: 10.1115/1.4029999.

3. Bihs H. and Kamath A. **Simulation of floating bodies with a combined level set/ghost cell immersed boundary representation**. Submitted to *International Journal for Numerical Methods in Fluids* 2015.

4. Ong M. C., Kamath A., Bihs H., Afzal, M. S. **Numerical simulation of free-surface waves past two partially-submerged horizontal circular cylinders in tandem**. Submitted to *Marine Structures* 2015.

Related conference papers not included in the thesis

1. Kamath A., Bihs H., Alagan Chella M., Arntsen Ø.A. (2015) **CFD simulations to determine wave forces on a row of cylinders**. *Procedia Engineering* 116, 623-630.

2. Kamath A., Bihs H., Arntsen Ø.A. (2015) **Three dimensional CFD modeling of flow around an OWC wave energy converter**. *36th IAHR World Congress*, Delft, The Netherlands.

3. Bihs H., Kamath A., Alagan Chella M., Arntsen Ø.A. (2015) **CFD simulations of roll motion of a floating ice block in waves using REEF3D**. *International Conference on Port and Ocean Engineering under Arctic Conditions*, Trondheim, Norway.

4. Kamath A., Bihs, H. and Arntsen Ø.A. (2015) **CFD simulations for fluid structure interaction due to breaking waves**. *Conference in Computational Mechanics-MekIT '15*, Trondheim, Norway.

5. Bihs H., Kamath A., Arntsen Ø.A. (2015) **Implementation and testing of a 6DOF algorithm for floating bodies in REEF3D**. *Conference in Computational Mechanics-MekIT 15*, Trondheim, Norway.

6. Aggarwal A., Kamath A., Bihs H., Arntsen Ø.A. (2015) **Validation of irregular wave generation in REEF3D**, *Conference in Computational Mechanics-MekIT '15*, Trondheim, Norway.

7. Kamath A., Bihs H., Alagan Chella M. and Arntsen Ø.A. (2015) **CFD simulations of wave propagation and shoaling over a submerged bar**. *Aquatic Procedia* 4, 308-316.

8. Kamath A., Bihs H., Arntsen Ø.A. (2014) **A CFD based 3D numerical wave tank to investigate wave interaction with rectangular cylinders**. 11*th International Conference on Hydroscience and Engineering*, Hamburg, Germany.

9. Kamath A., Bihs H., Arntsen Ø.A. (2014) **Comparison of 2D and 3D simulations of an OWC device in different configurations**. 34*th International Conference on Coastal Engineering*, Seoul, South Korea.

10. Kamath A., Bihs H., Olsen J.E., Arntsen Ø.A. (2014) **Effect of compressibility in CFD simulation of an oscillating water column device**. 10*th International Conference on CFD in Oil and Gas, Metallurgical and Process Industries*, Trondheim, Norway.

11. Bihs H., Kamath A., Arntsen Ø.A. (2014) **CFD multiphase simulation of two-fluid sloshing with free surface motion using the level set method**, 10*th International Conference on CFD in Oil and Gas, Metallurgical and Process Industries*, Trondheim, Norway.

12. Kamath A., Bihs H., Arntsen Ø.A. (2014) **Analysis of Wave Interaction with Cylinders using a 3D Numerical Wave Tank**. 33*rd* International Conference on Ocean, Offshore and Arctic Engineering, San Francisco, USA.

13. Kamath A., Bihs H., Arntsen Ø.A. (2013) **Investigating OWC Wave Energy Converters Using Two-Dimensional CFD Simulations**. *International Workshop on Ocean Wave Energy*, Chennai, India.

14. Kamath A., Bihs H., Arntsen Ø.A. (2013) **Evaluation of hydrodynamic efficiency of an oscillating water column device through CFD simulation**. 23*rd International Offshore and Polar Engineering Conference*, Anchorage, USA.

15. Bihs H., Kamath A., Arntsen Ø.A. (2013) **A 3D numerical wave tank using the level set method for the calculation of wave propagation and runup**. 23*rd International Offshore and Polar Engineering Conference*, Anchorage, USA.

16. Kamath A., Bihs H., Arntsen Ø.A. (2013) **Calculation of wave Forces on cylindrical piles using a 3D numerical wave tank**. 33*rd International Conference on Ocean, Offshore and Arctic Engineering*, Nantes, France.

17. Alagan Chella M., Bihs H., Kamath A., Muskulus M. (2013) **Numerical modeling of breaking waves over a reef with a level-set based numerical wave tank**. 33*rd International Conference on Ocean, Offshore and Arctic Engineering*, Nantes, France.

18. Kamath A., Bihs H., Arntsen Ø.A. (2013) **Application of porous media flow relation to simulate pressure drop across a nozzle in a two dimensional numerical wave tank**.*Conference in Computational Mechanics-MekIT '13*, Trondheim, Norway.

19. Bihs H., Ong M.C., Kamath A., Arntsen Ø.A. (2013) **A level set method based numerical wave tank for the calculation of wave forces on horizontal and vertical cylinders**. *Conference in Computational Mechanics-MekIT '13*, Trondheim, Norway.

Declaration of authorship

In the nine international journal papers appended to the thesis, the thesis author is listed as the first author of seven journal papers and was responsible for the writing of the paper, setup and running the simulations and analysis of the results. As the second author on Paper 1, the author was involved in development of the model leading to the paper, setting up and testing aspects relating to a part of the paper. As the second author in Paper 6, the author was involved in setup, running of the simulations and compiling of the results.

Mayilvahanan Alagan Chella, as a second author of some of the appended journal papers provided inputs on scenarios to be investigated and the analysis of the results for those journal papers. As a third author, he advised the first author on the discussion of the results.

Hans Bihs as co-supervisor and developer of the open source CFD model REEF3D, provided inputs regarding the numerical modeling, aided with the numerical aspects of the problem and with proof reading of the papers. As the first author of Papers 1 and 6, he was responsible for writing a major part of the paper and compiling results produced by the different authors for the paper.

Øivind A. Arntsen as the main supervisor contributed to discussions regarding the results obtained, scientific input from his expertise, quality control on the manuscript and proof reading the papers.
On all the other publications, as the first author, the thesis author was responsible for the setup, running of the simulations, analysis and writing of the manuscript. As the second or third author, the author provided minor inputs to the manuscript and contributed with discussion of the results, quality control and proof reading of the manuscript.

Declaration of contribution to the appended papers

Paper 1: The thesis author contributed to the development of the numerical model described in the paper through rigorous testing of the numerical wave tank by running simulations for waves generated using different wave theories, wave generation and absorption methods, density interpolation methods and several wave parameters. The results from the simulations were then analyzed through comparison to theoretical profiles to verify that the model produced the correct results. Also, grid convergence, time convergence and scaling of the numerical model on the supercomputing facility at the university was tested by

running several simulations. He was also responsible for the results in Section 2.5. Parallelization, Section 3.2 Density Location, Section 4.1. Grid and Time Step convergence and Section 4.3. Wave Interaction with a Vertical Circular Cylinder on the manuscript. He also supervised the work by a co-author Ankit Aggarwal, who contributed with results to Section 4.4. Wave propagation over a submerged bar.

Papers 2, 3, 4, 5, 7, 8, 9: The thesis author was responsible for the setup and execution of all the simulations presented on the paper, analysis of the results and the writing of the full manuscript.

Paper 6: The thesis author was responsible for the setup and execution of the simulations and the results presented on the paper.

Nomenclature

Symbols

$\Delta\theta$	phase difference
α	angle of the slope
ϵ	interface thickness
η	free surface elevation
η_{ci}	incident wave crest elevation
η_{owc}	hydrodynamic efficiency of an OWC
η_{ti}	incident wave trough elevation
μ	dynamic viscosity
$\xi = \frac{tan\alpha}{H/L_0}$	Iribarren number
ρ	density
ω_{f0}	resonant angular wave frequency
A_{cs}	cross-sectional area of the OWC vent
A_{fs}	cross-sectional area of the free surface in the OWC chamber
$C = 1/k_p$	permeability factor
D	cylinder diameter
F	inline force
F_0	inline force on a single cylinder
H	incident wave height
KC= $u_0 T/D$	Keulegan Carpenter number
L	incident wavelength
L_0	deep water wavelength
L_v	length of vent along direction of flow
P_{in}	incident wave power
S	spectral power density
S_{max}	maximum spectral power density for the given frequency
T	wave period
a	depth of immersion of the front wall of the OWC
b	length of the OWC device in the direction of wave propagation
c_g	wave group velocity
d	water depth
dx	grid size
f	incident wave frequency

g	acceleration due to gravity
k	wave number
k_p	intrinsic permeability of a porous medium
p_c	air pressure in the OWC chamber
q	volume flow rate of air through the OWC vent
r	cylinder radius
u_0	maximum horizontal water particle velocity at the free surface

Abbreviations

BEM	Boundary Element Method
BiCGStab	Bi-Conjugate Stabilized
CFD	Computational Fluid Dynamics
CFL	Courant-Friedrichs-Lewy's
FNPF	Fully Nonlinear Potential Flow
IBM	Immersed Boundary Method
MOWC	Multiresonant Oscillating Water Column
OWC	Oscillating Water Column
PTO	Power Take-Off
VoF	Volume of Fluids
WENO	Weighted Essentially Non Oscillatory

Chapter 1

Introduction

1.1 Background

Around 81% of the global energy production sources were made up by fossil fuels in 2009 (International Energy Agency, 2010). According to the the Intergovernmental Panel on Climate Change (IPCC) synthesis report (Core Writing Team et al., 2014), the burning of fossil fuels has resulted in the warmest 30-year period between 1983-2012 for the Northern Hemisphere in the last 800 years and has significantly impacted the global climate. Further, the report recommends that a greater portion of the energy be derived from renewable low-carbon sources by 2050 and completely phase out fossil fuels by 2100. The oceans cover about 71% of the Earth's surface and are one of the largest reservoirs of low-carbon renewable energy. Ocean renewable energy can be utilized in four major forms: tides, underwater currents, temperature differences and ocean surface waves (Lewis et al., 2011). The harnessing of tidal power requires construction of large obstructive structures. Extracting energy from underwater currents and temperature differences requires deep water constructions. On the other hand, energy from ocean surface waves can be harnessed close to the coastline and in deep water without large obstructive constructions. Considering the wave direction and the world coastline alignment, the potential for wave power extraction is about 16,000 to 18,500 TWh per year (Reguero et al., 2015), much higher than the current global energy demand. Also, wave energy is more consistent and spatially concentrated than wind energy, which generates waves (Falnes, 2007). In spite of the huge potential, the technology for wave energy extraction is still in its early stages of development.

Energy from ocean surface waves can be extracted through various mechanisms: wave overtopping systems, systems with buoyant oscillating bodies and oscillating water column devices. Wave overtopping systems generally consist of an obstruction over which the waves overtop. A reservoir traps the overtopped water and a turbine uses the stored water to generate electrical energy, like in a low-pressure hydro-electric power station (Kofoed, 2002). The advantage of this system is that it is similar to the conventional hydro-electric power plants in terms of energy conversion from

water stored in a reservoir. On the other hand, saline water poses higher challenges to mechanical parts that it comes in contact with, due to its highly corrosive nature compared to freshwater in the conventional hydro-electric power plants.

Systems with buoyant oscillating bodies utilize the more powerful wave regimes available in deeper waters, typically more than 40 m in depth. Hence, these wave energy converters are to be generally installed far offshore to obtain workable water depths. The buoyant bodies move in heave or rotational motion under the action of the waves and transfer the incident wave energy to an electrical generator. These systems involve complex moving parts and have had problems with mooring, access for maintenance and long electrical cables for connection to land (Falcão, 2010), which has held back their development to a large extent.

An Oscillating Water Column (OWC) wave energy device extracts energy from the action of incident waves on a pneumatic chamber. A principle sketch of a bottom-fixed OWC device is shown in Fig. (1.1). It consists of a chamber that is partially submerged in water so that the chamber contains an air column above the water column. The water column is excited by the incident waves and the air column is alternatively inhaled and exhaled from the chamber through a vent on the roof. The motion of the air drives a turbine that converts the kinetic energy from the air to electrical energy. The turbine or the power take-off (PTO) device has to account for the oscillatory nature of the air flow driven by the oscillating water column. The Wells turbine is one such turbine which has a unidirectional rotation irrespective of the direction of the air flow and is generally preferred as the PTO device in OWC prototypes.

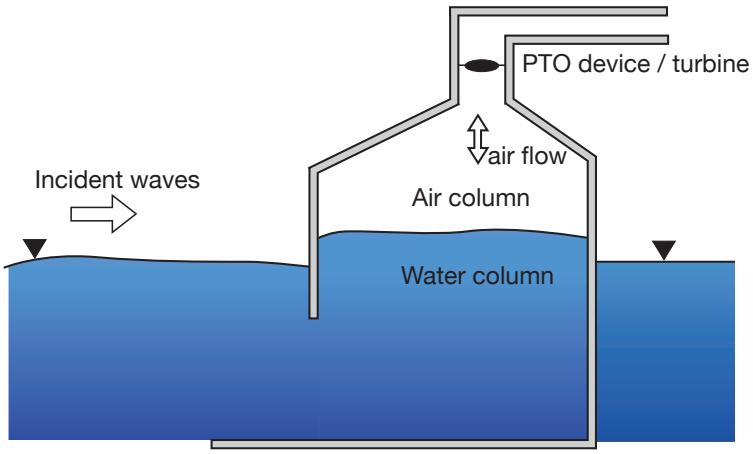

Figure 1.1: Principle sketch of a bottom-fixed OWC device

The sea water in an OWC is never in direct contact with the turbine and other mechanical parts susceptible to corrosion. A bottom-fixed OWC device can be installed close to the coastline, providing easier access for maintenance and energy

transmission, has a simple working principle, lesser complex moving parts and low contact with the corrosive sea water. The simplicity and the robustness of the OWC device makes it a promising concept that has to be further developed with focused research to enable commercial deployment (Duckers, 2004). OWC devices built close to the shoreline can also serve multiple purposes. They can be integrated into breakwaters around harbors or shore parallel breakwaters built to protect the shoreline (Sundar et al., 2010). In this way, the cost of construction and maintenance of the breakwater could be partially recovered through the clean energy obtained from the OWC devices.

The challenges in the development of a commercially viable OWC device are related to the design and construction of the device. The device should be able to withstand the large wave forces and accommodate the stochastic nature of the sea waves to economically supply electrical energy to the grid in a reliable manner. Some installed prototypes have been destroyed by storms and some have been rendered non-functional due to sediment accumulation in the OWC chamber. In terms of the hydrodynamics of the OWC device, the process of wave energy extraction involves complex hydrodynamics related to the interaction of the incident waves with the front wall of the device and fluid confinement due to the length of the device. Also, the effect of PTO damping on the pressure developed in the chamber and the resulting phase difference between the chamber pressure variation and the volume flux of air through the vent are parameters that affect the hydrodynamic performance of the device.

In order to develop an OWC device as a viable wave energy converter, detailed research regarding the hydrodynamics of the device has to be carried out. This includes several wave characteristics and device design parameters that affect the ability of an OWC in absorbing wave energy. Initial efforts into the development of wave energy devices were carried out with the basic theoretical knowledge regarding wave energy absorption (Falcão, 2010). With current advancements in high performance computing, complex wave hydrodynamics and wave interaction with structures can be studied in great detail. A numerical model providing a good representation of the wave physics can be used to rigorously test various parameters and their influence on the hydrodynamic efficiency of the device. After validating and establishing such a model on a generic OWC, further studies can be carried out to study the combination with breakwaters, deployment of device arrays and other complex problems of engineering interest.

1.2 Motivation and Objectives

Most of the current knowledge regarding OWC devices is from the few experimental investigations carried out at model scale (Sarmento, 1992; Thiruvenkatasamy and Neelamani, 1997; Morris-Thomas et al., 2007). Numerical studies have been generally carried out using methods based on potential theory (Evans, 1982; Sarmento and Falcão, 1985; Wang et al., 2002), with focus on optimization of the power take-off

from the device. To obtain more insight into the complex hydrodynamics around the device, the fluid physics has to be resolved in detail with few assumptions. Here, a realistic representation of the device hydrodynamics with a Computational Fluid Dynamics (CFD)-based numerical wave tank can be very useful. In this context, it is essential that the CFD model produce good quality waves, be able to propagate the waves throughout the tank with low numerical diffusion, account for the complex wave transformations occurring in the coastal zone and provide a sharp representation of the free surface oscillations inside the device. This requires the numerical model to be developed with a special focus on the complex problems of wave hydrodynamics. The oscillatory nature of the flow and the interaction between air and water requires the development of a two-phase CFD model with a special focus on a sharp representation of the free surface.

The OWC devices are expected to be deployed in arrays or in combination with breakwaters. Before such deployments are undertaken, numerical studies are to be carried out to obtain a better understanding of the fluid physics and the hydrodynamics of the device. In order to generate confidence in a numerical model developed for this purpose, the numerical model has to be validated to account for the different wave engineering problems in the coastal region such as wave-structure interaction, evaluation of wave forces, wave transformation in the coastal region, modeling of breaking waves and evaluation of breaking wave forces. Keeping these points in mind, the numerical model REEF3D is first validated for wave interaction with structures, modeling of wave transformation processes, evaluation of breaking and non-breaking wave forces and finally simulations with an OWC device to study the hydrodynamics in the near field region. On the establishment of such a validated model, future work can be carried out for detailed parametric analysis of the device, to study OWC deployment in an array, wave diffraction and transmission across an array and the combination of OWCs with breakwaters.

The principal objective of the PhD study is to contribute to the development of and validate a CFD-based numerical wave tank that is capable of accurately simulating various wave-structure interaction problems and simulate the hydrodynamic interaction of an OWC device. The open source CFD model REEF3D, developed with a focus on free surface flows in hydraulic engineering is further developed into a numerical wave tank at the Department of Civil and Transport Engineering, NTNU. In order to test and validate the numerical wave tank for simulation of OWC devices, the following secondary objectives are set:

- *Development, validation and testing of the numerical wave tank including wave generation and absorption:* Incident wave characteristics such as wave amplitude and wavelength are important parameters influencing the hydrodynamic efficiency of the device. Thus, accurate wave generation, propagation and absorption must be ensured in the numerical wave tank using appropriate numerical recipes and grid architecture. This is presented in **Paper 1**.

- *Calculation of wave forces on structures:* The calculation of wave forces on structures is an important aspect in coastal and ocean engineering. The

accurate evaluation of non-breaking and breaking wave forces on structures should be verified. This provides essential information for the structural design aspects of an OWC device. These topics are discussed in **Papers 2, 3, 5, 6**.

- *Wave propagation and transformation:* Waves undergo deformations due to varying bottom topography, interaction with submerged and emerged obstacles. It is essential to ascertain that the numerical model represents the fluid physics involved in these interactions in a realistic manner. The incident waves on OWC devices can vary due to local bottom topography and neighboring devices in a OWC farm. The model should be able to represent the wave transformation process under these conditions and this is presented in **Paper 4**.

- *Two-dimensional simulations to build basic understanding of the OWC device characteristics and working principles with CFD simulations:* The OWC device operates on the principle that work done by an air column under pressure due to the power take-off device converts incident wave energy to kinetic energy at the turbine. The hydrodynamic efficiency of the device depends on various parameters and these relationships are investigated in **Paper 7**.

- *Investigating the effect of the power-take off device:* The influence of the pressure on the OWC chamber on the hydrodynamic efficiency due to the power take-off device is investigated. The PTO device is represented in such a way that the dimensions of the OWC are not altered. This is studied in **Paper 8**.

- *Effects of compressibility and air chamber volume:* The pressurized air column can be susceptible to compressibility and this effect is explored using CFD simulations. The interaction between the water and the air in the chamber is strongly coupled and the effect of the air volume in the chamber on the efficiency of the OWC is investigated in **Paper 9**.

An overview of the research carried out during the PhD study and the relevance of the individual papers in the wide context of deployment of OWC device arrays is presented in Fig. (1.2).

1.3 Scope and limitations of the PhD study

The scope of the PhD study covers the development of the CFD-based numerical wave tank, validation and testing of the wave tank and application of the model to study the hydrodynamics of an OWC device. The development of the numerical model covers incorporation of the best available numerical recipes to produce accurate results in the numerical wave tank, using higher-order discretization schemes to obtain a sharp representation of the free surface and avoiding numerical damping of the waves propagating in the wave tank. The testing and validation of the numerical wave tank is performed by carrying out simulations to study different water wave

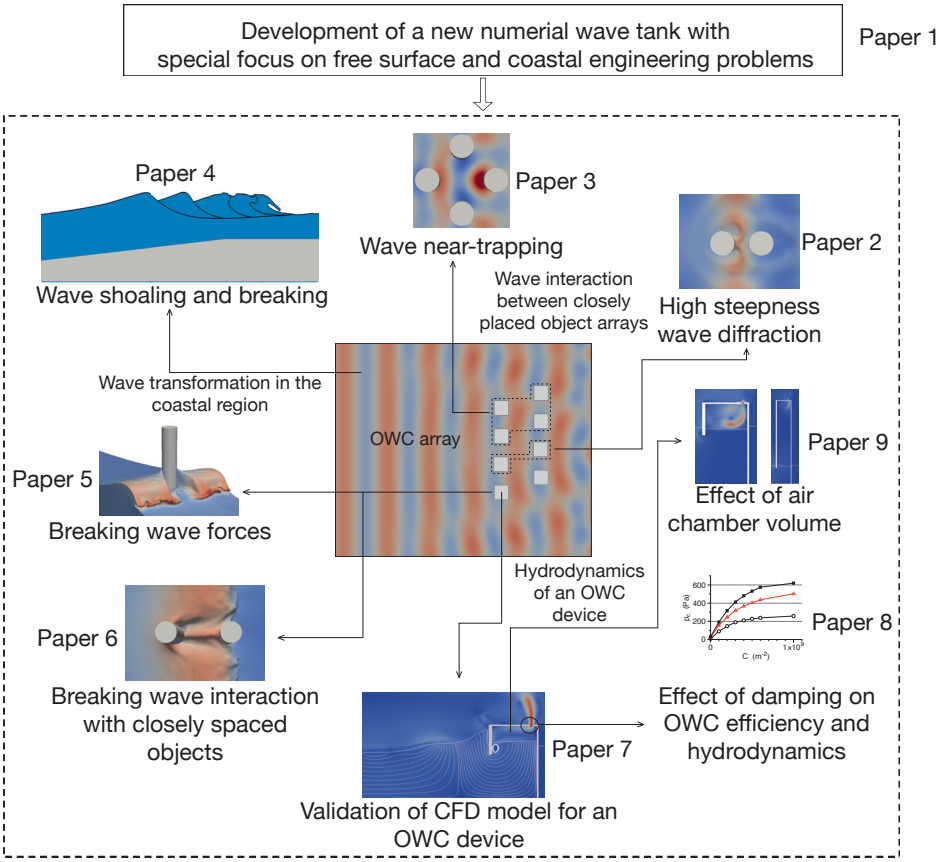

Figure 1.2: Overview of the research carried out in the PhD study

engineering problems in the coastal region including wave-structure interaction at low Keulegan-Carpenter (KC) numbers, wave diffraction, evaluation of breaking and non-breaking wave forces on structures, modeling of wave transformation process in the coastal zone such as wave shoaling, wave decomposition and wave breaking. The model is then used to numerically evaluate the hydrodynamics of a generic OWC device and the results are compared to experimental data.

The study focuses on the development of the numerical model and its validation for different coastal engineering processes and hydrodynamics of an OWC device. The development of a new design of an OWC, study of intricate structural details, studies on deployment of an OWC array, integration into other coastal structures and into the local power grid are outside the scope of the current work. Due to scarce availability of data from field trials, the numerical results are compared only to experimental data available in current literature.

1.4 Organization of the thesis

This thesis is submitted as a collection of nine international journal papers and the structure of the thesis is as follows: A brief overview of the subject along with motivation and objectives of the work are presented in Chapter 1. Chapter 2 gives a brief scientific background and literature review regarding numerical wave tanks and modeling of OWC devices. The major results from the research work carried out during the PhD study are summarized in Chapter 3. Chapter 4 presents the conclusions from the PhD study and the outlook from the present work. The nine research papers are appended in Chapter 5.

Chapter 2

Background and State-of-the-Art

2.1 Numerical wave tank

There are several methods that can be applied for wave modeling, depending on the level of detail required from the numerical model. Spectral models such as SWAN (Booij et al., 1999) are used for large-scale wave modeling, which provide information regarding wave transformation as they propagate from deep waters to shallow waters, through the evolution of the wave spectrum over space and time. Boussinesq models (Madsen et al., 1991; Nwogu, 1993) are employed when slightly higher amount of detail, with the calculation of the wave phase as it undergoes transformations such as shoaling and refraction are required. Numerical wave tanks are used to numerically simulate a physical wave tank and obtain more detailed information such as free surface features, fluid velocity and pressure at a point in the fluid, wave forces on a structure and wave breaking. Thus, every numerical wave tank has four basic functions:

- wave generation according to the kind of wave: linear waves, higher-order Stokes waves, solitary wave or Cnoidal waves, required for the investigation.
- propagation of the wave along the length of the wave tank without numerical dissipation of wave energy.
- wave absorption at the far end of the wave tank, without reflection of wave energy back into the domain.
- evaluating the different fluid parameters due to wave propagation, such as fluid velocity, pressure and the free surface.

Numerical wave tanks are generally classified into two classes, based on the governing equations used to describe the fluid flow: Fully Nonlinear Potential Flow (FNPF) models and Computational Fluid Dynamics (CFD) models.

2.1.1 Fully non-linear potential flow

FNPF-based numerical wave tanks are based on the potential flow theory. These models account for the non-linearity of the flow by including the non-linear terms in the kinematic and dynamic free surface boundary conditions to overcome the assumption of small wave steepness in potential theory. The Laplace equation is the governing equation and is solved using higher-order boundary element methods based on Green's identity or Cauchy's integral theorem formulations. These models ignore the effects of viscosity and rotational flow, like potential theory, but have smaller computational costs for a simulation. Also, as the fluid flow is dealt with as a boundary value problem, the free surface in the fluid domain is less susceptible to numerical dissipation over long distances. These models are generally applicable to wave propagation modeling up to the point of wave breaking with sufficient accuracy.

Dommermuth et al. (1988) presented an FNPF model to model the formation of plunging breaking waves with good agreement to experimental data. Computations were however carried out only until the initiation of wave breaking and the formation of the overturning wave crest due to the limitations of the model. Grilli et al. (1989) computed propagation of periodic waves of permanent form, steep waves and solitary waves in a 2D FNPF-based numerical wave tank. Wave generation was handled by simulating wavemaker motion using extended periodicity boundary conditions. Wave absorption in the numerical wave tank was only possible for simple periodic waves and solitary waves. The model was further improved with respect to wave absorption by Grilli and Horrillo (1997) using a numerical beach about four wavelengths long in combination with an absorbing piston at the end of the 2D numerical wave tank. The model was extended to three dimensions by Grilli et al. (2001) to simulate solitary wave propagation over constant depth and shoaling over a sloping ridge, but only up to the point of overturning. A recent advancement in the field of FNPF models is the application to the simulation of freely floating bodies by coupling non-linear potential flow with rigid body dynamics by Dombre et al. (2015) in a 2D numerical wave tank. The numerical results from the model showed good agreement with previously published literature for small amplitude decay motions, but showed large discrepancies for large amplitude motions due to the assumption of an inviscid fluid.

2.1.2 Computational fluid dynamics

CFD modeling solves the Navier-Stokes equations to resolve the flow problem in detail with the calculation of underlying variables such as the velocities, the pressure and turbulence. This is useful in evaluating complex flow problems associated with wave propagation such as wave breaking, wave interaction with structures and evaluation of wave forces with different coastal structures. The fluid flow problem is modeled with few assumptions, the viscosity of the fluid and the rotational flow due to wave-wave and wave-structure interaction are included in the solution of the fluid flow problem. Thus, non-linear effects due to wave steepness, non-linear wave-wave and wave-structure interactions are accounted for, providing a realistic representation

of the wave hydrodynamics involved. Two-phase CFD-based numerical wave tanks also consider the interaction of the free surface with the air. The air-water interaction plays an important role in wave transformation and in OWC devices. CFD methods have been said to be computationally expensive and time consuming, but with the advances in computational power in recent years, large scale simulations can be carried out on fine grids to obtain a detailed solution of the wave field.

CFD modeling has been presented by several authors in current literature to investigate problems in the field of hydraulic engineering to study complex free surface flows such as ship hydrodynamics (Wang et al., 2009; Yang and Stern, 2009), bubble and droplet deformation (Croce et al., 2010) and floating structures (Calderer et al., 2014). These models provided detailed information on problems involving complex free surface deformations using advanced methods for handling the numerical grid and for obtaining the free surface. While these studies advanced the field of CFD modeling, they did not focus on the highly demanding task of the numerical wave tank and the complex water wave engineering problems that can be addressed using numerical wave tanks. The development of a CFD-based numerical wave tank demands underlying numerical recipes that ensure good quality wave generation, wave propagation without numerical diffusion, correct representation of wave dispersion and wave absorption at the end of the domain. A failure to meet any one of the criteria can produce erroneous results in the numerical wave tank due to spurious currents and reflected waves propagating in the wave tank in addition to the generated waves.

Few articles in recent literature have presented numerical wave tanks using CFD methods based on the open-source CFD code OpenFOAM such as Jacobsen et al. (2012) and Higuera et al. (2013). These numerical wave tanks use the Volume-of-Fluid (VoF) method to obtain the free surface with second-order accurate finite volume discretization schemes on an unstructured collocated grid. Wave generation and absorption is carried out using the relaxation method (Jacobsen et al., 2012) or the active wave generation and absorption method (Higuera et al., 2013). The models have been applied to several problems in the field of coastal and ocean engineering such as wave interaction with porous coastal structures (Higuera et al., 2014), slamming forces on bridge decks (Seiffert et al., 2014), wave forces on a cylinder due to non-linear waves, focussed irregular waves and multi-directional irregular waves (Paulsen et al., 2014); showing detailed flow features and accurately evaluating wave forces. These studies show that simulations in a CFD-based numerical wave tank can be used to investigate detailed wave hydrodynamics related to near-field wave-structure interaction which are not offered by other modeling approaches.

In the numerical model used in the current study, REEF3D, the level set method (Osher and Sethian, 1988) is used for free surface capturing, the fifth-order Weighted Essentially Non Oscillatory (WENO) (Jiang and Shu, 1996) scheme for convection discretization scheme and a third-order Runge-Kutta scheme (Shu and Osher, 1988) for time discretization on a staggered grid for a tight velocity-pressure coupling. This provides numerically stable and accurate solutions to the Navier-Stokes equations

along with a sharp representation of the free surface and avoiding numerical damping of the waves propagating in the numerical wave tank.

With accurate representation of wave propagation and transformation in the numerical model, complex wave interaction problems involved in the case of OWC devices deployed in the shallow coastal waters can be investigated in detail. The current study aims at developing, validating and testing a numerical model to evaluate different wave transformation and interaction processes and use the model to investigate the hydrodynamics of an OWC. The information obtained from the simulations provides more knowledge regarding the hydrodynamic processes in and around the OWC chamber and the influence of various parameters on the hydrodynamic efficiency of the device. This is a step towards effective harvesting of ocean surface wave energy and increasing the share of clean renewable energy sources in the total energy sources used in the world.

2.2 Oscillating water column wave energy device

The concept of a bottom-fixed OWC device has been widely discussed in current literature and some general working principles of the device are well-known. The schematic diagram in Fig. (2.1a) shows some of the important geometric parameters to be considered with respect to the hydrodynamic performance of a bottom-fixed OWC device. The environmental conditions such as the water depth d at the installation site and the incident wave climate are the initial conditions that define the geometry of the device. The chamber length b is to be smaller than the incident wavelength, so that the motion of the water column in the chamber is close to a rigid piston-like motion. The depth of immersion of the front wall a, affects the natural frequency of oscillation of the water column as it influences the water particle excursion required to enter the OWC chamber. The thickness of the front wall δ is also seen to effect the hydrodynamic performance of the device (Morris-Thomas et al., 2007). Another geometric parameter that influences the hydrodynamics of an OWC is the shape of the front wall lip. A hydrodynamically smooth front wall lip results in lower entry losses, whereas a lip with sharp edges can lead to flow separation and wave energy could be trapped in eddies formed behind the front wall. Also, the area of the chamber entrance under the immersed lip should be of similar order as the area of the OWC chamber to avoid hydraulic losses due to flow contraction or expansion.

The air column is inhaled from and exhaled to the atmosphere through a vent in the roof of the OWC, where the PTO device is placed. This leads to a pressure drop across the vent, which determines the pressure developed and the motion of the free surface in the chamber. In model scale experiments and numerical simulations, the vent is used to represent the PTO device as well and the width of the vent V, determines the pressure drop on the chamber. The presence of the PTO device pressurizes the air column and the wave energy absorbed by the OWC is measured as the work done by the motion of the pressurized air column. In order to extract the maximum possible incident wave energy, an optimal amount of damping is required.

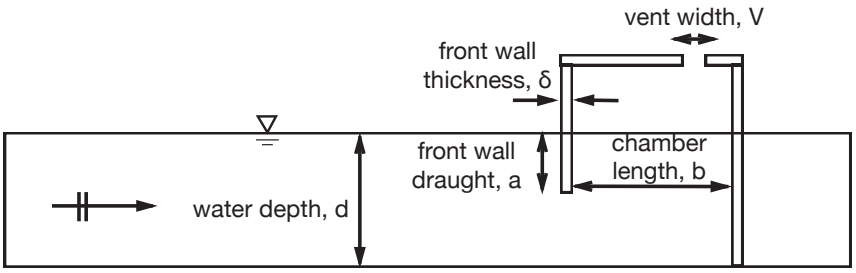

(a) schematic figure showing pertinent geometric parameters

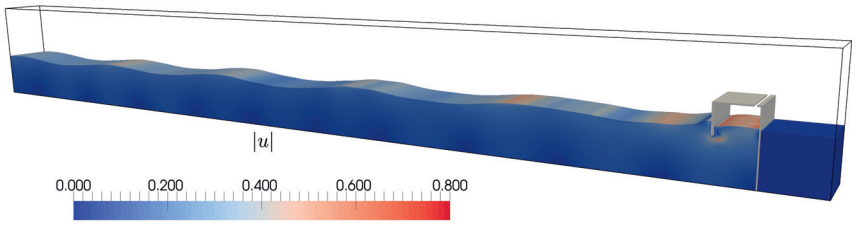

(b) 1 : 12.5 scale model OWC device in a 3D numerical wave tank with water particle velocity magnitude $|u|$

Figure 2.1: Principle sketch and a 1 : 12.5 scale model of an OWC device (Kamath et al., under review)

The setup of a 1:12.5 scale model OWC, used in the experiments by Morris-Thomas et al. (2007), in REEF3D's numerical wave tank is presented in Fig. (2.1b) to provide an impression of the dimensions of a typical OWC. The OWC is placed in a 3D numerical wave tank 20 m long, 1 m wide and 2.20 m high in a water depth of $d = 0.92$ m. The device chamber is 1.275 m high with a 0.355 m high air column. The front wall draught $a = 0.15$ m, front wall thickness $\delta = 0.04$ m, chamber length $b = 0.64$ m and the width of the vent is $V = 0.05$ m. The OWC device extends along the entire width of the 3D numerical wave tank. The vent is now a slot running along the entire length of the OWC as in the experiments by Morris-Thomas et al. (2007). This configuration of the OWC shows resonant behavior with maximum hydrodynamic efficiency at an incident wavelength of $L = 4.07$ m or a wave frequency of $f = 0.584$ Hz.

OWC devices have been studied using analytical methods, time-domain methods using boundary element equations, few experimental investigations in wave flumes and some field trials. Since the data from the field trials is scarcely available, most of the current knowledge regarding OWCs comes from the experimental investigations and the analytical models. There is some recent literature where CFD modeling of OWC devices is presented. The modeling approaches for OWC devices in current literature can be broadly classified into two major categories: lumped parameter models and CFD-based models. Experimental investigations have also been carried out to validate the different theoretical models proposed in literature and to gain more insight into the working of an OWC device.

2.2.1 Lumped parameter modeling

The lumped parameter modeling approach can handle OWC devices through three different routes:

- applying the equations for rigid body motion from linear hydrodynamic approximation to the water column which is assumed to be a weightless piston.
- considering the pressure distribution on the free surface of the oscillating water column.
- expressing the working of the OWC using coefficients for excitation and radiation to the hydrodynamic pressure of the water column and the air flow.

Early mathematical models analyzed bottom fixed OWC devices using the equations for rigid body motion to evaluate the hydrodynamics involved. Evans (1978) calculated the efficiency of a wave energy converter device modeled as a pair of parallel vertical plates with a float connected to a spring-dashpot on the free surface as the wave energy absorber. This model considered the length of the chamber to be small compared to the waves and that the water column moved like a weightless piston resulting in a one-dimensional rigid motion of the free surface. This representation of an OWC device provides a good general understanding the working principles, response of the device to various incident waves and occurrence of resonance under ideal conditions. But in reality, a non-uniform motion of the free surface in the chamber can occur under the action of different incident waves, due to the coupled motion of the water column and the air column. A similar approach was used by Evans (1981) to mathematically express the hydrodynamics of rigid oscillating bodies.

An improvement over considering the water column to be a weightless rigid body is the pressure distribution model which includes the spatial variation of the free surface in the OWC chamber due to the surface pressure. Evans (1982) presented such a mathematical model and it is considered more realistic as it accounts for the non-uniform motion of the free surface seen in experimental investigations. Also, this method is found to provide a better prediction of the non-linear aspects involved in OWC energy converters such as PTO devices, optimizing techniques to maximize power capture and to compute the hydrodynamics in the time domain (Evans and Porter, 1995). Though this provides a better description of the OWC device, it is based on the linear water wave theory, which is valid only at very low incident wave heights and does not take into account the rotation of the flow and the viscous losses. The water depth is considered to be infinite and the depth of immersion of the device to be negligible. So, it does not completely cover the fluid physics involved in the near-field of an OWC device.

Sarmento and Falcão (1985) developed a theory to evaluate the hydrodynamic efficiency of an OWC considering a finite water depth, air compressibility and linear

and non-linear PTO devices. The wave diffraction due to the immersed part of the OWC device was ignored except for the reflective back wall of the device. The model predicted that with a non-linear PTO, the OWC efficiency was only marginally lower compared to the linear system. It was also proposed that the efficiency of the device could be improved by incorporating phase control, where the pressure developed in the chamber is controlled independently of the flow rate.

The main feature of the lumped parameter modeling approach is that it is based on linear wave theory, covering small incident wave heights, linear hydrodynamics considering irrotational flow and an inviscid fluid. The ideal conditions considered in these models result in a maximum hydrodynamic efficiency of 100% (Evans and Porter, 1995), as the various hydrodynamic losses are not considered in these models.

2.2.2 Experimental investigations

In order to obtain a better understanding of an OWC device, several researchers carried out experimental investigations and added to the knowledge gained through the mathematical analysis of oscillating rigid bodies and surface pressures. Sarmento (1992) carried out wave flume experiments on an OWC using a small incident amplitude-to-wavelength ratio and validated the theory presented by Sarmento and Falcão (1985). The experimental investigations studied the effect of a linear PTO system by placing porous filter material on the vent in the roof of the OWC chamber. Orifice plates were used to represent non-linear PTO systems. The hydrodynamic efficiency of the OWC device, η_{owc} (referred to as power ratio by Sarmento (1992)) was determined using the formula:

$$\eta_{owc} = \frac{1}{P_{in}} \frac{1}{T} \int_0^T p_c(t) \cdot q(t) dt \tag{2.1}$$

where, P_{in} is the incident wave energy flux, T is the wave period, p_c is the chamber pressure developed in the OWC device and q is the volume flow rate of air through the vent.
The incident wave energy flux is calculated as the product of the total incident wave energy and the wave group velocity:

$$P_{in} = \frac{1}{2} \rho g \left(\frac{H}{2} \right)^2 c_g \tag{2.2}$$

where ρ is the density of water, g is the acceleration due to gravity, H is the incident wave height and c_g is the group velocity. Due to the assumptions of an inviscid fluid and irrotational flow in the theory (Sarmento and Falcão, 1985), the experimental hydrodynamic efficiency in Sarmento (1992) was found to be lower than the theoretical prediction and never reached the predicted value of unity at resonance. So, it was observed from these experiments that the hydrodynamic efficiency of an OWC device in reality can never be 100%, where all the incident wave power is absorbed by the OWC and transferred to the PTO system.

Thiruvenkatasamy and Neelamani (1997) studied the hydrodynamics of a Multi-resonant OWC (MOWC), where two parallel projecting side walls are provided on the two sides of the device, projecting in the direction of the incident waves. This design feature of the OWC is expected to provide a higher wave power absorbing capacity to the OWC. The experiments investigated the effect of the incident wave steepness (H/L), relative water depth (d/L) and the area of the vent in the OWC roof relative to the plan area of the free surface in the chamber (A_{cs}/A_{fs}). The damping provided by the vent is used to represent the PTO system in the experiments. A smaller vent area with respect to the free surface area signifies a higher external damping over the device chamber and a larger vent represents a lower damping. The OWC chamber, the oscillating water free surface, the corresponding motion of the air and the damping from the PTO system together form a tightly coupled, inter-related system. The parameter A_{cs}/A_{fs} gives an approximation of the PTO system required for efficient absorption of the incident wave power by the OWC, which is delivered to the PTO system for conversion to electrical energy. The experiments found that for vent areas greater than 0.81% of the free surface area, there was a dramatic drop in the hydrodynamic efficiency of the OWC device. This was attributed to the low pressures developed in the chamber when the area of the vent was larger than 0.81% of the free surface area. It was also found that an increase in the incident wave steepness resulted in a decrease in the hydrodynamic efficiency of the MOWC. From these experiments, it was clear that predictions from previous analytical techniques could be wrong due to the assumptions made in the governing equations (Thiruvenkatasamy and Neelamani, 1997). Also, the influence of the PTO damping on the hydrodynamic efficiency of the device was found to be an important issue and the need for further research by accounting for the fluid physics with fewer assumptions was seen.

Further, Morris-Thomas et al. (2007) carried out experiments to determine the influence of wall thickness, shape of the front wall and the draught of the front wall for various wave parameters on the hydrodynamic efficiency of an OWC device. They reported that the front wall geometry did not have a major influence on the maximum hydrodynamic efficiency of the OWC obtained at resonance, but affected the overall shape and the bandwidth of the hydrodynamic efficiency curve over the range of incident wavelengths. A higher immersion depth of the front wall resulted in a narrower bandwidth of the efficiency curve, where the hydrodynamic efficiency reduced sharply for wavelengths shorter than the resonant wavelength. An increase in the thickness of the front wall also had a similar influence, though the reduction in the bandwidth was lesser than that due to a deeper depth of immersion of the front wall. It was also observed that the efficiency curve was similar for a curved front wall lip and for a square front wall lip. The major difference due to the shape of the front wall lip was seen at the resonance wavelength, where the OWC with the hydrodynamically smooth curved front wall lip produced a higher hydrodynamic efficiency. It was concluded that for longer incident wavelengths, the local geometric features do not have a significant influence on the wave power absorption. These features become more important closer to the resonant wavelength and the wavelengths shorter than the resonant wavelength.

2.2.3 Time-domain methods

The experimental investigations discussed in the previous section contributed to a great extent to the field of OWC hydrodynamics. In order to build upon this knowledge, studies with a large number of trials investigating different cases of wave incidence, shape parameters of the OWC and the response of the OWC in these different scenarios are required. It can be difficult and expensive to run such an extensive experimental campaign. This brings the focus back to numerical modeling of the OWC. The analytical methods discussed in Section 2.2.1 are mostly in the frequency domain, based on linear theory and do not account for a large part of the fluid physics, such as viscous effects and rotational flow. To account for the nonlinear effects, the PTO damping and exploring optimal control to increase the hydrodynamic efficiency of the OWC, time domain methods are more suitable compared to the frequency domain methods (Evans and Porter, 1995).

Boundary element methods

One of the numerical methods for time domain modeling prevalently used in the field of offshore hydrodynamics is the boundary element method (BEM). In these methods, boundary integral equations are solved to evaluate the boundary values to the solution of the governing partial differential equations. The approximate solution of the boundary value problem by BEM methods provides an exact solution of the differential in the domain, but they require an explicit knowledge of the fundamental solution of the differential equation, which is available for only linear partial differential equations.

Wang et al. (2002) investigated the hydrodynamics of an OWC using a BEM based on the Wehausen and Laitone (1960) shallow water Green's function. The effects of the bottom slope were included using a linearized approximation. The numerical results were compared to experimental data and a good agreement was obtained for the free surface oscillation in the chamber, but the chamber pressure and the hydrodynamic efficiency of the OWC was under-predicted, especially around resonance. This was attributed to the importance of the non-linear effects, which become important when the OWC is in resonance.

Delauré and Lewis (2003) presented 3D hydrodynamic modeling of an OWC device using BEM, solving the regular wave interaction with the OWC using a first-order mixed distribution panel method. The study focused on the diffraction effects and obtained good agreement to experimental results for mean diffraction response, total amplification of the free surface oscillation and the pneumatic damping, but only very small wave heights were tested. The internal free surface was represented by an approximation based on two modes of oscillation. Delauré and Lewis (2003) proposed that though the hydrodynamic coefficients produced from this method could match the experimental results, this may not produce an accurate representation of the free surface behavior.

Rezanejad et al. (2015) studied a dual-chamber OWC, where two OWC chambers are placed adjacent to each other with independently working turbines in the two chambers. A standard boundary integral equations approach is used to solve the velocity potential. They showed that due to the radiation interaction between the between the two chambers of the device, maximum power absorption can occur at multiple frequencies unlike in the conventional OWC with a single chamber. The study ignored viscous effects and assumed irrotational flow, but stressed that these effects are to be taken into account to obtain a more realistic prediction of the system behavior.

Computational Fluid Dynamics models

Due to the amount of detail provided by CFD models as discussed in Section 2.1.2, CFD-based numerical wave tanks have been used by several authors to investigate the hydrodynamics of an OWC device. In this approach to model an OWC device, the full fluid dynamical system is solved by discretizing the fluid domain. With higher-order discretization and methods for sharp representation of the free surface, a CFD-based numerical wave tank can be used to investigate the near-field hydrodynamics of an OWC device in detail. Wave interaction with the device over a wide range of wave steepnesses, viscous and fluid rotational effects, effect of PTO damping, the application of control mechanisms to improve wave power absorption by an OWC device can be studied in detail.

Sentürk and Özdamar (2011) used the commercial CFD code Fluent to simulate an OWC device in a numerical wave tank. They compared the numerical results for the free surface inside and outside the chamber and air velocity through the vent with an analytical model, but their results differed from the analytical results in phase and amplitude of oscillation of these parameters.

Zhang et al. (2012) simulated the experiments presented by Morris-Thomas et al. (2007) with a CFD-based numerical model and presented the variation of pressure and free surface elevation in the device chamber, though without comparison to experimental data. They reported a reasonable agreement to experimental data for hydrodynamic efficiency of the OWC, with a slight over-prediction, as the model could not handle the complex pressure changes in the chamber. They used a level set-based numerical wave tank with a combination of the upwind scheme and the central difference scheme for convection discretization. In the case of wave propagation and wave interaction with structures, it is essential to have a higher order discretization than the second-order central difference scheme to ensure a more accurate solution. In addition, the high air velocities in the OWC vent due to its small width relative to the cross sectional area of the device chamber also requires special handling.

López et al. (2014) carried out numerical investigations to optimize the PTO damping on an OWC chamber using a 2D CFD model with the VoF algorithm to capture the free surface. They carried out simulations with regular and irregular waves. Their study concluded that there exists an optimal value of PTO damping to

extract the maximum possible wave energy for a given incident wave. PTO damping was expressed by a parabolic equation to relate the damping coefficient to the chamber pressure and the volume flow rate of air through the OWC vent. They also concluded that the incident wave height does not have a significant influence on the performance of the device, but only waves of low incident steepnesses ($H/L \approxeq 0.014$-0.029) were investigated.

Thus, amongst the methods currently used to study the hydrodynamics of an OWC device, lumped parameter models provide a basic approximation of the device behavior, BEM-based methods can account for PTO damping and be used to study optimization of the PTO damping. CFD methods are relatively new in current literature. With recent advances in computational power enabling researchers to run simulations accounting for most of the physics in a detailed manner, more insight into the hydrodynamics of an OWC in the near-field, accounting for the viscous losses, vortex formation under the front wall of the device and hydrodynamic effects from the PTO damping is gained. Thus, further studies on the OWC using CFD-based numerical wave tanks can provide more details of the near-field flow features, which are critical for the design and performance of an OWC device.

After a thorough review of the literature on numerical wave tanks and numerical modeling of OWC devices, the following points are taken into account for the PhD study:

- A numerical wave tank requires high-order discretization schemes to account for the complex flow regime due to wave propagation and wave interaction with structures.
- The free surface motion and the chamber pressure in the OWC are the most important aspects in the study of OWC hydrodynamics and a numerical model has to accurately calculate these parameters, with few assumptions.
- PTO damping plays a significant role in the power absorbed by an OWC. This has to represented in a realistic manner to reflect the effect of the damping on the hydrodynamics of the OWC device.
- There are several open questions regarding the effect of bottom topography, the flow features in front of the device, effect of high steepness incident waves and the effect of air compressibility.

Investigation of an OWC device using a CFD-based numerical model can definitely add to the knowledge regarding its operation and design. In order to address the issues mentioned above, the numerical model should be able to represent wave propagation, wave interaction, wave transformation in the coastal zone and the free surface features in an accurate manner. This problem is dealt with in this PhD study through the development of a CFD model focused on wave propagation and an accurate representation of the free surface. The application of the CFD model to a generic OWC device is studied and the model is validated to perform further research into the hydrodynamics of an OWC device deployed in the coastal region.

Chapter 3

Summary of Major Results

The thesis work is presented as a collection of journal papers prepared during the course of the PhD study. Each paper validates the numerical model by investigating different problems in the field of coastal and marine engineering. Further investigations are carried out using the numerical model to obtain deeper insights into the different wave interaction phenomena dealt with on each paper. This includes studies regarding high steepness wave diffraction around a single and multiple cylinders; wave shoaling, breaking and decomposition over a submerged bar and breaking wave interaction with a single and pair of tandem vertical cylinders. The specialized case of the OWC is then simulated and the model is validated by comparisons to experimental data from Morris-Thomas et al. (2007). The interaction of high steepness waves with an OWC, the effect of PTO damping, air chamber volume and compressibility is investigated to obtain a better understanding of the OWC hydrodynamics using the CFD model. The following section presents a summary of the results presented in the papers appended to the thesis.

3.1 Paper Overview

3.1.1 Paper 1: A New Level Set Numerical Wave Tank with Improved Density Interpolation for Complex Wave Hydrodynamics

In this paper, the complete description of the numerical model used in this study with several benchmark applications in the field of coastal engineering is presented. The fluid dynamics associated with wave propagation and wave interaction with structures is very computationally demanding and requires high-order discretization schemes coupled with other numerical techniques to produce accurate results in a computationally efficient manner. The salient features of the numerical model are:

- conservative fifth-order finite difference Weighted Essentially Non Oscillatory (WENO) (Jiang and Shu, 1996) scheme for convection discretization.

- third-order Runge-Kutta scheme (Shu and Osher, 1988) for time advancement.
- level set method (Osher and Sethian, 1988) for the free surface.
- Chorin's projection method (Chorin, 1968) for pressure treatment.
- pre-conditioned BiCGStab (van der Vorst, 1992) solver for the Poisson equation.
- staggered Cartesian grid for tight velocity-pressure coupling.
- local directional ghost-cell Immersed Boundary Method (IBM) (Berthelsen and Faltinsen, 2008) adapted to three-dimensions for complex boundaries.
- MPI parallelization for execution on high performance computing systems.
- adaptive time stepping scheme to satisfy the Courant-Friederichs-Lewy (CFL) criterion for numerical stability.

The numerical recipes listed above were chosen in order to put together the best possible combination of the available numerical techniques and develop a numerical wave tank that can simulate wave propagation and wave-structure interaction in a realistic manner. The numerical model, REEF3D was tested on the Norwegian Metacenter for Computational Sciences (NOTUR) supercomputing facility at NTNU, *Vilje* which has 1404 nodes with two 8-core processors on each node with a total of 22464 cores. The parallel efficiency of the code was tested with a 2D numerical wave tank 62 m long and 4 m high with a grid size $dx = 0.005$ m totaling 9.92 million cells and a 3D numerical wave tank 250 m long, 5 m wide and 8 m high with grid size $dx = 0.1$ m totaling 10 million cells. The parallel speedup curves shown in Fig. (3.1) show that the code obtains almost ideal speedups even for a large number of processors for both 2D and 3D numerical wave tanks.

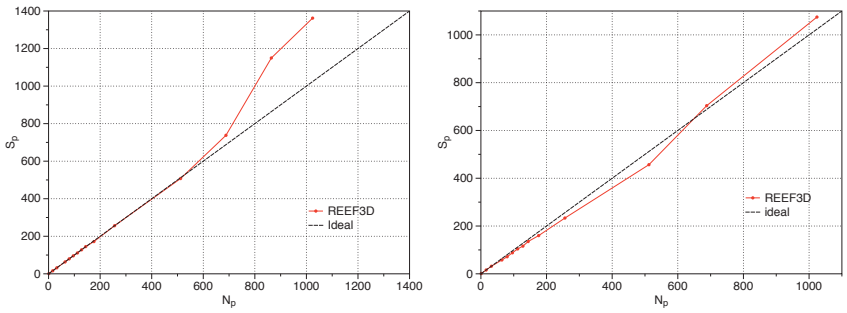

(a) 2D wave tank (b) 3D wave tank

Figure 3.1: Parallel speedup for REEF3D on the supercomputer Vilje at NTNU

In a two-phase numerical wave tank, there is a large jump in the density of the fluids at the interface as the density of water is several times higher than the density

of air. Also, a staggered grid approach needs the value for density at the cell faces for the calculation of the Poisson equation. In current literature, the density at the cell centers is determined using a regularized Heaviside function around the interface over an interface thickness of $\epsilon = 1.6dx$ on both sides of the interface. Then, the density at the cell faces is interpolated through simple averaging of the fluid densities at the centers of two neighboring cells. The authors observed that this two-step strategy can result in small scale oscillations on the free surface in the presence of low steepness waves as shown in Fig. (3.2a). This discrepancy is not seen for other free surface flows such as open-channel flow. The problem was identified to occur when the free surface was mildly sloped with respect to the orientation of the gridlines in the presence of a vertical velocity component, as is the case for waves. As a remedy, REEF3D calculates the density at the cell face in a single step with the smoothed Heaviside function over an interface thickness of $\epsilon = 2.1dx$, avoiding the oscillations on the free surface as seen in Fig. (3.2b).

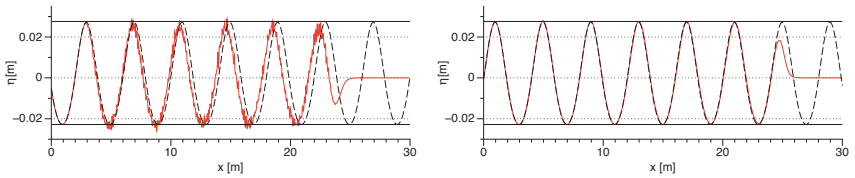

(a) conventional density calculation at cell centers producing free surface oscillations

(b) REEF3D density calculation at cell faces

Figure 3.2: Free surface oscillations due to density interpolation at the interface in a numerical wave tank

Wave generation and absorption in the numerical wave tank is handled using the relaxation method (Mayer et al., 1998). Here, the values for the fluid velocity and the free surface as prescribed by the required wave theory is moderated with the computational values in the numerical wave tank to smoothly introduce waves, using a relaxation function. At the numerical beach, the wave energy is absorbed by reducing the fluid velocities to zero and the bringing the free surface to the still water level. This is achieved using the relaxation function presented by Jacobsen et al. (2012). This method is found to be very accurate for wave generation and is efficient at absorbing waves at the numerical beach. The disadvantage with this method is that one wavelength long wave generation zone and a two wavelength long wave absorption zone have to be reserved from the domain. This can be a problem when dealing with very long waves of over 5 m length, where effectively 15 m of the wave tank are reserved for wave generation and absorption. The authors consider that computational efficiency of the numerical model and the quality of the waves generated justify the use of this approach in the numerical wave tank. Application of active wave generation and absorption or a combination of the relaxation method for wave generation and active absorption for the numerical beach are to be explored in future works.

Grid convergence and time step convergence tests are carried out with low and high steepness waves to test the general performance of the numerical wave tank. A 2D wave tank is used and waves of wavelength $L = 2.0$ m and wave height $H = 0.1$ m are generated on grid sizes of $dx = 0.05$ m, 0.025 m, 0.01 m and 0.005 m with CFL= 0.1. Also, the simulations are repeated with $dx = 0.01$ m for CFL=0.5, 0.25, 0.1 and 0.05. These simulations testing the wave propagation at a high steepness are used to identify the grid and time resolutions required to obtain accurate results under demanding conditions. It is found that even for high steepness waves with wave height $H = 0.1$ m and wavelength $L = 2.0$ m, a grid size of $dx = 0.01$ m, the wave propagation in the wave tank matches the analytical waveform prescribed by the $5th$-order Stokes wave theory. Only a slight deviation in the wave phase in seen for a larger grid size of $dx = 0.025$ m. In the simulations for time step convergence, it is found that some phase shift and wave damping is seen for CFL=0.5 and result converges to the theoretical expectation for CFL=0.1 and no further change is seen on further reducing the CFL number to 0.05.

The numerical wave tank resulting from the numerical methods described above is then tested for various benchmark problems in the field of coastal and marine engineering such as solitary wave interaction with a rectangular abutment, calculation of periodic wave forces on a single cylinder, wave propagation over a submerged bar and wave breaking on a slope. The results for these benchmark cases compared favorably to experimental data, showing that the developed numerical model is capable of accurately representing the fluid physics associated with wave propagation and wave interaction with structures. For further details, please refer to **Paper 1** in Chapter **5**.

3.1.2 Paper 2: CFD Investigations of Wave Interaction with a Pair of Large Tandem Cylinders

In this paper, the CFD model REEF3D is used to investigate wave forces on a single and a pair of large tandem cylinders under the action of incident waves of different steepnesses. The scenario of wave interaction with several coastal engineering constructions including OWC devices occurs at lower values of Keulegan-Carpenter numbers (KC$<$ 2). Under these conditions, when the ratio of the characteristic length of the structure D to the incident wavelength L is large ($D/L > 0.2$), the wave forces are inertia dominated. Linear potential theory is generally used to evaluate wave forces in this scenario, but they are applicable only under low incident wave steepness. This paper investigates the wave forces on a single cylinder at different incident wave steepnesses. A study of the diffraction regime around a single large cylinder and pair of large tandem cylinders can shed some light on the variations of the wave elevations around two OWCs deployed in an array and the wave forces on the OWCs.

Simulations are carried out in a 3D numerical wave tank 15 m long, 5 m wide and 1 m high with a water depth $d = 0.5$ m with incident waves of wavelength $L =$ 2.0 m. The incident wave height is varied in small increments resulting in wave

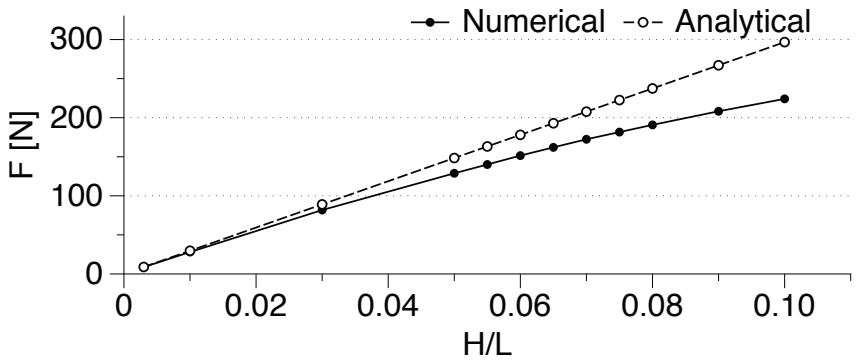

Figure 3.3: Comparison of numerical and analytical wave forces on a single cylinder at different wave steepnesses

steepnesses of $H/L = 0.003$, 0.01, 0.03, 0.05, 0.055, 0.06, 0.065, 0.07, 0.075, 0.08, 0.09 and 0.1 to study the influence of the wave steepness on the wave forces on the single cylinder. It is found that the MaCamy-Fuchs theory (MacCamy and Fuchs, 1954) over-predicts the wave forces at higher wave steepnesses and the gradual deviation of the numerical results from the analytical prediction is presented in Fig. (3.3). The study of the relative wave crest height (η/η_{ci}), the wave trough depth (η/η_{ti}) in front of the cylinder, the phase difference between the wave elevations in front and behind the cylinder and front and beside the cylinder reveals a difference in the wave diffraction process around a single cylinder for low and high incident wave steepness. In the case of low steepness incident waves with $H/L = 0.003$, the wave is symmetrical about the still water level with $\eta/\eta_{ci} = \eta/\eta_{ti} = 1.72$. Whereas in the case of high steepness waves with $H/L = 0.1$, $\eta/\eta_{ci} = 1.55$ and $\eta/\eta_{ti} = 0.95$, showing some asymmetrical behavior as expected from a higher-order, high steepness wave. It is notable though, that the relative crest height is lower in front of the cylinder for high steepness incidence in comparison to the relative crest height in front of the cylinder for low steepness waves. In an inertia-dominated regime, this shows that the total pressure acting on the cylinder is relatively lower at a higher incident wave steepness than expected by linear theory. In addition, the phase difference for the wave in front and beside the cylinder is 0.24π and the phase difference for the wave in front and behind the cylinder is 0.78π for low steepness incident waves. For high steepness waves, the phase difference in front and beside the cylinder is 0.20π and the phase difference in front and behind the cylinder is 0.80π. This shows that the high steepness waves move faster around the upstream half of the cylinder compared to the low steepness waves but they are slower to move around the downstream half of the cylinder compared to the low steepness waves. This points towards a higher deceleration of the water particles around the downstream half of the cylinder in the case of the high steepness waves. This leads to a difference in the diffraction regime around the cylinder, resulting in a lower force than predicted by linear theory.

The study is extended to investigate the wave forces on a pair of tandem cylinders

placed at different distances of separation and the incident wave steepness is varied in the same manner as for the single cylinder. A similar trend in the wave forces is seen here, with the numerical results matching the analytical predictions at lower wave steepnesses and then gradually deviating from the analytical prediction for higher wave steepnesses. The difference in the diffraction regime is seen from Fig. (3.4), where the wave elevation in the part of the numerical wave tank around the pair of tandem cylinders separated by a distance of 0.8 m is shown for low and high steepness wave incidence. The bending of the wavefront due to wave diffraction at low wave steepness is seen in Fig. (3.4a), whereas the formation of conspicuous semi-circular secondary wave fronts behind the first cylinder is seen in Fig. (3.4b) for high steepness wave incidence.

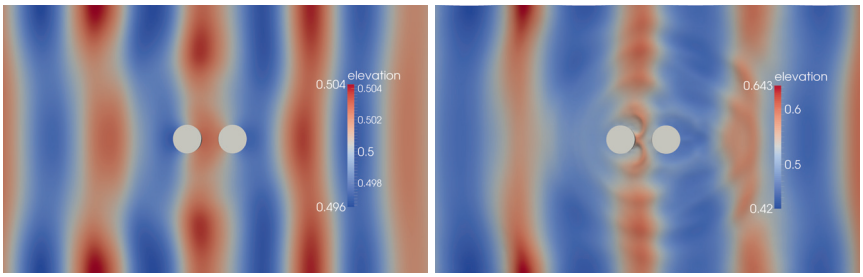

(a) low steepness wave $H/L = 0.003$ (b) high steepness wave $H/L = 0.1$

Figure 3.4: Free surface elevations around a pair of tandem cylinders for low and high steepness incident waves

Thus, the non-linear effects due to the incident wave steepness have a significant effect on the wave forces on cylinders even at a low KC number, inertia-dominated force regime. The difference seen in the wave diffraction process is seen to lower the wave force on the cylinder as compared to predictions from potential theory. This has implications for the design an OWC device. It has been presented in earlier literature that a larger thickness of the front wall reduces the hydrodynamic efficiency of an OWC device. The knowledge of a lower than expected wave force at a higher incident wave steepness can be used to reduce the thickness of the front wall of the OWC device, without harming the structural integrity of the device. Also, the wave transmission characteristics around cylinders placed in tandem can be used to study the arrangement of OWCs in an array, so as to reduce the wave forces on a device and to avoid large forces due to resonant phenomena in wave interaction with closely spaced objects. For further details, please refer to **Paper 2** in Chapter **5**.

3.1.3 Paper 3: Upstream and Downstream Cylinder Influence on the Hydrodynamics of a Four Cylinder Group

In this paper, wave interaction between four closely spaced large cylinders is studied, where the cylinders arranged in the form of a square with two opposite corners along

the direction of wave propagation. The focus of the investigation is the phenomenon of wave near-trapping and the influence of the cylinders along the direction of wave propagation on the wave hydrodynamics of the group. Wave near-trapping refers to the phenomenon where only a small amount of scattered wave energy in the region between closely placed cylinders is radiated outwards and a near standing wave is formed. The free surface is amplified close to the cylinders and is associated with large pressures on the cylinders, resulting in large wave forces on the cylinders. This phenomenon occurs for certain combinations of incident wavelength, cylinder group arrangement and spacing. In the case of OWC devices, which operate on the principle of a water column being excited by incident waves, this resonant phenomenon may be used to an advantage when a deployed in a closely placed group. But, the occurrence of this phenomenon and the potential increase in the wave forces on the devices due to wave near-trapping have to be further studied.

In order to study wave near-trapping and the influence of the cylinders along the direction of wave propagation, simulations are carried out with three different arrangements: Setup 1 with four cylinders; Setup 2 without the downstream cylinder; Setup 3 without the upstream cylinder. The three different setups are illustrated in Fig. (3.5). It was shown by Linton and McIver (2001) using potential theory, that wave near-trapping occurs for a four cylinder arrangement with cylinders of diameter $D = d$, the water depth and at the corners of a square of side 2D with two corners inline with the the direction of wave propagation for a diffraction parameter of $kr = 1.70$, where k is the wave number and r is the radius of the cylinder. This setup is directly used in the numerical simulations to investigate wave near-trapping and the effect of the inline cylinders on the cylinder group. Also, simulations are carried out for three different incident wave steepnesses $H/L = 0.004$, 0.06 and 0.1 for all the three arrangements to study the effect of incident wave steepness on wave near-trapping and the diffraction regime. Two incident wavelengths are selected, corresponding to diffraction parameter $kr = 1.70$, for wave near-trapping and $kr = 0.94$, away from wave near-trapping.

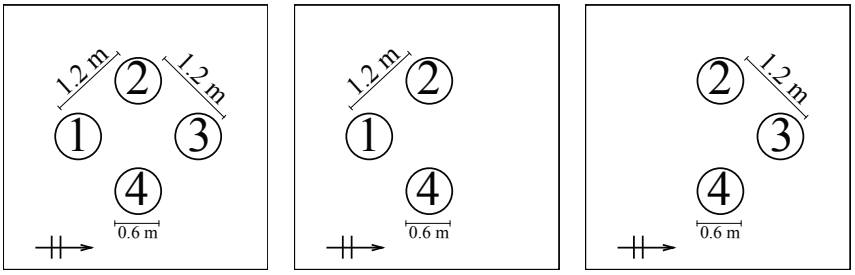

(a) Setup 1 (b) Setup 2 (c) Setup 3

Figure 3.5: Three setups used to investigate wave near-trapping and influence of inline cylinders on the wave hydrodynamics of a four cylinder group

The numerical results at a low wave steepness of $H/L = 0.004$ for the diffraction

parameter of $kr = 1.70$ reproduced the wave near-trapping predicted analytically. The wave force on the upstream cylinder is found to be two times the force on a single cylinder (F_0). Further, the upstream and downstream cylinders are removed from the group and the wave forces on the remaining cylinders are calculated. The cylinders on the diagonal perpendicular to the direction of wave propagation experienced $1.1F_0$ in all the three configurations. The downstream cylinder experienced similar forces of $1.60F_0$ in all three configurations. Thus, under conditions leading to wave trapping, the upstream cylinder is most influenced in the cylinder group by the presence of a downstream cylinder, experiencing $2.00F_0$ in presence of the downstream cylinder and $1.30F_0$ in the absence of the downstream cylinder.

Away from conditions leading to wave near-trapping, for $kr = 0.94$, the presence of the upstream leads to lower forces on the central cylinders and a higher force on the downstream cylinder in comparison to when the upstream cylinder is absent. Further, simulations with higher wave steepnesses of $H/L = 0.06$ and 0.1 are carried out and the phenomenon of wave near-trapping is found to break-down for $kr = 1.70$ and the wave forces are lower than expected using the analytical formula by Linton and McIver (2001). For further details, please refer to **Paper 3** in Chapter **5**.

3.1.4 Paper 4: Shoaling and Decomposition of Breaking and Non-Breaking Waves over a Submerged Bar

In this paper, the wave transformation processes including shoaling, breaking and decomposition of a wave as it propagates over a submerged bar is studied. In the case of coast-based OWC devices, the incident wave energy on the device can vary from the available offshore wave energy due to the local effects of shoaling and wave breaking in the near-field region, which cannot be completely accounted for using spectral wave models. It is also essential to understand the wave transformation and the resulting energy transmission in the near-shore region that can be affected using submerged obstacles with a view on coastal protection.

The energy transfer between the higher harmonics formed due to wave decomposition and the total energy transmitted across the bar is investigated for both non-breaking and breaking waves in this study. The numerical setup for the submerged bar is the same as that in the experimental investigation by Beji and Battjes (1993) and the numerical results for the free surface are compared with the experimental data for two cases of non-breaking waves and one case of spilling breaking wave. Good agreement is seen for both the phase information and the amplitude of the decomposed harmonics produced after propagation over the submerged bar, for both non-breaking and spilling breaking waves.

An observation made in the course of this study is that spilling breakers are seen on the bar crest for an Iribarren number $\xi = 1.0623$ and plunging breakers for $\xi = 0.9547$. According to previous classifications for wave breaking on an emerged slope (Battjes, 1974), these values for the Iribarren number correspond to plunging breaking, whereas for wave breaking over a bar, both spilling and plunging waves are

seen. Thus, the original classifications for wave breaking over an emerged beach can not be directly applied to wave breaking on a submerged bar and further studies on wave breaking on a bar are required to develop classification applicable to this case.

The energy transfer amongst the harmonics is studied using the power spectral density at various locations along the submerged bar for waves of period $T = 2.5$ s. The variation of the power spectral density of the fundamental frequency during propagation over the bar for the different wave heights considered in the study is presented in Fig. (3.6a). It is seen that for the lowest incident wave height studied, $H_1 = 0.022$ m, 76% of the energy is lost from the fundamental frequency ($f_0 = 0.4$Hz) after propagation over the bar. As the incident wave height is increased to $H_2 = 0.035$ m, $H_3 = 0.042$ m and $H_3 = 0.052$ m, the about 90% of the energy is lost from the fundamental frequency.

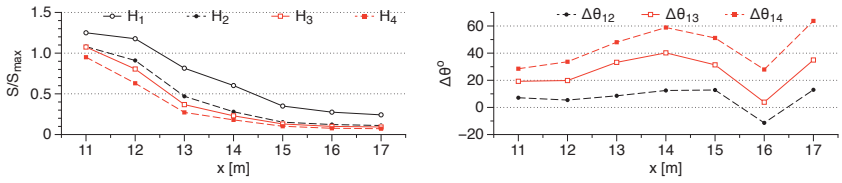

(a) power spectral density for the fundamental frequency at various locations

(b) phase difference between the primary wave crest of the different incident waves

Figure 3.6: Variation of the power spectral density for the fundamental frequency and the phase difference between primary crests of the different incident waves during propagation over the submerged bar

The wave transformation for different wave heights over the bar is studied using the relative phase difference between the primary wave crest of the lowest incident wave and the other waves investigated in the study at different locations along the bar. Figure (3.6b) shows that the higher incident waves move faster than the lower incident waves as they propagate over the upward slope of the bar. This is attributed to higher shoaling of the higher incident waves. In shallow water, the wave celerity is directly related to the free surface elevation and a higher shoaling leads to higher wave celerity. All the incident waves slow down over the downward slope and a sharp minima is seen in Fig. (3.6b) at $x = 16$ m, on the downward slope of the bar, where the phase difference between the primary crest of the lowest non-breaking wave and the higher incident waves, is a minimum. At the toe of the bar, the phase differences return to the values at obtained at the end of the bar crest $x = 14$ m.

On further analysis of the variation of the energy content in the different harmonics, it is observed that most of the energy which is in the fundamental frequency at the toe of the bar in the beginning, moves to the first harmonic as the wave propagates over the upward slope, then into the third harmonic when the wave is on the flat bed and is finally concentrated in the second harmonic to the end of the bar. This is seen as a general trend for all the waves irrespective of incident wave height or type of wave breaking. During this energy transfer process, the breaking waves lose

most of their energy after the flat bed, where wave breaking occurs. In the case of the smallest non-breaking wave, $H_1 = 0.022$ m the loss of energy is the least and loses only about 40% of the total initial incident energy and has most of its energy in the second and the third harmonics over end of the downward slope of the bar. For further details, please refer to **Paper 4** in Chapter **5**.

3.1.5 Paper 5: Breaking Wave Interaction with a Vertical Cylinder and the Effect of Breaker Location

This paper investigates the interaction of plunging breaking waves with a vertical cylinder for different incident wave heights and location of the cylinder with respect to the wave breaking location. Breaking wave interaction with structures involves complex free surface transformations and evaluating the total breaking wave forces are challenging due to the impulsive nature of the force. The total breaking wave forces also depend on the geometric and kinematic properties of breaking waves, and the distance between the breaking location and the structure.

A 3D numerical wave tank is 54 m long, 5m wide and 7m high with a grid size $dx = 0.05$ m resulting in a total of 15.12 million cells. A 23 m long 1:10 slope, reaching a height of 2.3 m is placed 21.0 m, followed by a flat bed extending for 10 m to the end of the tank. A combination of the relaxation method for wave generation and the active absorption (Schäffer and Klopman, 2000) is used to generate and absorbs waves in the wave tank. The cylinder is placed with its center at the top of the slope such that the breaking point of the incident wave with height $H = 1.30$ m, period $T = 4.0$ s and wavelength $L = 20.5$ s, is exactly at the cylinder and the total wave force is calculated. The free surface elevation near the wall of the tank along the frontline of the cylinder and the total wave force is compared to the experimental data from Irschik et al. (2002) and a good agreement is seen in Fig. (3.7).

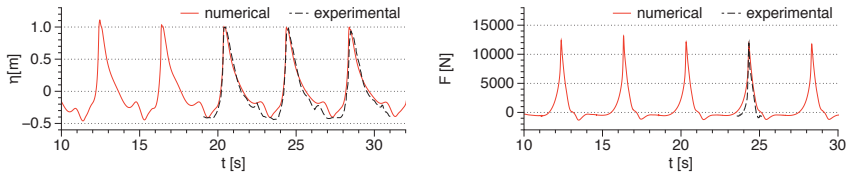

(a) free surface elevation near the wall along the frontline of the cylinder

(b) total breaking wave force on the cylinder

Figure 3.7: Comparison of numerical results with experimental data for breaking wave interaction with a vertical cylinder

Further, the different stages of wave breaking are identified from a 2D numerical wave tank as shown in Fig. (3.8). This is used to place the cylinder at different locations with respect to the breaking point to investigate the wave forces on a cylinder when placed at different distances from the breaking point as identified by Wienke et al. (2000) and Irschik et al. (2002):

1. wave breaking behind the cylinder.
2. wave breaking at the cylinder.
3. overturning wave crest impacting the cylinder at crest level.
4. overturning wave crest impacting the cylinder just below crest level.
5. overturning wave crest impacting the cylinder much below crest level.

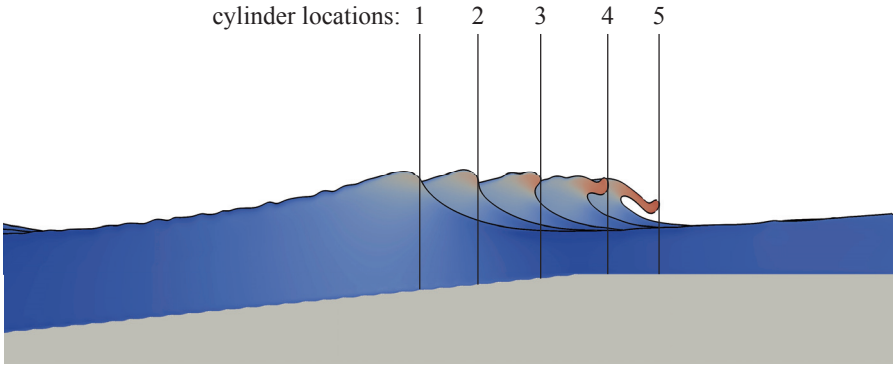

Figure 3.8: Different stages of breaking wave used to identify different locations of the cylinder with respect to the wave breaking point

The numerical results agree with the experimental findings that the maximum breaking wave force is experienced by the cylinder when the breaker tongue impacts the cylinder just below the wave crest level. Further, simulations are carried out with wave heights of $H = 1.44$ m and $H = 1.23$ m and the simulations are carried out for the five different locations described in Fig. (3.8). In all the wave heights simulated, the maximum breaking wave force is calculated for the scenario where the overturning wave crest impacts the cylinder just below the wave crest level. The difference between the maximum and the minimum force calculated for each wave height is 30-35%. This shows that the location of the cylinder with respect to the breaking point is indeed an important factor in the evaluation of breaking wave forces. The simulations also revealed interesting free surface features around the cylinders with an impinging jet forced behind the cylinder and diverging waves around the cylinder after the overturning crest has passed, which could have important consequences on other objects placed in the vicinity.

From the point of view of OWC devices, the evaluation of breaking wave forces is important for the structural design aspects as previously installed prototypes have been destroyed by storms. The knowledge obtained through the simulation of breaking waves on a single vertical cylinder has to be extended to multiple objects placed close together and to investigate the transition in the wave regime from steep non-breaking wave interaction with cylinders to the impact-nature of breaking wave interaction with cylinders. For further details, please refer to **Paper 5** in Chapter **5**.

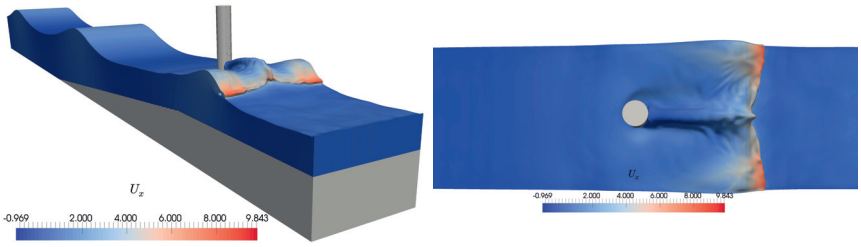

(a) isometric view (b) top view

Figure 3.9: Free surface around the cylinder for the broken wave passing the cylinder after breaking on it

3.1.6 Paper 6: Breaking Wave Interaction with Tandem Cylinders under Different Impact Scenarios

This paper studies the interaction of plunging breaking waves with a pair of tandem cylinders. It builds upon the knowledge gained with breaking wave interaction with a single vertical cylinder in **Paper 5**. The free surface features such as the impinging jet formed behind the cylinder is seen to be different for different wave impact scenarios described in Fig.(3.8). Thus, it can have different consequences for a second cylinder placed behind the first cylinder directly exposed to the breaking wave. So, the influence of the distance of the breaking point from the first cylinder and the distance between the two cylinders on the total breaking wave forces on both cylinders is investigated.

Three locations for the upstream cylinder 1 are chosen: overturning wave crest impacting the cylinder just below the wave crest, wave breaking at the cylinder and wave breaking behind the cylinder. Then, three locations for the second cylinder are chosen for each case, with distances of separation 1D, 2D and 3D. The wave forces on both cylinders in the three cases for each wave impact scenario are calculated. It is observed that the breaking wave force on cylinder 1 are equal or slightly less than the breaking wave force on a single cylinder in every scenario. In the scenario where cylinder 1 experiences the maximum forces, when the breaker tongue impacts the cylinder just below wave crest level, the second cylinder is effectively in the shadow region and it experiences lower forces than the first cylinder. On the other hand, when the wave breaks at the upstream cylinder or behind it, the wave forces on the second cylinder are seen to be higher than the wave force on the upstream cylinder. Thus, the shadowing effect from the upstream cylinder is overcome by the overturning wave crest and the impinging jet formed behind the cylinder, leading to larger forces on the second cylinder.

As an example the wave interaction with the pair of cylinders in the scenario where the wave breaks behind the upstream cylinder with a distance of 3D between the two cylinders is shown in Fig. (3.10). The formation of the impinging water jet due to the meeting of the wave from either side of cylinder is seen in Fig. (3.10a). As the breaking wave propagates further, the wave impacts the second cylinder in

Fig. (3.10b), and the focussing of the breaking wave on cylinder 2 is seen along with the diverging waves formed around cylinder 1 after the passing of the incident wave crest.

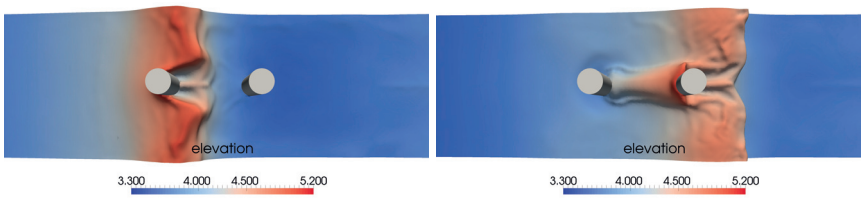

(a) wave impact on the upstream cylinder 1, $t/T = 2.12$

(b) wave impact on the downstream cylinder 2, $t/T = 3.25$

Figure 3.10: Free surface around the cylinders for the scenario where the wave breaks behind the upstream cylinder 1

In this study, it is found that the sheltering effect of the upstream cylinder can be overcome by the breaking wave under certain circumstances, resulting in a larger force on the downstream cylinder compared to the upstream cylinder directly exposed to the incident waves. This is of concern in an OWC device array, where the devices in the second and third rows of the arrays can also be subject to extreme wave events and large forces. The numerical model provides a realistic representation of the complex breaking wave interaction with a pair of tandem cylinders and further work can be carried out to simulate entire OWC farms arranged in arrays and to calculate the breaking wave forces on the individual OWC devices and optimal arrangement strategies to reduce breaking and non-breaking wave forces with maximum possible wave energy absorption. For further details, please refer to **Paper 6** in Chapter **5**.

3.1.7 Paper 7: Numerical Investigations of the Hydrodynamics of an Oscillating Water Column Device

After the validation of the numerical model for various problems in the field of coastal and marine engineering, the wave interaction with an OWC device is investigated with a focus on the hydrodynamics, the motion of the water particles in the near field and the representation of the PTO device in the OWC vent. The numerical results are compared to experimental data from Morris-Thomas et al. (2007) and a good agreement is obtained for the free surface motion, the velocity of the vertical motion of the free surface and the chamber pressure for different incident wavelengths. The wave interaction with the OWC at high and low incident wave steepnesses and the hydrodynamic efficiency of the OWC in these cases is studied.

Due to the oscillating nature of the waves, the air column alternatively changes its direction of motion. In order to account for this, a self-rectifying turbine such as the Wells turbine is generally proposed as the PTO system in an OWC. The

characteristics of a Wells turbine are considered to be fairly linear Falcão and Henriques (2014). The Wells turbine is represented using porous membranes in experimental and numerical model testing. Self-rectifying impulse turbines have also been proposed and tested (Falcão and Henriques, 2014) and these have non-linear characteristics. In experimental model testing the impulse turbines are represented using orifices. in this paper, the PTO system in the vent of the OWC is represented using theory for flow through porous media. In the experiments, the PTO system is represented by a vent of width $V = 0.005$ m. Such a small vent width leads to very high velocities in the vent and can lead to long computational times or to numerical instability. This problem is overcome using the theory for flow through porous media. The chamber pressure p_c and the flow rate q in the experiments for the resonant case is known. Darcy's formula for flow through porous media is then applied to determine the permeability factor $C = 1/k_p$:

$$q = \frac{-k_p A_{cs}}{\mu} \frac{p_c}{L_v} \tag{3.1}$$

where A_{cs} is the cross-sectional area of the vent, μ is the dynamic viscosity of air and L_v is the length of the vent along the direction of air flow.
The value of $C = 1/k_p$ is determined from the above equation and the simulations are carried out for different incident wavelengths and heights. In reality the values for the pressure drop from the turbine and the flow rate are known from the characteristics of the turbine.

Two-dimensional simulations are carried out in the numerical wave tank for different incident wavelengths with a wave height of $H = 0.12$ m and the numerically obtained chamber pressure, oscillation of the free surface in the chamber and the velocity of the motion of the free surface is compared to the experimental data from Morris-Thomas et al. (2007), showing a good agreement. Consequently the hydrodynamic efficiency curve also matches the one presented by Morris-Thomas et al. (2007). Further, simulations are carried out for the different incident wavelengths with uniform wave steepnesses of $H/L = 0.03$ and $H/L = 0.1$ and the hydrodynamic efficiency of the OWC is calculated, plotted with the relative depth parameter κd in Fig. (3.11).

It is observed that for a low incident wave steepness, the hydrodynamic efficiency curve is similar to that obtained in the experiments, which consisted of wave steepnesses between $H/L = 0.024$-0.061. On the other hand, for an incident wave steepness of $H/L = 0.1$, the hydrodynamic efficiency of the OWC is significantly reduced. Thus, for low incident wave steepnesses, the hydrodynamic efficiency is not significantly affected by the incident wave steepness, whereas at a high incident wave steepness, the hydrodynamic efficiency of the OWC is reduced.

It is observed that for the cases resulting in higher hydrodynamic efficiency, the phase difference between the chamber pressure and the vertical velocity of the free surface in the chamber is a minimum. This happens at the resonance wavelength and at wavelengths close to resonance. Moving away from the resonant wavelength, even if the chamber pressure is large for longer incident waves, the velocity of the

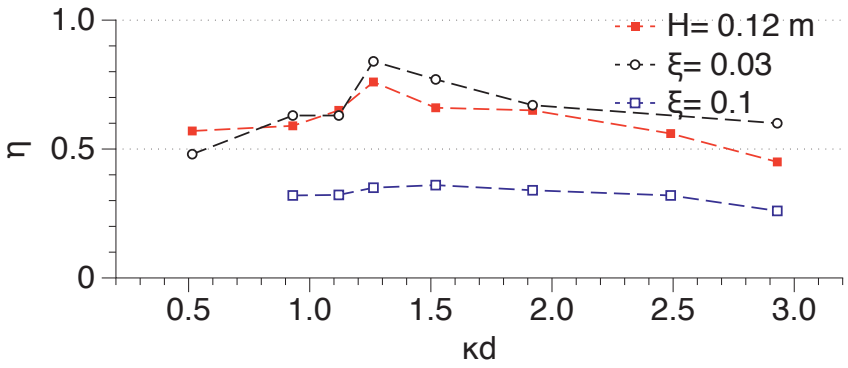

Figure 3.11: Hydrodynamic efficiency of the OWC for wave steepness $H/L = 0.03$, 0.1 and for uniform wave height of $H = 0.12$ m for different incident wavelengths

free surface motion is out of phase to the chamber pressure and the hydrodynamic efficiency of the OWC is reduced. In previous analytical works, the ratio of the length of the chamber to the water depth b/d was considered to be small ($b/d \ll 0.1$) and the resonant angular wave frequency ω_{f0} is determined to be:

$$\omega_{f0} = \sqrt{g/a} \tag{3.2}$$

where a is the depth of immersion of the front wall. Using this equation, the resonant wavelength for the OWC simulated is 0.95 m, whereas from the experiments and the numerical simulations, it is determined to be 4.07 m. This is because in reality, the value of b/d is significant and in this case it is $b/d = 0.70$, resulting in the large deviation of the experimental and numerical results from the analytical prediction.

In the case of high steepness incident waves, the chamber pressures developed are generally large but often out of phase with the vertical velocity of the free surface and thus, the efficiency of the OWC is significantly reduced. The streamlines inside and in front of the OWC for low steepness and high steepness incident waves is examined at the maximum position of the free surface to study the difference in the flow features in Fig. (3.12). It can be seen that the free surface inside the chamber is almost horizontal in Fig. (3.12a) for low steepness incidence, whereas it is more irregular for high steepness incidence in Fig. (3.12b). The streamlines also show strong vortices behind the front wall of the OWC for high steepness waves, whereas the vortices have been pushed to the bottom, towards the back wall for low steepness incident waves. Also the free surface outside the OWC is closer in phase to the motion inside the chamber for low steepness waves than in the case of the high steepness waves. These differences in the hydrodynamics of an OWC at low and high steepness wave incidence result in lower hydrodynamic efficiency of the OWC at high steepness wave incidence.

In conclusion, the paper presented the porous media theory to represent the PTO system in an OWC device which provides good representation of the hydrodynamic

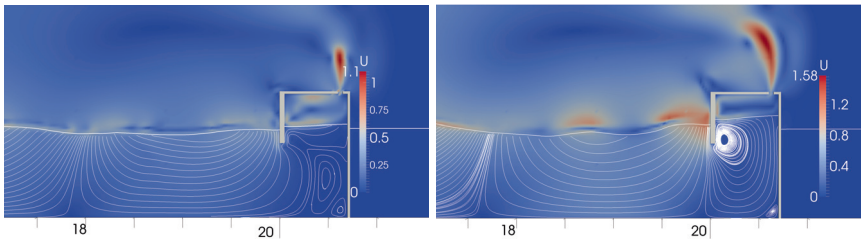

(a) flow features at maximum free surface elevation during low steepness wave incidence

(b) flow features at maximum free surface elevation during high steepness wave incidence

Figure 3.12: Streamlines inside and in front of the OWC for resonant wavelength at low and high wave steepness

effects of the PTO system, while avoiding high velocities resulting from the small size of the vent provided in the model and reducing the computational cost of the simulations. This method also provides a convenient approach to vary the PTO damping without changing the dimensions of the vent. The verification of this method opens future possibilities to actively vary the PTO damping with the incident wavelength to absorb the maximum possible incident wave power. Although in the current study, only a turbine with linear characteristics is studied, the model is capable of representing the non-linear characteristics of an impulse turbine and this can be studied in future investigations. For further details, please refer to **Paper 7** in Chapter **5**.

3.1.8 Paper 8: Numerical Modeling of Power Take-off Damping in an Oscillating Water Column Device

This paper investigates the influence of the PTO damping on an OWC device, building upon the work presented in **Paper 7**. The PTO system in the vent of the OWC is represented using the theory for flow through porous media, validated in Paper 7. The hydrodynamic efficiency of an OWC is investigated for three different wavelengths: the resonant wavelengths and two wavelengths on either side of resonance. Three sets of simulations are carried out, two with a constant incident wave height of $H = 0.06$ m and $H = 0.12$ m and one set with a constant wave steepness of $H/L = 0.03$. Eight different values of the permeability factor C are considered starting with no damping to a very high damping of $10{\times}10^8$ m^{-2}. The equivalent permeability factor in the experiments by Morris-Thomas et al. (2007) is determined to be $5{\times}10^8$ m^{-2} in **Paper 7**. Other permeability factors are chosen around this value to understand the change in the different hydrodynamic parameters and the hydrodynamic efficiency due to the change in the permeability factor.

The chamber pressure developed due to a given incident wavelength is found to increase with increasing PTO damping and consequently, the free surface and the velocity of the motion of the free surface is reduced. The results for the hydrodynamic

efficiency obtained from the 72 different simulations carried out are presented in Fig. (3.13). The hydrodynamic efficiency over the range of the permeability factors at lower wave height of $H = 0.06$ m is found to be higher than the efficiency at a higher incident wave height of $H = 0.12$ m. The variation of the hydrodynamic efficiency with the permeability factor for a low incident wave steepness $H/L = 0.03$ is found to be similar to the results obtained for the lower wave height studied.

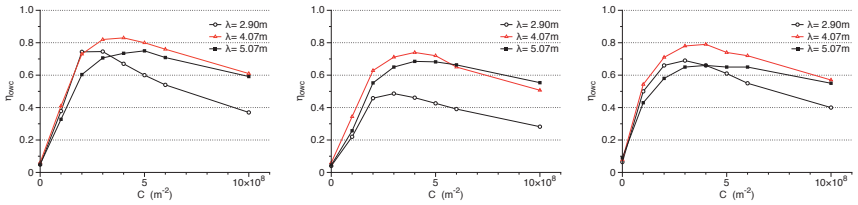

(a) $H = 0.06$ m (b) $H = 0.12$ m (c) $H/L = 0.03$

Figure 3.13: Hydrodynamic efficiency of the OWC device for different incident wave heights and wave steepness

It is also observed that the maximum hydrodynamic efficiency for the lowest wavelength $L = 2.90$ m is obtained at $C = 3{\times}10^8$ m^{-2}, for $L = 4.07$ m at $C = 4{\times}10^8$ m^{-2} and for $L = 5.07$ m at $C = 5{\times}10^8$ m^{-2} respectively in all the cases. Thus, an optimal value of PTO damping exists for an given incident wavelength this value increases with increasing incident wavelength. It is also seen that the maximum hydrodynamic efficiency is always obtained for the resonant wavelength. So, the PTO damping does not affect the resonant wavelength of the OWC. This information is crucial to incorporate active control of the OWC, where the PTO damping can be varied depending on the prevalent wave conditions to extract the maximum possible wave energy using the OWC.

The flow features inside and in front of the OWC for different damping parameters at the lowest free surface elevation in the OWC is examined in Fig. (3.14) for the resonant wavelength of $L = 4.07$ m. It is seen that under no additional PTO damping, the water and the air in the OWC chamber show strong rotational effects and most of the incident wave energy is trapped in these vortices, resulting in very low hydrodynamic efficiency. As the value of C is increased, the vorticity in the water and the air os reduced significantly in Figs. (3.14c) and (3.14d). This leads to more incident wave energy being absorbed by the PTO system and the highest hydrodynamic efficiency is calculated for these values of PTO damping. On further increase in the PTO damping, the motion of both the water and the air column is restricted and the hydrodynamic efficiency is reduced again, after obtaining the maximum efficiency at the optimal value of PTO damping.

In conclusion, an optimal value of PTO damping should be used to extract the maximum possible wave energy for a given incident wavelength. The PTO damping does not alter the wavelength at which resonance occurs, but it can significantly increase the hydrodynamic efficiencies for wavelengths away from resonance. This

knowledge can be used in active control of an OWC to improve the wave energy extraction under varying incident wave conditions. For further details, please refer to **Paper 8** in Chapter **5**.

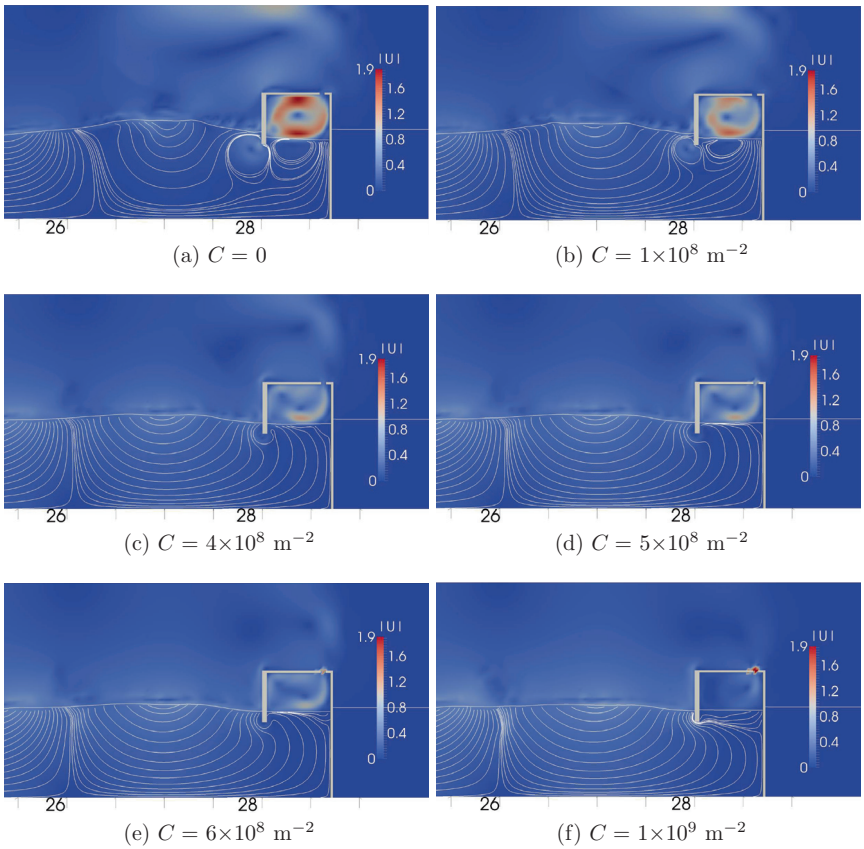

(a) $C = 0$ (b) $C = 1{\times}10^{8}$ m^{-2}

(c) $C = 4{\times}10^{8}$ m^{-2} (d) $C = 5{\times}10^{8}$ m^{-2}

(e) $C = 6{\times}10^{8}$ m^{-2} (f) $C = 1{\times}10^{9}$ m^{-2}

Figure 3.14: Streamlines inside and in front of the OWC for different values of PTO damping C for resonant wavelength $L = 4.07$ m

3.1.9 Paper 9: Study of Air Chamber Volume and Compressibility Effects in an Oscillating Water Column Wave Energy Device

Simulations of an OWC device using a two phase CFD model have been generally carried out under the assumption of incompressible fluids. This is a valid assumption for water, whereas the compressibility of air could be an issue in an OWC device. This paper investigates the influence of air compressibility and the volume of the air chamber on the hydrodynamics of the OWC. Air is modeled as a compressible medium using the ideal gas law to relate the chamber pressure to the density of the air in the chamber to account for the compressibility of air. Falcão and Henriques

(2014) proposed that to the effects from air compressibility are a function of the air volume in the chamber and to correct represent the effects of compressibility in a model scale device, the ratio of the air chamber volume to the water free surface area in the model should be similar to that in a prototype, about 3-5 m. In accordance with this, the air chamber is enlarged by increasing the height of the device while keeping the cross-sectional area of the chamber the same, so that the ratio of the air volume to the water free surface area is 3.2 m. The results for the enlarged chamber are compared with results obtained for a 1:12.5 model scale simulation.

First, 2D and 3D simulations are carried out for a 1:12.5 scale model of the OWC with and without compressible treatment of the air phase, see Fig. (3.15). From the variation of the chamber pressure and the free surface in the OWC chamber, it is found that at this scale, the effect of air compressibility is negligible both in 2D and 3D simulations. Also, the results in the 2D and 3D simulations are found to be the same and further simulations are carried out in 2D.

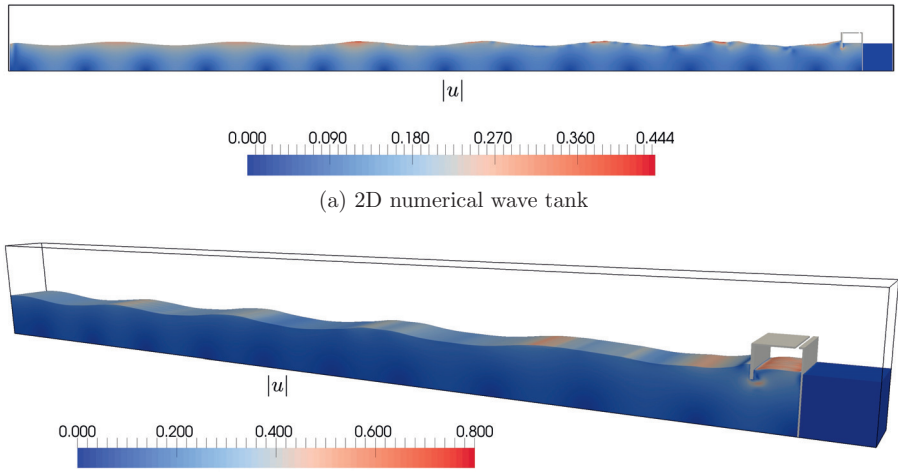

(a) 2D numerical wave tank

(b) 3D numerical wave tank

Figure 3.15: Numerical wave tank setup for 2D and 3D simulations for 1:12.5 scale model of an OWC

Further, 2D simulations are carried out for the device with an enlarged air chamber, with both compressible and incompressible treatment of air. Similar results are obtained for both the chamber pressure and the variation of the free surface in the chamber with compressible and incompressible treatment of air. So, the effect of air compressibility is found to be negligible even in a device with an enlarged chamber. The chamber pressure and the free surface oscillations in the case of the enlarged chamber are compared to the values calculated for the model scale device in Fig. (3.16). It is seen that the for the same given incident wavelength and wave height, the chamber pressure is reduced significantly and the amplitude of the free surface oscillation is increased. This leads to a reduction in the hydrodynamic efficiency of the device.

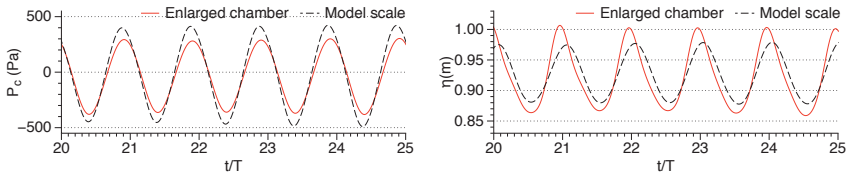

(a) variation of chamber pressure (b) variation of free surface

Figure 3.16: Comparison of pressure and free surface in the OWC chamber in a model scale and enlarged chamber

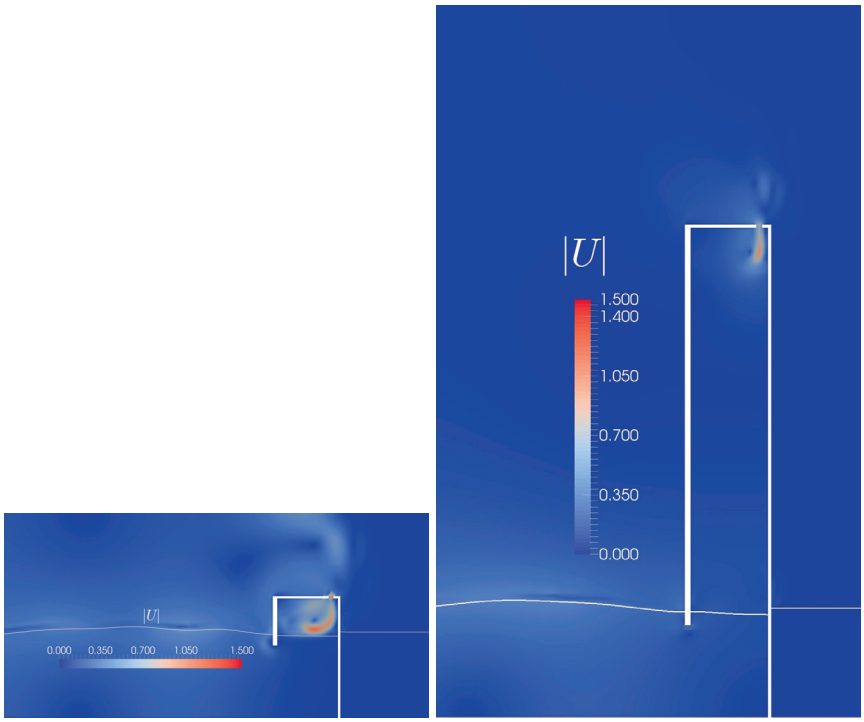

(a) 1:12.5 model scale device (b) device with enlarged chamber

Figure 3.17: Air velocity distribution in a model scale device and device with an air chamber enlarged by increasing the height of the air chamber

A difference is also seen in the distribution of air velocities in the OWC chamber of the model scale device and the device with an enlarged chamber. The stream of high air velocity extends up to the free surface in the case of a model scale device in Fig. (3.17a) whereas it is restricted to a small region around the vent in the device with an enlarged chamber in Fig. (3.17b). The phase difference between the pressure oscillation and the vertical velocity of the free water surface is examined for the model scale device and for the device with an enlarged chamber in Fig. (3.18). The

in-phase variation of the chamber pressure and the vertical velocity of the free surface is seen in Fig. (3.18a), whereas a the variation is out of phase for the device with an enlarged chamber in Fig. (3.18b). This is the reason for the reduced efficiency when the volume of the air chamber is enlarged. The air column and the water column form a tightly coupled system that is sensitive to the relative volumes of air and water in the chamber. Thus, the effects of air compressibility can not be represented in a model scale device by a simple enlargement of the air chamber. Also, given the magnitude of the pressure and air velocity variation, which are much lower than the atmospheric pressure and the speed of sound respectively, the effect of air compressibility in the OWC chamber is negligible.

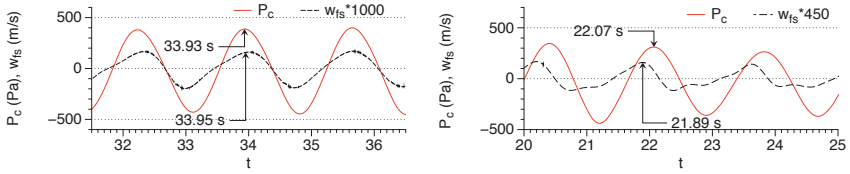

(a) model scale device

(b) device with enlarged chamber

Figure 3.18: Comparison of pressure and free surface in the OWC chamber in a model scale and enlarged chamber

For further details, please refer to **Paper 9** in Chapter **5**.

Chapter 4

Conclusions and Outlook

4.1 Conclusions

A new numerical wave tank, REEF3D is developed with a focus on problems in the field of coastal and marine engineering and free surface flows. A $5th$-order WENO scheme for convection discretization, $3rd$-order Runge-Kutta scheme for time advancement, the level set method for the free surface capturing along with a staggered grid for tight pressure-velocity coupling is incorporated and found to be very efficient on high performance computing systems, even with a large number of processors. The numerical wave tank in REEF3D is applied to various problems such as non-breaking wave forces, wave shoaling, breaking and breaking wave forces and very good agreement is seen with experimental results. Various flow features are identified in the case of low and high steepness waves and breaking waves; the related fluid physics and the influence on the objects placed in the wave field are studied. The numerical model is then used to simulate the wave interaction with an OWC and investigate the hydrodynamics. The following conclusions can be drawn from the study:

- The numerical wave tank in REEF3D provides a realistic representation of the fluid physics involved in wave propagation, transformation and interaction problems encountered in the field of coastal engineering.
- The non-breaking wave forces on large cylinder in a low KC number flow regime, requires the use of CFD methods as the wave interaction process is not completely captured by potential flow theory for higher wave steepnesses, even though the forces are inertia dominated. The differences in the diffraction regime at low and high incident wave steepness are presented and discussed. This new information is useful for structural design decisions for an OWC.
- The total breaking wave force on a cylinder is sensitive to the location of the wave breaking point with respect to the cylinder. This is also true in the case of tandem cylinders and the sheltering effect from the upstream cylinder can be

overcome by the breaking wave, resulting in a larger force on the downstream cylinder. These findings provide an idea regarding the wave forces on an OWC during an extreme event and also for arrangement of the OWCs in an array.

- The CFD investigations revealed certain differences between analytically predicted results and the results obtained from experimental and CFD investigations for the hydrodynamics of an OWC device. The resonance conditions calculated using simplifications for linearization of the problem can provide erroneous results with practical design parameters of an OWC.

- The hydrodynamics of an OWC is significantly influenced by the PTO damping. The porous media theory in the vent provides a good representation of the PTO damping while avoiding the large velocities that can occur when the dimensions of the vent are small. This method can also be used in further studies to actively vary the PTO damping to improve the hydrodynamic efficiency under varying incident wave conditions.

- The motion of the air and water column of an OWC are tightly coupled and a change in the volume of the air chamber can significantly influence the hydrodynamics of the OWC. The effect of compressibility is negligible at model scale. No effect of compressibility is seen even on increasing the air volume in the chamber.

4.2 Outlook

The present work demonstrates the capability of the numerical model to simulate the hydrodynamics of an OWC along with an accurate representation of the various wave transformation processes that are encountered in the region where the bottom-fixed OWC would be deployed. In addition, several phenomena related to wave propagation and hydrodynamics in the field of coastal and marine engineering have been modeled with good agreement to experimental data.

The use of the porous media theory to represent the PTO damping allows efficient computation of the hydrodynamic aspects of the device by avoiding the large velocities due to the vent of small dimensions that is generally used in current literature. It also avoids the need to change the dimensions of the vent to modify the PTO damping. The current work has covered the validation of this method and for investigation with regular waves to obtain a basic understanding about the influence of the PTO damping on the OWC hydrodynamics. This feature can be used to further explore the concept of varying the PTO damping with respect to then incident wave climate and improve the hydrodynamic efficiency of the device in future works.

This work is carried out under an international collaboration with Indian Institute of Technology-Madras, where experimental investigations are being carried out on in their shallow wave basin facilities. Experimental investigations cover the effect of bottom profile, quantification of the damping due to the PTO device, the interaction

with irregular waves, wave forces on the OWC, combination of the OWC with detached breakwaters and the action of oblique waves on the OWC. The numerical model can be used to further investigate the wave interaction with an OWC and further the knowledge about the device. This will add to the existing understanding of the hydrodynamics of an OWC and also provide insight into innovative deployment of the OWCs in combination with detached breakwaters to provide combined clean energy and coastal protection.

Bibliography

Battjes, J.A., 1974. Surf similarity, in: Proc., 14*th* International Conference on Coastal Engineering, Copenhagen, Denmark, pp. 466–480.

Beji, S., Battjes, J.A., 1993. Experimental investigation of wave propagation over a bar. Coastal Engineering 19, 151–162.

Berthelsen, P.A., Faltinsen, O.M., 2008. A local directional ghost cell approach for incompressible viscous flow problems with irregular boundaries. Journal of Computational Physics 227, 4354–4397.

Booij, N., Ris, R.C., Holthuijsen, L.H., 1999. A third-generation wave model for coastal regions, 1. model description and validation. Journal of Geophysical Research 104, 7649–7666.

Calderer, A., Kang, S., Sotiropoulos, F., 2014. Level set immersed boundary method for coupled simulation of air/water interaction with complex floating structures. Journal of Computational Physics 277, 201–227.

Chorin, A., 1968. Numerical solution of the Navier-Stokes equations. Mathematics of Computation 22, 745–762.

Core Writing Team, Pachauri, R.K., Meyer L. A. (Eds.), 2014. IPCC, 2014: Climate Change 2014: Synthesis Report. Contribution of Working Groups I, II and III to the Fifth Assessment Report of the Intergovernmental Panel on Climate Change. IPCC, Geneva, Switzerland.

Croce, R., Griebel, M., Schweitzer, M.A., 2010. Numerical simulation of bubble and droplet deformation by a level set approach with surface tension in three dimensions. International journal for numerical methods in fluids 62, 963–993.

Delauré, Y.M.C., Lewis, A., 2003. 3D hydrodynamic modelling of fixed oscillating water column wave power plant by a boundary element methods. Ocean engineering 30, 309–330.

Dombre, E., Benoit, M., Violeau, D., Peyrard, C., Grilli, S.T., 2015. Simulation of floating structure dynamics in waves by implicit coupling of a fully non-linear potential flow model and a rigid body motion approach. Journal of Ocean Engineering and Marine Energy 1, 55–76.

Dommermuth, D.G., Yue, D.K.P., Lin, W.M., Rapp, R.J., Chan, E.S., Melville, W.K., 1988. Deep-water plunging breakers: a comparison between potential theory and experiments. Journal of Fluid Mechanics 189, 423–442.

Duckers, L., 2004. Ch. 8, Wave energy. Oxford University Press, Oxford, UK.

Evans, D.V., 1978. Oscillating water column wave energy convertors. IMA Journal of Applied Mathematics 22, 423–433.

Evans, D.V., 1981. Power from water waves. Annual review of fluid mechanics 13, 157–187.

Evans, D.V., 1982. Wave power absorption by systems of oscillating surface pressure distributions. Journal of Fluid Mechanics 114, 481–499.

Evans, D.V., Porter, R., 1995. Hydrodynamic characteristics of an oscillating water column device. Applied Ocean Research 17, 155–164.

Falcão, A.F.de.O., 2010. Wave energy utilization: A review of the technologies. Renewable and sustainable energy reviews 14, 899–918.

Falcão, A.F.de.O., Henriques, J.C..C., 2014. Model-prototype similarity of oscillating-water-column wave energy converters. International Journal of Marine Energy 6, 18–34.

Falnes, J., 2007. A review of wave-energy extraction. Marine Structures 20, 185–201.

Grilli, S.T., Guyenne, P., Dias, F., 2001. A fully non-linear model for three-dimensional overturning waves over an arbitrary bottom. International Journal for Numerical Methods in Fluids 35, 829–867.

Grilli, S.T., Horrillo, J., 1997. Numerical generation and absorption of fully nonlinear periodic waves. Journal of Engineering Mechanics 123, 1060–1069.

Grilli, S.T., Skourup, J., Svendsen, I.A., 1989. An efficient boundary element method for nonlinear water waves. Engineering Analysis with Boundary Elements 6, 97–107.

Higuera, P., Lara, J.L., Losada, I.J., 2014. Three-dimensional interaction of waves and porous coastal structures using OpenFOAM®. Part II: Application. Coastal Engineering 83, 259–270.

Higuera, P., Lara, L.J., Losada, I.J., 2013. Realistic wave generation and active wave absorption for Navier-Stokes models application to OpenFOAM. Coastal Engineering 71, 102–118.

International Energy Agency, 2010. Key World Energy Statistics 2010. IEA, Paris, France.

Irschik, K., Sparboom, U., Oumeraci, H., 2002. Breaking wave characteristics for the loading of a slender pile, in: Proc. 28*th* International Conference on Coastal Engineering, Cardiff, Wales.

Jacobsen, N.G., Fuhrman, D.R., Fredsøe, J., 2012. A wave generation toolbox for the open-source CFD library: OpenFOAM. International Journal for Numerical Methods in Fluids 70, 1073–1088.

Jiang, G.S., Shu, C.W., 1996. Efficient implementation of weighted ENO schemes. Journal of Computational Physics 126, 202–228.

Kamath, A., Bihs, H., Arntsen, Ø.A., under review. Study of air chamber volume and compressibility effects in an oscillating water column wave energy device. Submitted to the International Journal of Marine Energy .

Kofoed, J.P., 2002. Wave overtopping of marine structures. Ph.D. thesis. Aalborg University, Denmark.

Lewis, A., Estefen, S., Huckerby, J., Musial, W., Pontes, T., Torres-Martinez, J., 2011. Ocean energy, IPCC special report on renewable energy sources and climate change mitigation. Cambridge University Press.

Linton, C.M., McIver, P., 2001. Handbook of mathematical techniques for wave structure interactions. Chapman and Hall CRC.

López, I., Pereiras, B., Castro, F., Iglesias, G., 2014. Optimisation of turbine-induced damping for an OWC wave energy converter using a RANS-VOF numerical model. Applied Energy 127, 105–114.

MacCamy, R., Fuchs, R., 1954. Wave forces on piles: A diffraction theory. University of California, Dept. of Engineering.

Madsen, P.A., Murray, R., Sørensen, O.R., 1991. A new form of the boussinesq equations with improved linear dispersion characteristics. Coastal Engineering 15, 371–388.

Mayer, S., Garapon, A., Sørensen, L.S., 1998. A fractional step method for unsteady free surface flow with applications to non-linear wave dynamics. International Journal for Numerical Methods in Fluids 28, 293–315.

Morris-Thomas, M.T., Irvin, R.J., Thiagarajan, K.P., 2007. An investigation into the hydrodynamic efficiency of an oscillating water column. Journal of Offshore Mechanics and Arctic Engineering 129, 273–278.

Nwogu, O., 1993. Alternative form of boussinesq equations for nearshore wave propagation. Journal of Waterways, Port, Coastal, and Ocean Engineering 119, 618–638.

Osher, S., Sethian, J.A., 1988. Fronts propagating with curvature- dependent speed: algorithms based on Hamilton-Jacobi formulations. Journal of Computational Physics 79, 12–49.

Paulsen, B.T., Bredmose, H., Bingham, H.B., 2014. An efficient domain decomposition strategy for wave loads on surface piercing circular cylinders. Coastal Engineering 86, 57–76.

Reguero, B.G., Losada, I.J., Méndez, F.J., 2015. A global wave power resource and its seasonal, interannual and long-term variability. Applied Energy 148, 366–380.

Rezanejad, K., Bhattacharjee, J., Soares, C.G., 2015. Analytical and numerical study of dual-chamber oscillating water columns on stepped bottom. Renewable Energy 75, 272–282.

Sarmento, A.J.N.A., 1992. Wave flume experiments on two-dimensional oscillating water column wave energy devices. Experiments in Fluids 12, 286–292.

Sarmento, A.J.N.A., Falcão, A.F.de.O., 1985. Wave generation by an oscillating surface pressure and its application in wave energy extraction. Journal of Fluid Mechanics 150, 467–485.

Schäffer, H.A., Klopman, G., 2000. Review of multidirectional active wave absorption methods. Journal of Waterway, Port, Coastal, and Ocean Engineering 126, 88–97.

Seiffert, B., Hayatdavoodi, M., Ertekin, R.C., 2014. Experiments and computations of solitary-wave forces on a coastal-bridge deck. Part I: flat plate. Coastal Engineering 88, 194–209.

Sentürk, U., Özdamar, A., 2011. Modelling the interaction between water waves and the oscillating water column wave energy device. Mathematical and Computational Applications 16(3), 630–640.

Shu, C.W., Osher, S., 1988. Efficient implementation of essentially non-oscillatory shock capturing schemes. Journal of Computational Physics 77, 439–471.

Sundar, V., Moan, T., Hals, J., 2010. Conceptual design of OWC wave energy converters combined with breakwater structures, in: Proc., 29th International Conference on Ocean Offshore and Arctic Engineering.

Thiruvenkatasamy, K., Neelamani, S., 1997. On the efficiency of wave energy caissons in array. Applied Ocean Research 19, 61–72.

van der Vorst, H., 1992. BiCGStab: A fast and smoothly converging variant of Bi-CG for the solution of nonsymmetric linear systems. SIAM Journal on Scientific and Statistical Computing 13, 631–644.

Wang, D.J., Katory, M., Li, Y.S., 2002. Analytical and experimental investigation on the hydrodynamic performance of onshore wave-power devices. Ocean Engineering 29, 871–885.

Wang, Z., Yang, J., Koo, B., Stern, F., 2009. A coupled level set and volume-of-fluid method for sharp interface simulation of plunging breaking waves. International Journal of Multiphase Flow 35, 227–246.

Wehausen, J.V., Laitone, E.V., 1960. Surface waves. Springer.

Wienke, J., Sparboom, U., Oumeraci, H., 2000. Breaking wave impact on a slender cylinder, in: Coastal Engineering Conference, pp. 1787–1798.

Yang, J., Stern, F., 2009. Sharp interface immersed-boundary/level-set method for wave–body interactions. Journal of Computational Physics 228, 6590–6616.

Zhang, Y., Zou, Q.P., Greaves, D., 2012. Air-water two phase flow modelling of hydrodynamic performance of an oscillating water column device. Renewable Energy 41, 159–170.

Chapter 5

Appended publications

Paper 1 Bihs H., Kamath A., Alagan Chella M., Aggarwal A. and Arntsen Ø.A. **A New Level Set Numerical Wave Tank with Improved Density Interpolation for Complex Wave Hydrodynamics**. Submitted to *Computers and Fluids* 2015.

Paper 2 Kamath A., Alagan Chella M., Bihs H. and Arntsen Ø.A. (2015) **CFD Investigations of Wave Interaction with a Pair of Large Tandem Cylinders**. *Ocean Engineering* 108, 738-748.

Paper 3 Kamath A., Bihs H., Alagan Chella M., Arntsen Ø.A. **Upstream and Downstream Cylinder Influence on the Hydrodynamics of a Four Cylinder Group**. Submitted to *Journal of Waterway, Port, Coastal, and Ocean Engineering* 2015.

Paper 4 Kamath A., Alagan Chella M., Bihs H. and Arntsen Ø.A. **Shoaling and Decomposition of Breaking and Non-Breaking Waves over a Submerged Bar**. Submitted to *Coastal Engineering Journal* 2015.

Paper 5 Kamath A., Alagan Chella M., Bihs H. and Arntsen Ø.A. **Breaking Wave Interaction with a Vertical Cylinder and the Effect of Breaker Location**. Submitted to *Ocean Engineering* 2015.

Paper 6 Bihs H., Kamath A., Alagan Chella M. and Arntsen Ø.A. **Breaking Wave Interaction with Tandem Cylinders under Different Impact Scenarios**. Submitted to *Journal of Waterway, Port, Coastal, and Ocean Engineering* 2015.

Paper 7 Kamath A., Bihs H. and Arntsen Ø.A. 2015. **Numerical Investigations of the Hydrodynamics of an Oscillating Water Column Device**. *Ocean Engineering* 102, 40-50.

Paper 8 Kamath A., Bihs H. and Arntsen Ø.A. 2015. **Numerical Modeling of Power Take-off Damping in an Oscillating Water Column Device**. *International Journal of Marine Energy* 10, 1-16.

Paper 9 Kamath A., Bihs H. and Arntsen Ø.A. **Study of Air Chamber Volume and Compressibility Effects in an Oscillating Water Column Wave Energy Device**. Submitted to *International Journal of Marine Energy* 2015.

Paper 1

A New Level Set Numerical Wave Tank with Improved Density Interpolation for Complex Wave Hydrodynamics

Bihs H., Kamath A., Alagan Chella M., Aggarwal A. and Arntsen Ø.A.
Submitted to *Computers and Fluids* 2015.

A New Level Set Numerical Wave Tank with Improved Density Interpolation for Complex Wave Hydrodynamics

Hans Bihs[a,*], Arun Kamath[a], Mayilvahanan Alagan Chella[a], Ankit Aggarwal[a], Øivind Asgeir Arntsen[a]

[a]*Department of Civil and Transport Engineering, Norwegian University of Science and Technology (NTNU), NO-7491 Trondheim, Norway*

Abstract

The three-dimensional numerical wave tank REEF3D is developed for the calculation of wave propagation and wave hydrodynamics by solving the incompressible Navier-Stokes equations. The free surface is modeled with the level set method based on a two-phase flow approximation, allowing for the simulation of complex phenomena such as wave breaking. The convection terms of the momentum and the level set equations are discretized with the finite difference version of the fifth-order WENO scheme. Time stepping is handled with the third-order TVD Runge-Kutta scheme. The equations are solved on a staggered Cartesian grid, with a ghost cell immersed boundary method for the treatment of irregular cells. Waves are generated at the inlet and dissipated at the numerical beach with the relaxation method. The choice of the numerical grid and discretization methods leads to excellent accuracy and stability for the challenging calculation of free surface waves. The performance of the numerical model is validated and verified through several benchmark cases: solitary wave interaction with a rectangular abutment, wave forces on a vertical cylinder, wave propagation over a submerged bar and plunging breaking waves on a sloping bed.

Keywords: numerical wave tank, wave propagation, wave hydrodynamics, breaking waves, wave forces

1. Introduction

The choice of model for the wave propagation and transformation calculation depends on the required detail and resolution. For large scale wave modeling, such as the wave transformation from deep to shallow waters, spectral wave models such as SWAN [5] are used. This type of model solves the wave action or energy balance equation, which describes the wave

*Corresponding author
Email address: hans.bihs@ntnu.no (Hans Bihs)

spectrum evolution in space and time. The modeled waves are consequently phase averaged. Spectral wave models have been successfully applied to a variety of coastal problems [37][49]. For a range of water wave engineering problems, more detail is required concerning the wave transformation process, including phase information. Phase resolving models based on the Boussinesq equations [27][33] or the parabolic mild-slope equation [24] have the capability to accurately model wave reflection and diffraction. The mild-slope approach is based on the assumption of a mildly sloping sea bottom and linear monochromatic waves. Standard Boussinesq-type models are based on the shallow water equations for non-dispersive linear wave propagation. Extended versions of the Boussinesq equations make it possible to predict wave propagation and transformation from deep to shallow water with the help of improved dispersive terms [26]. When it comes to engineering applications, such as wave propagation in nearshore and harbor areas, Boussinesq-type models are often the preferred engineering solution.

Yet another approach to wave modeling is the class of Fully Nonlinear Potential Flow Models (FNPF), which neglect the effects of viscosity and rotational flow. Here, the Laplace equation for the flow potential is solved with the Boundary Element Method. The method works well for a range of problems, such as wave propagation in deep water [9] or wave shoaling in shallow water [14]. All mentioned wave models have in common, that they give up a certain level of detail for the benefit of reduced computational cost. For a lot of water wave engineering problems, this is a perfectly reasonable choice.

On the other hand there are complex cases, such as breaking wave kinematics or flow around slender structures, where a more detailed solution is required in order to capture the relevant flow physics. The solution of the three-dimensional Navier-Stokes equations resolves even more detail of the flow processes. Here, the approach is to solve for the basic underlying flow variables, such as the velocities, the pressure and turbulence. Together with the appropriate algorithms for the interface capturing, the free surface and resulting water wave dynamics can be calculated based on the three-dimensional flow field. In order to avoid the unphysical damping of propagating waves due to numerical diffusion, the usage of the Navier-Stokes equations imposes strict criteria for the mesh resolution, the time step size as well as the general accuracy of the numerical algorithm. There have been several papers where a Navier Stokes solver in conjunction with interface capturing schemes has been used to calculate complex free surface flows such as [45], [52], [8] and [6]. In contrast, the current model focuses on the very demanding problem of wave propagation and wave hydrodynamics. Some successful

efforts have been made to use a CFD program as a numerical wave tank, e.g. [21] or [17]. In these methods, the CFD model calculates the free surface with a Volume-of-Fluid (VOF) algorithm, based on convection of the fraction function and interface-compression [46]. The governing equations are solved on a collocated unstructured grid with second-order accuracy for the spatial and temporal discretization. In both cases, algorithms for the wave generation and absorption were implemented, resulting in a three-dimensional numerical wave tank. The models were applied to typical laboratory experiments for wave propagation, showing that with today's efficient numerical models and computational resources, very complex wave propagation simulations can be performed [35][19][38].

In this work, the open-source model REEF3D [1] is presented with alternative approaches for the underlying grid architecture, discretization of the governing equations and treatment of the complex free surface. As mentioned above, numerical accuracy and stability are essential for the good performance of a Navier-Stokes equations based numerical wave tank. Under that premise, the appropriate numerical algorithms were chosen in REEF3D. The level set method is used for the capturing of the free water surface [34]. It has been used for describing two-phase flow with water-air interfaces in several studies [52][51][8]. Geometric Volume-of-Fluid (VOF) algorithms have shown to give better mass conservation properties than the level set method [45]. On the other hand, high-order temporal and spatial discretization can be used for the level set function, which avoid unphysical damping of the propagating water waves. Further, the equations of fluid motion are solved on a staggered grid, ensuring tight velocity-pressure coupling. The Cartesian grid makes it possible to employ the fifth-order Weighted Essentially Non-Oscillatory (WENO) scheme [23] for convection discretization, which delivers accurate and stable solutions. Also for the discretization in time, a high-order method is selected with the third-order total variation diminishing (TVD) Runge-Kutta scheme [39]. As a result, wave propagation and transformation can be calculated throughout the wave steepness range up to the point of wave breaking and beyond, with no artificially high air velocities impacting the quality of the free surface. In Section 2, the numerical methods for the solution of the Navier-Stokes equations are discussed. In Section 3, the free surface treatment and the details of the numerical wave tank implementation are presented. The numerical results of several benchmark wave applications are given in Section 4, before the conclusion in Section 5.

2. Numerical Model

2.1. Governing Equations

The incompressible fluid flow is described by the three-dimensional Reynolds-Averaged Navier-Stokes equations (RANS), which are solved together with the continuity equation for prescribing momentum and mass conservation:

$$\frac{\partial u_i}{\partial x_i} = 0 \tag{1}$$

$$\frac{\partial u_i}{\partial t} + u_j \frac{\partial u_i}{\partial x_j} = -\frac{1}{\rho}\frac{\partial p}{\partial x_i} + \frac{\partial}{\partial x_j}\left[(\nu + \nu_t)\left(\frac{\partial u_i}{\partial x_j} + \frac{\partial u_j}{\partial x_i}\right)\right] + g_i \tag{2}$$

where u is the velocity averaged over time t, ρ is the fluid density, p is the pressure, ν is the kinematic viscosity, ν_t is the eddy viscosity and g the acceleration due to gravity.

The eddy viscosity ν_t in the RANS equations is determined through the two-equation k-ω model [48], with the equations for the turbulent kinetic energy k and the specific turbulent dissipation ω as follows:

$$\frac{\partial k}{\partial t} + u_j \frac{\partial k}{\partial x_j} = \frac{\partial}{\partial x_j}\left[\left(\nu + \frac{\nu_t}{\sigma_k}\right)\frac{\partial k}{\partial x_j}\right] + P_k - \beta_k k\omega \tag{3}$$

$$\frac{\partial \omega}{\partial t} + u_j \frac{\partial \omega}{\partial x_j} = \frac{\partial}{\partial x_j}\left[\left(\nu + \frac{\nu_t}{\sigma_\omega}\right)\frac{\partial \omega}{\partial x_j}\right] + \frac{\omega}{k}\alpha P_k - \beta\omega^2 \tag{4}$$

where P_k is the turbulent production rate, the coefficients have the values $\alpha = \frac{5}{9}$, $\beta_k = \frac{9}{100}$, $\beta = \frac{3}{40}$, $\sigma_k = 2$ and $\sigma_\omega = 2$. In the oscillatory flow motion that characterizes the wave flow field, the mean rate of strain $\mathbf{S}$ can be large. In order to avoid overproduction of turbulence in highly strained flow outside the boundary layer, the turbulent eddy viscosity ν_t is bounded through the following limited formulation [10]:

$$\nu_t = \min\left(\frac{k}{\omega}, \sqrt{\frac{2}{3}}\frac{k}{|\mathbf{S}|}\right) \tag{5}$$

The turbulent length scales in the water are reduced in the proximity of the free surface, leading to increased turbulent dissipation in this region. Also, the turbulent fluctuations normal to the free surface are damped, as their intensity is redistributed to the ones parallel to the interface. When modeling two-phase flow, this behavior is not directly captured by a RANS turbulence model. As $\mathbf{S}$ can be large especially in the vicinity of the interface between

water and air, standard RANS turbulence closure will incorrectly predict maximum turbulence intensity at the free surface. Through the implementation of an additional turbulence damping scheme, a more realistic representation of the free surface effect on the turbulence can be achieved [31]. The specific turbulent dissipation at the free surface is defined as:

$$\omega_s = \frac{c_\mu^{-\frac{1}{4}}}{\kappa} k^{\frac{1}{2}} \cdot \left(\frac{1}{y'} + \frac{1}{y^*} \right) \tag{6}$$

where $c_\mu = 0.07$ and $\kappa = 0.4$. The variable y' is the virtual origin of the turbulent length scale, and was empirically found to be 0.07 times the mean water depth [20]. Including the distance y^* from the nearest wall gives a smooth transition from the free surface value to the wall boundary value of ω. The term for the specific turbulent dissipation ω_s is activated around the interface of thickness ϵ by multiplying it with the Dirac delta function $\delta(\phi)$:

$$\delta(\phi) = \begin{cases} \frac{1}{2\epsilon} \left(1 + \cos\left(\frac{\pi\phi}{\epsilon} \right) \right) & if \ \ |\phi| < \epsilon \\ 0 & else \end{cases} \tag{7}$$

The pressure gradient term in the RANS equations is modeled with Chorin's projection method [7] for incompressible flow on a staggered grid. The staggered grid configuration ensures a tight velocity-pressure coupling. The pressure gradient is removed from the momentum equations. The updated velocity after each Euler step of the Runge-Kutta time discretization is the intermediate velocity u_i^*. Then the Poisson equation for the pressure is formed by calculating the divergence of the intermediate velocity field:

$$\frac{\partial}{\partial x_i} \left(\frac{1}{\rho(\phi^n)} \frac{\partial p}{\partial x_i} \right) = -\frac{1}{\Delta t} \frac{\partial u_i^*}{\partial x_i} \tag{8}$$

The Poisson equation is solved using the fully parallelized Jacobi-preconditioned BiCGStab algorithm [43]. The pressure is then used to correct the intermediate velocity field, resulting in the divergence free velocity at the new time step:

$$u_i^{n+1} = u_i^* - \frac{\Delta t}{\rho(\phi^n)} \frac{\partial p}{\partial x_i} \tag{9}$$

2.2. Discretization of the Convective Terms

The convective terms of the RANS equations are discretized with the fifth-order WENO scheme [23] in the conservative finite-difference framework. The convection term of the velocity component in x-direction is approximated as follows:

$$u_i \frac{\partial u_i}{\partial x_i} \approx \frac{1}{\Delta x} \left(\widetilde{u}_{i+1/2} \; u_{i+1/2} - \widetilde{u}_{i-1/2} \; u_{i-1/2} \right) \tag{10}$$

Here $\widetilde{u}$ is the convection velocity, which is obtained at the cell faces through simple interpolation. For the cell face $i + 1/2$, $u_{i+1/2}$ is reconstructed with the WENO procedure:

$$U^{\pm}_{i+1/2} = \omega_1^{\pm} U^{1\pm}_{i+1/2} + \omega_2^{\pm} U^{2\pm}_{i+1/2} + \omega_3^{\pm} U^{3\pm}_{i+1/2} \tag{11}$$

The $\pm$ sign indicates the upwind direction. U^1, U^2 and U^3 represent the three possible ENO stencils. For upwind direction in the positive i-direction, they are:

$$\begin{aligned} U^{1-}_{i+1/2} &= \frac{1}{3} u_{i-2} - \frac{7}{6} u_{i-1} + \frac{11}{6} u_i, \\ U^{2-}_{i+1/2} &= -\frac{1}{6} u_{i-1} + \frac{5}{6} u_i + \frac{1}{3} u_{i+1}, \\ U^{3-}_{i+1/2} &= \frac{1}{3} u_i + \frac{5}{6} u_{i+1} - \frac{1}{6} u_{i+2} \end{aligned} \tag{12}$$

The nonlinear weights $\omega_n^{\pm}$ are determined for each ENO stencil and calculated based on the smoothness indicators IS [23]. Large smoothness indicators indicate a non-smooth solution in the particular ENO stencil. Accordingly, the non linear weights ω_n for this stencil will be small. The WENO scheme favors stencils with a smooth solution and assigns them the largest weights ω_n. As a result the scheme can handle large gradients right up to the shock very accurately. In the worst-case situation, the WENO scheme will achieve a third-order of accuracy. In the areas where the solution is smooth, it will deliver fifth-order accurate results. In comparison to high resolution schemes such as MUSCL [44] or TVD [16] schemes, the WENO scheme does not smear out the solution. Instead, it maintains the sharpness of the extrema. The conservative WENO scheme is used to treat the convective terms for the velocities u_i, while the Hamilton-Jacobi version is used for the variables of the free surface and turbulence algorithms.

2.3. Time Advancement Scheme

For the time treatment of the momentum and the level set equations, a third-order accurate TVD Runge-Kutta scheme is employed, consisting of three Euler steps [39].

$$\begin{aligned}\phi^{(1)} &= \phi^n + \Delta t L\left(\phi^n\right) \\ \phi^{(2)} &= \frac{3}{4}\phi^n + \frac{1}{4}\phi^{(1)} + \frac{1}{4}\Delta L\left(\phi^{(1)}\right) \\ \phi^{n+1} &= \frac{1}{3}\phi^n + \frac{2}{3}\phi^{(2)} + \frac{2}{3}\Delta L\left(\phi^{(2)}\right)\end{aligned} \tag{13}$$

This scheme provides a high-order of temporal accuracy, and for CFL numbers below 1 it shows very good numerical stability through its TVD properties. Adaptive time stepping is used in order to control the CFL number and takes the influence from velocity, diffusion and the source term S, such as for example gravity, into account [13]. The time step size Δt is determined as follows:

$$\Delta t \leq 2\left(\left(\frac{|u|_{max}}{dx} + D\right) + \sqrt{\left(\frac{|u|_{max}}{dx} + D\right)^2 + \frac{4\,|S_{max}|}{dx}}\right)^{-1} \tag{14}$$

with the contribution from the diffusion term D:

$$D = max\left(\nu + \nu_t\right) \cdot \left(\frac{2}{(dx)^2} + \frac{2}{(dy)^2} + \frac{2}{(dz)^2}\right) \tag{15}$$

For a RANS model, where the turbulence magnitude is expressed through the eddy viscosity, the diffusion criterion of the order $\nu_{\max}/dx^2$ can become prohibitively restrictive. As a solution, the diffusion part of the RANS equation is treated implicitly in the current numerical model, thus removing it from the CFL criterion. The third-order accurate TVD Runge-Kutta scheme is used for all transport equations in the numerical wave tank with the exception of the turbulence model. A special characteristic of two-equation turbulence models is that they are mostly source term driven, namely by the turbulent production and dissipation terms. In comparison to the momentum equation, the convective and diffusive terms play only a minor role. For explicit time discretization of the k and ω equations, the large source terms result in a significantly smaller time step than for the momentum equations due to the CFL criterion. Instead of letting the turbulence model determine the time step, its equations are discretized with a first-order implicit Euler scheme.

2.4. Immersed Boundary

The numerical model uses a Cartesian grid in order to employ high-order discretization schemes. An additional benefit comes from the straightforward implementation of numerical

algorithms, as the geometry of the numerical cells is trivial in this case. The challenge of irregular, non-orthogonal solid boundaries is overcome with the implementation of the immersed boundary method. In REEF3D, a ghost cell immersed boundary method (GCIBM) is used [4]. In this method, the solution is analytically continued through the solid boundary by updating fictitious ghost cells in the solid region by extrapolation. This way, the numerical discretization does not need to account for the boundary conditions explicitly, instead they are enforced implicitly. The algorithm is based on the local directional approach [4], which was implemented in two dimensions. For the current model it has been extended to three dimensions. In the original GCIBM, the fluid values are extrapolated orthogonal to the boundary into the solid [42][29], which can become difficult for sharp corners. In the local directional GCIBM the values from the fluid are extrapolated into the solid along the coordinate directions [4].

In REEF3D, grids can be generated based on geometric primitives, such as boxes, cylinders and wedges. More complex geometries can be read in .STL format and immersed into the Cartesian grid, following the strategy presented in [50]. For natural bathymetries with measured x, y and z coordinates, the solid boundary can be represented by a level set function. Then, the location of the level set function is calculated from the coordinates with either inverse-distance or kriging interpolation.

2.5. Parallelization

The efficient computation of CFD results depends to a large extent on the strategy for the parallelization of the numerical model. In REEF3D, parallelization is achieved through domain decomposition. Here the simulation domain is split into smaller parts, each of them communicating with their neighbors through ghost cells. Because REEF3D already uses the ghost cell method for the solid boundaries, this approach is straightforward to code and consistent with the treatment of the other domain boundaries. The message passing interface (MPI) is used for the implementation of the ghost cell value exchange. Since a fifth-order WENO scheme is used for the convection discretization of the velocities, the level set function and the variables of the turbulence model, three ghost cell levels are required. For the pressure, only one level of ghost cells is needed. The code is employed on NOTUR's supercomputer Vilje [32], which is an "SGI Altix 8600" cluster. Vilje consists of 1404 nodes with two 8-core processors on each node, resulting in a total of 22464 cores. In order to investigate the parallel efficiency of REEF3D, 2D and 3D tests were performed. For the 2D test, a

rectangular wave tank with the domain size ($L_x \times L_z = 62$ m $\times$ 4 m) and a mesh size of $dx = 0.005$ m has a total of 9.92 million cells. For the 3D test, a wave tank with the domain size of ($L_x \times L_y \times L_z = 250$ m $\times$ 5 m $\times$ 8 m), a mesh size of $dx = 0.1$ m and a total of 10 million cells is used. As seen from Fig. (1a), the parallel speedup for the 2D case follows the ideal scaling closely up to 256 processors. After that, a speedup is still achieved, but visibly reduced as the parallel communication overhead increases more than the parallelization gains. For the 3D test case, the parallel speedup of the model is close to the ideal situation up to 144 processors. The speedup is reduced for 256 processors and flattens out towards 512 processors. As expected, the parallel scaling for 2D cases is more efficient than for 3D, as messages have to be passed in one dimension lesser.

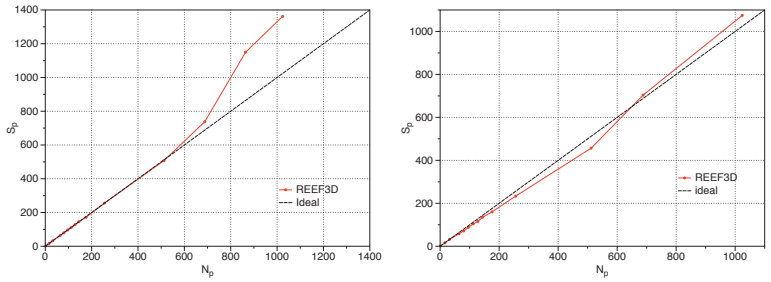

(a) 2D (b) 3D

Figure 1: Parallel scaling test for 2D and 3D wave tanks

3. Numerical Wave Tank

3.1. Free Surface Capturing

The location of the free water surface is represented implicitly by the zero level set of the smooth signed distance function $\phi(\vec{x}, t)$ [34]. The level set function gives the closest distance to the interface Γ and the two phases are distinguished by the change of the sign. This results in the following properties:

$$\phi(\vec{x}, t) \begin{cases} > 0 \; if \; \vec{x} \in phase \; 1 \\ = 0 \; if \; \vec{x} \in \Gamma \\ < 0 \; if \; \vec{x} \in phase \; 2 \end{cases} \tag{16}$$

In addition, the Eikonal equation $|\nabla \phi| = 1$ is valid. When the interface Γ is moved under an externally generated velocity field $\vec{u}$, a convection equation for the level set function is

obtained:

$$\frac{\partial \phi}{\partial t} + u_j \frac{\partial \phi}{\partial x_j} = 0 \tag{17}$$

The convection term in Eq. (17) is solved with the Hamilton-Jacobi version of the WENO scheme [22]. For time stepping, the third-order TVD Runge-Kutta scheme is used [39]. When the interface evolves, the level set function loses its signed distance property. In order to maintain this property and to ensure mass conservation, the level set function is reinitialized after each time step. In the present paper, a PDE based reinitialization equation is solved [40]:

$$\frac{\partial \phi}{\partial t} + S(\phi) \left(\left| \frac{\partial \phi}{\partial x_j} \right| - 1 \right) = 0 \tag{18}$$

where $S(\phi)$ is the smoothed sign function [36].

3.2. Density Location

With the level set function in place, the material properties of the two phases can be defined for the whole simulation domain. On a staggered grid, the cell face density is required for the calculation of the Poisson equation for the pressure in Eq. (8) and the correction of the velocity with the pressure gradient in Eq. (9). In previous level set based numerical models with staggered grids [45], [6], the density is usually determined at the cell centers with the smoothed Heaviside function in a first step:

$$\rho_i = \rho_1 H(\phi_i) + \rho_2 (1 - H(\phi_i)), \tag{19}$$

with ρ_1 and ρ_2 representing the densities of the two fluids and the Heaviside function defined as:

$$H(\phi_i) = \begin{cases} 0 & if\ \phi_i < -\epsilon \\ \frac{1}{2}\left(1 + \frac{\phi_i}{\epsilon} + \frac{1}{\pi} sin\left(\frac{\pi \phi_i}{\epsilon}\right)\right) & if\ |\phi_i| < \epsilon \\ 1 & if\ \phi_i > \epsilon \end{cases} \tag{20}$$

Typically the thickness of the smoothed out interface is chosen to be $\epsilon = 1.6dx$ on both sides of the interface. In a second step, the density at the cell faces is evaluated through

simple averaging of the density at the two neighboring cell centers [8]:

$$\rho_{i+\frac{1}{2}} = \frac{1}{2}\left(\rho_i + \rho_{i+1}\right) \tag{21}$$

In another example [51], the cell face density is calculated through a linear interpolation based on the location of the interface in the second step. In the current numerical model for the calculation of propagating waves, it was observed that this two-step strategy for the cell face density evaluation leads to small scale oscillations of the free surface. For other types of free-surface flows, such as open-channel flow, this phenomenon could not be reproduced. For the simulation of waves, the oscillations are more pronounced for lower steepness waves. In general, the problem occurs when the free surface is mildly sloped with respect to the orientation of the gridlines in the presence of a vertical velocity component, as is the case for waves.

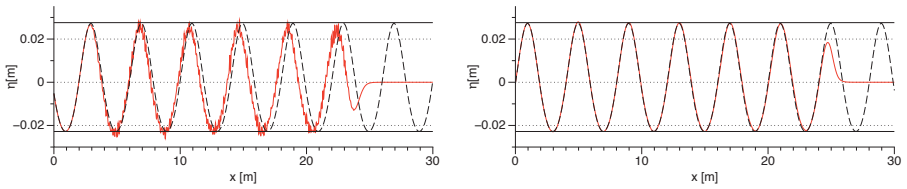

(a) Density calculation at cell centers

(b) Density calculation at cell faces

Figure 2: Influence of cell face density calculation on the free surface for periodic waves with wave length $L = 4$ m, wave height $H = 0.05$ m and still water level $d = 0.5$ m in a 30 m long wave flume with $dx = 0.01$ m after 90 s. The black dashed line shows the wave theory, the black solid line the theoretical wave envelope and the red line the numerical model.

In order to illustrate the effect, 2nd-order Stokes waves with a wavelength $L = 4$ m and a wave height $H = 0.05$ m are generated in a 30 m long and 1 m high 2D wave flume with a water depth $d = 0.5$ m on a mesh with $dx = 0.01$ m. Fig. (2a) shows the computed wave surface elevation after 90 s. Comparing it with the theoretical wave profile along the wave flume, the free surface oscillations and a phase shift become visible. The relatively long simulation time of 90 s is chosen, so that the oscillations are fully developed. Even though the quality of the numerical results is clearly degraded, the numerical solution remains stable throughout the simulation with neither excess velocities nor pressure values occurring. As a remedy for the free surface oscillations, the density at the cell faces is calculated in a modified manner. Using a single step, the density at the cell face is calculated with the smoothed Heaviside function right away:

$$\rho_{i+\frac{1}{2}} = \rho_1 H\left(\phi_{i+\frac{1}{2}}\right) + \rho_2\left(1 - H\left(\phi_{i+\frac{1}{2}}\right)\right), \tag{22}$$

The level set function at the cell face is calculated through averaging:

$$\phi_{i+\frac{1}{2}} = \frac{1}{2}\left(\phi_i + \phi_{i+1}\right) \tag{23}$$

As can be seen in Fig. (2b), the resulting free surface is oscillation-free and the numerical solution matches the theoretical wave profile in both amplitude and phase. Similar to the current findings, [47] identified the importance of the density averaging for the quality of the free surface in the context of the VOF method on a staggered grid. Fig. (3) shows the density profile for the cell faces i across the interface, in a case where the interface is normal to the x-direction. Three different situations are considered: the interface located directly on the cell face, between the cell face and the cell center and directly at the cell center. The density calculation at the cell centers is denoted ρ_{center}, and the density calculation at the cell faces ρ_{face}. Compared to the curve for the cell-centered density evaluation ρ_{center} with $\epsilon = 1.6dx$, the density profile is actually less smoothed out across the interface for ρ_{face} with $\epsilon = 1.6dx$,

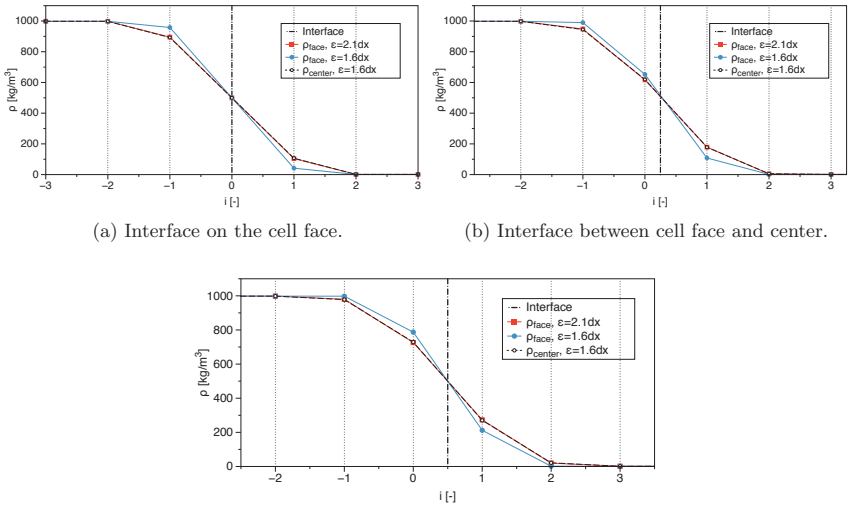

(a) Interface on the cell face.

(b) Interface between cell face and center.

(c) Interface on the cell center.

Figure 3: Density profile along the interface at the cell faces for different interface locations and density evaluation schemes. The x-axis i represents the cell centers.

because the second step with the averaging of the densities is missing. In order to account for this, the current method of the cell face density evaluation uses the interface thickness $\epsilon = 2.1dx$. As can be seen from Fig. (3), for ρ_{face} with $\epsilon = 2.1dx$, the width of the density transition area and the magnitude of the density gradient across the interface at the cell faces is the same as for ρ_{center} with $\epsilon = 1.6dx$.

3.3. Wave Generation and Absorption

Typical inlet boundary conditions for free surface flow applications are of Dirichlet type. When generating waves at the inlet, the free surface is in constant motion and the flow direction is changing periodically. As a result, simple Dirichlet type wave generation does not necessarily deliver waves of the highest quality. In REEF3D, waves are generated with the relaxation method, which is presented in [28] and extended for CFD models in [21]. Here, the wave generation takes place in a relaxation zone with a typical size of one wavelength (see Fig. (4)).

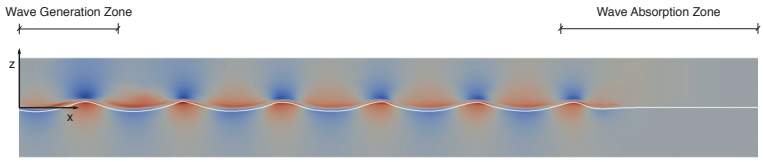

Figure 4: Sketch of the numerical wave tank with wave generation and absorption zones. The contour shows the horizontal velocity component.

The values for the velocities and the free surface are ramped up from the computational values to the values obtained from wave theory (Eq. (24)). The waves are generated without any disturbances occurring at the interface. In addition, reflected waves that travel back towards the inlet are absorbed with this method. At the outlet of a wave flume, the waves need to be dissipated in order to avoid reflections that can negatively impact the numerical results. This can be achieved with the relaxation method. In the numerical beach relaxation zone, the computational values for the horizontal and vertical velocities are smoothly reduced to zero, the free surface to the still water level and the pressure is relaxed to the hydrostatic distribution for the still water level. Thus, the wave energy is effectively absorbed and reflections are prevented.

$$
\begin{aligned}
u(\widetilde{x})_{relaxed} &= \Gamma(\widetilde{x})u_{analytical} + (1-\Gamma(\widetilde{x}))u_{computational} \\
w(\widetilde{x})_{relaxed} &= \Gamma(\widetilde{x})w_{analytical} + (1-\Gamma(\widetilde{x}))w_{computational} \\
p(\widetilde{x})_{relaxed} &= \Gamma(\widetilde{x})p_{analytical} + (1-\Gamma(\widetilde{x}))p_{computational} \\
\phi(\widetilde{x})_{relaxed} &= \Gamma(\widetilde{x})\phi_{analytical} + (1-\Gamma(\widetilde{x}))\phi_{computational}
\end{aligned}
\tag{24}
$$

The relaxation function presented in [21] is used. The wave generation zone has the length of one wavelength, the numerical beach extends over two wavelengths.

$$
\Gamma(\widetilde{x}) = 1 - \frac{e^{(\widetilde{x}^{3.5})} - 1}{e-1} \; for \; \widetilde{x} \in [0;1] \tag{25}
$$

The coordinate $\widetilde{x}$ is scaled to the length of the relaxation zone. Several wave theories are implemented in REEF3D: linear waves, second-order and fifth-order Stokes waves, first-order and fifth-order cnoidal waves, first-order and fifth-order solitary waves and first-order irregular and focused waves. In case of linear waves for general water depths, the horizontal and vertical velocities u and w and the level set function ϕ for the free surface location are given as:

$$
\begin{aligned}
u(x,z,t)_{analytical} &= \frac{\pi H}{T}\frac{cosh\left[k\left(z+d\right)\right]}{sinh\left(kd\right)}cos\theta \\
w(x,z,t)_{analytical} &= \frac{\pi H}{T}\frac{sinh\left[k\left(z+d\right)\right]}{sinh\left(kd\right)}sin\theta \\
\phi(x,z,t)_{analytical} &= \frac{H}{2}cos\theta - z + d
\end{aligned}
\tag{26}
$$

The wave number k and the wave phase θ are defined as follows:

$$
\begin{aligned}
k &= \frac{2\pi}{L} \\
\theta &= kx - \omega t
\end{aligned}
\tag{27}
$$

where H is the wave height, L the wavelength, T the wave period, ω the angular wave frequency and z the vertical coordinate with the origin at the still water level d. In the wave generation zone, the pressure is not prescribed in the current numerical model, in order not to over define the boundary conditions. The omission of the pressure prescription in the wave

generation zone has not shown a loss in wave quality. At the numerical beach, the pressure is always set to its hydrostatic values based on the still water level d, independent of the wave input.

3.4. Numerical Calculation of Wave Forces

Wave forces can be determined by the numerical model in a straightforward manner. The pressure and the normal component of viscous stress tensor τ are integrated over the surface Ω of the structure. The integration is performed in a discrete manner, by using p and τ for each cell surface of the structure:

$$F = \int_{\Omega} (-\mathbf{n}p + \mathbf{n} \cdot \tau) d\Omega \tag{28}$$

here $\mathbf{n}$ is the unit normal vector to the surface, pointing into the fluid. The Navier-Stokes equations in Eq. (2) are solved including the gravity term. Then the pressure obtained from the projection method includes the hydrostatic part in addition to the dynamic part. Consequently, it is the total force acting on a structure that is determined by Eq. (28).

4. Results

In this section, several numerical results for wave propagation benchmark cases are presented. The numerical model is tested in order show the numerical accuracy and convergence in addition to the overall capabilities of REEF3D.

4.1. Grid and Time Step Convergence Tests

At first the general performance of the numerical model regarding wave propagation is tested in a rectangular wave flume with a two-dimensional setup. Regular waves are generated based on wave theory. Since there is no obstacle or other change in geometry along the wave flume, no wave transformation should take place and the wave should maintain the exact same shape and propagation speed as in the generation zone. As a consequence, the grid and time step convergence tests can be evaluated by comparing the numerical wave profile along the wave flume with the theoretical profile.

For these tests, a wave height of $H = 0.1$ m and a wave length of $L = 2$ m are selected for a still water depth of $d = 0.5$ m in a 20 m long wave flume. The resulting wave is of relatively high steepness ($\xi = 0.05$), requiring wave generation with fifth-order Stokes theory [11]. This makes it also more challenging for the numerical model to maintain the wave height along the

flume without numerical damping. The grid convergence test is performed on four different meshes with $dx = (0.05\text{ m}, 0.025\text{ m}, 0.01\text{ m}, 0.005\text{ m})$. For the comparisons in Figs. (5) and (6), the result after 90 s is used. For the grid convergence, the CFL number is kept at 0.1. Fig. (5a) shows the result for $dx = 0.05$ m. Here, the simulated wave troughs and crests are damped out. Also, the wave goes slightly out of phase. For $dx = 0.025$ m (Fig. (5b)) the numerical result improves. Wave crest damping occurs only towards the second half of the wave flume and the wave is in phase. From $dx = 0.01$ m on, the numerical model converges to the theoretical solution (Fig. (5c)). For both $dx = 0.01$ m and $dx = 0.005$ m, no wave crest damping occurs. Only a very slight under prediction of the wave troughs can be observed.

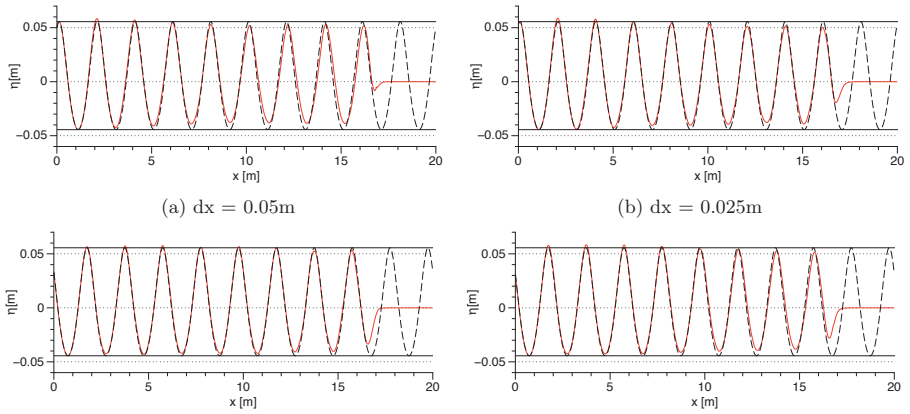

(a) dx = 0.05m

(b) dx = 0.025m

(c) dx = 0.01m

(d) dx = 0.005m

Figure 5: Grid convergence test in a 20 m long 2D wave flume with wave height $H = 0.1$ m, wave length $L = 2$ m and a CFL number of 0.1.The black dashed line shows the wave theory, the black solid line the theoretical wave envelope and the red line the numerical model.

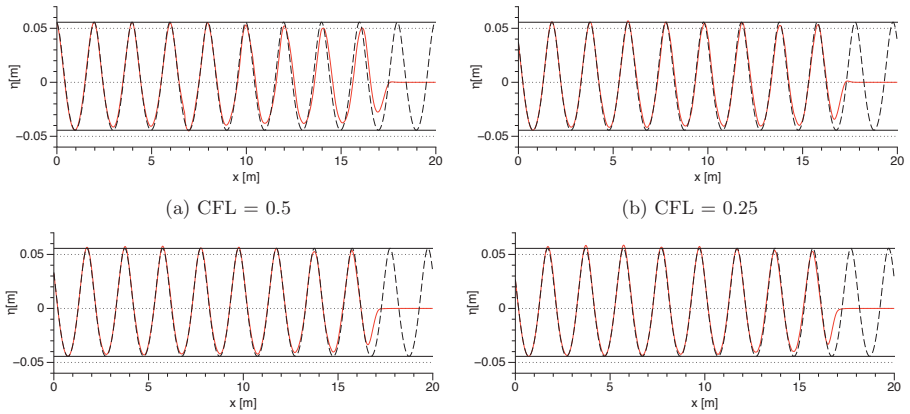

(a) CFL = 0.5

(b) CFL = 0.25

(c) CFL = 0.1

(d) CFL = 0.05

Figure 6: Time step convergence test in a 20 m long 2D wave flume with wave height $H = 0.1$ m, wave length $L = 2$ m and $dx = 0.01$ m. The black dashed line shows the wave theory, the black solid line the theoretical wave envelope and the red line the numerical model.

For the time step convergence test, the same wave conditions as for the grid convergence are used. Since the grid convergence tests showed a converged solution for $dx = 0.01$ m for these wave conditions, this grid size is used here. As presented above, the numerical model employs adaptive time stepping, so instead of testing fixed time step sizes, the CFL numbers 0.5, 0.25, 0.1 and 0.05 are tested. Fig. (6a) with CFL = 0.5 shows wave damping and a phase shift towards the end of the flume. For CFL = 0.25, the wave is in phase, but minor wave crest damping occurs at the end of the flume. For CFL = 0.1 and CFL = 0.05, the numerical results look similar (Fig. (6c-d)). No wave crest damping is observed, just a slight under prediction of the the wave trough. The CFL number incorporates information about the mesh width dx, so CFL = 0.1 is used for all of the following numerical applications. The mesh width on the other hand is tested for all cases individually.

4.2. Solitary Wave Interaction with a Rectangular Abutment

In this benchmark case, solitary wave propagation and the interaction with a rectangular abutment is investigated. The simulated results are compared with experimental data [25][18]. In the experiments, a rectangular abutment is placed in a 0.58 m wide wave flume, obstructing the flow over a width of 0.28 m. The side wall and the bottom of the wave flume are made of glass. The still water level is $d = 0.45$ m, a solitary wave with height $H = 0.1$ m is generated with a piston-type wavemaker. A fully reflective wall is placed at the end of the wave flume. In Fig. (7a) the plan view of the setup, including the wave gage locations, can

be seen. In the numerical model, the solitary wave is generated from third-order theory [15] in a relaxation zone with the length $l = 8$ m. The numerical domain has the size of ($L_x \times L_y \times L_z = 23.8$ m $\times 0.58$ m $\times 0.9$ m). The front face of the abutment is located 14.84 m away from the inlet boundary. This distance is 4 m longer than in the experimental setup, in order to accommodate the wave generation zone. For the grid convergence tests, four different meshes are used with $dx = (0.1\text{ m}, 0.05\text{ m}, 0.02\text{ m}, 0.01\text{ m})$, resulting in meshes with totals of 0.012 million, 0.1 million, 1.54 million and 12.36 million cells. As can be seen in Fig. (7a), there are nine wave gages placed around the abutment, both in the experimental and the numerical setup and the free surface data comparison is shown in Fig. (8).

All wave gages show two peaks. The first one is for the incoming solitary wave originating from the wavemaker. Then the wave passes the vertical structure and is reflected from the downstream wall. The reflected wave is recorded by the wave gages as the second peak. In order to perform the grid convergence tests, wave gage 7 is selected for comparison, as it is located downstream of the abutment and the influence of the structure can be seen for the first wave. Remarkably, the first peak is reproduced equally well on all four grids. Only for the reflected wave, the coarsest grid with $dx = 0.1$ m shows a reduced wave peak. The solitary wave is a single crest wave. The higher order WENO discretization of the convection terms ensures that there is no damping of the soliton, making the accurate solution less dependent

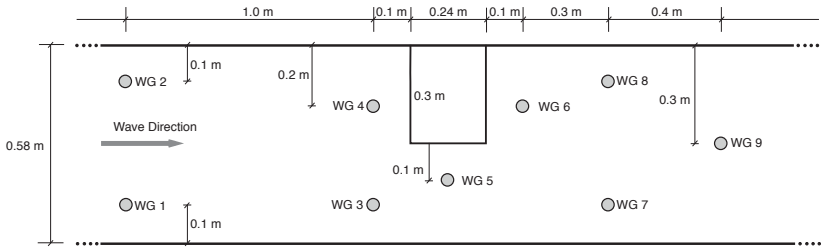

(a) Top view of the setup with wave gage locations.

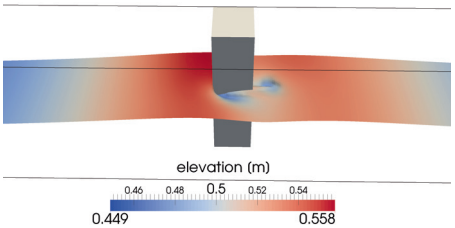

(b) Incident solitary wave just before passing the abutment.

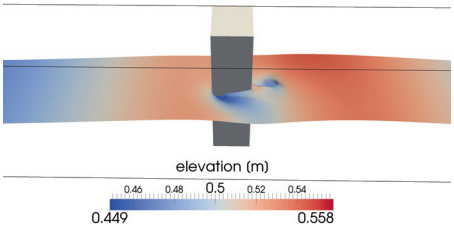

(c) Incident solitary wave just after it passing the abutment.

Figure 7: Solitary wave interaction with a rectangular abutment with setup and numerical free surface results.

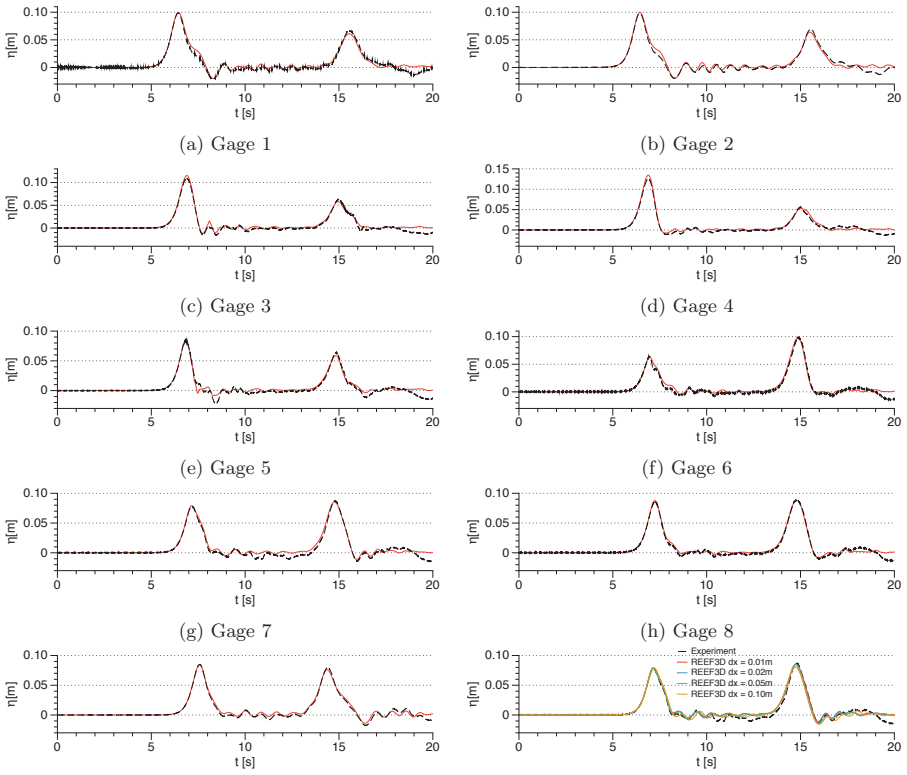

(a) Gage 1 (b) Gage 2

(c) Gage 3 (d) Gage 4

(e) Gage 5 (f) Gage 6

(g) Gage 7 (h) Gage 8

(i) Gage 9 (j) Gage 7, Grid Convergence

Figure 8: Solitary wave interaction with a vertical structure, black lines are laboratory experiments, red lines are REEF3D.

on the grid size. In Figs. (8a-8i), the results from the fine grid $dx = 0.01$ m are presented.

Gage 1 and 2 in Fig. (8a-b) show the generated solitary wave. The crest of the incident solitary wave is still unaffected by the abutment, maintaining the input wave height of $H = 0.1$ m. Directly after the peak, a slight bump in the wave shape occurs, which is attributed to the partial reflection from the abutment structure. The second peak resulting from the wave reflected by the downstream wall is clearly reduced. Gages 3 and 4 in Fig. (8c-d) show the effect of the channel narrowing. The numerical model calculates increased waves heights of $H = 0.11$ m and $H = 0.13$ m respectively for the incoming wave, slightly higher than the experimental data. For gage 4, the reflected wave is reduced with $H = 0.05$ m as it is the shadowed by the vertical structure. Wave gage 5 (Fig. (8e)) is located in the part of the flume that is constricted by the abutment. Here the incoming wave height is reduced. As the flow accelerates and the pressure decreases, a considerable drop in the free surface elevation in the

vicinity of the abutment can be observed (Fig. (7b-c)) for the incoming wave. Wave gage 6 (Fig. (8f)) is situated on the downstream side of the abutment. Here the incoming wave height is lower than the reflected wave, mirroring the behavior for gage 4. For gages 7 to 9 (Fig. (7g-i)), the incoming and reflected waves are nearly of the same magnitude. The reason is that between the incoming wave and the reflection, the wave is not further transformed. In general, the numerical model maintains all the wave peaks and also predicts the wave celerity correctly.

4.3. Wave Interaction with a Vertical Circular Cylinder

The data from the experiments carried out at the Large Wave Flume (GWK), Hannover, Germany presented by [30] is used for the comparison of the numerical results for wave interaction with a single vertical cylinder. The wave tank in the experiments is 309 m long, 5 m wide and 7 m deep. A cylinder of diameter $D = 0.7$ m is placed at a distance of 110 m from the wavemaker. Regular waves of period $T = 4$ s and wave height $H = 1.20$ m are generated in a water depth of $d = 4.76$ m. The wave force on the cylinder is measured using two strain gages placed at the top and the bottom of the cylinder. The free surface elevation near the wall of the wave flume along the frontline of the cylinder, in front of the cylinder, behind the cylinder and beside the cylinder are measured.

The water particle velocities at depths of $z = -0.93$ m, -1.53 m and -2.73 m from the still water level are measured near the wall along the frontline of the cylinders using ADVs. Fifth-order Stokes waves of height $H = 1.20$ m, period $T = 4.0$ s are generated in a water depth $d = 4.76$ m. The numerical wave tank is 132 m long, 5 m wide and 8 m high and a cylinder of diameter $D = 0.7$ m is placed at a distance of 44 m from the wave generation zone.

The computed wave force on the cylinder is compared to the experimental result in Fig.(9i) and a good agreement is seen. A grid resolution study is carried out with $dx = (0.2\text{ m}, 0.15\text{ m}, 0.1\text{ m})$ and the computed wave force converges to the experimental result at $dx = 0.1$ m resulting in 5.28 million cells in the numerical domain. The selected grid resolution is found to be sufficient for the computation of the wave force on the cylinder. The computed free surface elevations near the wall of the flume (WG 1) and around the cylinder (WG2, WG3 and WG4) are compared to the experimental observations in Fig. (9b-9e). The results are scaled with $\eta_{max,wall}$, the maximum elevation at $t/T =$ 5 in Fig. (9b). A good agreement is seen between the computed and experimental results. The presence of the cylinder does not affect the free surface elevation close to the wall, which is equal to the

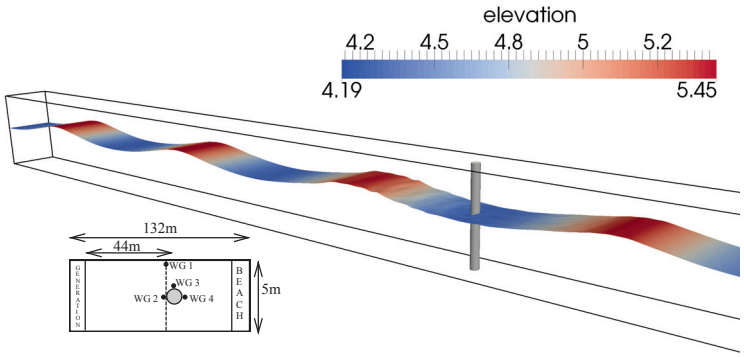

(a) Vertical circular cylinder setup.

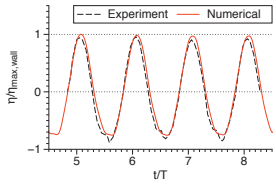

(b) Free surface, front line of the cylinder near the wall, WG 1.

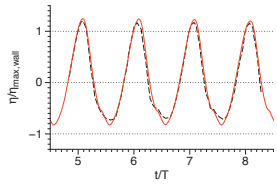

(c) Free surface, in front of the cylinder, WG 2.

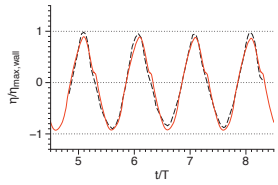

(d) Free surface, at the side of the cylinder, WG 3.

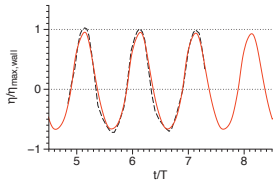

(e) Free Surface, behind the cylinder, WG 4.

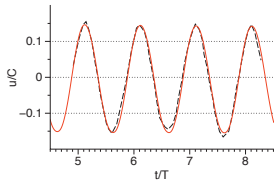

(f) Inline horizontal velocity $z = -0.93$m.

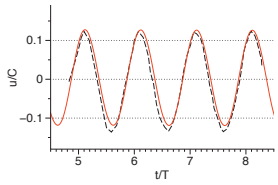

(g) Inline horizontal velocity $z = -1.53$m.

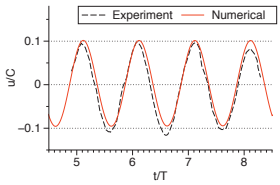

(h) Inline horizontal velocity $z = -2.73$m.

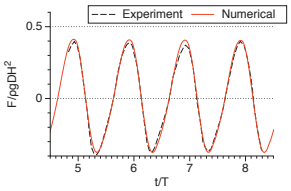

(i) Inline Wave Force, numerical vs. experimental.

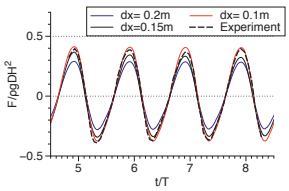

(j) Grid convergence study for forces.

Figure 9: Wave forces on a vertical cylinder

incident wave profile. A higher free surface elevation is seen in front of the cylinder compared to the back of the cylinder. This leads to a pressure difference around the cylinder, resulting in a net inline force on the cylinder. The computed horizontal water particle velocities at depths of $z = -0.93$ m, -1.53 m and -2.73 m from the still water level are compared to the experimental data scaled with the wave celerity C in Fig. (9f-9h) and a good agreement is seen. The horizontal water particle velocity is seen to reduce with increasing depth from the free surface as the influence of the wave on the water particle decreases.

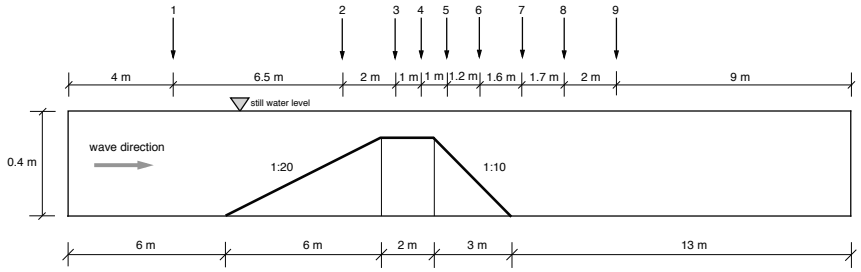

Figure 10: Submerged Bar setup with wave gage locations

4.4. Wave Propagation over a Submerged Bar

A well known benchmark is the submerged bar case by [2]. Here, monochromatic regular waves are generated in a rectangular wave flume of size ($L_x \times L_y \times L_z = 37.7$ m$\times 0.8$ m$\times 0.75$ m). A trapezoidal submerged bar is placed 6 m downstream of the wave maker, see Fig. (10). Nine wave gages are placed along the wave flume. The incident wave height is $H = 0.02$ m with a wave period of $T = 2$ s, resulting in a wavelength $L = 3.73$ m. In the numerical model, linear waves are generated in a relaxation zone of one wavelength. On the upslope of the bar, the waves shoal, yet breaking does not occur. After the crest of the bar, wave decomposition takes place and higher wave harmonics are formed. As a result, the free surface is typically very difficult to predict in the downslope and downstream region of the bar [3]. High-order numerical discretization schemes are needed in order to predict the correct dispersion characteristics and avoid wave crest damping and wave phase shifting. Thus, this case is well suited to test the accuracy of the proposed numerical wave tank. For the grid convergence study, two wave gages are selected: wave gage 4 on the crest of the submerged bar and wave gage 9 on the downstream side. Grids with $dx = (0.05$ m$, 0.02$ m$, 0.01$ m$, 0.005$ m) are tested. Fig. (11j) reveals that the two finer meshes closely match the experimentally observed effect from shoaling. For the two coarser meshes, the shoaling is under predicted

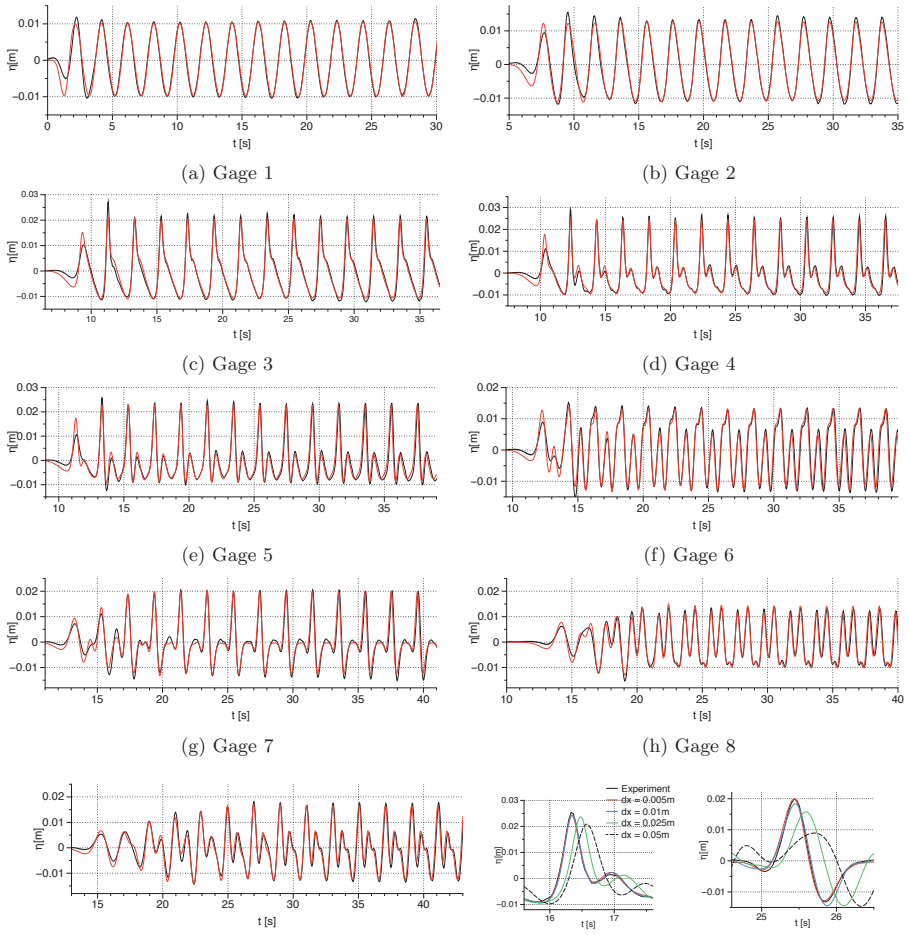

(a) Gage 1 (b) Gage 2

(c) Gage 3 (d) Gage 4

(e) Gage 5 (f) Gage 6

(g) Gage 7 (h) Gage 8

(i) Gage 9 (j) Gage 4, Grid Convergence (k) Gage 9, Grid Convergence

Figure 11: Wave transformation on a submerged bar, black lines are laboratory experiments, red lines are REEF3D.

with lower free surface elevations in addition to slower moving waves. In Fig. (11k), it can be seen that the mesh with $dx = 0.005$ m can capture the transformed wave very well, both in amplitude and phase. The phase is also maintained for $dx = 0.01$ m, while the wave crest is slightly reduced. For $dx = 0.025$ m, the phase shift and the amplitude reduction is clearly visible, for $dx = 0.05$ m even more. As a result, the mesh with $dx = 0.005$ m is selected for the comparison with the experimental data. Wave gage 1 shows the input wave, with the wave crests and trough symmetric around the still water level, the typical characteristics for

linear waves. Wave gage 2 shows the beginning of the shoaling on the sloping bed, but the waves maintain their sinusoidal shape. Gages 3 and 4 show the waves on the crest of the submerged bar. The loss of the sinusoidal shape indicates appearance of the secondary crests. This becomes more prominent on the downslope (gages 5 and 6) and on the downstream side of the submerged bar (gages 7-8). For all gages, the free surface predicted by the numerical model closely follows the one recorded in the laboratory experiment. This demonstrates the capabilities of REEF3D due to the high-order spatial WENO and temporal TVD Runge-Kutta discretization in addition to the staggered grid arrangement. Also, the immersed boundary handles the irregular grid cells well on the slopes of the submerged bar.

4.5. Plunging Breaking Waves over a Sloping Bed

In the previous section, shoaling non-breaking waves were modeled. A more difficult situation arises, when the shoaling effect is so strong, that the steepened wave crest becomes unstable and breaks. A sloping seabed with a slope of 1/35 is chosen for the case study of wave breaking over a plane slope. The computational setup and wave parameters in the present case study are similar to the experimental conditions reported by [41]. The wave tank has a horizontal bed with the water depth of $d = 0.4$ m. A 4 m long stretch with a flat bottom is followed by the slope. The laboratory arrangements and the computational domain for the plunging breaker case are shown in Fig. (12). The origin of the horizontal and vertical coordinates is at the toe of the slope at the still water level. A fifth-order cnoidal wave theory developed by [12] is used to represent the incident wave with the height of $H = 0.128$ m and period of $T = 5.0$ s. A simulation length of 30 s is used to obtain a quasi-steady state for the mean wave quantities. Then the simulated values from the last five waves are used for the evaluation of the breaking point and breaking height.

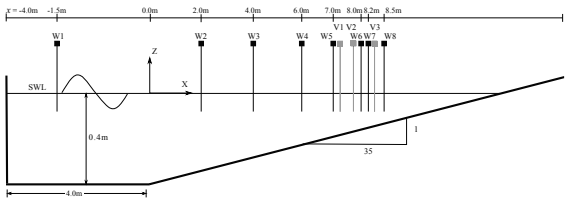

Figure 12: Computational set-up: W1-W8 are wave gauge locations and V1-V3 are velocity probe locations

The sensitivity of the computational results to the grid resolution is investigated with four different mesh sizes $dx = (0.025\text{ m}, 0.01\text{ m}, 0.005\text{ m}, 0.0025\text{ m})$. The simulated breaking location (x_b) and the breaker height (H_b) are compared with the measured data in Fig. (13).

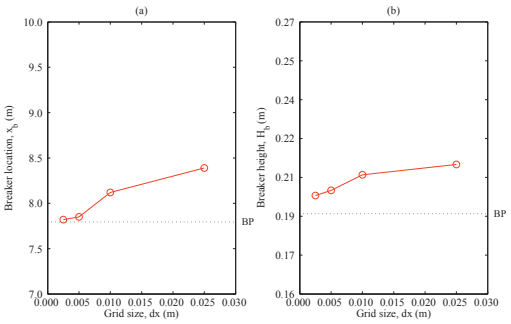

Figure 13: Grid sensitivity study on simulated results (a) breaker location (x_b) and (b) breaker height (H_b). The dotted line shows the breaking point observed in the experiments.

The simulated waves break later shoreward with slightly larger breaker height on coarser grids ($dx = 0.025$ m and $dx = 0.01$ m) than in the experiments. Whereas on finer grids ($dx = 0.005$ m and $dx = 0.0025$ m) waves break at almost the same location $x_b = 7.84$ m with the breaker height $H_b = 0.205$ m as in the experiments, where waves break at $x_b = 7.795$ m with $H_b = 0.196$ m. The comparison of the experimental and numerical values indicates that the best comparison with experimental data occurs with the finer grids ($dx = 0.005$ m and $dx = 0.0025$ m). The grid size $dx = 0.005$ m is selected for the computation since the simulated waves on this grid size yield good results with reasonable computational time and the difference between the $dx = 0.005$ m and $dx = 0.0025$ m is also insignificant. Compared to the previous section, a finer mesh is required. Here, the additional challenge arises not from the wave shoaling, but from the breaking process. The breaking occurs at a much smaller scale, than the wave propagation itself. Also, wave breaking is a true two-phase flow problem, where complex interface deformations occur.

The simulated free surface elevations are compared with experimental data at different locations along the wave tank in order to assess the ability of the numerical model to simulate hydrodynamic processes from wave generation to the surf zone. The free surface elevations are computed at eight different locations (W1-W8): $x = -1.5$ m, 2.0 m, 4.0 m, 6.0 m, 7.0 m, 8.0 m, 8.2 m and 8.5 m from the toe of the slope (see Fig. (12)). Fig. (14) shows the comparison of the simulated free surface elevations with the experimental measurements [41] for the plunging breaker case. The free surface profile evolves continuously from a wide crest to a narrow and steep crest. The wave height increases due to shoaling, as the wave propagates over the slope. The wave crest becomes unstable and breaks at $x_b = 7.84$ m with a breaker

height of $H_b = 0.205$ m. The numerical breaking condition is almost the same as measured in the experiments. It can be seen from Figs. 14 (f), (g) and (h), that the wave height diminishes after breaking as the wave approaches the shore. The simulated free surface profiles precisely represent the characteristics of the cnoidal waves in shallow water and display a good match with the experimental data.

The computed horizontal component of the fluid velocity at $x = 7.295$ m (incipient breaking), $x = 7.795$ m (during breaking) and $x = 8.345$ m (after breaking) are compared with the experimental data in Fig. (15) - Fig. (17). As can be seen from Fig. (15), in the region just prior to breaking, the variation of the horizontal velocity is almost constant with the water depth, which is consistent with the experimental observation by [41]. As the wave propagates further over the slope, the wave height increases due to shoaling. This leads to a rise in the potential energy in the region close to the wave crest. When the fluid particle velocity exceeds the wave speed, wave breaking occurs at $x = 7.84$ m, with the maximum velocity at the tip of

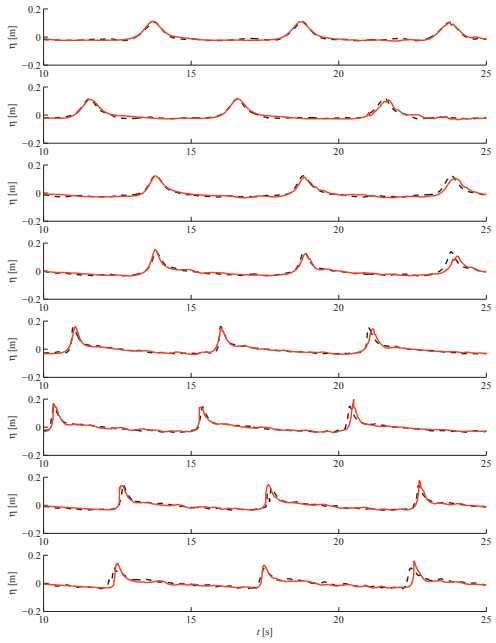

Figure 14: Comparison of simulated and measured water surface elevations for plunging breaker case at x= -1.5 m (a), 2.0 m (b), 4.0 m (c), 6.0 m (d), 7.0 m (e), 8.0 m (f), 8.2 m (g) and 8.5 m (h). Red lines: present numerical model; Black lines: experimental data by [41]

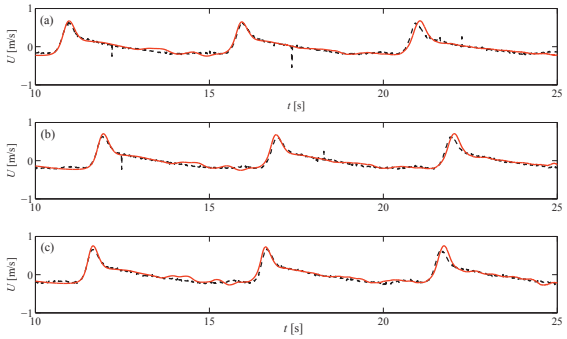

Figure 15: Comparison of simulated and measured horizontal velocities for plunging breaker case at x=7.275 m and z=-0.05 m (a), -0.10 m (b), and -0.15 m (c). Red lines: present numerical model; Black lines: experimental data by [41]

the horizontal overturning jet followed by a small velocity gradient over the depth (Fig. (16)). At the point of jet impingement, the horizontal velocity increases as the distance from the free surface increases, as shown in Fig. (17). This is due to the penetration of the large scale water jet into the preceding wave surface. The present model predicts the horizontal velocity variation along the water depth accurately and the simulated results are in good agreement with the experimental measurements.

The evolution of the wave breaking process with the velocity magnitude and velocity vector distribution is shown in Fig. (18). At the incipient breaking stage, the wave profile gets steeper and sharper and a portion of the wave crest attains the maximum fluid velocity. The total wave energy is focused near the wave crest and eventually wave breaking occurs. The portion of the wave crest with high velocity moves forward and evolves into an overturning plunging jet (Fig. (18a)). When the plunging jet impinges on the surface of the preceding wave (Fig. (18b)), a splash-up occurs as shown in Fig. (18c) and Fig. (18d). This creates a secondary wave followed by a pocket of air with different characteristics than the original wave. The rapid transition from a strong plunger vortex into small scale turbulence at the free surface takes place over a short distance. The simulated physical flow features of the plunging breaker during the wave breaking process such as wave profile evolution, the generation of the overturning water jet, the enclosed air pocket and the secondary wave, the splash-up phenomenon and the mixing of air and water in the surf zone are consistent with the experimental observation [41].

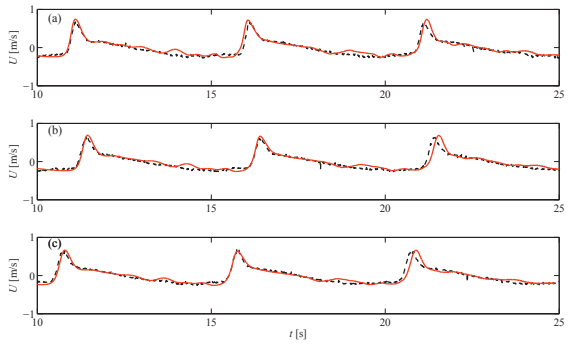

Figure 16: Comparison of simulated and measured horizontal velocities for plunging breaker case at x=5.945 m and z=-0.05 m (a), -0.10 m (b), and -0.145 m (c). Red lines: present numerical model; Black lines: experimental data by [41]

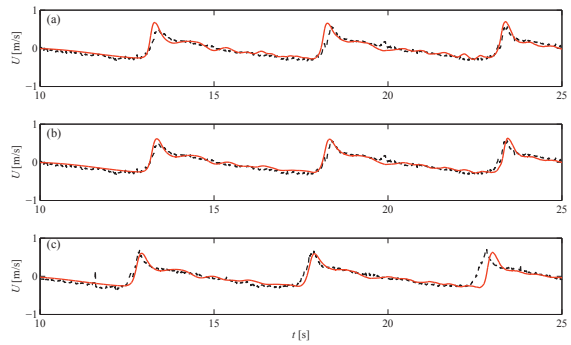

Figure 17: Comparison of simulated and measured horizontal velocities for plunging breaker case at x=6.665 m and z=-0.05 m (a), -0.10 m (b), and -0.13 m (c). Red lines: present numerical model; Red lines: experimental data by [41]

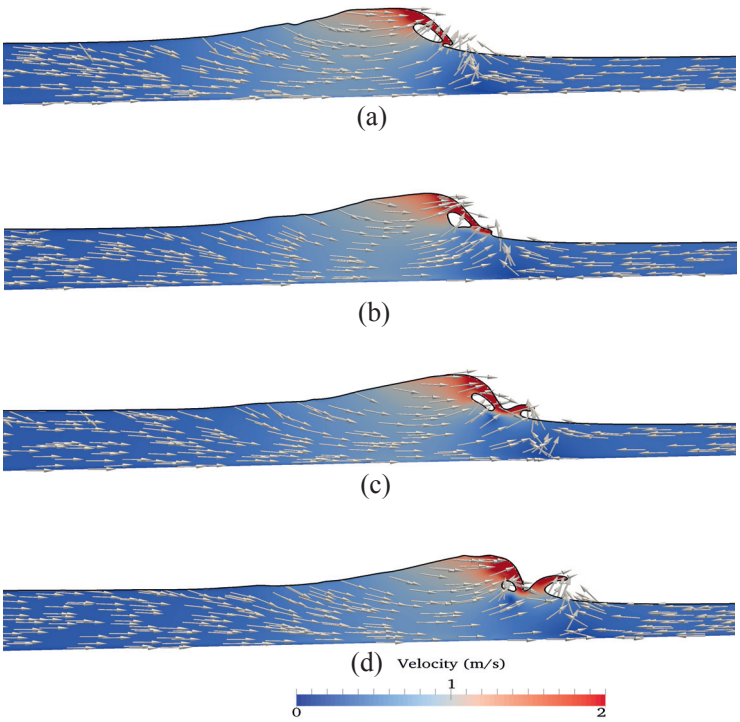

Figure 18: Snapshots of simulated wave profile during breaking process over a slope at $t = 10.90$ s (a), 10.95 s (b), 11.00 s (c) and 11.05 s (d)

5. Conclusions

The new numerical wave tank REEF3D has been presented. The incompressible Navier-Stokes equations are solved with RANS turbulence closure. In order to achieve stable and accurate wave propagation results, high-order numerical discretization schemes on a Cartesian mesh are selected. For the convection terms of the momentum equations, the fifth-order WENO scheme is chosen. Time-stepping is performed with the third-order TVD Runge-Kutta scheme. The pressure is solved on a staggered grid with the projection method, ensuring tight pressure-velocity coupling. Irregular boundaries are taken into account with an extension of an existing ghost cell immersed boundary method to three dimensions. The numerical model is fully parallelized based on the domain decomposition strategy and MPI (message passing interface). The free surface is modeled with the level set method. Special attention has been given to the evaluation of the density. It was found that density evaluation at the cell center leads to small-scale free surface oscillations, when periodic regular waves are simulated. The proposed density calculation scheme at the cell face showed a much improved free surface, comparing well against the theoretical wave profile. The waves are generated and absorbed with the relaxation method.

The performance of the proposed numerical wave tank has been tested with several benchmark applications. At first, grid and time step convergence tests have been performed for periodic regular waves. Next, the interaction of a solitary wave with a vertical structure was calculated. The comparison with experimental free surface measurements showed good agreement. Also, the coarse grids performed well for the solitary wave propagation problem. Further, the model was used to calculate non-breaking wave forces on a vertical cylinder. The model matched the experimental free surface, velocity and wave force data well, showing that the model also predicts the wave kinematics and wave dynamics very realistically. The challenging submerged bar case revealed that the numerical wave tank has the capability to accurately predict wave shoaling and the following wave transformation. In the last test, plunging breaking waves were modeled. The model compared favorably against the experimentally recorded free surface and velocity data. The plunging breaking waves were simulated in a realistic manner and all the stages of the breaking process were captured. The benchmark tests show that the new numerical wave tank REEF3D achieves the goal of accurately representing the physics of wave propagation and hydrodynamics, including the complex problem of wave breaking.

Acknowledgment

The authors would like to thank Prof. Iñigo J. Losada for providing the experimental data for the solitary wave interaction with a vertical structure. The authors would also like to thank Dr. James Kirby and Dr. Francis Ting for sharing the experimental data of the plunging breaking waves case. This study has been carried out under the OWCBW project (No. 217622/E20) and the authors are grateful to the grants provided by the Research Council of Norway. This study was supported in part with computational resources at the Norwegian University of Science and Technology (NTNU) provided by NOTUR, http://www.notur.no.

References

[1] M. Alagan Chella, H. Bihs, D. Myrhaug, and M. Muskulus. Breaking characteristics and geometric properties of spilling breakers over slopes. *Coastal Engineering*, 95:4–19, 2015.

[2] S. Beji and J. A. Battjes. Experimental investigation of wave propagation over a bar. *Coastal Engineering*, 19:151–162, 1993.

[3] S. Beji and J. A. Battjes. Numerical simulation of nonlinear wave propagation over a bar. *Coastal Engineering*, 23:1–16, 1994.

[4] P. A. Berthelsen and O. M. Faltinsen. A local directional ghost cell approach for incompressible viscous flow problems with irregular boundaries. *Journal of Computational Physics*, 227:4354–4397, 2008.

[5] N. Booij, R. C. Ris, and L. H. Holthuijsen. A third-generation wave model for coastal regions, 1. model description and validation. *Journal of Geophysical Research*, 104:7649–7666, 1999.

[6] A. Calderer, S. Kang, and F. Sotiropoulos. Level set immersed boundary method for coupled simulation of air/water interaction with complex floating structures. *Journal of Computational Physics*, 277:201–227, 2014.

[7] A. Chorin. Numerical solution of the Navier-Stokes equations. *Mathematics of Computation*, 22:745–762, 1968.

[8] R. Croce, M. Griebel, and M. A. Schweitzer. Numerical simulation of bubble and droplet deformation by a level set approach with surface tension in three dimensions. *International Journal for Numerical Methods in Fluids*, 62:963–993, 2010.

[9] D. G. Dommermuth, D. K. P. Yue, W. M. Lin, R. J. Rapp, E. S. Chan, and W. K. Melville. Deep-water plunging breakers : a comparison between potential theory and experiments. *Journal of Fluid Mechanics*, 189:434–442, 1988.

[10] P. A. Durbin. Limiters and wall treatments in applied turbulence modeling. *Fluid Dynamics Research*, 41:1–18, 2009.

[11] J. D. Fenton. A fifth-order Stokes theory for steady waves. *Journal of Waterway, Port, Coastal and Ocean Engineering*, 111(2):216–234, 1985.

[12] J. D. Fenton. *The cnoidal theory of water waves*, chapter 2, pages 55–100. Developments in Offshore Engineering, Gulf, Houston. J. B. Herbich edition, 1999.

[13] M. Griebel, T. Dornseifer, and T. Neunhoeffer. *Numerical Simulation in Fluid Dynamics, a Practical Introduction*. SIAM, 1998.

[14] S. T. Grilli, R. Subramanya, I. A. Svendsen, and J. Veeramony. Shoaling of solitary waves on plane beaches. *Journal Waterway Port Coastal and Ocean Enigneering*, 120(6):609–628, 1994.

[15] R. Grimshaw. The solitary wave in water of variable depth. part 2. *Journal of Fluid Mechanics*, 46:611–622, 1971.

[16] A. Harten. High resolution schemes for hyperbolic conservation laws. *Journal of Computational Physics*, 49:357–393, 1983.

[17] P. Higuera, L. J. Lara, and I. J. Losada. Realistic wave generation and active wave absorption for Navier-Stokes models application to OpenFOAM. *Coastal Engineering*, 71:102–118, 2013.

[18] P. Higuera, L. J. Lara, and I. J. Losada. Simulating coastal engineering processes with OpenFOAM. *Coastal Engineering*, 71:119–134, 2013.

[19] P. Higuera, L. J. Lara, and I. J. Losada. Three-dimensional interaction of waves and porous coastal structures using OpenFOAM. Part II: Application. *Coastal Engineering*, 83:259–270, 2014.

[20] M. S. Hossain and W. Rodi. Mathematical modeling of vertical mixing in stratified channel flow. *2nd Symposium on Stratified Flows, Trondheim, Norway*, 1980.

[21] N. G. Jacobsen, D. R. Fuhrman, and J. Fredsøe. A wave generation toolbox for the open-source CFD library: OpenFOAM. *International Journal for Numerical Methods in Fluids*, 70(9):1073–1088, 2012.

[22] G. S. Jiang and D. Peng. Weighted ENO schemes for Hamilton Jacobi equations. *SIAM Journal of Scientific Computing*, 21:2126–2143, 2000.

[23] G. S. Jiang and C. W. Shu. Efficient implementation of weighted ENO schemes. *Journal of Computational Physics*, 126:202–228, 1996.

[24] J. T. Kirby and R. A. Dalrymple. A parabolic equation for the combined refraction-diffraction of Stokes waves by mildly varying topography. *Journal of Fluid Mechanics*, 136:453–466, 1983.

[25] L. J. Lara, M. del Jesus, and I. J. Losada. Three-dimensional interaction of waves and porous coastal structures part II: Experimental validation. *Coastal Engineering*, 64:26–46, 2012.

[26] P. A. Madsen, H. B. Bingham, and H. Liu. A new Boussinesq method for fully nonlinear waves from shallow to deep water. *Journal of Fluid Mechanics*, 462:1–30, 2002.

[27] P. A. Madsen, R. Murray, and O. R. Sørensen. A new form of the Boussinesq equations with improved linear dispersion characteristics. *Coastal Engineering*, 15:371–388, 1991.

[28] S. Mayer, A. Garapon, and L. S. Sørensen. A fractional step method for unsteady free surface flow with applications to non-linear wave dynamics. *International Journal for Numerical Methods in Fluids*, 28:293–315, 1998.

[29] R. Mittal, H. Dong, M. Bozkurttas, F. M. Najjar, A. Vargas, and A. von Loebbecke. A versatile sharp interface immersed boundary method for incompressible flows with complex boundaries. *Journal of Computational Physics*, 227:4825–4852, 2008.

[30] W. Mo, K. Irschik, H. Oumeraci, and P. L.-F. Liu. A 3D numerical model for computing non-breaking wave forces on slender piles. *Journal of Engineering Mathematics*, 58:19–30, 2007.

[31] D. Naot and W. Rodi. Calculation of secondary currents in channel flow. *Journal of the Hydraulics Division, ASCE*, 108(8):948–968, 1982.

[32] NOTUR. Notur - the Norwegian Metacenter for Computational Science. http://www.notur.no, 2015.

[33] O. Nwogu. Alternative form of Boussinesq equations for nearshore wave propagation. *Journal of Waterways, Port, Coastal, and Ocean Engineering*, 119(6):618–638, 1993.

[34] S. Osher and J. A. Sethian. Fronts propagating with curvature-dependent speed: Algorithms based on Hamilton-Jacobi formulations. *Journal of Computational Physics*, 79:12–49, 1988.

[35] B. T. Paulsen, H. Bredmose, and H. Bingham. An efficient domain decomposition strategy for wave loads on surface piercing circular cylinders. *Coastal Engineering*, 86:57–76, 2014.

[36] D. Peng, B. Merriman, S. Osher, H. Zhao, and M. Kang. A PDE-based fast local level set method. *Journal of Computational Physics*, 155:410–438, 1999.

[37] W. E. Rogers, J. M. Kaihatu, L. Hsu, R. E. Jensen, J. D. Dykes, and K. T. Holland. Forecasting and hindcasting waves with the SWAN model in the Southern California Bight. *Coastal Engineering*, 54:1–15, 2007.

[38] B. Seiffert, M. Hayatdavoodi, and R. C. Ertekin. Experiments and computations of solitary-wave forces on a coastal-bridge deck. Part I: Flat plate. *Coastal Engineering*, 88:194–209, 2014.

[39] C. W. Shu and S. Osher. Efficient implementation of essentially non-oscillatory shock capturing schemes. *Journal of Computational Physics*, 77:439–471, 1988.

[40] M. Sussman, P. Smereka, and S. Osher. A level set approach for computing solutions to incompressible two-phase flow. *Journal of Computational Physics*, 114:146–159, 1994.

[41] F. C. K. Ting and J. T. Kirby. Dynamics of surf-zone turbulence in a strong plunging breaker. *Coastal Engineering*, 24:177–204, 1995.

[42] Y. H. Tseng and J. H. Ferziger. A ghost-cell immersed boundary method for flow in complex geometry. *Journal of Computational Physics*, 192:593–623, 2003.

[43] H. van der Vorst. BiCGStab: A fast and smoothly converging variant of Bi-CG for the solution of nonsymmetric linear systems. *SIAM Journal of Scientific Computing*, 13:631–644, 1992.

[44] B. van Leer. Towards the ultimate conservative difference scheme V. A second order sequel to Godunovs method. *Journal of Computational Physics*, 32:101–136, 1979.

[45] Z. Wang, J. Yang, and F. Stern. A coupled level set and volume-of-fluid method for sharp interface simulation of plunging breaking waves. *International Journal of Multiphase Flow*, 35:227–246, 2009.

[46] H. G. Weller. A new approach to VOF-based interface capturing methods for incompressible and compressible flow. *Technical Report. OpenFOAM*, 2008.

[47] R. Wemmenhove. *Numerical Simulation of Two-Phase Flow in Offshore Environments*. PhD thesis, Faculty of Mathematics and Natural Sciences, University of Groningen, 2008.

[48] D. C. Wilcox. *Turbulence Modeling for CFD*. DCW Industries Inc., La Canada, California., 1994.

[49] F. Xu, W. Perrie, B. Toulany, and P. C. Smith. Wind-generated waves in Hurricane Juan. *Ocean Modeling*, 16:188–205, 2007.

[50] J. Yang and F. Stern. Robust and efficient setup procedure for complex triangulations in immersed boundary simulations. *Journal of Fluids Engineering*, 135(10):101107.1–101107.11, 2014.

[51] J. Yang, Z. Wang, and F. Stern. Sharp interface immersed-boundary/level-set method for wave–body interactions. *Journal of Computational Physics*, 228:6590–6616, 2009.

[52] W. Yue, C.-L. Lin, and V. C. Patel. Numerical simulation of unsteady multidimensional free surface motions by level set method. *International Journal for Numerical Methods in Fluids*, 42:853–884, 2003.

Paper 2

CFD Investigations of Wave Interaction with a Pair of Large Tandem Cylinders

Kamath A., Alagan Chella M., Bihs H. and Arntsen Ø.A. (2015)
Ocean Engineering, 108, 738-748.

Ocean Engineering 108 (2015) 738–748

Contents lists available at ScienceDirect

Ocean Engineering

journal homepage: www.elsevier.com/locate/oceaneng

CFD investigations of wave interaction with a pair of large tandem cylinders

Arun Kamath *, Mayilvahanan Alagan Chella, Hans Bihs, Øivind A. Arntsen

Department of Civil and Transport Engineering, Norwegian University of Science and Technology, 7491 Trondheim, Norway

ARTICLE INFO

Article history:
Received 6 January 2015
Accepted 25 August 2015
Available online 20 September 2015

Keywords:
Wave forces
Wave interaction
Vertical cylinders
Numerical wave tank
CFD

ABSTRACT

Wave forces and the flow field around cylinders placed in a periodic wave field are investigated with a numerical model using the Reynolds-averaged Navier–Stokes equations. The numerical model is validated by simulating the wave interaction with a single cylinder and comparing the numerical results with experimental data from a large scale experiment. Then, the wave interaction with a single large cylinder and a pair of large cylinders placed in tandem for different incident wave steepnesses is studied. The numerically calculated forces are compared with predictions from potential theory. The numerical results are seen to match the predictions at low incident wave steepness but differ at higher incident wave steepnesses. The wave diffraction pattern around the tandem cylinders for waves of low and high steepness is investigated and the evolution of a strong diffraction pattern is seen in the case of high steepness waves, which results in the difference between the wave forces predicted by potential theory and the numerical model at higher steepnesses.

1. Introduction

Circular cylindrical structures are commonly used in the support structures of offshore wind turbines, oil and gas platforms, offshore mooring dolphins in deep and intermediate waters and nearshore coastal structures. Understanding the interaction of waves with these structures is important for the accurate prediction of the hydrodynamic loads on them. Moreover, the interaction of waves with large cylindrical structures always modifies the characteristics of the incident wave field and influences the wave induced processes of wave radiation and diffraction. The modified kinematics of the flow field changes the flow processes such as the wave run-up, reflection and transmission. In the case of a circular cylinder, the contribution of drag and inertia forces to the total forces is determined by the KC number and the diffraction parameter. When the diffraction parameter, which is the ratio of the cylinder diameter (D) to the incident wavelength (L), is greater than 0.2 ($D/L > 0.2$) and the KC number is smaller than 2, the flow is inertia dominated and wave diffraction effects are important (Isaacson, 1979). Lower-order solutions can be obtained with analytical formulations based on potential theory by assuming that the fluid is inviscid, the flow irrotational and the wave amplitude small compared to the diameter of the cylinder. The methods based on potential theory are limited by these assumptions, when the incident wave is steep. The importance of non-linear interactions arising from diffracted waves and the viscous effects in an unseparated flow regime have to be investigated by accounting for these phenomena and comparing the results with predictions from potential theory.

MacCamy and Fuchs (1954) derived an equation using linear potential theory to obtain the first-order wave force on a single large cylinder using the wave diffraction potential. This equation is commonly used to determine wave forces on a single large cylinder exposed to regular waves. Chakrabarti and Tam (1973) carried out experimental studies on large cylinders exposed to small amplitude waves and found good agreement with predictions from linear potential theory. Some studies proposed certain methods to evaluate higher order forces using potential theory (Lighthill, 1979; Molin, 1979), but had difficulties in obtaining convergent solutions.

In a diffraction regime, the incident wave train is affected by its interaction with the cylinder and its effects are seen even outside the immediate vicinity of the cylinder. This results in a complex hydrodynamic problem when groups of large cylinders are placed in a wave field. Ohkusu (1974) proposed an iterative method to evaluate successive water wave scattering by floating bodies, based on the work by Twersky (1952) for electromagnetic and acoustic waves. The velocity potential functions used in this approach become harder to work with as the number of cylinders is increased. Spring and Monkmeyer (1974) proposed a method where all the boundary conditions are enforced at once and the wave forces are determined by solving a set of linear equations.

* Corresponding author. Tel.: +47 73 59 46 40; fax: +47 73 59 70 21.
E-mail address: arun.kamath@ntnu.no (A. Kamath).

http://dx.doi.org/10.1016/j.oceaneng.2015.08.049
0029-8018/

Linton and Evans (1990) improved the method by Spring and Monkmeyer (1974) and proposed a method with a simplified expression for the velocity potential to obtain the maximum first-order force, the mean second-order force on the cylinder and to calculate the free surface amplitudes for equally spaced identical cylinders. Using this analytical method, it is possible to evaluate the amplitude of the wave forces on cylinders placed in a group and to determine the maximum variation of the free surface around the cylinders.

The limitation of analytical formulae based on potential theory is that they have to be modified to deal with different scenarios, for example, to study structures of different geometries, to study non-linear wave–wave and wave–body interactions due to waves of high steepnesses. Numerical modeling based on boundary integral equations (Ferrant, 1995; Boo, 2002; Song et al., 2010) have the same limitations as potential theory, on which they are based. On the other hand, Computational Fluid Dynamics (CFD) modeling provides an immense amount of detail regarding the wave hydrodynamics by representing most of the wave physics with few assumptions. CFD modeling of wave interaction with large cylinders placed close to each other can provide more insight into the physical processes, such as the effect of wave diffraction on neighboring objects including the wave elevation, wave forces, water particle velocities, the influence of the center-to-center distance and the incident wave steepness. The scale and geometries considered in studies using a CFD model may not be directly applicable to determining the hydrodynamic loads on an offshore structure, but the validation of such a model provides the first step towards establishing such methods to an eventual application to larger and more complicated problems, with realistic geometries and scales in the future, since full scale data and field observations are generally lacking. Another application is to extend the studies to random wave forces (Boccotti et al., 2012) after establishing the numerical model for regular waves in this study. The validated numerical model can be used to gain further insight into the applicability of the Morison equation in the case of random waves and build upon the knowledge gained from the field experiments in recent literature (Boccotti et al., 2013).

In this study, the open source CFD model, REEF3D (Alagan Chella et al., 2015) is used to analyse wave interaction with bottom-fixed vertical cylinders in a 3D numerical wave tank. The paper presents studies with a large number of simulations investigating the changes in the wave hydrodynamics with small incremental changes in parameters using CFD simulations. The model is validated by comparing the computed wave forces on a single cylinder, free surface elevations around the cylinder and the water particle velocities with the experimental data from the large-scale experiments carried out at the Large Wave Flume (GWK) in Hannover, Germany by Mo et al. (2007). Then, the wave forces on a single cylinder and on a pair of tandem cylinders for different wave steepnesses and center-to-center distances are calculated in 108 numerical simulations. The wave forces on a single cylinder due to waves of different steepnesses are studied, along with the wave elevation around the cylinder. The wave forces experienced by a pair of tandem cylinders with different center-to-center distances and different incident wave steepnesses are evaluated. A total of 96 simulations are carried out to investigate the change in the wave forces with respect to the center-to-center distance and the wave steepness. The wave elevation in the vicinity of the cylinders is studied to gain more knowledge about the wave propagation and the evolution of wave diffraction patterns between the neighboring cylinders. In addition, the analytical formula proposed by Linton and Evans (1990) is used to compare the wave forces on the tandem cylinders for low wave steepnesses where linear potential theory is valid.

2. Numerical model

2.1. Governing equations

REEF3D uses the incompressible Reynolds-averaged Navier–Stokes (RANS) equations together with the continuity equation to solve the fluid flow problem:

$$\frac{\partial u_i}{\partial x_i} = 0 \tag{1}$$

$$\frac{\partial u_i}{\partial t} + u_j\frac{\partial u_i}{\partial x_j} = -\frac{1}{\rho}\frac{\partial p}{\partial x_i} + \frac{\partial}{\partial x_j}\left[(\nu+\nu_t)\left(\frac{\partial u_i}{\partial x_j}+\frac{\partial u_j}{\partial x_i}\right)\right] + g_i \tag{2}$$

where u is the time averaged velocity, ρ is the density of the fluid, p is the pressure, ν is the kinematic viscosity, ν_t is the eddy viscosity and g is the acceleration due to gravity. The pressure is determined using the projection method (Chorin, 1968) and the resulting Poisson equation is solved with a preconditioned BiCG-Stab solver (van der Vorst, 1992). Turbulence modeling is carried out using the two equation k–ω model proposed by Wilcox (1994). The strain in the flow due to the waves leads to unphysical overproduction of turbulence in the wave tank. To avoid this, eddy viscosity limiters are used as shown by Durbin (2009). Also, the strain due to the large difference in density at the interface between air and water causes an overproduction of turbulence at the interface. This is avoided by free surface turbulence damping around the interface as shown by Naot and Rodi (1982). The damping is carried out only around the interface using the Dirac delta function. REEF3D is fully parallelized using the domain decomposition strategy and MPI (Message Passing Interface).

2.2. Free surface

The free surface is determined with the level set method. The zero level set of a signed distance function $\phi(\vec{x}, t)$ is used to represent the interface between air and water (Osher and Sethian, 1988). Moving away from the interface, the level set function gives the shortest distance from the interface. The sign of the function distinguishes between the two fluids across the interface as shown in the following equation:

$$\phi(\vec{x}, t)\begin{cases} >0 & \text{if } \vec{x} \text{ is in phase 1} \\ =0 & \text{if } \vec{x} \text{ is at the interface} \\ <0 & \text{if } \vec{x} \text{ is in phase 2} \end{cases} \tag{3}$$

The level set function is moved under the influence of an external velocity field u_j with the convection equation:

$$\frac{\partial \phi}{\partial t} + u_j\frac{\partial \phi}{\partial x_j} = 0 \tag{4}$$

The level set function loses its signed distance property on convection and is reinitialized after every iteration using a partial differential equation based reinitialization procedure by Peng et al. (1999) to regain its signed distance property.

2.3. Discretization schemes

The fifth-order conservative finite difference Weighted Essentially Non-Oscillatory (WENO) scheme proposed by Jiang and Shu (1996) is applied for the discretization of the convective terms of the RANS equation. The level set function, turbulent kinetic energy and the specific turbulent dissipation rate are discretized using the Hamilton–Jacobi formulation of the WENO scheme by Jiang and

Peng (2000). The WENO scheme is a minimum third-order accurate and numerically stable even in the presence of large gradients. Time advancement for the momentum and level set equations is carried out using a Total Variation Diminishing (TVD) third-order Runge–Kutta explicit time scheme proposed by Shu and Osher (1988). Adaptive time stepping is employed to satisfy the CFL criterion based on the maximum velocity in the domain. This ensures numerical stability throughout the simulation with an optimal value of time step size. A first-order scheme is utilized for the time advancement of the turbulent kinetic energy and the specific turbulent dissipation, as these variables are mostly source term driven with a low influence of the convective terms. Diffusion terms of the velocities are also subjected to implicit treatment in order to remove the diffusion terms from the CFL criterion. The convergence studies for the simulations are then just carried out for the grid size to determine the accuracy of the results, since the adaptive time stepping approach determines the optimal time step required to maintain the numerical stability. As an example, in the case of non-breaking wave interaction with a vertical cylinder presented in this study, time steps are smaller, about 0.002 s during the first few seconds of the simulation as the waves are introduced into the wave tank and then increase to about 0.004 s as the periodic waves are established in the tank. In this way, the adaptive time stepping approach determines the optimal time step, reducing the cost of the simulation and avoiding numerical instability in a simulation which could occur with a fixed time step approach.

The numerical model uses a uniform Cartesian grid for the spatial discretization together with the Immersed Boundary Method (IBM) to represent the irregular boundaries in the domain. Berthelsen and Faltinsen (2008) developed the local directional ghost cell IBM to extend the solution smoothly in the same direction as the discretization, which is adapted to three dimensions in the current model.

2.4. Numerical wave tank

The numerical wave tank uses the relaxation method (Larsen and Dancy, 1983) for wave generation and absorption. This method requires a certain length of the wave tank to be reserved as wave generation and absorption zones. Relaxation functions are used to moderate the velocity and the free surface using a wave theory in the relaxation zones with

$$u_{relaxed} = \Gamma(x)u_{analytical} + (1 - \Gamma(x))u_{computational}$$
$$\phi_{relaxed} = \Gamma(x)\phi_{analytical} + (1 - \Gamma(x))\phi_{computational} \quad (5)$$

where $\Gamma(x)$ is the relaxation function and $x \in [0, 1]$ is the x-coordinate scaled to the length of the relaxation zone. The relaxation function proposed by Jacobsen et al. (2012), shown in (6), is used in the numerical model:

$$\Gamma(x) = 1 - \frac{e^{x^{3.5}} - 1}{e - 1} \quad (6)$$

The wave theory for moderating the numerical values is chosen according to the wave steepness and the water depth in the simulation. Typically, the wave generation zone is one wavelength long and the absorption zone is two wavelengths long. In the wave generation zone, the computational values of velocity and free surface are raised to the analytical values prescribed by wave theory. The generation zone releases waves into the working zone of the tank. The objects to be studied are placed in the working zone of the tank. The relaxation function in the generation zone also absorbs reflections from structures in the wave tank and prevents them from affecting wave generation. At the end of the tank, the wave enters the numerical beach. Here, the computational values of velocity and free surface are reduced to zero in a smooth manner. This simulates the effect of a beach where the wave energy is removed from the wave tank.

3. Calculation of wave forces

3.1. Numerical evaluation of wave forces

The numerical model evaluates the wave force F on an object as the integral of the pressure p and the surface normal component of the viscous shear stress tensor τ on the object according to the following equation:

$$F = \int_{\Omega} (-\mathbf{n}p + \mathbf{n}\cdot\tau)\, d\Omega \quad (7)$$

where $\mathbf{n}$ is the unit normal vector pointing into the fluid and Ω is the surface of the object. This is readily accomplished by the numerical model as the values for pressure and shear stress are available at every point in the domain at any given time of the simulation.

3.2. Analytical formulae for wave forces

Potential theory is used to obtain the wave diffraction potential and calculate the force on a single cylinder using the equation presented by MacCamy and Fuchs (1954), shown in the follwing equation:

$$|F| = \left| \frac{4\rho g i a \tanh(kd)}{k^2 H_1'(kr)} \right| \quad (8)$$

where $i = \sqrt{-1}$, a is the incident wave amplitude, $k = 2\pi/L$ is the wave number, d is the water depth and H_1' is the first derivative of the Hankel function of the first kind and r is the radius of the cylinder. An extension of the diffraction theory proposed by Linton and Evans (1990) to calculate wave forces on multiple cylinders placed in proximity is presented in the following equation:

$$A_m^l + \sum_{\substack{j=1 \\ \neq l}}^{N} \sum_{n=-M}^{M} A_j^n Z_n^j e^{i(n-m)\alpha_{jl}} H_{n-m}(kR_{jl}) = -I_l e^{im(\pi/2-\beta)}$$
$$l = 1,\ldots,N,\ \ m = -M,\ldots,M. \quad (9)$$

where M is the order of the solution, N is the number of cylinders, I is the incident wave potential, β is the angle of wave propagation with respect to the x-axis, H is the Hankel function of the first kind, R_{jl} is the length of the line joining the centers of the jth and the lth cylinder, α_{jk} is the angle between the x-axis and the line joining the centers of the cylinders and $Z = J'(kr_j)/H'(kr_j)$, where J is the Bessel function of the first kind. The unknown coefficients A are to be evaluated. This results in a set of $N(2M + 1)$ equations. Linton and Evans (1990) suggest that a value of $M=6$ provides sufficiently accurate solutions. So, $M=6$ is used in the equations to obtain the analytical prediction of wave forces in this study. The unknown coefficients A are evaluated by solving (9) and the wave forces are obtained using the following equation:

$$\left| \frac{F^j}{F} \right| = \frac{1}{2} |A_{-1}^j \pm A_1^j| \quad (10)$$

The subtraction of the coefficients on the right hand side gives the

wave force along the x-axis and the addition of the terms gives the wave force along the y-axis. In the current study, the angle of incidence $\beta = 0$ and the waves propagate along the x-axis.

4. Results

4.1. Validation of the numerical model

The numerical model is validated by simulating the experiments carried out at the Large Wave Flume (GWK), Hannover, Germany by Mo et al. (2007). The numerically computed values for the free surface elevation around the cylinder, the water particle velocity in the numerical wave tank and the wave force on the cylinder are compared with the experimental data to confirm that the numerical model accurately calculates the wave kinematics and dynamics. The wave flume in the experiments is 309 m long, 5 m wide and 7 m deep. A cylinder of diameter $D=0.7$ m is placed 111 m from the wavemaker and strain gages are placed at the top and bottom of the cylinder in order to measure wave forces. Wave gages are placed at several locations around the cylinder to measure the time histories of the free surface elevation. Four acoustic Doppler velocimeters (ADVs) are placed at the side wall along the front line of the cylinder at various depths to measure the water particle velocities.

The numerical wave tank used in this simulation is 132 m long, 5 m wide and 8 m high. Fifth-order Stokes waves with a wave height $H=1.2$ m, wave period $T=4.0$ s, wavelength $L=21.9$ m are generated with a water depth $d=4.76$ m on a grid of $dx=0.1$ m. The grid in the numerical wave tank is $1320 \times 50 \times 80$ cells resulting in a total number of 5.28 million cells. The cylinder is placed in the center with respect to the side walls as seen in the numerical setup in Fig. 1. The diffraction parameter $D/L = 0.032$ and KC=6.1 in this case.

A net inline force acts on the cylinder due a difference in pressure in front and behind the cylinder. The calculated force on the cylinder is compared with the experimental data and a good agreement is seen in Fig. 2a. Mo et al. (2007) noted that the force measured in the experiments matched the inertial force given by the Morison formula with $C_m=2$. So, it appears that the forces are inertia dominated, although the KC number is 6.1 in this case. A grid convergence study for the forces is carried out by repeating the simulations with grid sizes of $dx=0.15$m and 0.2 m. The force in these cases is compared with the calculated force using a grid size of $dx=0.1$ m and the experimental result. It is seen that the numerical result converges to the experimental value at a grid size of $dx=0.1$ m in Fig. 2b. Thus, the selected grid size is sufficiently small to accurately calculate the force on the cylinder.

The numerically obtained free surface elevation near the wall along the front line of the cylinder is compared with the experimental data in Fig. 3a. The amplitude at the first crest is considered the maximum amplitude of the wave elevation recorded by the gage near the wall, $\eta_{max,wall}$. The comparisons of the computed and measured free surface elevation in front, at the side and behind the cylinder are presented in Fig. 3b, c and d respectively. The difference in pressure in front and behind the cylinder is seen in the free surface elevation around the cylinder. The numerically obtained free surface elevation data shows a good match with the experimental measurements. The water particle velocity calculated by the numerical model is compared with the experimental measurements at 0.93 m, 1.53 m and 2.73 m below the still water level at the side wall of the tank along the front line of the cylinder in Fig. 4. The numerical results are scaled with the numerically calculated wave celerity, $C=5.48$ m/s. The water particle velocity is expected to reduce with increasing distance from the free surface as seen in Fig. 4 with the amplitude of the velocity being the lowest in Fig. 4a at 2.73 m from the still water level. The water particle velocities calculated by the model match the values observed in the experiments very well, showing that the numerical model is able to represent the wave kinematics correctly.

4.2. Grid convergence study for wave propagation

Accurate wave generation and propagation in the numerical wave tank is verified with a grid convergence study. A two-dimensional wave tank with a length of 15 m, height of 1.0 m and water depth $d=0.5$m is used. Fifth-order Stokes waves are generated with a wave height of $H=0.1$ m, wavelength of $L=2.0$ m and wave period $T=1.14$ s. This setup of the numerical wave tank is used in the following sections to simulate the wave interaction with large cylinders. The grid convergence is carried out for the most stringent case with the highest wave steepness used in the study. The grid size dx in the wave tank is varied from 0.1 m to 0.01 m. The results are presented in Fig. 5. It is seen that the free surface elevation η conforms to the required value at a grid size of $dx=0.025$ m. The damping of the wave amplitude at grid sizes of 0.1 m and 0.05 m is seen in the figure. This is reduced as the grid size is reduced to 0.025 m and the improvement in the results on further reducing the grid size is negligible. Thus, a grid size of $dx=0.025$ m is selected for the following simulations in the current study.

4.3. Wave interaction with a single large cylinder

Simulations are carried out with a cylinder of diameter $D=0.5$ m in a wave tank 15 m long, 5 m wide and 1 m high with a

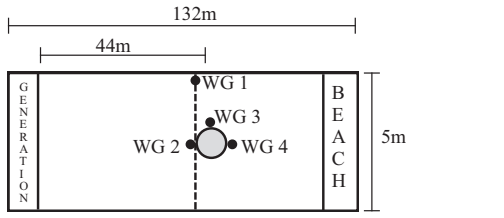

Fig. 1. Numerical setup used for validation of the model.

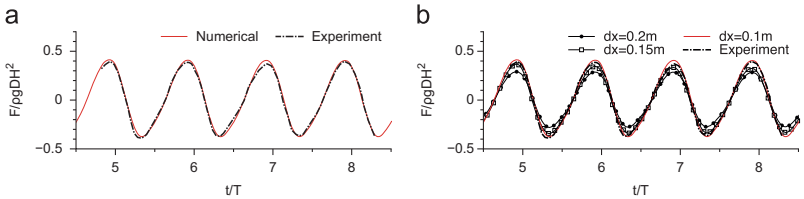

Fig. 2. Comparison of experimental and numerical results for the inline wave force on the cylinder: (a) wave force on a single circular cylinder and (b) convergence study for wave force calculation.

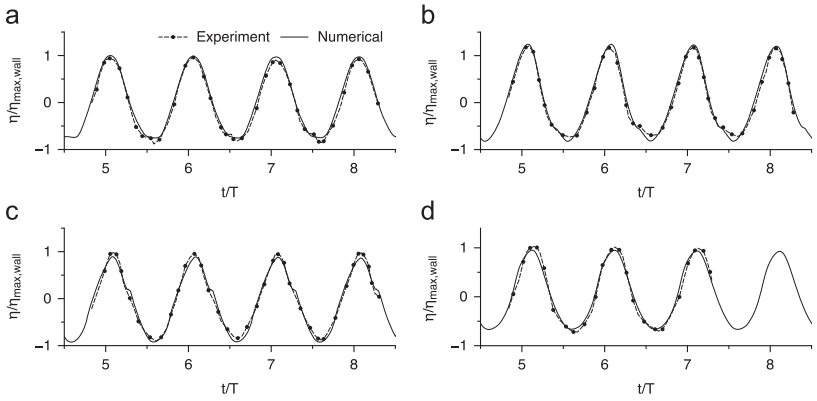

Fig. 3. Comparison of experimental and numerical results for free surface elevations around the cylinder: (a) along the frontline near the wall, (b) in front of the cylinder, (c) behind the cylinder, and (d) beside the cylinder.

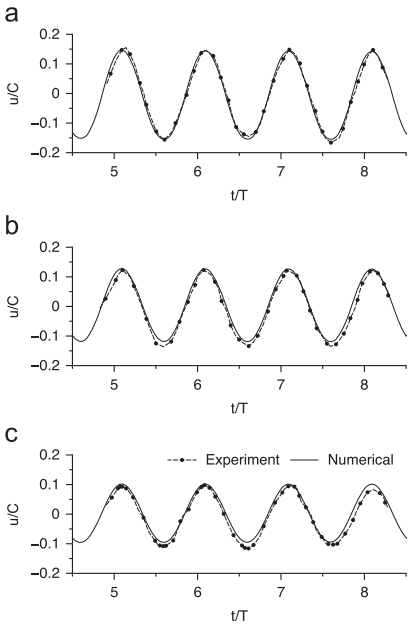

Fig. 4. Comparison of experimental and numerical results for wave particle velocity in the wave tank: (a) $z = -0.93$ m , (b) $z = -1.53$ m, and (c) $z = -2.73$ m.

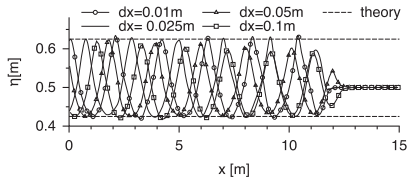

Fig. 5. Grid convergence study for wave propagation.

water depth of $d=0.5$ m. Linear waves of height $H=0.006$ m and 0.02 m, second-order Stokes waves with $H=0.06$ m and 0.1 m, fifth-order Stokes waves with $H=0.11$ m, 0.12 m, 0.13 m, 0.14 m, 0.15 m, 0.16 m, 0.18 m and 0.2 m with a wavelength $L=2$ m are incident on the cylinders resulting in $D/L=0.25$. The KC numbers for these simulations are between 0.04 and 1.37. The resulting wave steepnesses and the incident wave frequency for the different cases are listed in Table 1. The linear and 2*nd*-order Stokes waves have the same wave frequency for different incident wave heights but in the case of 5*th*-order Stokes waves the wave height is included in the dispersion relation and a small decrease in the wave frequency is seen with increasing wave height. The computed inline wave force on the cylinder for $H/L = 0.003$ is compared to the analytically predicted maximum and minimum value from the MacCamy–Fuchs equation and a good agreement is seen in Fig. 6a. The computed wave force on the cylinder for different wave steepnesses is compared with the prediction from the MacCamy–Fuchs equation in Fig. 6b. It is seen that the numerical results agree with the predictions at lower wave steepnesses but the numerical results for the higher wave steepnesses are seen to be lower than the predictions from the equation. According to the MacCamy–Fuchs equation, the wave force on the cylinder increases linearly with an increase in the incident wave height H for a given cylinder diameter D. The variation of the computed force on the cylinder with increasing steepness suggests that the total force on the cylinder is reduced due to non-linear interaction of high-steepness waves with the cylinder and the diffracted waves.

The variation of the free surface elevation η in front, behind and beside the cylinder for an incident wave of low steepness $H/L = 0.003$ shows 1.72 times the incident wave crest height η_{c_i} in front of the cylinder in Fig. 7a. The phase difference between the wave elevations in front and behind the cylinder is 0.78π and it is 0.24π between the elevations in front and beside the cylinder. In the case of an incident wave with the high steepness of $H/L = 0.1$ in Fig. 7b, the evolution of wave asymmetry is apparent with the crest height $1.55\eta_{c_i}$ and the trough $0.95\eta_{c_i}$ in front of the cylinder. The phase difference between the wave elevations in front and behind the cylinder is 0.80π and it is 0.20π for the elevations in front and beside the cylinder. Thus, the high steepness waves move faster around the upstream half of the cylinder but slower around the downstream half of the cylinder, in comparison to the waves of low steepness. This points towards a deceleration of the water particles in the region after the upstream half of the cylinder. The waveform behind the cylinder is also highly asymmetrical, resulting in shallower troughs behind the cylinder, when a crest is incident in front of the cylinder. This increased asymmetry points towards a different pressure difference regime in the case of the high-steepness waves. As a result of the deceleration of the water

Table 1
Combination of parameters for simulations with a single large cylinder of diameter $D=0.5$ m in a water depth of $d=0.5$ m.

L (m)	H/L											
	Linear waves		2*nd*-Order Stokes		5*th*-Order Stokes							
2.0	0.003	0.01	0.03	0.05	0.055	0.06	0.065	0.07	0.075	0.08	0.09	0.10
f (Hz)	0.846	0.846	0.846	0.846	0.862	0.865	0.868	0.872	0.876	0.880	0.889	0.899

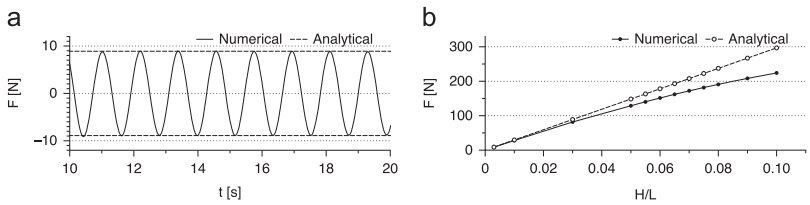

Fig. 6. Comparison of analytical and numerical results for the inline wave force on a single large cylinder: (a) $H=0.006$ m and (b) wave force for different incident wave steepnesses.

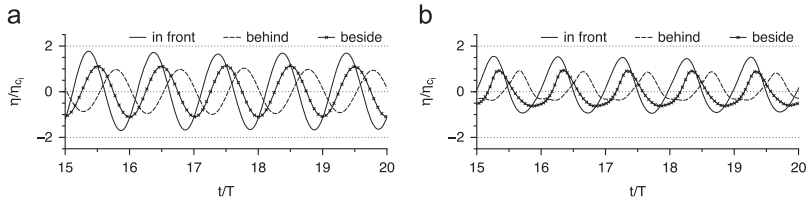

Fig. 7. Relative free surface elevations around the single cylinder for incident waves of low and high steepness: (a) $H/L = 0.003$ and (b) $H/L = 0.1$.

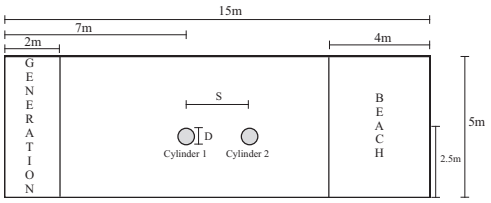

Fig. 8. Schematic diagram of the setup used for the simulations with two tandem cylinders.

particles and the asymmetry of the wave, the force acting on the cylinder due to an incident wave of high steepness is lower than the prediction from MacCamy–Fuchs equation based on linear potential theory.

4.4. Wave interaction with a pair of tandem cylinders

A set of simulations is carried out to study the wave interaction with two cylinders placed in tandem in the direction of wave propagation. Cylinders with a diameter $D=0.5$ m are placed in a wave tank that is 15 m long, 5 m wide and 1 m high with a water depth $d=0.5$ m on a grid of $dx=0.025$ m. A schematic diagram illustrating the numerical setup is given in Fig. 8. The grid is $600 \times 200 \times 40$ cells resulting in a total of 4.80 million cells in the numerical wave tank. Linear waves with a wave height $H=0.006$ m and 0.02 m, second-order Stokes waves with $H=0.06$ m and 0.1 m, fifth-order Stokes waves with $H=0.11$ m, 0.12 m, 0.13 m, 0.14 m, 0.15 m, 0.16 m, 0.18 m and 0.2 m with a wavelength $L=2$m are incident on the cylinders. The KC numbers in these cases range between 0.04 and 1.37. For each of the incident wave heights, center-to-center distance between the two cylinders $S=0.8$ m, 1.2 m, 1.6 m, 1.8 m, 2.0 m, 2.3 m and 3.37 m are simulated. The different combinations of incident wave steepness and the center-to-center distance for the 96 simulations are listed in Table 2. The cylinder directly facing the incident waves is cylinder 1 and the downstream cylinder is cylinder 2. Previous works using analytical methods (Linton and Evans, 1990; McIver and Evans, 1984; Malenica et al., 1999) have shown that the wave forces on tandem cylinders are influenced by not only the incident wave height and the spacing between the cylinder, but also by the incident wave frequency. In order to maintain the focus on the effect of the incident wave height with small increments in wave steepness for different distances between the cylinder, the effect of the incident wave frequency is not analysed in this paper.

The variation of the computed inline wave force on the cylinders with center-to-center distances S for different incident wave steepnesses H/L is presented in Fig. 9. The prediction from the formula by Linton and Evans (1990) is also included for obtaining a baseline comparison. It is clearly seen that the analytical prediction matches the computed wave force closely at the lowest wave steepness of $H/L = 0.003$ for both cylinders, in Fig. 9(a) and (b). The computed wave forces show a similar form of variation for $H/L = 0.05$ as predicted by the analytical formula but with lower magnitudes in Fig. 9(c) and (d). The deviation from the predictions by the analytical formula is clear in Fig. 9(e) and (f) for the highest wave steepness simulated, $H/L = 0.1$. In addition to the amplitude of the force, the form of the variation is also different at longer distances of separation S. Cylinder 1 experiences large changes in the wave force when the center-to-center distance between the cylinders is changed. The difference between the largest force at $S=0.8$ m and the lowest force at $S=3.37$ m is 35% for $H/L = 0.003$ and $H/L = 0.05$, but about 22% for $H/L = 0.1$. The change in the center-to-center distance S strongly affects cylinder 2 at small values of $S=0.8$ m and $S=1.2$ m, with a change of 17.4% for $H/L = 0.003$, 18% for $H/L = 0.05$ and 16% for $H/L = 0.1$. Whereas, the difference in the forces at $S=2.0$ m and $S=3.37$ m is 8% for

Table 2
Combination of parameters for simulations with two tandem large cylinders with diameter D=0.5 m, incident wavelength L=2.0 m in a water depth d=0.5 m.

S (m)	H/L											
	Linear waves		2*nd*-Order Stokes		5*th*-Order Stokes							
0.8	0.003	0.01	0.03	0.05	0.055	0.06	0.065	0.07	0.075	0.08	0.09	0.10
1.2	0.003	0.01	0.03	0.05	0.055	0.06	0.065	0.07	0.075	0.08	0.09	0.10
1.6	⋮	⋮	⋮	⋮	⋮	⋮	⋮	⋮	⋮	⋮	⋮	⋮
1.8	⋮	⋮	⋮	⋮	⋮	⋮	⋮	⋮	⋮	⋮	⋮	⋮
2.0	⋮	⋮	⋮	⋮	⋮	⋮	⋮	⋮	⋮	⋮	⋮	⋮
2.3	⋮	⋮	⋮	⋮	⋮	⋮	⋮	⋮	⋮	⋮	⋮	⋮
2.8	⋮	⋮	⋮	⋮	⋮	⋮	⋮	⋮	⋮	⋮	⋮	⋮
3.37	0.003	0.01	0.03	0.05	0.055	0.06	0.065	0.07	0.075	0.08	0.09	0.10

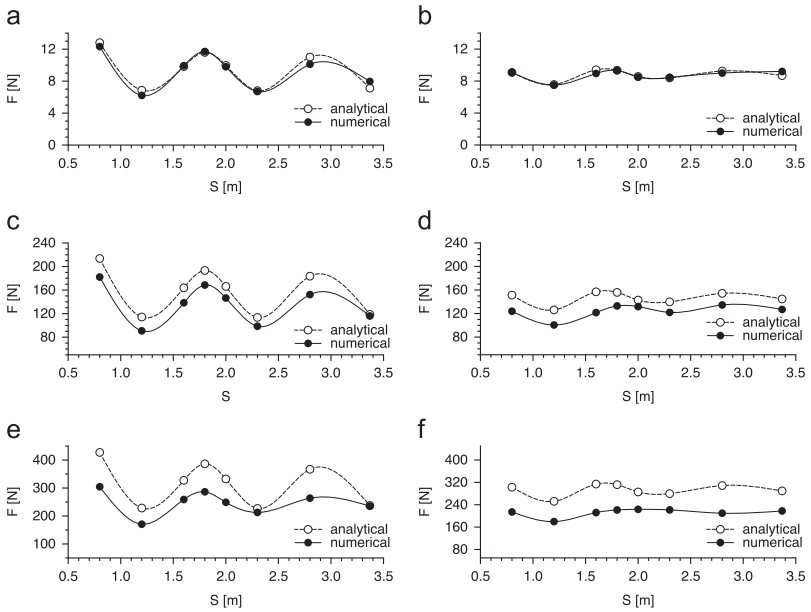

Fig. 9. Variation of the inline wave forces on tandem cylinders with center-to-center distance for different wave steepnesses: (a) cylinder 1 for H/L = 0.003, (b) cylinder 2 for H/L = 0.003, (c) cylinder 1 for H/L = 0.05, (d) cylinder 2 for H/L = 0.05, (e) cylinder 1 for H/L = 0.1, and (f) cylinder 2 for H/L = 0.1.

H/L = 0.003, 4% for H/L = 0.05 and 2.5% for H/L = 0.1. It is observed that the Bessel wave-like variation of the wave forces with the center-to-center distance is damped out with increasing incident wave steepness for both cylinders. Even though, the analytically predicted wave force on cylinder 1 matches the computed wave force at S=3.37 m for H/L = 0.05 in Fig. 9c and S=2.3 m, S=3.37 m for H/L = 0.1 in Fig. 9e, the wave force variation with S is clearly different.

The variation of the wave forces on the two cylinders for different center-to-center distances S at various incident wave steepnesses H/L is presented in Fig. 10. It is seen that the wave forces on both cylinders match the analytical prediction at lower H/L = 0.003 and 0.01. On increasing the wave steepness, the computed wave forces gradually deviate from the analytical prediction. The computed forces are lower than the predictions from the analytical formula. The computed wave force on cylinder 1 at S=0.8 m for H/L = 0.1 is 30% lower than the analytical prediction and 35% lower on cylinder 2 (Fig. 10a). It is also observed that at a center-to-center distance of S = 3.37 m (Fig. 10h), the wave forces on both the cylinders are almost equal. At this point, the effect of diffraction in between the two cylinders is reduced significantly and it does not influence the wave forces on the cylinders anymore.

Wave gages are placed in front ($F1$, $F2$), behind ($B1$, $B2$), beside each of the cylinders ($C1$, $C2$) and at the midpoint between the two cylinders ($C0$) at locations shown in Fig. 11 for H/L = 0.003 and H/L = 0.1 with S=0.8 m. In the case of low steepness incident waves of H/L = 0.003, the variation of the free surface elevation is sinusoidal around both the cylinders in Fig. 12(a) and (b). It is observed that the crest height is increased in front of the cylinders due to the incident wave interaction with the cylinders ($F1$, $F2$) and due to the superposing of the incident waves and the reflected waves behind the cylinder ($B1$). The computed free surface elevations at $B1$, $F2$ and $C0$ have the same amplitude and phase, implying uniform heave motion of the water along the line joining the centers of the two cylinders.

In the case of high steepness incident waves of H/L = 0.1, the incident waveform is asymmetrical with shallow troughs and sharp crests in Fig.12(c) and (d), characteristic of fifth-order Stokes waves. The waveform computed at $C1$ shows increased asymmetry compared to the incident waves. This is attributed to the interaction of the incident waves with the out of phase reflected waves

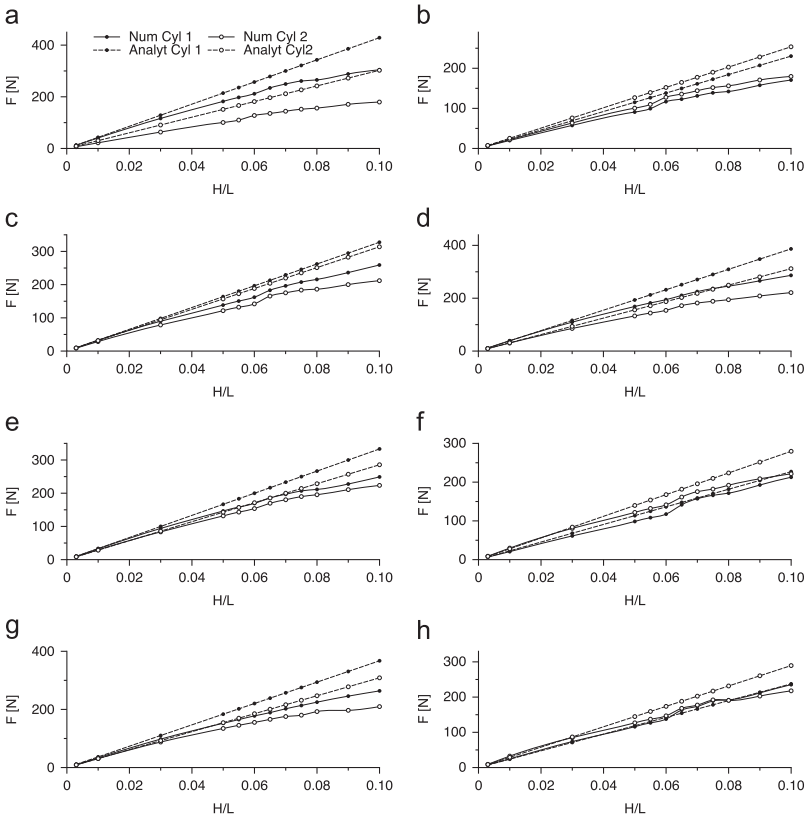

Fig. 10. Variation of the inline wave forces on tandem cylinders with wave steepness for different center-to-center distances: (a)S=0.8 m, (b) S=1.2 m, (c) S=1.6 m, (d) S=1.8 m, (e) S=2.0 m, (f) S=2.3 m, (g) S=2.8 m, and (h) S=3.37 m.

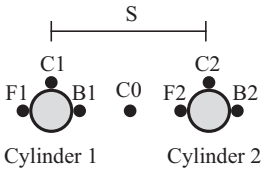

Fig. 11. Schematic diagram of the domain around the two tandem cylinders showing wave gage locations.

from the cylinder. Wage gages $B1$, $C0$ and $F2$ show a continuously increasing crest elevation as the wave propagates away from cylinder 1 and towards cylinder 2, due to the strong diffraction regime between the two cylinders. The crest elevation then reduces at $C2$ and $B2$, as the wave propagates around cylinder 2. Also, the free surface elevations at $B1$, $C0$ and $F2$ are slightly out of phase and have different amplitudes signifying a complex wave diffraction regime in the region between the cylinders.

Several differences are observed between the interaction of low and high steepness waves with a pair of tandem cylinders. The incident high steepness fifth-order waves are asymmetrical by nature with a shallow trough and a sharp crest. This characteristic of the waves is magnified as it interacts with the large cylinders and the waveform becomes more asymmetrical. This is in contrast to the interaction of the low steepness linear waves, where the waveforms remain sinusoidal. The relative crest height η/η_{c_i} in front of the cylinders is similar for both high and low steepness waves. This is clearly seen in the case of the downstream cylinder 2, where the relative crest height in front of the cylinder looks similar in Fig. 12(b) and (d) but the waveform is highly asymmetrical for $H/L = 0.1$. Also, the free surface elevation is seen to continuously increase as the wave propagates away from cylinder 1 and towards cylinder 2. This large variation is not seen for the low steepness waves, where the free surface elevation behind cylinder 1, in front of cylinder 2 and at the midpoint between the two cylinders is seen to be the same. A uniform heave motion of the water is observed along the line joining the centers of the cylinders for low steepness waves and this is absent in the case of high steepness waves. These changes seen in the wave interaction with a pair of tandem cylinders for incident waves of low and high steepness result in different flow regimes in the two cases. This justifies the large deviation observed in the calculated wave force compared to the analytical predictions for high wave steepnesses.

In order to obtain further clarity on the wave field around the two tandem cylinders with S=0.8 m, the diffraction patterns around the cylinders for $H/L = 0.003$ and $H/L = 0.1$ are studied. The free surface elevation around the cylinders in the numerical wave tank for $H/L = 0.003$ over one wave period is presented in Fig. 13. The increase in the free surface elevation when the crest is incident on cylinder 1 is seen in Fig. 13(a) and Fig. 13(b) shows the change in the wavefront due to wave diffraction around cylinder 1. The decrease in the free surface elevation as the wave travels around the upstream half of cylinder 1 is seen in Fig. 13(c).

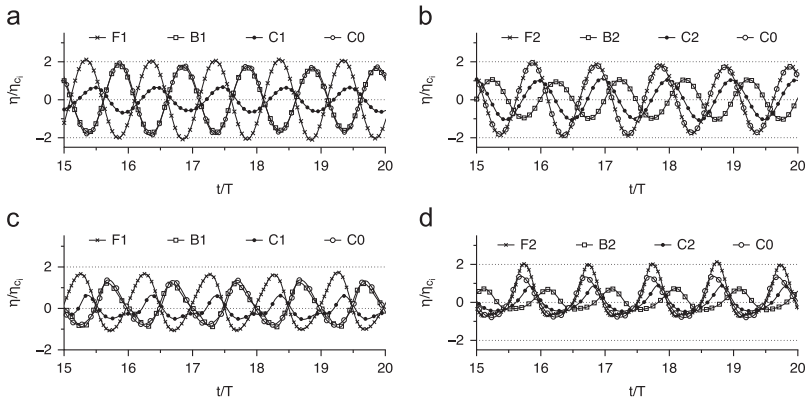

Fig. 12. Relative free surface elevations around two cylinders placed in tandem with $S = 0.8$ m for incident waves of low and high steepnesses: (a) cylinder 1: H/L=0.003, (b) cylinder 2: H/L=0.003, (c) cylinder 1: H/L=0.1, and (d) cylinder 2: H/L=0.1.

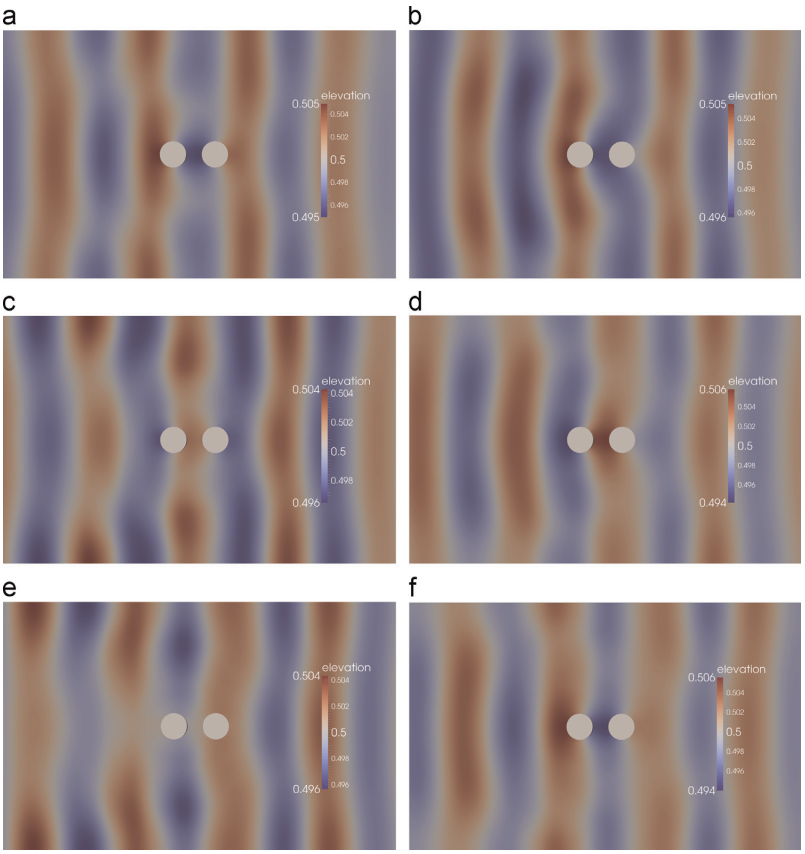

Fig. 13. Free surface elevation in a part of the domain around the cylinders with $S = 0.8$ m for H/L=0.003: (a) $t/T = 32.2$, (b) $t/T = 32.4$, (c) $t/T = 32.6$, (c) $t/T = 32.8$, (d) $t/T = 33.0$, and (e) $t/T = 33.2$.

Fig. 13(d) shows the increase in the free surface elevation as the crest is incident on cylinder 2 and reduced free surface elevations are seen in behind cylinder 2 in Fig. (13) (e) and (f). The region between the two cylinders with equal free surface elevation contours in all the figures is the region with the uniform heave motion of the free surface.

Fig. 14 shows the variation of the free surface elevation around the two tandem cylinders with S=0.8 m for $H/L = 0.1$ over one wave period. The increase in the free surface elevation in front of

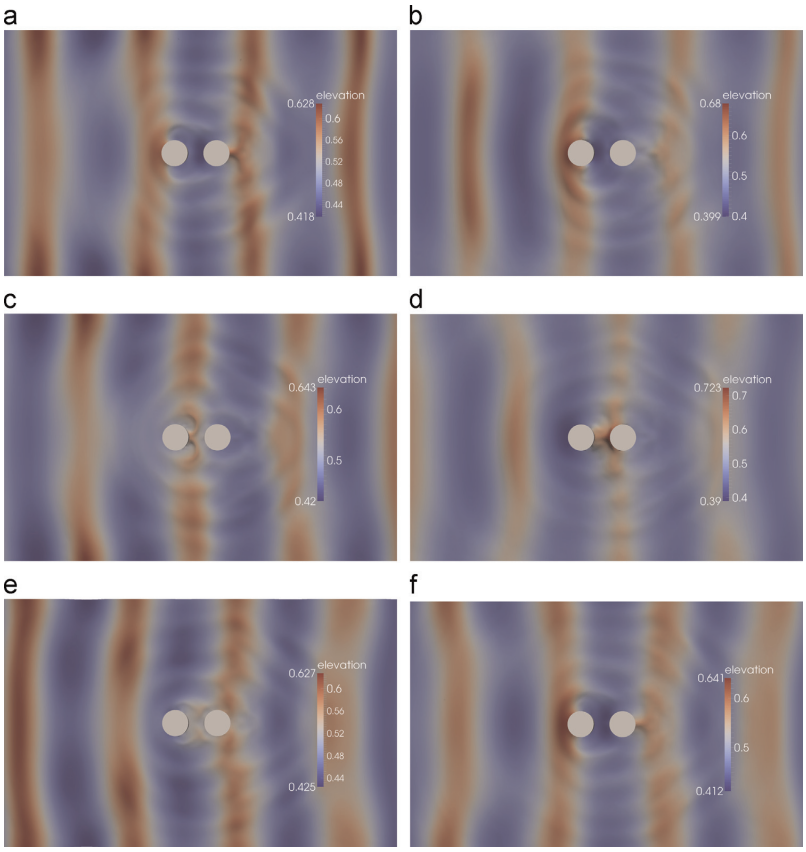

Fig. 14. Free surface elevation in a part of the domain around the cylinders with $S = 0.8$ m for $H/L = 0.1$. (a) t/T = 32.2, (b) t/T = 32.4, (c) t/T = 32.6, (d) t/T = 32.8, (e) t/T = 33.0 and (f) t/T = 33.2.

the cylinder and the formation of distinct reflected waves are seen in Fig. 14a and b. The incident and reflected waves meet behind cylinder 1 in Fig. 14c and the intersection of two semi-circular waves is seen. The constructive interference of the two semi-circular waves in the region between the two cylinders leads to a continuous increase in the free surface elevation around the line joining the centers of the cylinders in Fig. 14d. The resulting large free surface elevation in front of cylinder 2 is also seen in the figure. Fig. 14e shows the reflected waves in between the cylinders over the trough of the incident wave. The circular diffracted waves formed in the wave tank around the two cylinders are seen in Fig. 14f.

The free surface elevation contours around the tandem cylinders in the simulations with a low wave steepness of $H/L = 0.003$ and a high wave steepness of $H/L = 0.1$ show that the wave regime is different in the two cases. The incident straight wavefronts transform to a bent wavefront due to diffraction in the case of low steepness waves. In the case of the high steepness waves, formation of several semi-circular diffracted wavefronts are seen in addition to the bending of the incident wavefront. A uniform heave motion of the free surface is seen for the waves of low steepness in the region between the two cylinders. In the case of the high steepness waves, distinct semi-circular diffracted waves interfere constructively in the region between the two cylinders. The large free surface elevation is concentrated around the line joining the centers of the two cylinders. It is seen in the numerical results that the interaction of high steepness waves is different from low steepness waves due to the strong diffraction pattern and the transformation of the high steepness waves. The nonlinear wave interaction in the case of high steepness waves is not accounted for in the analytical formulae based on potential theory. This results in the difference between the computed wave forces on the cylinders compared to those predicted by the analytical formulae.

5. Conclusions

The calculation of wave forces on a single cylinder using the open source CFD model REEF3D is validated by comparison of experimental data for wave forces, wave elevation around the cylinder and water particle velocity with the computed results from the numerical wave tank. Simulations are carried out to study the wave interaction with a large cylinder for different wave steepnesses. The numerically calculated wave forces match the predictions by MacCamy–Fuchs equation for low wave steepnesses. Whereas for higher wave steepnesses, the computed wave forces are lower than the predictions by the equation. The wave elevation around the cylinder is investigated and the evolution of an asymmetrical waveform is seen in the case of high steepness waves, whereas low steepness waves maintain their symmetrical sinusoidal form. The difference in the wave phase in front, beside

and behind the cylinder suggests a deceleration of water particles around the downstream half of the cylinder in the case of high steepness waves.

Further, simulations with a pair of large tandem cylinders are carried out with different incident wave steepnesses and center-to-center distances between the two cylinders. The computed wave forces are compared with the predictions from an analytical formula based on potential theory. It is observed that the computed wave forces match the predicted wave forces for lower wave steepnesses. The computed wave forces are lower than the analytically predicted wave forces for higher wave steepness, with about a 35% lower force for the highest wave steepness simulated in the study. The analytical formulae predict a linear increase in the wave force with an increase in the incident wave height, for a given cylinder diameter and incident wavelength. The numerical results show that due to the wave transformation and the resulting asymmetrical nature of the higher steepness waves, the computed wave forces on the cylinders from these waves are lower than the predictions based on potential theory. The predictions from the CFD model at the scales considered in these studies are good and provide insight into the interaction between two relatively closely spaced cylinders. In the case of longer arrays of cylinders additional resonant effects such as wave near-trapping can occur, which have not been studied in this paper.

The diffraction patterns around tandem cylinders at different wave steepnesses and the wave elevation around the tandem cylinders are also studied. The evolution of semi-circular diffracted waves are seen in the case of high steepness waves, which meet on the downstream side of the first cylinder. Whereas, in the case of low steepness waves, the wavefront is only bent as a result of wave diffraction. A uniform heave motion of the free surface elevation is observed in the region in between the cylinders in the case of low steepness waves. The complex diffraction regime in the case of high steepness with clearly formed semi-circular diffracted waves results in an increasing free surface elevation as the wave crest propagates away from the upstream cylinder and towards the downstream cylinder.

Thus, clear differences are seen between the interaction of low and high steepness waves with large cylinders. In the case of a single large cylinder, the asymmetry of the steep incident waves results in a different diffraction regime, which results in lower forces on the cylinders than predicted by linear potential theory. For a pair of tandem cylinders, the center-to-center-distance between the cylinders contributes to further change the diffraction regime, in addition to the effects due to wave asymmetry. The evolution of distinct semi-circular reflected waves around the cylinders in the case of high incident wave steepness has a consequence on objects close to the cylinders. The current results show a smooth deviation from the linear results as the incident wave steepness is increased. Further work is needed to determine the transition of the wave force regime from non-breaking wave forces where the wave forces vary at a frequency similar to the incident wave to breaking wave forces which are impulsive in nature with a sharp peak over a period much shorter than the incident wave period. Application of the numerical model to determine random wave forces can also be explored.

Acknowledgement

This study has been carried out under the OWCBW project (No. 217622/E20) and the authors are grateful to the grants provided by the Research Council of Norway. This research was supported in part with computational resources at the Norwegian University of Science and Technology (NTNU) provided by The Norwegian Metacenter for Computational Science (NOTUR, Project no. NN2620K), http://www.notur.no

References

Alagan Chella, M., Bihs, H., Myrhaug, D., Muskulus, M., 2015. Breaking characteristics and geometric properties of spilling breakers over slopes. Coast. Eng. 95, 4–19.
Berthelsen, P.A., Faltinsen, O.M., 2008. A local directional ghost cell approach for incompressible viscous flow problems with irregular boundaries. J. Comput. Phys. 227, 4354–4397.
Boccotti, P., Arena, F., Fiamma, V., Barbaro, G., 2012. Field experiment on random wave forces acting on vertical cylinders. Probab. Eng. Mech. 28, 39–51.
Boccotti, P., Arena, F., Fiamma, V., Romolo, A., 2013. Two small-scale field experiments on the effectiveness of Morison's equation. Ocean Eng. 57, 141–149.
Boo, S.Y., 2002. Linear and nonlinear irregular waves and forces in a numerical wave tank. Ocean Eng. 29, 475–493.
Chakrabarti, S.K., Tam, W.A., 1973. Gross and local wave loads on a large vertical cylinder – theory and experiment. In: Proceedings of Offshore Technology Conference, Dallas, USA.
Chorin, A., 1968. Numerical solution of the Navier–Stokes equations. Math. Comput. 22, 745–762.
Durbin, P.A., 2009. Limiters and wall treatments in applied turbulence modeling. Fluid Dyn. Res. 41, 1–18.
Ferrant, P., 1995. Time domain computation of nonlinear diffraction loads upon three dimensional floating bodies. In: Proceedings of 5th International Offshore and Polar Engineering Conference, The Hague, The Netherlands.
Isaacson, M., 1979. Wave Induced Forces in the Diffraction Regime. Pitman Advanced Publishing Program, London, England.
Jacobsen, N.G., Fuhrman, D.R., Fredsøe, J., 2012. A wave generation toolbox for the open-source CFD library: OpenFOAM. Int. J. Numer. Methods Fluids 70, 1073–1088.
Jiang, G.S., Peng, D., 2000. Weighted ENO schemes for Hamilton–Jacobi equations. SIAM J. Sci. Comput. 21, 2126–2143.
Jiang, G.S., Shu, C.W., 1996. Efficient implementation of weighted ENO schemes. J. Comput. Phys. 126, 202–228.
Larsen, J., Dancy, H., 1983. Open boundaries in short wave simulations—a new approach. Coast. Eng. 7, 285–297.
Lighthill, J., 1979. Waves and hydrodynamic loading. In: Proceedings of 2nd International Conference on Behaviour of Offshore Structures, London, England.
Linton, C.M., Evans, D.V., 1990. The interaction of waves with arrays of vertical circular cylinders. J. Fluid Mech. 215, 549–569.
MacCamy, R., Fuchs, R., 1954. Wave Forces on Piles: A Diffraction Theory. U.S. Army Corps of Engineers Beach Erosion Board, Technical Memorandum no. 69, Washington DC, USA.
Malenica, S., Taylor, R.E., Huang, J.B., 1999. Second-order water wave diffraction by an array of vertical cylinders. J. Fluid Mech. 390, 349–373.
McIver, P., Evans, D.V., 1984. Approximation of wave forces on cylinder arrays. Appl. Ocean Res. 6, 101–107.
Mo, W., Irschik, K., Oumeraci, H., Liu, P., 2007. A 3D numerical model for computing non-breaking wave forces on slender piles. J. Eng. Math. 58, 19–30.
Molin, B., 1979. Second order diffraction loads upon three-dimensional bodies. Appl. Ocean Res. 1, 197–202.
Naot, D., Rodi, W., 1982. Calculation of secondary currents in channel flow. J. Hydraul. Div., ASCE 108, 948–968.
Ohkusu, M., 1974. Hydrodynamic forces on multiple cylinders in waves. In: Proceedings of International Symposium on Dynamics of Marine Vehicles and Structures in Waves, London, England, pp. 107–112.
Osher, S., Sethian, J.A., 1988. Fronts propagating with curvature-dependent speed: algorithms based on Hamilton–Jacobi formulations. J. Comput. Phys. 79, 12–49.
Peng, D., Merriman, B., Osher, S., Zhao, H., Kang, M., 1999. A PDE-based fast local level set method. J. Comput. Phys. 155, 410–438.
Shu, C.W., Osher, S., 1988. Efficient implementation of essentially non-oscillatory shock capturing schemes. J. Comput. Phys. 77, 439–471.
Song, H., Tao, L., Chakrabarti, S., 2010. Modelling of water wave interaction with multiple cylinders of arbitrary shape. J. Comput. Phys. 229, 1498–1513.
Spring, B., Monkmeyer, P.L., 1974. Interaction of plane waves with vertical cylinders. In: Proceedings of International Conference on Coastal Engineering, ASCE, Copenhagen, pp. 1828–1847.
Twersky, V., 1952. Multiple scattering of radiation by an arbitrary configuration of parallel cylinders. J. Acoust. Soc. Am. 24, 42–46.
van der Vorst, H., 1992. BiCGStab: a fast and smoothly converging variant of Bi-CG for the solution of nonsymmetric linear systems. SIAM J. Sci. Stat. Comput. 13, 631–644.
Wilcox, D.C., 1994. Turbulence Modeling for CFD. DCW Industries Inc., La Canada, California.

Paper 3

Upstream and Downstream Cylinder Influence on the Hydrodynamics of a Four Cylinder Group

Kamath A., Bihs, H., Alagan Chella M. and Arntsen Ø.A.
Submitted to *Journal of Waterway, Port, Coastal, and Ocean Engineering* 2015

Upstream and Downstream Cylinder Influence on the Hydrodynamics of a Four Cylinder Group

Arun Kamath [1], Hans Bihs[1], Mayilvahanan Alagan Chella[1], and Øivind A. Arntsen[1]

ABSTRACT

The wave interaction at low KC numbers with a group of four large cylinders arranged in the form of a square with one diagonal along the direction of wave propagation is studied with focus on the hydrodynamic effects of the most upstream and the downstream cylinders in the group. This is studied by removing them and comparing the wave forces and the free surface elevations around the three remaining cylinders with the four cylinder configuration. The theoretically predicted wave near-trapping in the case of the four cylinder group is also investigated for low and high steepness incident waves. The numerical results are compared with analytical formulae based on potential theory and differences are observed between the results for high wave steepnesses. It is observed that the downstream cylinder has a significant influence on the wave forces acting on the cylinders in the four cylinder group. It is also found that the numerical model correctly represents the wave near-trapping predicted by the analytical formula at a low incident wave steepness. For a high incident wave steepness, the diffraction regime is found to be different, with significant wave radiation from the cylinders, consequently the conditions for wave near-trapping break-down.

Keywords: CFD, cylinder groups, wave trapping, wave diffraction

INTRODUCTION

Coastal constructions such as wave energy devices operate under low KC number regimes and are designed with dimensions such that their equivalent diameters D are

[1]Dept. of Civil and Transport Engineering., Norwegian University of Science and Technology, Trondheim, 7491, Norway. E-mail: arun.kamath@ntnu.no

comparable to the incident wavelength L such that $D/L > 0.2$. Under these conditions, the diffraction effects dominate the wave interaction process and significantly modify the wave field around the devices. The variation of the free surface around a group of deployed devices is an important parameter for device operation and the wave forces are important from a structural design perspective. This scenario can be studied using wave interaction with groups of large cylinders in intermediate water depths. At small distances of separation between the cylinders, each of the cylinders in the group is influenced by the wave diffraction and reflection from the neighboring cylinders. These interactions can lead to wave near-trapping, where the free surface is amplified close to the cylinders and large forces are experienced by the cylinders, for certain combinations of incident wavelength, cylinder array arrangement and spacing.

Wave diffraction and multiple reflection amongst multiple cylinders placed in proximity has been studied using potential theory formulations by several authors such as Ohkusu (1974) Spring and Monkmeyer (1974) and Linton and Evans (1990) Walker and Taylor (2005). Malenica et al. (1999) estimated the second-order and third-order potentials to calculate higher-order forces on a cylinder array. Although these methods have provided a lot of information regarding the near-trapping phenomena at the first and the second order, the assumptions of a small incident wave amplitude, inviscid fluid and irrotational flow limit the application of these methods. Further, the interaction of high steepness waves with large cylinders can be significantly different from that with low steepness waves due to the occurrence of non-linear wave-body and wave-wave interactions. Many authors have studied the near-trapping phenomenon in the case of cylinder groups composed of four and more cylinders in a polygonal formation (Evans and Porter (1997); Walker et al. (2008)), demonstrating the importance of studying the wave diffraction effects in these cases. Huang (2004) developed a semi-analytical method to study the wave diffraction around two, three and four cylinders and computed the free surface elevations around the array and reported higher interaction in the case of a three cylinder array compared to the four cylinder array. Ohl et al. (2001) carried

out experiments to study wave diffraction by an array of large cylinders and concluded that predictions from potential theory agreed well with the observations, whereas the semi-analytical theory by Malenica et al. (1999) over predicted the second-order contribution to the free surface elevations. Experimental investigations by Barnard et al. (1983) reported the absence of the theoretically predicted pronounced resonant response due to wave near-trapping. Duclos and Clément (2004) showed that a small amount of disorder, of the order of 0.5% of the cylinder spacing in their analysis, can substantially reduce the forces due to wave near-trapping. Thus, wave interaction with an array of large cylinders at low KC numbers depends on many factors including the arrangement of the cylinders, the number of cylinders and the incident wave steepness. But the effect of wave steepness has not been the focus of previous studies in current literature. In this regard, further insight can be obtained by studying wave interaction with a four cylinder array with cylinders at the vertices and oriented with one diagonal arranged in the direction of wave propagation for both low and high steepness incident waves. The investigation into the variation of the free surface elevation around the four cylinder array and the wave forces on the cylinders compared to the free surface variations and wave forces in the absence of the most upstream and downstream cylinders can provide further knowledge about the changes in the wave field in the different scenarios.

In this study, the open-source CFD model REEF3D (Alagan Chella et al., 2015) is used to simulate the wave interaction with cylinder arrays with three and four cylinders as shown in Fig. (1). The objective of the study is to investigate the wave field around the array with four cylinders and three cylinders obtained by removing one of the cylinders from the four cylinder array, evaluate the consequences of the arrangement on the wave forces experienced by the cylinders and the difference between low and high steepness wave interaction with the cylinder arrays. The most upstream and downstream cylinders are removed from the arrangements in turns to obtain two arrangements of three cylinders to obtain insights into the influence of these cylinders on the wave forces experienced by the other cylinders in the array. The free surface in the vicinity of the

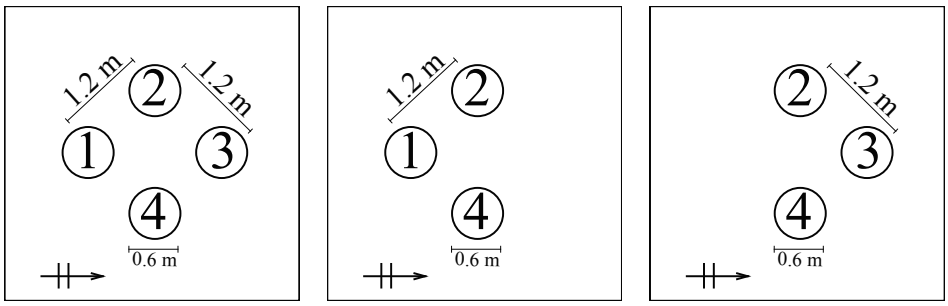

(a) setup 1 (b) setup 2 (c) setup 3

Fig. 1. Different arrangements used in the study

cylinders and the wave forces on the cylinders are computed for incident waves for two different incident wavelengths at both low and high wave steepnesses are studied. The formula by Linton and McIver (2001) is used for the validation of the numerical results for the four cylinder array at a low incident wave steepness.

NUMERICAL MODEL

Governing equations

The incompressible Reynolds-averaged Navier-Stokes (RANS) equations together with the continuity equation are used in the numerical wave tank in REEF3D:

$$\frac{\partial u_i}{\partial x_i} = 0 \tag{1}$$

$$\frac{\partial u_i}{\partial t} + u_j \frac{\partial u_i}{\partial x_j} = -\frac{1}{\rho}\frac{\partial p}{\partial x_i} + \frac{\partial}{\partial x_j}\left[(\nu + \nu_t)\left(\frac{\partial u_i}{\partial x_j} + \frac{\partial u_j}{\partial x_i}\right)\right] + g_i \tag{2}$$

where u is the velocity, ρ is the density of the fluid, p is the pressure, ν is the kinematic viscosity, ν_t is the eddy viscosity and g the acceleration due to gravity.

The projection method (Chorin, 1968) is used for pressure treatment and a preconditioned BiCGStab solver (van der Vorst, 1992) is used to solve the resulting Poisson pressure equation. Turbulence modeling is carried out using the two equation k-ω model

proposed by Wilcox (1994). The large strain in the flow due to wave propagation leads to unphysical overproduction of turbulence in the wave tank. Eddy viscosity limiters as shown by Durbin (2009) are used to avoid this. In a two-phase CFD model, the large difference in density at the interface between air and water causes an overproduction of turbulence at the interface. This is avoided by free surface turbulence damping around the interface as shown by Naot and Rodi (1982). The damping is carried out only around the interface using a smoothed Dirac delta function. REEF3D is fully parallelized using the domain decomposition strategy and MPI (Message Passing Interface).

Free Surface

The free surface is determined with the level set method, where the zero level set of the signed distance function $\phi(\vec{x},t)$ is used to represent the interface between air and water (Osher and Sethian, 1988). The level set function gives the shortest distance from the interface for all the points in the flow domain. The sign of the function distinguishes between the two fluids across the interface as shown in Eq. (3):

$$\phi(\vec{x},t) \begin{cases} > 0 & if\ \vec{x}\ is\ in\ phase\ 1 \\ = 0 & if\ \vec{x}\ is\ at\ the\ interface \\ < 0 & if\ \vec{x}\ is\ in\ phase\ 2 \end{cases} \tag{3}$$

The level set function is moved under the influence of an external velocity field u_j with the convection equation in Eq. (4):

$$\frac{\partial \phi}{\partial t} + u_j \frac{\partial \phi}{\partial x_j} = 0 \tag{4}$$

The level set function loses its signed distance property on convection and is reinitialized after every iteration using a partial differential equation based reinitialisation procedure by Peng et al. (1999) to regain its signed distance property.

Discretization schemes

The fifth-order conservative finite difference Weighted Essentially Non-Oscillatory (WENO) scheme proposed by Jiang and Shu (1996) is applied for the discretization of the convective terms of the RANS equation. The level set function, turbulent kinetic energy and the specific turbulent dissipation rate are discretized using the Hamilton-Jacobi formulation of the WENO scheme by Jiang and Peng (2000). The WENO scheme is a minimum third-order accurate and numerically stable even in the presence of large gradients. Time advancement for the momentum and level set equations is carried out using a Total Variation Diminishing (TVD) third-order Runge-Kutta explicit time scheme proposed by Shu and Osher (1988). Adaptive time stepping is employed to satisfy the CFL criterion based on the maximum velocities in the domain and the source term contributions to the Navier-Stokes equations. This ensures numerical stability and accuracy throughout the simulation with an optimal value of time step size. A first-order scheme is used for the time advancement of the turbulent kinetic energy and the specific turbulent dissipation, as these variables are mostly source term driven with a low influence of the convective terms. Diffusion terms of the velocities are also subjected to implicit treatment in order to remove the diffusion terms from the CFL criterion.

The numerical model uses a uniform Cartesian grid for the spatial discretization together with the Immersed Boundary Method (IBM) to represent the irregular boundaries in the domain. Berthelsen and Faltinsen (2008) developed the local directional ghost cell IBM to extend the solution smoothly in the same direction as the discretization, which is adapted to three dimensions in the current model.

Wave generation and absorption

The numerical wave tank uses the relaxation method (Larsen and Dancy, 1983) for wave generation and absorption. This method requires a certain length of the wave tank to be reserved as wave generation and absorption zones. Relaxation functions are used to moderate the velocity and the free surface using a wave theory in the relaxation

zones with Eq. (5):

$$\begin{aligned} u_{relaxed} &= \Gamma(x)u_{analytical} + (1-\Gamma(x))u_{computational} \\ \phi_{relaxed} &= \Gamma(x)\phi_{analytical} + (1-\Gamma(x))\phi_{computational} \end{aligned} \tag{5}$$

where $\Gamma(x)$ is the relaxation function and $x \in [0,1]$ is the x-coordinate scaled to the length of the relaxation zone. The relaxation function proposed by Jacobsen et al. (2012), shown in Eq. (6) is used in the numerical model.

$$\Gamma(x) = 1 - \frac{e^{(1-x)^{3.5}} - 1}{e-1} \tag{6}$$

The wave theory for moderating the numerical values is chosen according to the wave steepness and the water depth in the simulation. Typically, the wave generation zone is one wavelength long and the absorption zone is two wavelengths long. In the wave generation zone, the computational values of velocity and free surface are raised to the analytical values prescribed by wave theory. The generation zone releases waves into the working zone of the tank, where the objects to be studied are placed. The relaxation function in the generation zone also absorbs reflections from structures in the wave tank and prevents them from affecting the generated waves. At the end of the tank, the wave enters the numerical beach. Here, the computational values of velocity and free surface are reduced to zero in a smooth manner. This simulates the effect of a beach, where the wave energy is removed from the wave tank and avoids reflections.

CALCULATION OF WAVE FORCES

Numerical evaluation of wave forces

The numerical model evaluates the wave force F on an object as the integral of the pressure p and the surface normal component of the viscous shear stress tensor τ on

the object according to Eq. (7):

$$F = \int_{\Omega} (-\mathbf{n}p + \mathbf{n} \cdot \tau) d\Omega \tag{7}$$

where $\mathbf{n}$ is the unit normal vector pointing into the fluid and Ω is the surface of the object.

This is readily accomplished by the numerical model as the values for the pressure and shear stress are available at every point in the domain at any given time of the simulation.

Analytical formula for wave forces

Potential theory is used to obtain the wave diffraction potential and calculate the force on a single cylinder using the equation presented by MacCamy and Fuchs (1954), shown in Eq. (8):

$$|F| = \left| \frac{4\rho g i a \ tanh(kd)}{k^2 H_1'(kr)} \right| \tag{8}$$

where $i = \sqrt{-1}$, a is the incident wave amplitude, $k = 2\pi/L$ the wave number, d the water depth and H_1' the first derivative of the Hankel function of the first kind and r the radius of the cylinder. The parameter kr represents the ratio of the diameter of the cylinder to the incident wavelength and thus a measure of the diffraction, with higher values of kr signifying a stronger diffraction regime.

An extension of the diffraction theory proposed by Linton and McIver (2001) to calculate wave forces on multiple cylinders placed in proximity is presented in Eq. (9):

$$A_m^l + \sum_{\substack{j=1 \\ \neq l}}^{N} \sum_{n=-M}^{M} A_j^n Z_n^j e^{i(n-m)\alpha_{jl}} H_{n-m}(kR_{jl}) = -I_l e^{im(\frac{\pi}{2}-\beta)}$$

$$l = 1, \ldots, N, \ m = -M, \ldots, M. \tag{9}$$

where, M is the order of the solution, N is the number of cylinders, I is the incident wave potential, β is the angle of wave propagation with respect to the x-axis, H is the Hankel

function of the first kind, R_{jl} is the length of the line joining the centers of the jth and the lth cylinder, α_{jk} is the angle between the x-axis and the line joining the centers of the cylinders and $Z = J'(kr_j)/H'(kr_j)$, where J is the Bessel function of the first kind. The unknown coefficients A are to be evaluated. This results in a set of $N(2M + 1)$ equations. Linton and McIver (2001) suggest that a value of $M = 6$ provides sufficiently accurate solutions and is used in the equations to obtain the analytical prediction of wave forces for low steepness incident waves. The unknown coefficients A are evaluated by solving Eq. (9) and the first-order wave force magnitudes $|F^j|$ on the jth cylinder are obtained using Eq. (10):

$$\left|\frac{F^j}{F}\right| = \frac{1}{2}\left|A^j_{-1} \pm A^j_1\right| \tag{10}$$

The subtraction of the coefficients on the right hand side gives the wave force along the x-axis and the addition of the terms gives the wave force along the y-axis. In the current study, the angle of incidence $\beta = 0$ and the waves propagate along the x-axis.

RESULTS AND DISCUSSION

Wave interaction with three arrangements of the cylinder array as shown in Fig. (1) with two different incident wavelengths at small and large wave steepness are considered. The first arrangement consists of four cylinders placed with a diagonal along the direction of wave propagation (Fig. 1a). In the second arrangement, the downstream cylinder on the inline diagonal is removed, resulting in a triangular arrangement of three cylinders (Fig. 1b) and in the third setup, a triangular arrangement is obtained by removing the upstream cylinder on the inline diagonal (Fig. 1c). Cylinders of diameter $D = 0.60$ m are arranged at the vertices of a square of side 1.20 m in a water depth of $d = 0.60$ m. The numerical wave tank used for the simulations is 16 m long, 8 m wide and 1.20 m high with a grid size of $dx = 0.025$ m resulting in 9.83 million cells. An overview of the simulations carried out is listed in Table 1. According to the equations by Linton and Evans (1990), wave interaction with the arrangement of four cylinders in Fig. (1a) results in wave near-trapping for a diffraction parameter

$kr = 1.70$. Thus, simulations are carried out for $kr = 0.94$ to simulate the wave interaction away from wave near-trapping (setup A1) and for $kr = 1.70$ (setup B1) to simulate wave near-trapping at a low incident wave steepness of $H/L = 0.004$. Further, the wave interaction for the same values of the diffraction parameter kr is simulated at a higher wave steepness of $H/L = 0.060$ to investigate the differences in the diffraction regime and wave forces from that seen for the low incident wave steepness.

Table 1. Details of the setups used in the different simulations

No.	H (m)	L (m)	H/L	kr	$F_0(N)$	Arrangement
A1						Setup 1
A2	0.008	2.00	0.004	0.94	16.20	Setup 2
A3						Setup 3
B1						Setup 1
B2	0.004	1.11	0.004	1.70	3.90	Setup 2
B3						Setup 3
C1						Setup 1
C2	0.120	2.00	0.06	0.94	178.20	Setup 2
C3						Setup 3
D1						Setup 1
D2	0.066	1.11	0.06	1.70	50.50	Setup 2
D3						Setup 3

At first, the numerical computation of the wave forces on cylinders is validated by simulating wave interaction with a single cylinder and a group of four cylinders (setup A1) with low steepness incident waves ($H/L = 0.004$) of wavelength $L = 2.00$ m and height $H = 0.008$ m. The numerical results for the single cylinder $F_0 = 16.20$ N are compared with the analytically expected values using the MacCamy-Fuchs theory $F_{0t} = 15.90$ N in Eq. (8) in Fig. (2) with only a difference of 1.8%. In the case of the four cylinders, the computed forces on each of the cylinders is compared with the

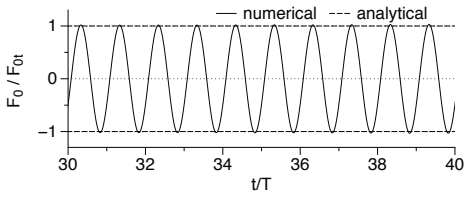

Fig. 2. Comparison of numerical and analytical wave forces on a single cylinder for $H = 0.004$ m and $L = 2.00$ m

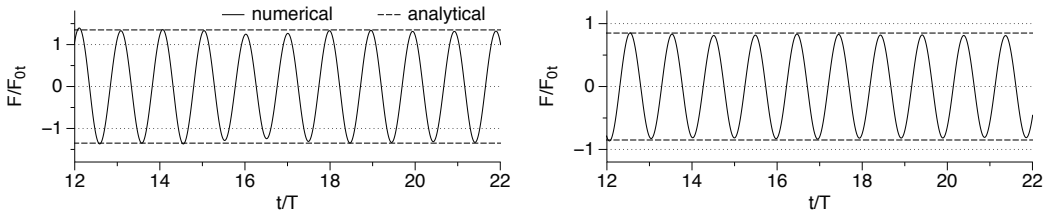

(a) cylinder 1

(b) cylinder 2, 4

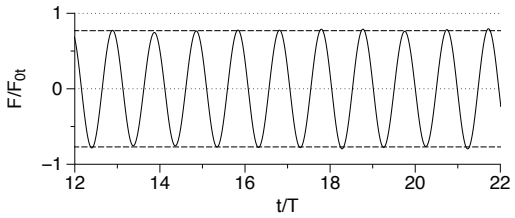

(c) cylinder 3

Fig. 3. Comparison of the numerical and analytical wave forces on the four cylinders in setup A1 with $H = 0.004$ m and $L = 2.00$ m for $kr = 0.94$

analytical prediction using Eq. (10) in Fig. (3) and a good agreement is seen for all the four cylinders, with differences less than 2.0%.

In the following sections, the wave interaction with the three setups illustrated in Fig. (1) is investigated with low and high steepness waves for two different wavelengths.

Wave interaction with incident waves of low steepness

The wave forces on cylinders for the setups A1, A2 and A3 with incident wavelength $L = 2.00$ m and height $H = 0.008$ m resulting in a low wave steepness of $H/L = 0.004$

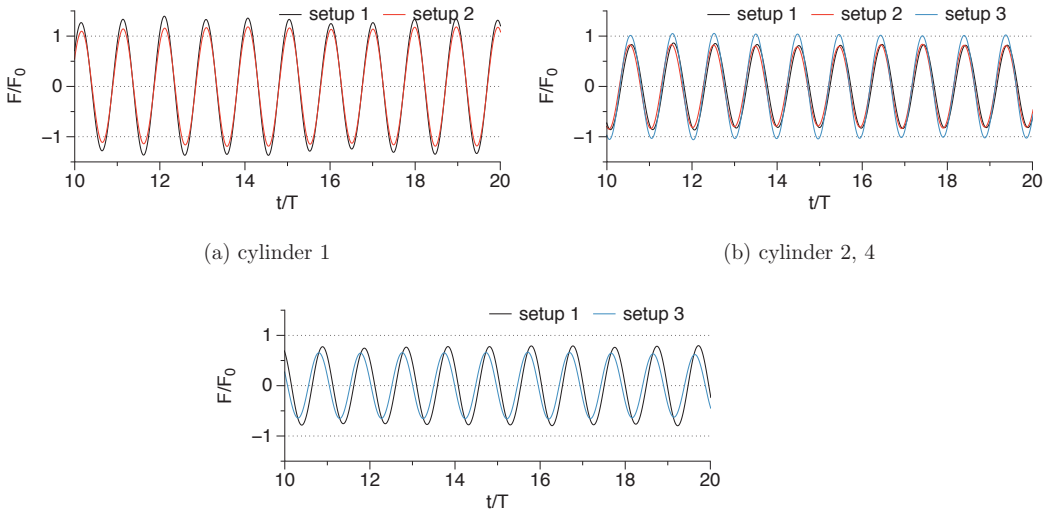

(a) cylinder 1

(b) cylinder 2, 4

(c) cylinder 3

Fig. 4. Comparison of wave forces on each of the cylinders in setups A1, A2 and A3 for low steepness incident waves with $H = 0.004$ m and $L = 2.00$ m for $kr = 0.94$

and diffraction parameter $kr = 0.94$ are computed as listed in Table (1). The computed wave forces on each cylinder are scaled to the numerically determined force on a single cylinder, $F_0 = 16.20$ N and presented in Fig. (4). It is seen from Fig. (4a) that cylinder 1 experiences the highest wave forces in both setups 1 and 2. It is also observed that in the presence of the downstream cylinder 3, in setup 1, the wave force on the upstream cylinder 1 is higher with $1.30F_0$ compared to $1.15F_0$ in the absence of the downstream cylinder 3 in setup 2. In the case of cylinders 2 and 4, the highest wave forces are experienced in setup 3, when the upstream cylinder 1 is removed from the arrangement as seen in Fig. (4b). In the presence of the upstream cylinder 1, cylinders 2 and 4 experience similar wave forces for both setups 1 and 2. From Fig. (4c), the downstream cylinder 3 experiences the highest wave forces in the presence of the upstream cylinder 1 and lower forces in the absence of the upstream cylinder. Thus, in the four cylinder arrangement shown in Fig. (1a), the presence of the upstream cylinder reduces the wave forces on cylinders 2 and 4 behind it, but leads to a higher wave force on the

downstream cylinder 4.

Further, the diffraction parameter is changed to $kr = 1.70$ and the wave forces on the cylinders for the setups B1, B2 and B3 with incident wavelength $L = 1.11$ m and height $H = 0.004$ m (H/L=0.0036) are computed. In this arrangement, the equations by Linton and McIver (2001) predict large wave forces on the cylinders in setup 1, due to near-wave trapping. The numerical results follow with this prediction and the wave forces on all four cylinders in setup 1 experiences larger forces than the wave force computed for a single cylinder, $F_0 = 3.90$ N. In the case of cylinder 1, the wave force is $2.00F_0$ in setup 1, whereas it is lowered to $1.30F_0$ when the downstream cylinder is removed in setup 2 as seen in Fig. (5a). For cylinders 2 and 4, the wave forces are similar ($1.10F_0$) in all the three setups from Fig. (5b). The downstream cylinder 3 also experiences similar forces of $1.60F_0$ both in the presence and absence of the upstream cylinder in Fig. (5c). So, under conditions resulting in near wave trapping for the four cylinder arrangement, the wave forces on the upstream cylinder is highly influenced by

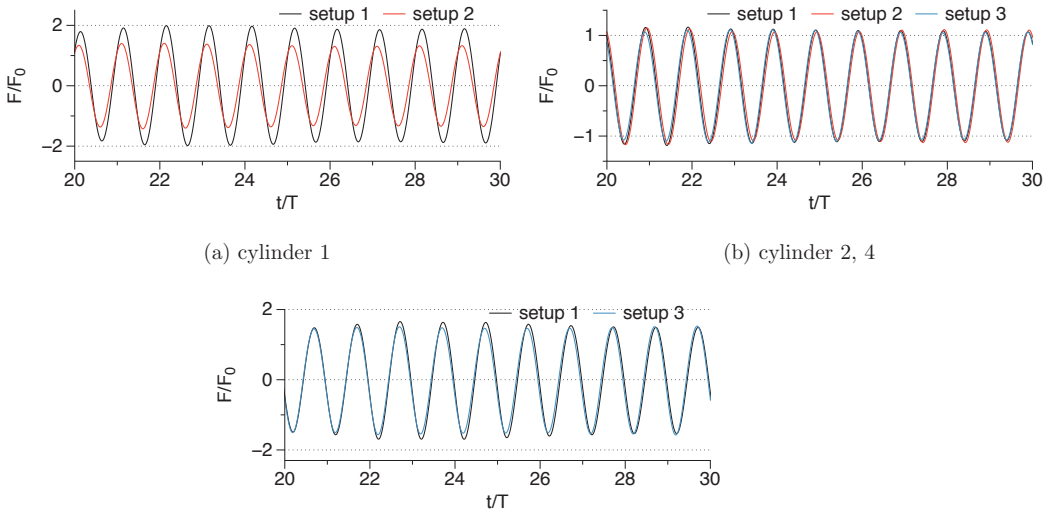

(a) cylinder 1

(b) cylinder 2, 4

(c) cylinder 3

Fig. 5. Comparison of wave forces on each of the cylinders in setups B1, B2 and B3 for low steepness incident waves with $H = 0.002$ m and $L = 1.11$ m for $kr = 1.70$

the presence of the downstream cylinder but the effect of the upstream cylinder on the other cylinders in the arrangement is negligible.

From the simulations presented above, it is observed that the wave forces on cylinders in different arrangements is influenced both by the neighboring cylinders and the incident wavelength. The effect of wave near-trapping for setup 1 for diffraction parameter $kr = 1.70$ predicted by the analytical formula (Eq. 10) is replicated in the simulation for setup B1. Under conditions resulting in near-trapping of incident waves for the four cylinder arrangement, the wave force on the upstream cylinder is two times the force on a single cylinder. On the hand, the force on cylinder 1 is reduced in the absence of the downstream cylinder 3 in setup B2. The wave forces on the other cylinders are slightly influenced by the presence of the upstream cylinder and experience forces higher than the force on a single cylinder in all the arrangements. With diffraction parameter $kr = 0.94$, there is no near-trapping of waves in setup A1 and the presence of the upstream cylinder influences all the other cylinders in the arrangement as seen from the results for setups A2 and A3. The upstream cylinder itself experiences higher wave forces in the presence of the downstream cylinder. In addition, the downstream cylinder experiences higher forces in the presence of the upstream cylinder. So, away from conditions leading to wave near-trapping, the neighboring cylinders have a significant influence on the wave forces experienced by a cylinder in the group.

To obtain a better understanding of the wave regime around the cylinders, the free surface elevation around the cylinder arrays is studied when the incident wave crest is in the region enclosed by the cylinders. The diffracted waves in the region between the cylinders in setups B1-B3 is presented in Fig. (6). In setup B1 with four cylinders (Fig. 6a), a higher free surface elevation in the region in between the cylinders is seen along with a deep trough in front of cylinder 3. The wave near-trapping in this case results in large variations in the free surface in the region in between the region. The large difference in the free surface elevations correspond to large differences in the pressure around cylinders 1 and 3, resulting in large forces on the cylinders. On

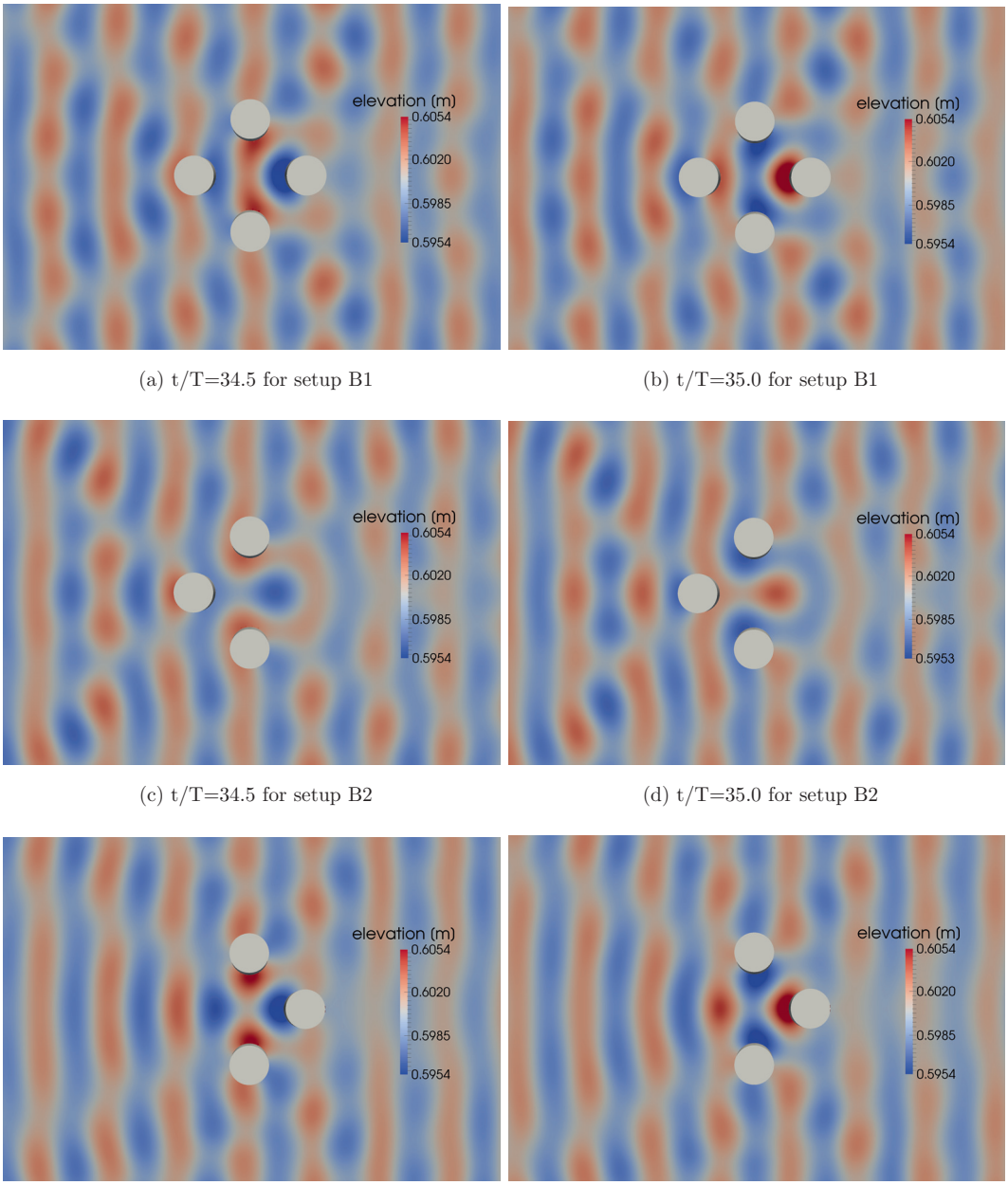

(a) t/T=34.5 for setup B1

(b) t/T=35.0 for setup B1

(c) t/T=34.5 for setup B2

(d) t/T=35.0 for setup B2

(e) t/T=34.5 for setup B3

(f) t/T=35.0 for setup B3

Fig. 6. Free surface elevations in the part of the domain around the cylinders for low steepness incident waves in setups B1, B2 and B3 with wavelength $L = 1.11$ m, $H/L = 0.004$ for $kr = 1.70$

removing the downstream cylinder 3 from the arrangement in setup B2 (Fig. 6b), the region in between the cylinders has lower free surface elevations than in setups B1 and B2. In the absence of the downstream cylinder 3, wave trapping in the region between the cylinders does not occur and cylinder 1 experiences lower forces. The free surface elevation in the immediate vicinity of cylinders 2 and 4 is largely unaltered from the pattern seen for setup B1. In Fig. (6c), when cylinder 1 is removed, the high free surface elevation is around cylinders 2 and 4 is similar to setup B1 except for the lower free surface elevation in the region in the center. This shows that the pressure difference around cylinders 2 and 4 is similar in all the three arrangements and justifies the similar wave forces computed using Eq. (7) for cylinders 2 and 4 for all the arrangements. The free surface elevation around the downstream cylinder is also similar to to that in setup B1, corresponding to similar pressure differences and resulting in similar forces on the downstream cylinder 3 in both setups B1 and B3.

Wave interaction with incident waves of high steepness

In order to investigate the difference in the wave interaction with the cylinder groups under the the influence of high steepness incident waves, simulations are carried out with the same wavelengths as in the previous section but with a higher incident wave steepness of $H/L = 0.06$.

The wave forces on all the cylinders in setups C1, C2 and C3 ($kr = 0.94$) with incident wavelength $L = 2.00$ m, height $H = 0.12$ m are presented in Fig. (7). From Fig. (7a), the wave forces on the upstream cylinder 1 are higher ($1.60F_0$) in the presence of the downstream cylinder 3 in setup 1, than in the absence of the downstream cylinder 3 in setup 2 ($1.40F_0$). Cylinders 2 and 4 experience similar forces in all the three setups, almost the same force as that on a single cylinder, $F_0 = 178.20$ N as seen in Fig. (7b). The downstream cylinder 3 experiences a wave force of $0.75F_0$ in the presence of the upstream cylinder 1 and a lower force of $0.55F_0$ in the absence of the upstream cylinder in Fig. (7c). It is also observed that the wave forces on the downstream cylinder are the lowest in the group and lesser than the force on a single cylinder. Further, the wave

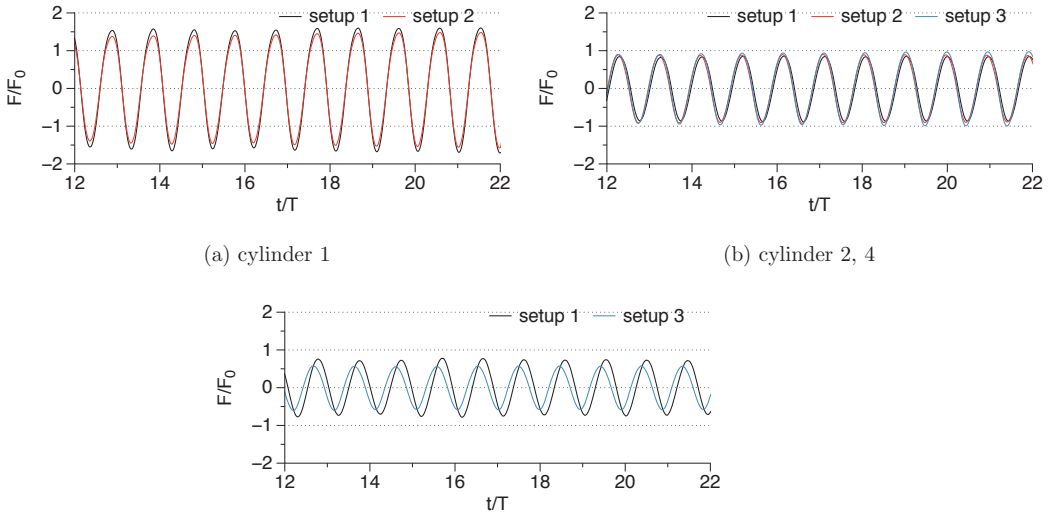

(a) cylinder 1

(b) cylinder 2, 4

(c) cylinder 3

Fig. 7. Comparison of wave forces on each of the cylinders in setups C1, C2 and C3 for high steepness incident waves with $H = 0.06$ m and $L = 2.00$ m for $kr = 0.94$

forces computed on all the cylinders in setups D1, D2 and D3 ($kr = 1.70$) with incident wavelength $L = 1.11$ m and height $H = 0.066$ m (H/L=0.06) are presented in Fig. (8) scaled to $F_0 = 50.50$ N. The upstream cylinder 1 experiences wave forces of about $1.20F_0$ both in the presence and absence of the downstream cylinder 3. Cylinders 2 and 4 experience similar forces of about $0.90F_0$ in all the arrangements. The downstream cylinder 3 experiences wave forces of about $0.85F_0$. Thus, also in this case, the upstream cylinder experiences the highest forces in all the arrangements and all the other cylinders experience forces lower than F_0 for all arrangements.

From the simulations for high steepness incident waves, the upstream cylinder experiences the highest forces and all the other cylinders in the arrangement experience lower forces. The large wave forces on the cylinders seen in setup B1 with low incident wave steepness, due to wave near-trapping is not seen for the high steepness waves in setup D1 for the same diffraction parameter $kr = 1.70$. This points towards the break-down of the wave near-trapping condition at higher wave steepnesses.

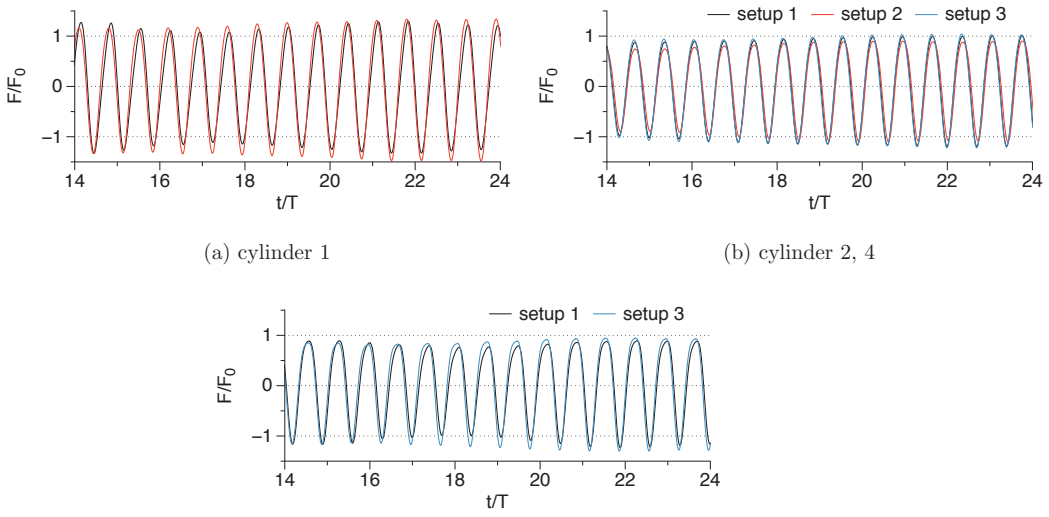

(a) cylinder 1

(b) cylinder 2, 4

(c) cylinder 3

Fig. 8. Comparison of wave forces on each of the cylinders in setups D1, D2 and D3 for high steepness incident waves with $H = 0.033$ m and $L = 1.11$ m for $kr = 1.70$

To further understand the difference in the force regime in the two cases, the wave forces on the upstream cylinder 1 and the downstream cylinder 3 in setup B1 with low steepness incident waves and setup D1 with high steepness incident waves are compared with the analytical predictions using Linton and Evans (1990) formula in Eq. (10). The comparison of the forces in Fig. (9) shows that the numerical results agree with the analytical predictions for the case with the low steepness incident waves of $H/L = 0.004$ in setup B1 for both the upstream and the downstream cylinders. On the other hand, in the case of the high steepness incident waves with $H/L = 0.06$ in setup D1, the computed forces significantly differ from the analytical predictions, showing that the diffraction regime in the case of the high steepness waves is different from that in the case of the low steepness waves.

Further insight is obtained regarding the wave diffraction effects for high steepness incident waves by studying the free surface elevations in the region around the cylinder arrays for setups D1-D3, with incident wavelength $L = 1.11$ m and wave steepness

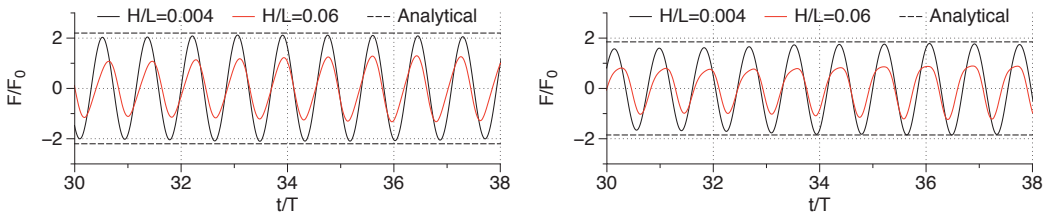

(a) upstream cylinder 1

(b) downstream cylinder 3

Fig. 9. Comparison of wave forces on the upstream and downstream cylinders in setups B1 (low steepness) and D1(high steepness) with the analytical prediction showing the difference in wave forces at different wave steepnesses for $kr = 1.70$

$H/L = 0.06$ in Fig. (10). The formation of multiple semi-circular diffracted waves around the cylinders in all three setups is seen. For setup D1, the region in between the cylinders does not show large free surface elevations and it can be concluded that the near-trapping phenomenon does not occur in this case. As a result, the cylinders do not experience extremely high wave forces in comparison to the wave force on a single cylinder. When the downstream cylinder 3 is removed from the cylinder array in setup D2 (Fig. 10b), the wave diffraction patterns around the cylinder is similar to that in setup D1 and the cylinders experience similar forces in both arrangements. In Fig. (10c), on removing cylinder 1, high free surface are seen but restricted to small regions around cylinder 2 and 4. The free surface elevations in front of cylinder 3 is similar to that seen in setup D1 with four cylinders and thus, it experiences similar forces in both arrangements.

The difference in the wave diffraction regime at low and high incident wave steepnesses is seen from the free surface elevations around the cylinder arrays. This difference results in the different forces seen in the case of high steepness waves than that predicted by analytical formula, that assumes low steepness incident waves. The formation of multiple semi-circular diffracted waves around the cylinders in seen for higher incident wave steepness. On the other hand, in the case of low steepness incident waves,

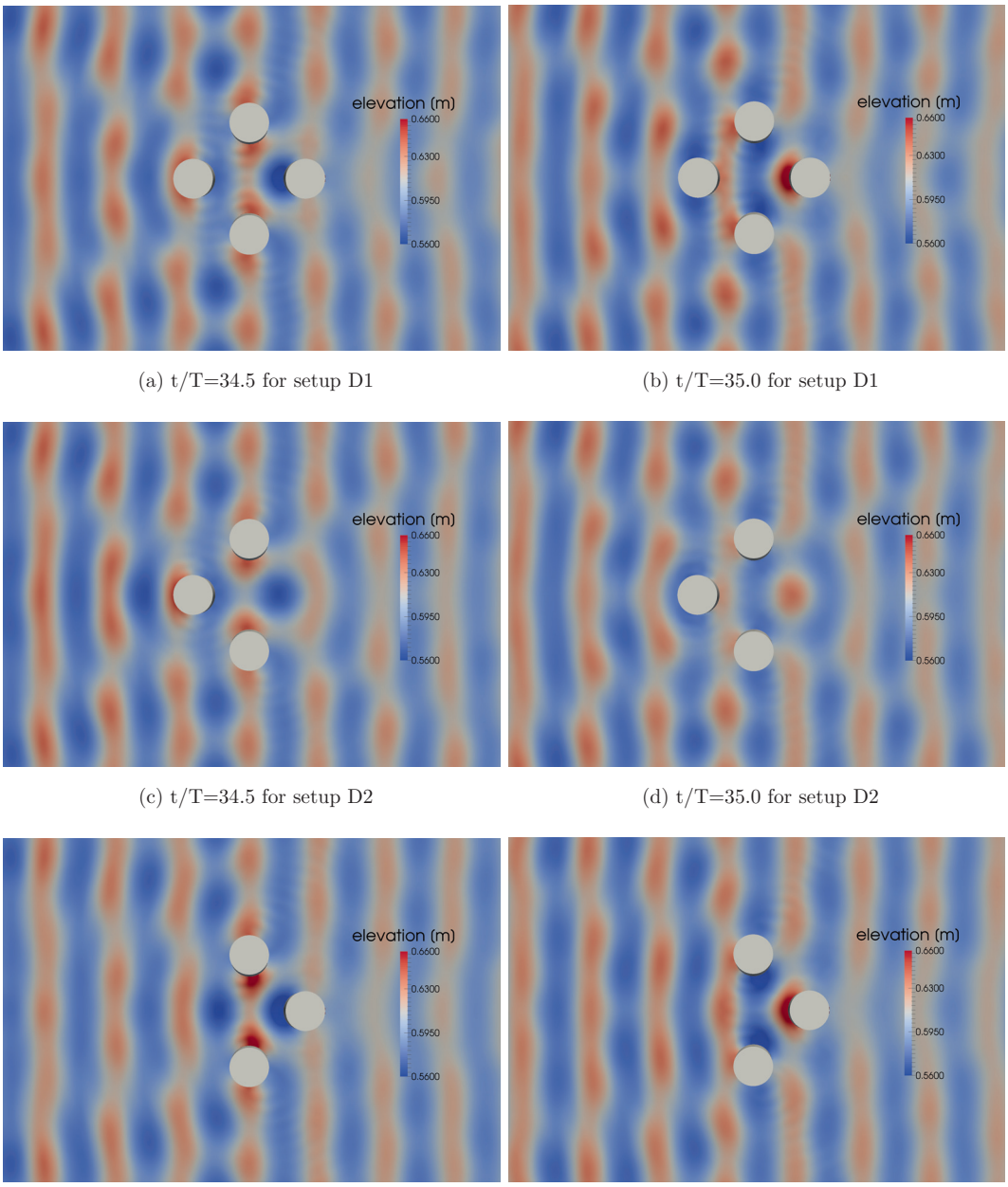

(a) t/T=34.5 for setup D1

(b) t/T=35.0 for setup D1

(c) t/T=34.5 for setup D2

(d) t/T=35.0 for setup D2

(e) t/T=34.5 for setup D3

(f) t/T=35.0 for setup D3

Fig. 10. Free surface elevation in the part of the domain around the cylinders for high steepness incident waves in setups D1, D2 and D3 with wavelength $L = 1.11$ m, $H/L = 0.06$

the wave diffraction results in bending of the waveform and for $L = 1.11$ m the phenomenon of near-trapping of waves is observed. The formation of multiple diffracted waves at a higher incident wave steepness results in a break down of the conditions leading to wave near trapping. Since potential theory assumes a low incident wave steepness, formulae based on potential theory cannot account for the diffraction effects at higher wave steepnesses. It is also observed that in the absence of cylinder 4 in the four cylinder array, the wave forces on the upstream cylinder 1 are reduced.

CONCLUSION

The open source CFD model REEF3D is used to simulate wave interaction with arrays of cylinders to study the change in the hydrodynamics and the wave forces in the presence and absence of cylinders along the the direction of wave propagation. The numerical model was validated using equations based on potential theory for low incident wave steepness for both a single cylinder and an arrangement of four cylinders. The phenomenon of wave near-trapping resulting in large free surface elevations in the vicinity of the cylinders and large wave forces on the cylinders is observed at low wave steepness in accordance with analytical expectation. The difference in the wave diffraction for different incident wavelengths and wave steepnesses is also studied and found that significant radiating waves are reflected from the cylinders at higher wave steepnesses, which are not observed at lower wave steepnesses. The phenomenon of wave near-trapping is seen to breakdown for higher incident wave steepness due this difference in the diffraction pattern.

The presence of the downstream cylinder generally results in a higher wave force on the upstream cylinder with a 30% increase for low steepness waves and a 60% increase for high steepness waves compared to the force on a single cylinder, at conditions away from theoretical near-wave trapping. Under theoretical conditions for wave near-trapping, the upstream experiences about two times the force on a single cylinder at low steepness and a 20% higher force for high steepness waves. However, at a higher incident wave steepness and break-down of the near-trapping, though the wave forces on

the upstream cylinder are the highest in the array, the rest of the cylinders experience lower forces. It can be concluded that the wave interaction with a four cylinder array with a given center-to-center distance depends not only on the incident wavelength but also the incident wave steepness. The effect of higher steepness incident waves cannot be effectively accounted for using formulae based on potential theory.

ACKNOWLEDGEMENTS

This study has been carried out under the OWCBW project (No. 217622/E20) and the authors are grateful to the grants provided by the Research Council of Norway. This research was supported in part with computational resources at the Norwegian University of Science and Technology (NTNU) provided by NOTUR, http://www.notur.no (NN2620K).

REFERENCES

Alagan Chella, M., Bihs, H., Myrhaug, D., and Muskulus, M. (2015). "Breaking characteristics and geometric properties of spilling breakers over slopes." *Coastal Engineering*, 95, 4–19.

Barnard, B. J. S., Pritchard, W. G., and Provis, D. G. (1983). "Experiments on wave trapping by a submerged cylindrical island." *Geophysical and Astrophysical Fluid Dynamics*, 24, 23–48.

Berthelsen, P. A. and Faltinsen, O. M. (2008). "A local directional ghost cell approach for incompressible viscous flow problems with irregular boundaries." *Journal of Computational Physics*, 227, 4354–4397.

Chorin, A. (1968). "Numerical solution of the Navier-Stokes equations." *Mathematics of Computation*, 22, 745–762.

Duclos, G. and Clément, A. H. (2004). "Wave propagation through arrays of unevenly spaced vertical piles." *Ocean Engineering*, 31, 1655–1668.

Durbin, P. A. (2009). "Limiters and wall treatments in applied turbulence modeling." *Fluid Dynamics Research*, 41, 1–18.

Evans, D. V. and Porter, R. (1997). "Near-trapping of waves by circular arrays of vertical cylinders." *Applied Ocean Research*, 19, 83–99.

Huang, J. B. (2004). "Nonlinear free surface action with an array of vertical cylinders." *Acta Mechanica Sinica*, 20(3), 247–262.

Jacobsen, N. G., Fuhrman, D. R., and Fredsøe, J. (2012). "A wave generation toolbox for the open-source CFD library: OpenFOAM." *International Journal for Numerical Methods in Fluids*, 70(9), 1073–1088.

Jiang, G. S. and Peng, D. (2000). "Weighted eno schemes for Hamilton-Jacobi equations." *SIAM Journal on Scientific Computing*, 21, 2126–2143.

Jiang, G. S. and Shu, C. W. (1996). "Efficient implementation of weighted ENO schemes." *Journal of Computational Physics*, 126, 202–228.

Larsen, J. and Dancy, H. (1983). "Open boundaries in short wave simulations - a new approach." *Coastal Engineering*, 7, 285–297.

Linton, C. M. and Evans, D. V. (1990). "The interaction of waves with arrays of vertical circular cylinders." *Journal of Fluid Mechanics*, 215, 549–569.

Linton, C. M. and McIver, P. (2001). *Handbook of mathematical techniques for wave structure interactions*. Chapman and Hall CRC.

MacCamy, R. and Fuchs, R. (1954). *Wave forces on piles: A diffraction theory*. University of California, Dept. of Engineering.

Malenica, S., Taylor, R. E., and Huang, J. B. (1999). "Second-order water wave diffraction by an array of vertical cylinders." *Journal of Fluid Mechanics*, 390, 349–373.

Naot, D. and Rodi, W. (1982). "Calculation of secondary currents in channel flow." *Journal of the Hydraulics Division, ASCE*, 108(8), 948–968.

Ohkusu, M. (1974). "Hydrodynamic forces on multiple cylinders in waves." *Proc., International Symposium on Dynamics of Marine Vehicles and Structures in Waves, London*, 107–112.

Ohl, C. O. G., Taylor, R. E., Taylor, P. H., and Borthwick, A. G. L. (2001). "Water wave diffraction by a cylinder array. Part 1. Regular waves." *Journal of Fluid Mechanics*, 442, 1–32.

Osher, S. and Sethian, J. A. (1988). "Fronts propagating with curvature- dependent speed: algorithms based on Hamilton-Jacobi formulations." *Journal of Computational Physics*, 79, 12–49.

Peng, D., Merriman, B., Osher, S., Zhao, H., and Kang, M. (1999). "A PDE-based fast local level set method." *Journal of Computational Physics*, 155, 410–438.

Shu, C. W. and Osher, S. (1988). "Efficient implementation of essentially non-oscillatory shock capturing schemes." *Journal of Computational Physics*, 77, 439–471.

Spring, B. and Monkmeyer, P. L. (1974). "Interaction of plane waves with vertical cylinders." *Proc., International Conference on Coastal Engineering, ASCE, Copenhagen*, 1828–1847.

van der Vorst, H. A. (1992). "BiCGStab: A fast and smoothly converging variant of Bi-CG for the solution of nonsymmetric linear systems." *SIAM Journal on Scientific and Statistical Computing*, 13, 631–644.

Walker, D. A. G. and Taylor, R. E. (2005). "Wave diffraction from linear arrays of cylinders." *Ocean Engineering*, 32, 2053–2078.

Walker, D. A. G., Taylor, R. E., Taylor, P. H., and Zang, J. (2008). "Wave diffraction and near-trapping by a multi-column gravity-based structure." *Ocean Engineering*, 35, 201–209.

Wilcox, D. C. (1994). *Turbulence modeling for CFD*. DCW Industries Inc., La Canada, California.

Paper 4

Shoaling and Decomposition of Breaking and Non-Breaking Waves over a Submerged Bar

Kamath A., Alagan Chella M., Bihs H. and Arntsen Ø.A.
Submitted to *Coastal Engineering Journal* 2015

Shoaling and Decomposition of Breaking and Non-Breaking Waves over a Submerged Bar

Arun Kamath[1], Mayilvahanan Alagan Chella, Hans Bihs, Øivind A. Arntsen

Department of Civil and Transport Engineering, Norwegian University of Science and Technology, 7491 Trondheim, Norway

Abstract

Wave propagation over a submerged bar is simulated using the open source CFD model REEF3D with various incident wave heights to study shoaling, wave breaking features and the process of wave decomposition into higher harmonics for long waves of $T = 2.5$s. The computed free surface elevations are compared with experimental data and a good agreement is obtained for both non-breaking and spilling breaking waves. The differences in the mode of wave shoaling over the weatherside slope and the wave decomposition over the leeside slope of the submerged bar are discussed. The evolution of spilling breakers and plunging breakers over the bar crest is also studied. It is found that the free surface elevation continuously increases due to shoaling in the case of non-breaking waves, whereas breaking waves propagate with much lower free surface elevations after breaking over the bar crest. The power spectra of the free surface elevations at various locations indicate that the wave energy in the fundamental frequency is reduced by 76% for the lowest incident wave and by about 90% for all the other cases due to energy dissipation and energy transfer to higher harmonic components as the wave propagates over the submerged bar.

Keywords: wave decomposition, wave breaking, shoaling, submerged bar, numerical wave tank, CFD, REEF3D

[1]Corresponding Author, Email: arun.kamath@ntnu.no, Ph: (+47) 73 59 46 40, Fax: (+47) 73 59 70 21

1. Introduction

Wave propagation in shallow waters is influenced by the sea bottom topography and wave transformation processes such as diffraction, shoaling and wave breaking are observed. Wave shoaling refers to the phenomenon where the incident wave height is changed as the deep water wave propagates to water depths less than half the wavelength. Shoaling results in asymmetry in the wave profile with sharper crests and shallower troughs, creating an imbalance in the local wave energy distribution and leading to wave deformation. The wave crest heights reach a limiting value, beyond which the wave breaks to balance the local increase in the wave energy. The additional challenge in wave propagation over a submerged obstacle is the wave decomposition process which occurs behind the obstacle, in the region of increasing water depth, leading to the evolution of higher-order harmonics and rapidly varying waveforms. These processes can only be represented in a numerical model, which accounts for for nonlinearity and has good dispersion characteristics (Beji and Battjes, 1994).

The accurate evaluation of the wave kinematics in the near-shore area is important due to their impact on hydrodynamic properties such as wave forces, wave run-up and sediment transport. The mode of wave breaking is generally classified using the surf similarity parameter, $\xi = \frac{tan\alpha}{\sqrt{H/L_0}}$, where α is the angle of the slope, H is the incident wave height over the toe of the slope and $L_0 = \frac{g}{2\pi}T^2$ is the deep water wavelength where T is the wave period. Battjes (1974) presented the relationships between ξ and various flow parameters, and also the classification of breaker types on emergent plane sloping beaches. Gourlay (1994) carried out experiments on waves breaking on a submerged reef and Blenkinsopp and Chaplin (2008) on a submerged slope and found out that the classification presented by Battjes (1974) for emergent sloping beaches is not directly applicable for submerged structures. Wave propagation over sub-

merged structures has been studied through experimental investigations on a submerged bar (Beji and Battjes, 1993), a rectangular obstacle (Chang et al., 2001) and processes such as wave decomposition and vortex generation have been identified. Numerical modeling of wave propagation over a submerged obstacle has been carried out using Boussinesq equations (Beji and Battjes, 1994; Bosboom et al., 1996; Brocchini et al., 1992) and shallow water equations (Kobayashi et al., 1987) with good results for the wave shoaling process. According to Lemos (1992), the drawback of these methods is that they cannot account for the wave breaking process and was the first to present simulations of breaking waves using the Reynolds Averaged Navier-Stokes (RANS) equations. Lin and Liu (1998) and Zhao et al. (2004) employed single-phase CFD (Computational Fluid Dynamics) models to simulate breaking waves, which could not provide the complete picture on wave breaking as they cannot account for the air-water interaction responsible for the complex free surface deformations.

The knowledge of wave transformation and transmission across submerged structures finds its application in coastal protection measures such as submerged breakwaters, ecological conservation and recreational measures such as artificial reefs. The wave decomposition process modifies the waves transmitted over the submerged structure and this can be usefully exploited in a combined submerged bar- floating breakwater coastal protection measure. For the design of recreational artificial reefs and bars, it is essential to have a better idea regarding the breaking wave characteristics on the crest of the bar to provide sufficient breaker heights for surfing. It has been presented in previous studies on wave breaking that the wave breaking characteristics vary significantly under different breaking conditions (Battjes, 1974; Gourlay, 1994; Blenkinsopp and Chaplin, 2008). In addition, the many existing numerical and theoretical models for wave transformation over submerged breakwaters are based on the potential flow assumption, which cannot describe the rotational flow that occurs during the breaking process (Takikawa et al., 1997). CFD

modeling solves the fluid flow problem by solving the Navier-Stokes equations, accounting for most of the fluid physics with few assumptions. This method has been previously applied to the simulation of breaking waves over a slope by Hieu et al. (2004) and Jacobsen et al. (2012) using a Volume of Fluids (VoF) -based interface capturing method and Alagan Chella et al. (2015) using the level set method to obtain the interface. Alagan Chella et al. (2015) obtained good agreement to experimental data, with a sharp representation of the breaking wave and the formation air pockets, due to the higher order discretization schemes used in the model along with the level set method, compared to the lower order schemes used in previous studies. Numerical modeling with a two-phase CFD model resolves all the physics involved in the wave breaking process with few assumptions. Along with higher order discretization schemes and sharp interface capturing, it can account for the complex free surface process involved during wave transformation including breaking and decomposition. These processes can be evaluated in a more detailed manner compared to models based on the Boussinesq and shallow water equations.

In the current study, the open source CFD model REEF3D (Alagan Chella et al., 2015) is used to simulate wave propagation over a submerged bar. The numerical results are compared with the experimental data from Beji and Battjes (1993). Several previous studies regarding this have numerically calculated the wave propagation only for the non-breaking wave cases (Morgan et al., 2010; Roeber et al., 2010; Stelling and Zijlema, 2003). The breaking wave case was modeled by Tissier et al. (2012), but they reported deviations from the experimental observations from the point of wave breaking. Thus, numerical models accounting for both breaking and non-breaking waves over a submerged bar (Beji and Battjes, 1993) with good agreement to experimental data for both the free surface elevation and the wave phase have not been presented in current literature. This is especially true for the longer wave with $T = 2.5$ s, where the wave decomposition process is seen to be much stronger

in the experiments compared to the shorter waves with $T = 1$ s, which have been presented by several authors. An initial study for only non-breaking wave shoaling on a submerged bar was presented with comparison to experimental data (Kamath et al., 2015). In this paper, the study is significantly extended to cover the evolution of spilling and plunging breakers on the bar crest, with comparison of the free surface elevation in the spilling case. In addition, the shoaling process for the different incident waves is examined through the comparison of the relative wave crest elevations, evaluation of the maximum wave crest steepness and the relative phase differences between the primary wave crests of the transformed waves in the different cases. The decomposition process with transfer of wave energy to higher harmonics is also examined using the power spectral density computed from the free surface elevations and the redistribution of the wave energy amongst the harmonics is discussed. The effect of wave breaking on the wave propagation and decomposition process is also discussed.

2. Numerical Model

2.1. Governing equations

The numerical model uses the Reynolds Averaged Navier Stokes (RANS) equations along with the continuity equation to evaluate the fluid flow:

$$\frac{\partial u_i}{\partial x_i} = 0 \tag{1}$$

$$\frac{\partial u_i}{\partial t} + u_j \frac{\partial u_i}{\partial x_j} = -\frac{1}{\rho}\frac{\partial p}{\partial x_i} + \frac{\partial}{\partial x_j}\left[(\nu + \nu_t)\left(\frac{\partial u_i}{\partial x_j} + \frac{\partial u_j}{\partial x_i}\right)\right] + g_i \tag{2}$$

where u_i is the time averaged velocity, ρ is the density of the fluid, p is the pressure, ν is the kinematic viscosity, ν_t is the eddy viscosity, t is time and g is the acceleration due to gravity. The projection method (Chorin, 1968) is used for pressure treatment and the resulting Poisson pressure equation is solved

using a preconditioned BiCGStab solver (van der Vorst, 1992). Turbulence modeling is carried out using the two-equation $k-\omega$ model proposed by Wilcox (1994). Wave propagation is characterized by large gradients in the velocities resulting in a highly strained flow. Since, the production of turbulence in the $k-\omega$ model depends on the gradients in the velocity field, this results in unphysical overproduction of turbulence in a numerical wave tank. A stress limiter in the definition of eddy viscosity using assumption by Bradshaw et al. (1967) as shown by Durbin (2009) is implemented to avoid this. The free surface is a natural boundary for the turbulent eddies which is not accounted for in the k-ω model, resulting in an overproduction of turbulence at the free surface in a two-phase CFD model, due to the large strain caused by the large difference in the density of air and water. Free surface turbulence damping using a limiter around the interface as shown by Naot and Rodi (1982) is carried out to avoid the overproduction of turbulence at the interface. The limiter is activated only around the interface using the Dirac delta function.

2.2. Discretization schemes

The fifth-order conservative finite difference Weighted Essentially Non Oscillatory (WENO) scheme (Jiang and Shu, 1996) is used for the discretization of the convective terms in the RANS equations and the level set function, the turbulent kinetic energy and the specific turbulence dissipation rate are discretized using the Hamilton-Jacobi formulation of the WENO scheme (Jiang and Peng, 2000). Time advancement is carried out using a four-step scheme proposed by Choi and Moin (1994) with implicit treatment of convective and viscous terms. An adaptive time stepping approach is used to satisfy the Courant-Frederich-Lewy (CFL) condition for numerical stability. The numerical model uses a uniform Cartesian grid for spatial discretization facilitating an easy implementation of higher order schemes. The staggered grid approach is used with pressure at the cell centers and velocities at the cell faces, providing a tight coupling between the pressure and the velocity. A local directional

ghost cell immersed boundary method (Berthelsen and Faltinsen, 2008) extended to three dimensions is employed to handle complex geometries. The numerical model completely parallelized using the MPI library and can be executed on high performance computing systems.

2.3. Free surface

The free surface in the numerical wave tank is captured using the level set method (Osher and Sethian, 1988). Here, the interface is represented by the zero level set of the signed distance level set function . The level set function provides the least distance of each point in the domain from the interface. The different fluids are distinguished by the sign of the level set function as shown in Eq. (3):

$$\phi(\vec{x},t)\begin{cases} > 0 & if\ \vec{x}\ is\ in\ phase\ 1 \\ = 0 & if\ \vec{x}\ is\ at\ the\ interface \\ < 0 & if\ \vec{x}\ is\ in\ phase\ 2 \end{cases} \tag{3}$$

The definition of the level set function makes it smooth across the interface and provides a sharp representation of the interface. The level set function is convected by the velocity field in the numerical wave tank. The signed distance property is lost on convection and is restored by re-initializing the level set function after every iteration with the partial differential equation re-initialization procedure by Peng et al. (1999).

2.4. Numerical wave tank

The numerical wave tank uses the relaxation method (Larsen and Dancy, 1983) for wave generation and absorption. In this method, relaxation functions are used to moderate the computational values to the expected values from wave theory to generate and absorb waves. This requires certain zones of the wave tank to be reserved as relaxation zones for wave generation and absorption. The numerical model uses the relaxation functions proposed by

Jacobsen et al. (2012) presented in Eq. (4):

$$\Gamma(x) = 1 - \frac{e^{(1-x)^{3.5}} - 1}{e - 1} \tag{4}$$

where $\Gamma(x)$ is the relaxation function and x is the coordinate along the x-axis scaled to the length of the relaxation zone. The relaxation functions prescribe the required values for free surface elevation and velocity from wave theory to the wave tank using Eq. (5):

$$\begin{aligned} u_{relaxed} &= \Gamma(x) u_{analytical} + (1 - \Gamma(x)) u_{computational} \\ \phi_{relaxed} &= \Gamma(x) \phi_{analytical} + (1 - \Gamma(x)) \phi_{computational} \end{aligned} \tag{5}$$

The relaxation function also absorbs reflections from the objects placed in the numerical wave tank, so that it does not affect wave generation and simulates a wavemaker with active absorption. At the numerical beach, the computational values from the wave tank are reduced to zero to smoothly absorb wave energy without spurious reflections from the beach.

3. Results

A grid refinement study is carried out first to select the grid size to be used for the simulations in the study. Then, wave propagation over a submerged bar are simulated for different incident wave heights and the numerical results are compared to experimental data. The wave transformation over the submerged bar is studied using the data obtained from the wave gages at different locations along the length of the bar. The evolution of spilling and plunging breakers on the bar crest in the simulation is also presented. The shoaling process for the different incident waves is examined through the variation of the relative wave crest elevations. The decomposition process with transfer of wave energy to higher harmonics is examined by calculating the power spectral densities of the computed free surface elevations at the different locations

in the wave tank.

3.1. Grid refinement study

Accurate wave generation and propagation in the numerical wave tank is verified by carrying out a grid refinement study. A two-dimensional wave tank of length 38 m and height 0.8 m is used to generate second-order Stokes waves with wave period $T = 2.5$ s, wavelength $L = 4.74$ m and wave height $H_1 = 0.022$ m in a water depth of $d = 0.4$ m. Grid sizes $dx = 0.04$ m, 0.02 m, 0.01 m and 0.005 m are used. The results presented in Fig. (1) show that the free surface elevations converge to the required values from a grid size of $dx = 0.02$ m onwards. Due to the high order discretization schemes used in the model and the relatively low wave steepness in the study, there is no significant difference in the wave heights obtained at the different grid sizes. But, in order to capture the evolution of wave shoaling and breaking in this study, a grid size of $dx = 0.005$ m is used for the simulations.

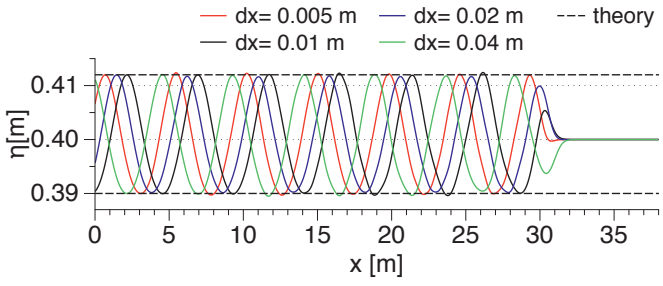

Figure 1: Grid refinement study with 2*nd*-order Stokes waves of T=2.525 s and $H_1 = 0.022$ m

3.2. Numerical wave tank setup

The simulations of wave propagation over a submerged bar are carried out based on the experimental studies by Beji and Battjes (1993). The submerged bar has a weatherside slope of 1 : 20, a leeside slope of 1 : 10 and a crest height of 0.3 m. The wave tank has a water depth of $d = 0.4$ m resulting in a depth of 0.1 m on the crest of the bar and incident waves of heights $H_1 = 0.022$ m, $H_2 = 0.035$ m, $H_3 = 0.042$ m and $H_4 = 0.052$ m are simulated. Wave gages are placed at various locations along the bar to evaluate the wave propagation over the bar as shown in Fig. (2). A two-dimensional numerical wave tank 38 m long and 0.8 m high with a grid size of 0.005 m is used, resulting in a total of 1.216 million cells. A wave generation relaxation zone of length 5 m and a numerical beach of length 9.5 m are used at the beginning and the end of the wave tank respectively to ensure good wave generation and absorption. The $x-$coordinate in the wave tank begins at the end of the wave generation relaxation zone and the same distances as in the experiments by Beji and Battjes (1993) are maintained.

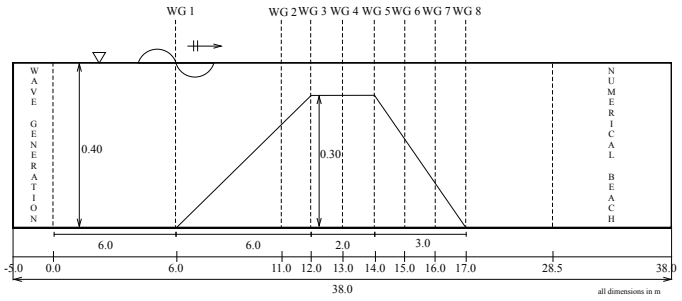

Figure 2: Schematic diagram of the setup used in the numerical simulations, all dimensions in m

3.3. Non-breaking wave propagation over a submerged bar

A simulation is carried out with second-order Stokes waves of wave height $H_1 = 0.022$ m, wave period $T = 2.5$ s and wavelength $L = 4.74$ m. The

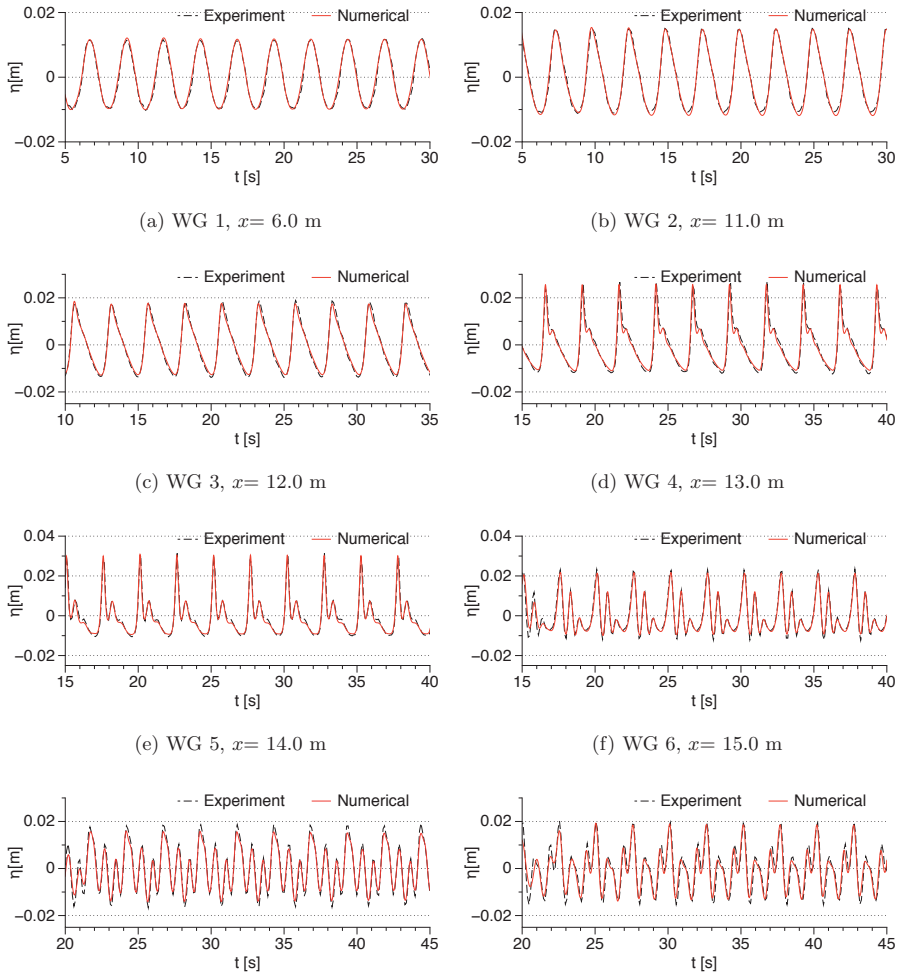

(a) WG 1, x= 6.0 m

(b) WG 2, x= 11.0 m

(c) WG 3, x= 12.0 m

(d) WG 4, x= 13.0 m

(e) WG 5, x= 14.0 m

(f) WG 6, x= 15.0 m

(g) WG 7, x= 16.0 m

(h) WG 8, x= 17.0 m

Figure 3: Free surface elevations at various locations along the wave flume for $H_1 = 0.022$ m

free surface elevations are computed at several locations along the submerged bar and are compared with the measured experimental data in Fig. (3) and a good agreement is seen in both the phase and amplitude of the transformed waves. As the waves propagate along the reducing water depth along the

upward slope of the bar, the wave profile is seen to be slightly deformed with the development of a saw-toothed profile at $x = 11.0$ m in Fig. (3b), which becomes prominent at $x = 12.0$ m in Fig. Fig. (3c). As a result of wave shoaling, high and sharp wave crests are formed over the bar crest $x = 13.0$ m in Fig. (3d). The decomposition of the wave with the development of higher harmonic components is also observed from $x = 14.0$ m (Fig. 3e) onwards, as the wave propagates over the end of the bar crest. As the wave propagates along the leeside slope of the bar, the water depth increases and a process opposite to wave shoaling takes place(Beji and Battjes, 1993). The free surface elevation begins to reduce compared to the elevations on the upward slope and the crest. The wave decomposition results in the formation of secondary and tertiary waves after the bar crest as seen in Figs. 3f, 3g, 3h.

3.4. Breaking wave propagation over a submerged bar

The incident wave height is further increased to $H_3 = 0.042$ m to simulate spilling breakers and the computed free surface elevations are compared with experimental data in Fig. (4). The computed results show a good agreement with the experimental data at most of the locations but some differences are seen in the amplitudes computed at $x = 13.0$ m, 14.0 m and 15.0 m, though the wave phases are in good agreement. This is due to the fact that the wave breaks over the crest of the bar, between $x = 13.0$ m and $x = 14.0$ m. The average difference between the primary wave crest heights in the numerical results and the experimental data are found to be about 0.012 m over a 25 s window which is 24% of the local wave height. The complex flow scenario due to small scale wave breaking over very shallow water ($d = 0.1$ m) over the bar crest results in instantaneous changes in the pattern of the free surface elevations in this region. It is challenging to capture these free surface effects resulting from violent mixing of air and water, both experimentally and numerically in the near post-breaking region. This accounts for the difference observed in the free surface elevations at $x = 13.0$ m and $x = 14.0$ m in

Fig. (4d) and (4e). The difference in the wave crest height reduces to 0.0036 m over a 25 s window at WG 7 at $x = 16.0$ m and the numerical results for WG 8 at $x = 17.0$ m match the experimental results again.

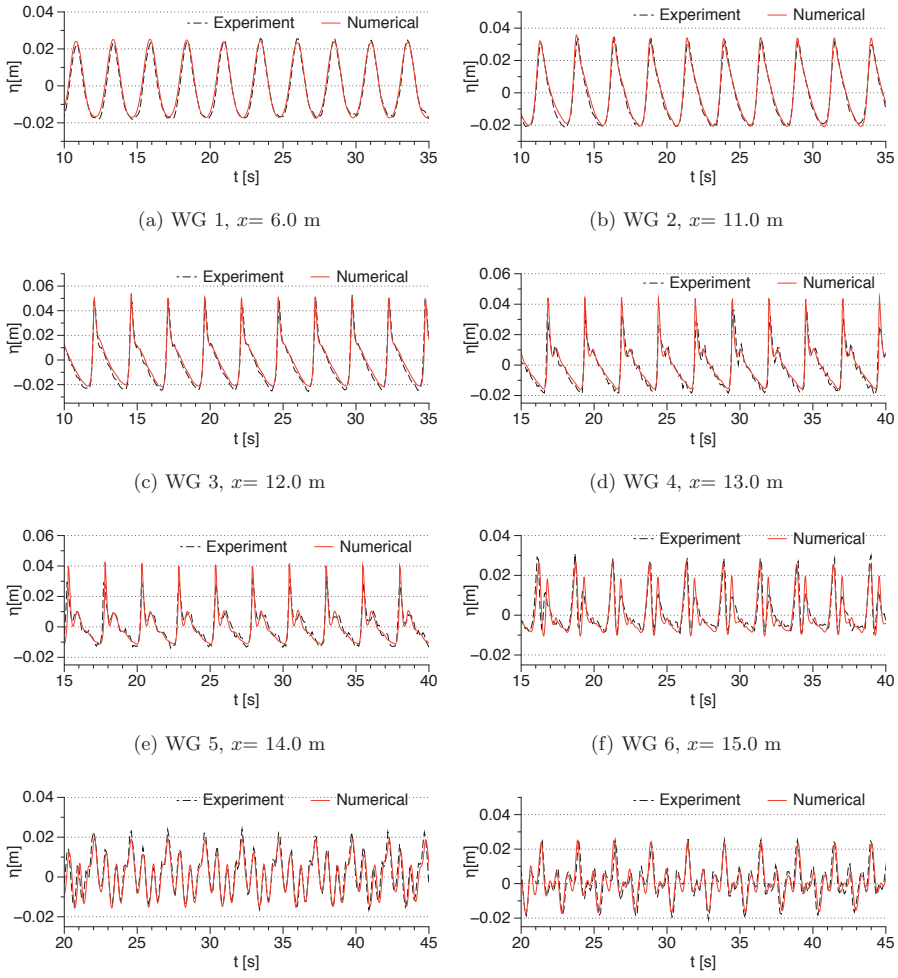

(a) WG 1, x= 6.0 m

(b) WG 2, x= 11.0 m

(c) WG 3, x= 12.0 m

(d) WG 4, x= 13.0 m

(e) WG 5, x= 14.0 m

(f) WG 6, x= 15.0 m

(g) WG 7, x= 16.0 m

(h) WG 8, x= 17.0 m

Figure 4: Free surface elevations at various locations along the wave flume for $H_3 = 0.042$ m

The evolution of the wave profile in the region of wave breaking in the

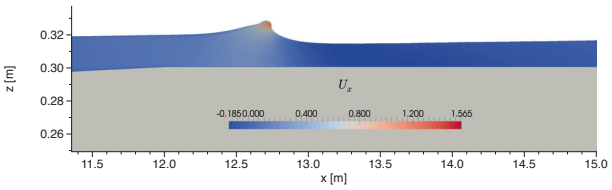

(a) t/T=8.89

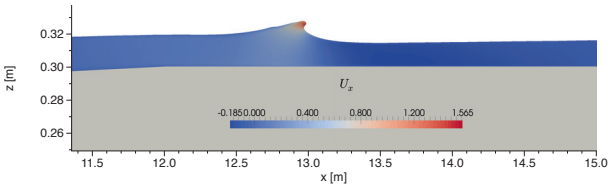

(b) t/T=8.93

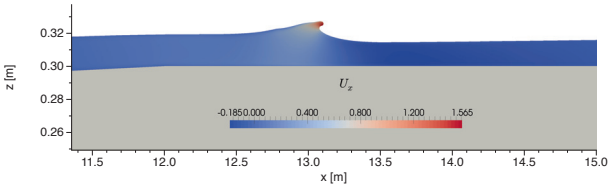

(c) t/T=8.95

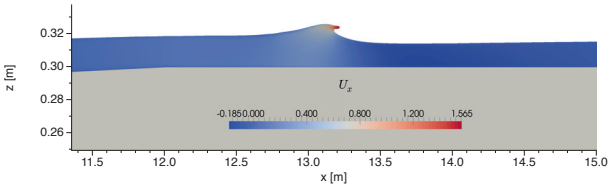

(d) t/T=8.97

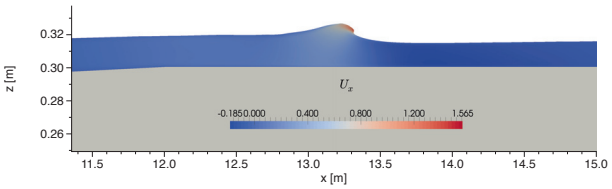

(e) t/T=8.99

Figure 5: Process of spilling wave breaking over the bar crest for $H_3 = 0.042$ m

simulation is presented in Fig. (5) to obtain further insight into the breaking process in this case. The shoaling of the wave due to the reducing water depth leads to a sharp wave crest on the bar crest as seen in Fig. (5a). The bar crest acts as a flat bottom with very low water depth and the wave propagates over the crest without much change to its amplitude, but with reduced wave celerity. The reduction in wave celerity combined with an increase in wave crest elevation due to shoaling leads to a local imbalance in the wave energy with wave crest particle velocities higher than the wave celerity. This increases the asymmetry of the wave and the appearance of a steep wave crest. The steep wave crest then stretches away from the main wave crest in Fig. (5b). Due to lack of further excess energy, the wave crest then begins to spill forward onto the main wave crest in Figs. (5c) and (5d), resulting in a small scale spilling breaker. The velocity contours in the figures demonstrate the large increase in the horizontal water particle velocity in the overturning crest compared to the rest of the free surface, signifying the complex hydrodynamics involved in the spilling breaking wave. The total duration from the near vertical wave crest profile until the wave crest rejoins the preceding trough is only $0.1T$, signifying the rapid and small scale nature of the spilling breaker in this case.

The wave transformation over the submerged bar is further investigated with an incident wave height of $H_4 = 0.052$ m and the wave elevations computed along the submerged bar are presented in Fig. (6). Since there was no experimental data available for this case, only the numerical results are presented. The effect of shoaling with saw-toothed asymmetry in the wave profile appears sooner than in the previous cases at $x = 11.0$ m in Fig. (6b). The wave profile then undergoes similar transformations as seen for the previous cases at $x = 12.0$ m, $x = 13.0$ m and $x = 14.0$ m with even more sharper wave crests, due to stronger shoaling of the higher incident wave. At $x = 15.0$ m, the decomposed waves consist of the primary crest and a secondary wave crest of similar magnitude, which further decompose to produce a tertiary wave crest at $x = 16.0$ m and a quaternary crest at $x = 17.0$ m.

The free surface deformation over the crest of the submerged bar are presented in Fig. (7) and the wave breaking process in this case is studied. The steep wave crest formed as a result of wave shoaling on the upward slope enters the shallow water region on the bar crest is observed in Fig. (7a). The steep crest stretches away from the main wave crest to form an overturning wave crest in Fig. (7b). The overturning wave crest then forms a plunging jet to rejoin with the free surface slightly in front of the primary wave crest,

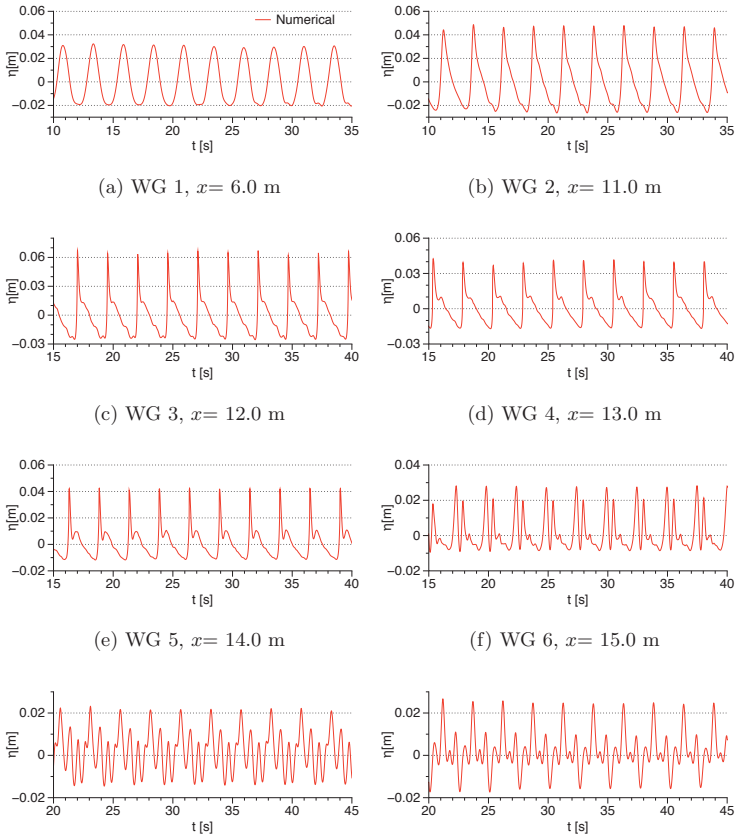

(a) WG 1, x= 6.0 m (b) WG 2, x= 11.0 m

(c) WG 3, x= 12.0 m (d) WG 4, x= 13.0 m

(e) WG 5, x= 14.0 m (f) WG 6, x= 15.0 m

(g) WG 7, x= 16.0 m (h) WG 8, x= 17.0 m

Figure 6: Free surface elevations at various locations along the wave flume for $H_4 = 0.052$ m

resulting in the formation of an air pocket in Fig. (7c). The splash up of the free surface after the plunging wave breaking is seen Fig. (7d). The horizontal velocity contours in Fig. (7) show the increase in the horizontal velocity at the free surface that leads to the formation of the overturning wave crest and eventually the plunging breaker. The wave crest goes from a near vertical profile to reconnection to the preceding wave crest in $0.12T$, which is slightly slower than the spilling breaker.

A grid refinement study for the plunging breaking wave obtained for $H_4 = 0.052$ m is carried with additional simulations at grid sizes $dx = 0.01$ m, $dx = 0.02$ m and $dx = 0.04$. From the free surface profiles in Fig. (8), it can be concluded that the breaker location has converged to $x = 17.2$ m from $dx = 0.01$ m onwards, but the vertical profile of the breaking wave crest is best represented by $dx = 0.005$ m. This confirms that the choice of $dx = 0.005$ m as the grid size for the simulations is justified. The very fine grid required to represent the wave breaking in this study arises from the fact that the incident waves are of low steepness and they undergo large and rapid changes in their wave steepness during propagation over the bar. This follows the conclusions by Alagan Chella et al. (2015), that incident waves with lower steepnesses undergo larger deformations than waves with larger incident steepnesses. An overview of the results obtained for the different simulations is presented in Table 1.

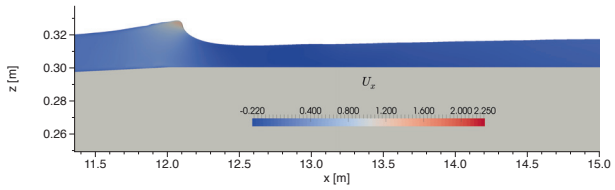

(a) t/T=7.74

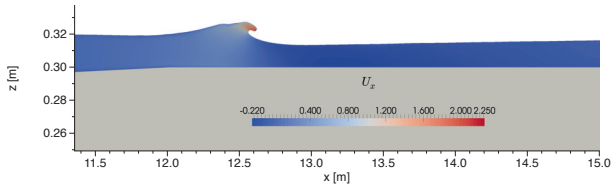

(b) t/T=7.82

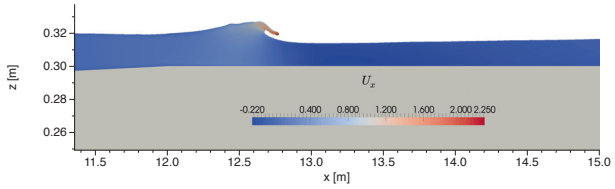

(c) t/T=7.84

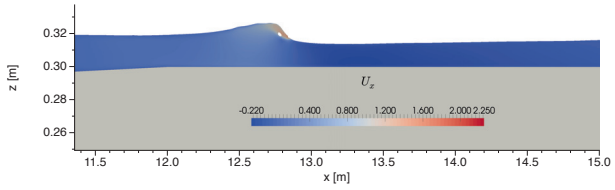

(d) t/T=7.86

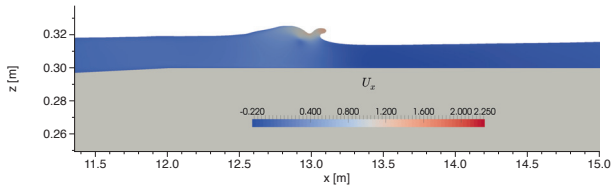

(e) t/T=7.90

Figure 7: Process of plunging wave breaking over the bar crest for $H_4 = 0.052$ m

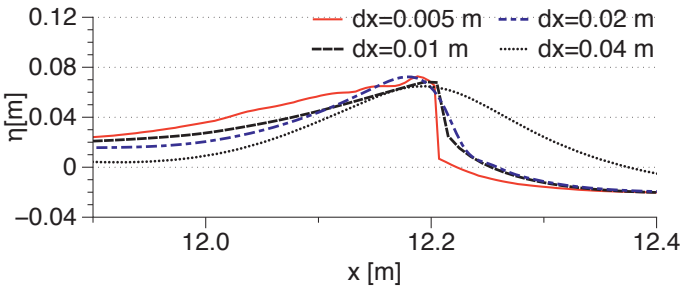

Figure 8: Grid refinement study for plunging breaker location for $H_4 = 0.052$ m

Table 1: Summary of the results from the different simulations in the study

Test	T (s)	H (m)	ξ	ϵ_{max}	breaking type
1.	2.5	0.022	1.4678	0.1275	non-breaking
2.	2.5	0.035	1.1637	0.2008	non-breaking
3.	2.5	0.042	1.0623	0.0526	spilling
4.	2.5	0.052	0.9547	0.0641	plunging

3.5. Wave transformation process

The variation in the relative wave crest elevations computed at the different wave gages is studied to gain a comparative perspective of the wave transformation process for both non-breaking and breaking waves. The incident waves at $x = 6.0$ m in Fig. (9a) show the small horizontal asymmetry in the wave profile with shallower troughs and sharper crests, which is characteristic of second-order Stokes waves. The breaking and non-breaking waves show certain differences in the transformation properties. In the case of the non-breaking waves with $H_1 = 0.022$ m and $H_2 = 0.035$ m, shoaling leads to saw-toothed asymmetry in the wave profile. The higher incident wave H_2 undergoes a higher increase in the relative crest elevation and attains a sharper saw-toothed asymmetry in Fig. (9b) at $x = 11.0$ m. As the wave reaches the crest of the bar at $x = 12.0$ m, the relative crest elevation is higher for H_2

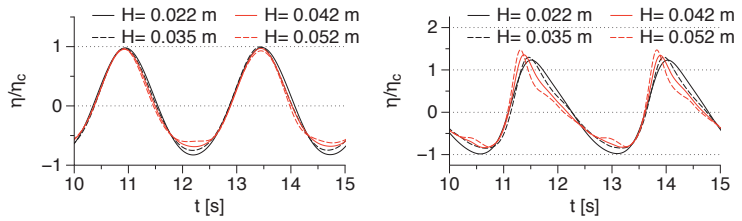

(a) WG 1, x= 6.0 m

(b) WG 2, x= 11.0 m

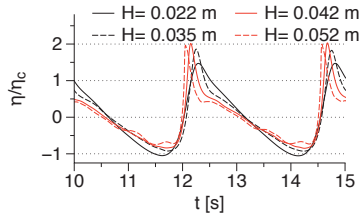

(c) WG 3, x= 12.0 m

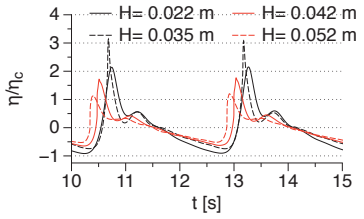

(d) WG 4, x= 13.0 m

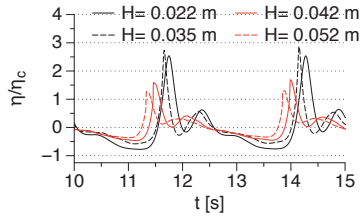

(e) WG 5, x= 14.0 m

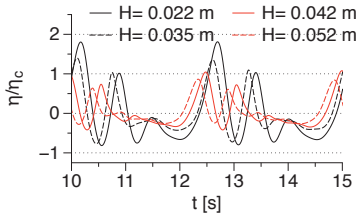

(f) WG 6, x= 15.0 m

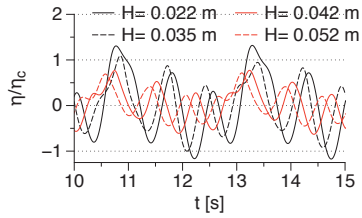

(g) WG 7, x= 16.0 m

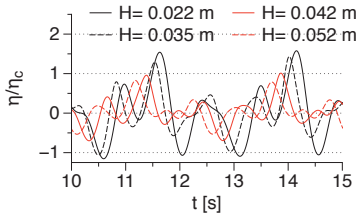

(h) WG 8, x= 17.0 m

Figure 9: Relative free surface elevations at various locations along the wave flume for the different wave heights simulated

compared to H_1 in Fig. (9c). In the region over the bar crest at $x = 13.0$ m and $x = 14.0$ m, the higher incident wave maintains a higher relative crest elevation in Figs. (9d) and (9e). The maximum wave crest steepness (Kjeldsen and Myrhaug, 1978) $\epsilon = \eta'/L'$, where η' is the wave crest height and L' the distance from the wave crest to the wave zero-crossing location, can be used to quantify the crest steepness. In the case of $H_2 = 0.035$ m, the maximum wave crest steepness $\epsilon_{max} = 0.2008$ is calculated for WG 4 at $x = 13.0$ m. The maximum wave crest steepness $\epsilon_{max} = 0.1275$ for $H_1 = 0.022$ m is obtained at $x = 14.0$ m at WG 5. Also, the higher incident wave (H_2) moves faster than the lower incident wave (H_1). This follows from shallow water wave propagation, where a higher wave propagates faster for a given wave period and water depth. The higher incident wave attains the highest crest elevation during its propagation over the upward slope and thus propagates faster over the shallow water depth over the crest.

The submerged bar crest ends at $x = 14.0$ m and the initiation of wave decomposition is seen in Fig. (9e), with the appearance of secondary crests. As the wave propagates further, the water depth increases over the downward slope of the submerged bar. This change in the water depth begins a process of de-shoaling (Beji and Battjes, 1993), where the waves reduce in amplitude as they propagate over gradually increasing water depths. Well-developed secondary wave crests are seen at $x = 15.0$ m in Fig. (9f). It is also observed that the reduction in the relative crest elevation is lower for the lower incident wave. The higher non-breaking wave H_2, which had the highest crest elevation at $x = 13.0$ m has a lower primary crest elevation and a higher secondary crest elevation compared to H_1, indicating that H_2 transfers a larger amount of wave energy to a higher frequency. In Figs. (9g) and (9h), the formation of a secondary and a tertiary wave crest is seen for both the non-breaking waves. The lower wave (H_1) continues to maintain a higher primary relative crest elevation throughout the wave decomposition process, whereas the higher wave has slightly higher secondary and tertiary relative crest elevations.

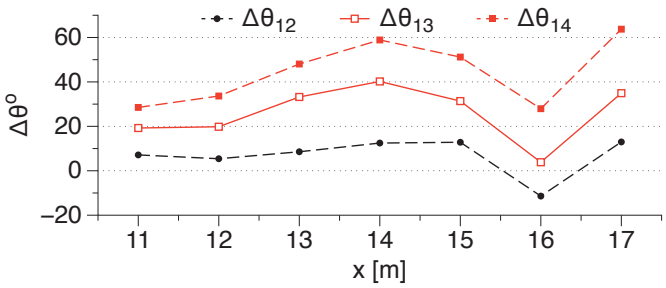

Figure 10: Relative phase difference between primary wave crests in the different cases simulated in the study with respect to the lowest incident wave with $H_1 = 0.022$ m

In the case of $H_3 = 0.042$ m and $H_4 = 0.052$ m spilling and plunging wave breaking is observed between $x = 12.0$ m and $x = 13.0$ m. During the shoaling process from $x = 6.0$ m to $x = 12.0$ m shown in Figs. (9b) and (9c), the waves have similar relative elevations. The breaking waves attain their maximum wave crest steepness of $\epsilon_{max} = 0.0526$ for H_3 and $\epsilon_{max} = 0.0641$ for H_4 at WG 3 at $x = 12.0$ m. At the wave gages after the breaking region, $x = 13.0$ m to $x = 17.0$ m, H_3 maintains a higher relative crest elevation in Figs. (9d)-(9h). This is justified by the fact that H_4 evolves into a plunging breaking wave and dissipates a larger part of its energy in the process compared to the spilling breaking wave formed by H_3. It is also noticed that the surf similarity number is $\xi = 1.0623$ for H_3 and $\xi = 0.9547$ for H_4. According to the classification by Battjes (1974), these correspond to plunging wave breaking on an emergent plane slope, but the results in this study show a spilling breaker for H_3 and plunging breaker for H_4. This indicates that the wave breaking on a bar crest has different breaker characteristics and the original classification for wave breaking on emergent plane slopes can not be directly applied to wave breaking over a submerged bar. In order to further understand the wave transformation process for the different cases simulated, the phase difference between the different waves during their propagation over the bar is analysed at the various gage locations. The relative phase difference $\delta\theta$ between the

primary wave crests for $H_2 = 0.035$ m, $H_3 = 0.042$ and $H_4 = 0.052$ m with respect to $H_1 = 0.022$ m is presented in Fig. (10). It can be concluded that the higher waves propagate faster and keep gaining on the lower incident waves until the bar crest ends. The phase differences between the free surface elevations show that H_4 leads H_1 by a maximum $\delta\theta_{14} = 60^\circ$ at $x = 14.0$ m. Over the leeside of the bar, the primary wave crests undergo a sudden reduction in their celerity during the decomposition process with H_2 lagging H_1 by $\delta\theta_{12} = 11.46^\circ$ and H_4 leading H_1 by only $\delta\theta_{14} = 27.94^\circ$ at $x = 16.0$ m (WG 7). As the waves propagate further to $x = 17.0$ m (WG 8), the phase differences return to the values obtained at the end of the bar crest at $x = 14.0$ m (WG 5).

Thus, the wave transformation process for all the incident waves is similar up to the region of wave breaking, with a higher incident wave attaining a higher relative crest elevation. After the region of wave breaking, the transformation of the breaking waves depends on the type of wave breaking, whereas the non-breaking waves continue with the trend seen on the weatherside slope. In the region of increasing water depth after the bar crest, the lower non-breaking wave maintains a higher primary relative crest elevation compared to the secondary relative crest elevation. The breaking waves show similar relative crest amplitudes. The higher incident waves are also seen to propagate faster and increase in celerity over the bar up to the end of the bar crest.

3.6. Wave decomposition process

The wave decomposition process is examined by calculating the power spectral densities for the different incident waves using the free surface elevations at the different locations. The frequencies to which the wave energy is transferred resulting in the evolution of the secondary and tertiary wave crests are identified. The normalized power spectra at the different wave gage locations along the bar are presented in Fig. (11). The power spectra for all

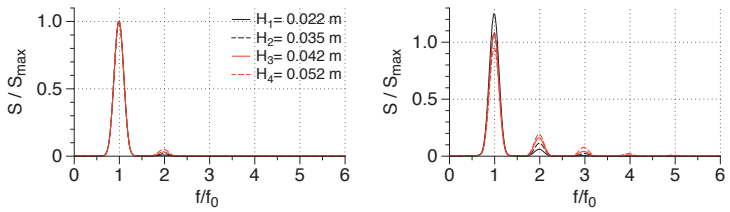

(a) WG 1, $x = 6.0$ m

(b) WG 2, $x = 11.0$ m

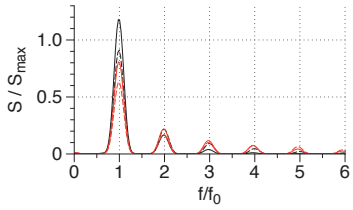

(c) WG 3, $x = 12.0$ m

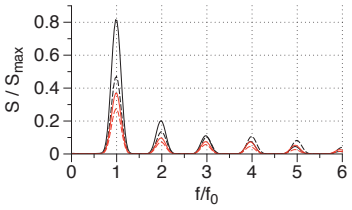

(d) WG 4, $x = 13.0$ m

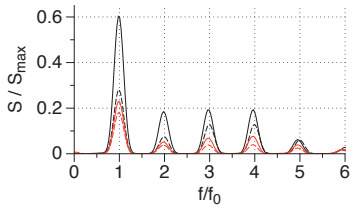

(e) WG 5, $x = 14.0$ m

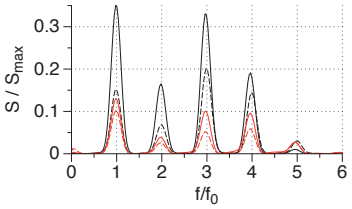

(f) WG 6, $x = 15.0$ m

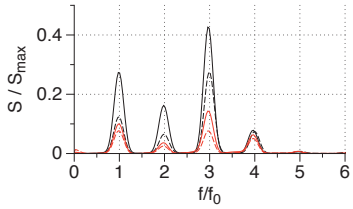

(g) WG 7, $x = 16.0$ m

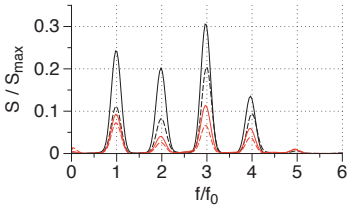

(h) WG 8, $x = 17.0$ m

Figure 11: Normalized spectra for the simulated waves showing decomposition of the incident wave into higher harmonics

the cases are normalized with the spectral amplitude at the primary wave frequency, $f_0 = 0.4$ Hz, S_{max} in Fig. (11a). The process of shoaling results in an increase of the energy content at the primary frequency and the first harmonic of the non-breaking waves. The lowest incident wave, H_1, adds $0.25S_{max}$ to its fundamental frequency f_0 whereas H_2 and H_3 gain 0.12 and 0.16 S_{max} respectively at the first harmonic at $x = 11.0$ m. On the other hand, the spectral power density for the highest incident wave H_4 is reduce by $0.05S_{max}$ at f_0 and increased by $0.14S_{max}$ at the first harmonic f_1. At $x = 12.0$ m, the waves reach the bar crest, and significant spectral densities are obtained up to the fourth harmonic f_4 with $0.024S_{max}$ for H_4. Wave breaking occurs between $x = 12.0$ m and $x = 13.0$ m for H_3 and H_4. This corresponds with a reduction of the spectral power density to $0.368S_{max}$ for H_3 and $0.272S_{max}$ for H_4 at f_0 at $x = 13.0$ m. In the case of the non-breaking waves, H_1 retains $0.82S_{max}$ at f_0 and transfers $0.20S_{max}$ and $0.11S_{max}$ to f_1 and f_2 respectively. As the waves propagate across the bar crest and in the region of increasing water depth at $x = 15.0$ m, the major portion of the energy is distributed between f_0 and f_2 for H_1. For H_2, H_3 and H_4 the major portion of the energy is distributed amongst f_0, f_2 and f_3 at $x = 15.0$ m in Fig. (11f). At $x = 16.0$ m, the spectral power density for all the four waves is mainly concentrated at f_0 and f_2 in Fig. (11g). As the waves reach a water depth of $d = 0.4$ m again at $x = 17.0$ m, H_1 similar power densities of $0.24S_{max}$ and $0.20S_{max}$ at f_0 and f_1 respectively and $0.31S_{max}$ at f_2. For the higher incident waves, the power spectra show a similar distribution as at $x = 16.0$ m, but with lower magnitudes.

The variation of the spectral power density in the first four harmonics over the submerged bar for all the four waves is presented in Fig. (12. The power spectral density at f_0 is reduced significantly at $x = 17.0$ m to $0.24S_{max}$, $0.11S_{max}$, $0.09S_{max}$ and $0.09S_{max}$ for H_1, H_2, H_3 and H_4 respectively in Fig. (12a). From Fig. (12b), it is seen that the first harmonic f_1 initially gains energy for all the cases, but loses its energy gradually for all the cases except

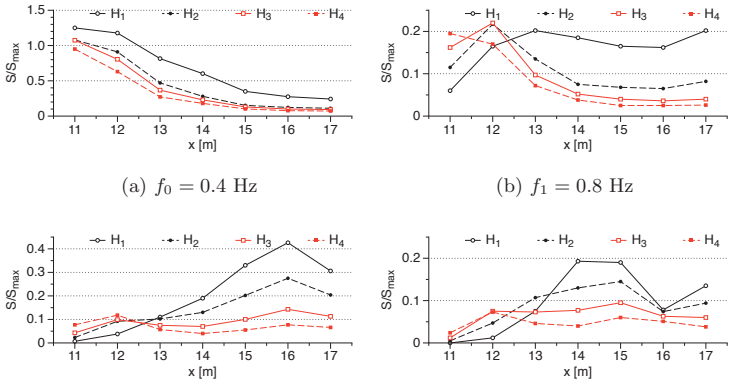

(a) $f_0 = 0.4$ Hz (b) $f_1 = 0.8$ Hz

(c) $f_2 = 1.2$ Hz (d) $f_3 = 1.6$ Hz

Figure 12: Variation of the normalized power density spectra at the first four harmonics for the different incident waves along the submerged bar

H_1. The second harmonic f_2 gradually gains energy as the propagate over the bar, with a maximum of $0.42S_{max}$ at $x = 16.0$ m for H_1 in Fig. (12c).

The maximum spectral power in the third harmonic f_3 is presents itself between $x = 14.0$ m and $x = 15.0$ m. The following distinct pattern emerges regarding the energy transfer between the different harmonics. The fundamental frequency gradually loses most of its energy as the wave propagates over the bar. The first harmonic gains energy initially on the weatherside slope, but loses this energy gradually. The second harmonic gains energy steadily and holds most of the wave energy towards the end of the bar. The third harmonic contains significant amounts of energy in the intermediate stages between $x = 13.0$ m and $x = 15.0$ m. Finally, the variation of the total energy in the first four harmonics over the length of the bar for all the cases is presented in Fig. (13). It is clear that all the waves lose significant amounts of energy except for H_1, with total spectral power densities of $0.89S_{max}$, $0.49S_{max}$, $0.31S_{max}$ and $0.30S_{max}$ for H_1, H_2, H_3 and H_4 respectively at $x = 17.0$ m, losing $12.5S_{max}$, $0.53S_{max}$, $0.73S_{max}$ and $0.85S_{max}$ during propagation of the bar.

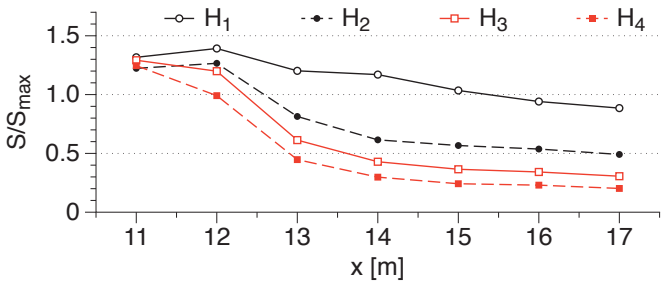

Figure 13: Variation of the total normalized power spectral density for the different incident waves along the submerged bar

4. Conclusion

The open-source CFD model, REEF3D is used to simulate wave propagation over a submerged bar including wave shoaling, breaking and decomposition for regular long waves with $T = 2.5$ s. The computed free surface elevations at several locations along the length of the flume are compared with experimental data and a general good agreement is seen both in terms of the phase and the elevation of the free surface variation for both non-breaking and spilling breaking waves. A good representation of the wave shoaling and decomposition during the propagation of the wave on the weatherside and leeside slopes respectively is obtained in the simulations. The high order discretization schemes in the model result in realistic modeling of the non-linear wave interactions and the dispersion characteristics of the decomposing waves for the more challenging case with long waves with $T = 2.5$ s, showing strong decomposition on the leeside of the bar. Spilling breakers are observed on the bar crest for an incident wave height of 0.042 m ($\xi = 1.0623$) and on further increase of the incident wave height to 0.052 m ($\xi = 0.9547$), plunging breakers are observed. The wave transformation and decomposition is thoroughly analysed and the following conclusions are made regarding the wave transformation process along the bar:

- Non-breaking waves with higher incident amplitude increase in crest elevation until the end of the bar crest.
- Breaking waves with higher incident amplitude increase in crest elevation until the breaking region on the bar crest.
- Breaker classification using the surf similarity numbers based on emergent sloping beaches can not be applied directly in this scenario.
- Higher incident waves keep increasing their celerity and gain in wave phase over the lower wave heights until end of the bar crest.

The power spectra of the free surface elevations along the bar provided the following results regarding the wave decomposition process:

- Significant reduction in the wave energy at the fundamental frequency is seen for all the cases simulated and higher incident waves transfer a larger amount of energy to their higher harmonics on the weatherside slope.
- Non-breaking waves preserve most of their energy throughout the wave tank, whereas a large amount of wave energy is lost due to the breaking process for the breaking waves.
- A distinct pattern is observed in energy transfer amongst the harmonics with the first, second and third harmonics containing their maximum energies at the initial, the final and in the intermediate stages over the bar respectively.

Acknowledgements

The authors are grateful to Prof. Serdar Beji, Istanbul Technical University for providing the experimental data. This study has been carried out under the OWCBW project (No. 217622/E20) and the authors are grateful to the grants provided by the Research Council of Norway. This research was supported in

part with computational resources at the Norwegian University of Science and Technology (NTNU) provided by NOTUR, http://www.notur.no (No. NN2620K).

References

Alagan Chella, M., Bihs, H., Myrhaug, D., Muskulus, M., 2015. Breaking characteristics and geometric properties of spilling breakers over slopes. Coastal Engineering 95, 4–19.

Battjes, J.A., 1974. Surf similarity, in: Proc., 14*th* International Conference on Coastal Engineering, Copenhagen, Denmark, pp. 466–480.

Beji, S., Battjes, J.A., 1993. Experimental investigation of wave propagation over a bar. Coastal Engineering 19, 151–162.

Beji, S., Battjes, J.A., 1994. Numerical simulation of nonlinear wave propagation over a bar. Coastal Engineering 23, 1–16.

Berthelsen, P.A., Faltinsen, O.M., 2008. A local directional ghost cell approach for incompressible viscous flow problems with irregular boundaries. Journal of Computational Physics 227, 4354–4397.

Blenkinsopp, C.E., Chaplin, J.R., 2008. The effect of crest submergence on wave breaking over submerged slopes. Coastal Engineering 55, 967–974.

Bosboom, J., Klopman, G., Roelvink, J., Battjes, J., 1996. Wave kinematics computations using boussinesq models, in: Proc. 25*th* International Conference on Coastal Engineering, Orlando, USA, pp. 109–122.

Bradshaw, P., Ferriss, D.H., Atwell, N.P., 1967. Calculation of boundary layer development using the turbulent energy equation. Journal of Fluid Mechanics 28, 593–616.

Brocchini, M., Drago, M., Iovenitti, L., 1992. The modelling of short waves in shallow water. comparison of numerical methods based on boussinesq and serre equations, in: Proc. 23*rd* International Conference on Coastal Engineering, New York, USA.

Chang, K.A., Hsu, T.J., Liu, P.L.F., 2001. Vortex generation and evolution of water waves propagating over a submerged rectangular obstacle. part i. solitary waves. Coastal Engineering 44, 13–36.

Choi, H., Moin, P., 1994. Effects of the computational time step on numerical solutions of turbulent flow. Journal of Computational Physics 113, 1–4.

Chorin, A., 1968. Numerical solution of the Navier-Stokes equations. Mathematics of Computation 22, 745–762.

Durbin, P.A., 2009. Limiters and wall treatments in applied turbulence modeling. Fluid Dynamics Research 41, 1–18.

Gourlay, M.R., 1994. Wave transformation on a coral reef. Coastal Engineering 23, 17–42.

Hieu, P.D., Katsutoshi, T., Ca, V.T., 2004. Numerical simulation of breaking waves using a two-phase flow model. Applied Mathematical Modeling 28, 983–1005.

Jacobsen, N.G., Fuhrman, D.R., Fredsøe, J., 2012. A wave generation toolbox for the open-source CFD library: OpenFOAM. International Journal for Numerical Methods in Fluids 70, 1073–1088.

Jiang, G.S., Peng, D., 2000. Weighted ENO schemes for Hamilton-Jacobi equations. SIAM Journal on Scientific Computing 21, 2126–2143.

Jiang, G.S., Shu, C.W., 1996. Efficient implementation of weighted ENO schemes. Journal of Computational Physics 126, 202–228.

Kamath, A., Alagan Chella, M., Bihs, H., Arntsen, Ø.A., 2015. Cfd simulations of wave propagation and shoaling over a submerged bar. Aquatic Procedia 4, 308–316.

Kjeldsen, S., Myrhaug, D., 1978. Kinematics and dynamics of breaking waves. River and Harbour Laboratory (NHL) The Norwegian Institute of Technology.

Kobayashi, N., Otta, A., Roy, I., 1987. Wave reflection and runup on rough slopes. Journal of Waterway, Port, Coastal and Ocean Engineering 3, 282–298.

Larsen, J., Dancy, H., 1983. Open boundaries in short wave simulations - a new approach. Coastal Engineering 7, 285–297.

Lemos, C.M., 1992. A simple numerical technique for turbulent flows with free surfaces. International Journal of Numerical Methods in Fluids 15, 127–146.

Lin, P., Liu, P.L.F., 1998. A numerical study of breaking waves in the surf zone. Journal of Fluid Mechanics 359, 239–264.

Morgan, G.C.J., Zang, J., Greaves, D., Heath, A., Whtilow, C.D., Young, J.R., 2010. Using the rasinterfoam CFD model for wave transformation and coastal modeling, in: Proc., Coastal Engineering Conference, Shanghai, China, pp. 1–9.

Naot, D., Rodi, W., 1982. Calculation of secondary currents in channel flow. Journal of the Hydraulic Division, ASCE 108, 948–968.

Osher, S., Sethian, J.A., 1988. Fronts propagating with curvature- dependent speed: algorithms based on Hamilton-Jacobi formulations. Journal of Computational Physics 79, 12–49.

Peng, D., Merriman, B., Osher, S., Zhao, H., Kang, M., 1999. A PDE-based fast local level set method. Journal of Computational Physics 155, 410–438.

Roeber, V., Cheung, K., Kobayashi, M., 2010. Shock-capturing boussinesq-type model for nearshore wave processes. Coastal Engineering 57, 407–423.

Stelling, G., Zijlema, M., 2003. An accurate and effcient fnite-difference algorithm for non-hydrostatic free-surface fow with application to wave propagation. International Journal for Numerical Methods in Fluids 43, 1–23.

Takikawa, K., Yamada, F., Matsumoto, K., 1997. Internal characteristics and numerical analysis of plunging breaker on a slope. Coastal Engineering 31, 143–161.

Tissier, M., Bonneton, P., Marche, F., Chazel, F., Lannes, D., 2012. A new approach to handle wave breaking in fully non-linear boussinesq models. Coastal Engineering 67, 54–66.

van der Vorst, H., 1992. BiCGStab: A fast and smoothly converging variant of Bi-CG for the solution of nonsymmetric linear systems. SIAM Journal on Scientific and Statistical Computing 13, 631–644.

Wilcox, D.C., 1994. Turbulence modeling for CFD. DCW Industries Inc., La Canada, California.

Zhao, Q., Armfield, S., Tanimoto, K., 2004. Numerical simulation of breaking waves by a multi-scale turbulence model. Coastal Engineering 51, 53–80.

Paper 5

Breaking Wave Interaction with a Vertical Cylinder and the Effect of Breaker Location

Kamath A., Alagan Chella M., Bihs H. and Arntsen Ø.A.
Submitted to *Ocean Engineering* 2015

Breaking Wave Interaction with a Vertical Cylinder and the Effect of Breaker Location

Arun Kamath[1], Mayilvahanan Alagan Chella, Hans Bihs, Øivind A. Arntsen

Department of Civil and Transport Engineering, Norwegian University of Science and Technology (NTNU), 7491 Trondheim, Norway

Abstract

The open-source CFD model REEF3D is used to simulate plunging breaking wave forces on a vertical cylinder. The numerical results are compared with data from the experiments carried out at the Large Wave Channel, Hannover, Germany to validate the model. Further, the location of the cylinder is changed so that the breaking wave impacts the cylinder at different stages of wave breaking and the resulting wave forces are evaluated. The different locations for the cylinder placement based on the breaker location are determined from the results obtained for the wave breaking process in a two-dimensional numerical wave tank. Maximum wave forces are found to occur when the breaking wave tongue impacts the cylinder just below the wave crest in all the cases simulated and the lowest wave forces are generally obtained when the wave breaks behind the cylinder. Several wave features such as the splashing on impact, the splitting and rejoining of the wave around the cylinder resulting in a chute-like jet formation are identified. The model provides a good representation of the breaking wave process and can be a useful tool to evaluate breaking wave forces on structures.

Keywords: breaking wave, wave forces, wave impact, vertical cylinder, Computational Fluid Dynamics, REEF3D

1. Introduction

A lot of research work has been carried out in the past on the evaluation of wave forces on structures exposed to waves due to their importance in coastal and offshore engineering. The wave forces on cylinders at higher KC numbers (KC > 2) and cylinder diameter to wavelength ratio $D/L < 0.2$ are generally determined using the Morison formula (Morison et al., 1950) to account for inertial and drag component of the wave forces using empirical force coefficients. In the case of breaking wave forces, Morison formula cannot be directly applied because

[1]Corresponding Author, Email: arun.kamath@ntnu.no, Ph: (+47) 73 59 46 40, Fax: (+47) 73 59 70 21

breaking waves are associated with impact forces of very high magnitudes acting over a short duration. In order to describe the total force from breaking waves with the Morison equation, an impact force term is considered in addition to the quasi-static forces (Goda et al., 1966). Present knowledge concerning the breaking wave forces is gained from experiments by Goda et al. (1966), Wienke and Oumeraci (2005), Arntsen et al. (2011) to name a few, but the measurement of velocity and acceleration under breaking waves and their interaction with structures is very demanding. The theoretical description of the impact force involves the use of several parameters such as slamming coefficients, curling factor, breaker shape and wave kinematics at breaking which have to be determined experimentally. Previous studies on breaking wave forces such as Chan and Melville (1988), Bullock et al. (2007), Wienke and Oumeraci (2005) have indicated that breaking wave impact characteristics depend on several parameters such as the depth inducing breaking, breaker type and the distance of the structure from the breaker location.

The modelling of breaking waves in shallow waters is challenging due to the complex nature of the physical processes including highly non-linear interactions. A considerable amount of numerical studies have been attempted to model wave breaking over plane slopes (Lin and Liu, 1998; Zhao et al., 2004; Alagan Chella et al., 2015b). These studies have helped extend the knowledge regarding breaking wave characteristics and the geometric properties of breaking waves. The quantification of these breaking wave parameters are an important input to improve the empirical coefficients used for the evaluation of breaking wave forces. Though many extensive numerical studies exist in current literature that study the wave breaking process, not many have been extended to study the forces due to breaking waves and the effect of breaker types on the wave forces. Bredmose and Jacobsen (2010) studied breaking wave impact forces due to focussed waves with the Jonswap wave spectrum for input and carried out computations for half the domain assuming lateral symmetry of the problem using OpenFOAM. Mo et al. (2013) measured and modelled solitary wave breaking and its interaction with a slender cylinder over a plane slope for a single case using the filtered Navier-Stokes equations with large eddy simulation (LES) turbulence modeling, also assuming lateral symmetry and showed that their numerical model sufficiently captured the important flow features. Choi et al. (2015) investigated breaking wave impact forces on a vertical cylinder and two cases of inclined cylinders for one incident wave using the modified Navier-Stokes equations with the volume of fluid (VOF) method for interface capturing to study the dynamic amplification factor due to structural response.

The study of breaking wave forces using computational fluid dynamics (CFD) can provide a very detailed description of the physical processes as the fluid physics are calculated with few assumptions. With high-order discretization schemes for the convection and time advancement, sharp representation of the free surface and tight velocity-pressure coupling in the model, the wave transformation, wave hydrodynamics and flow features can be represented very accurately and in a realistic manner. In the complex case of breaking wave interaction with structures, CFD simulations can be used to capture the details of the flow field that are challenging to capture in experimental studies due to various factors including cost, instrumentation and structural response. Different wave loading scenarios can be analysed as the breaker locations are easier to analyse and maintain in the simulations.

In the current study, the open source CFD model REEF3D (Alagan Chella et al., 2015b) is used to simulate periodic breaking wave forces on a slender cylinder in a three-dimensional wave tank without assuming lateral symmetry. The model has been previously used to simulate the wave breaking process under different conditions (Alagan Chella et al., 2015a,b) and the wave breaking kinematics were fully represented including the motion of the jet, air pocket formation and the reconnection of the jet with the preceding wave trough. The model provides a detailed representation of the free surface and is numerically stable for various problems related to wave hydrodynamics. It is fully parallelised, has shown very good scaling on the high performance computing system at NTNU provided by NOTUR (2012) and can be used to carry out complex simulations efficiently on a large number of processors.

This paper presents the breaking wave interaction with a vertical cylinder. Three different wave heights are simulated and the evolution of wave breaking over a $1:10$ slope is studied using two-dimensional simulations. The locations for the placement of the cylinder to investigate five different wave loading cases based on Irschik et al. (2002) are identified from these two-dimensional studies. Next, the wave forces in the different scenarios for the three different incident wave heights are evaluated in a three-dimensional numerical wave tank. The numerical model is validated by comparing the calculated wave forces and the free surface with experimental data from experiments carried out in the Large Wave Channel (GWK), Hannover, Germany. The wave interaction with the vertical cylinder in selected two different scenarios is investigated and the effect of the cylinder placement with respect to the breaker location on the free surface features is presented.

2. Numerical Model

The open-source CFD model REEF3D solves the fluid flow problem using the incompressible Reynolds-Averaged Navier-Stokes (RANS) equations along with the continuity equation:

$$\frac{\partial u_i}{\partial x_i} = 0 \tag{1}$$

$$\frac{\partial u_i}{\partial t} + u_j \frac{\partial u_i}{\partial x_j} = -\frac{1}{\rho}\frac{\partial p}{\partial x_i} + \frac{\partial}{\partial x_j}\left[(\nu + \nu_t)\left(\frac{\partial u_i}{\partial x_j} + \frac{\partial u_j}{\partial x_i}\right)\right] + g_i \tag{2}$$

where u is the velocity averaged over time t, ρ is the fluid density, p is the pressure, ν is the kinematic viscosity, ν_t is the eddy viscosity and g is the acceleration due to gravity.
The pressure is determined using Chorin's projection method (Chorin, 1968) and the resulting Poisson pressure equation is solved with a preconditioned BiCGStab solver (van der Vorst, 1992). Turbulence modeling is handled using the two-equation $k - \omega$ model proposed by Wilcox (1994), where the transport equations for the turbulent kinetic energy, k and the specific turbulent dissipation rate, ω are:

$$\frac{\partial k}{\partial t} + U_j \frac{\partial k}{\partial x_j} = \frac{\partial}{\partial x_j}\left[\left(\nu + \frac{\nu_t}{\sigma_k}\right)\frac{\partial k}{\partial x_j}\right] + P_k - \beta_k k\omega \tag{3}$$

$$\frac{\partial \omega}{\partial t} + U_j \frac{\partial \omega}{\partial x_j} = \frac{\partial}{\partial x_j}\left[\left(\nu + \frac{\nu_t}{\sigma_\omega}\right)\frac{\partial \omega}{\partial x_j}\right] + \frac{\omega}{k}\alpha P_k - \beta\omega^2 \tag{4}$$

$$\nu_t = \frac{k}{\omega} \tag{5}$$

where, P_k is the production rate and closure coefficients $\sigma_k = 2$, $\sigma_\omega = 2$, $\alpha = 5/9$, $\beta_k = 9/100$, $\beta = 3/40$.

The highly strained flow due to the propagation of waves in the tank results in an overproduction of turbulence in the numerical wave tank as the eddy viscosity is determined from the strain in the convective terms. The Bradshaw et al. (1967) assumption is used to limit the eddy viscosity as shown by Durbin (2009):

$$\nu_t \leq \sqrt{\frac{2}{3}}\frac{k}{|\mathbf{S}|} \tag{6}$$

where $\mathbf{S}$ stands for the source terms in the transport equations. In a two-phase CFD model, the large difference between the density of air and water leads to a large strain at the interface,

which leads to an overproduction of turbulence at the free surface. In reality, the free surface is a boundary at which eddy viscosity is damped naturally. The standard $k-\omega$ model does not account for this and the specific turbulence dissipation at the free surface is defined using the empirical relationship presented by Naot and Rodi (1982) is used at the interface.

The discretization of the convective terms of the RANS equations are discretized using the fifth-order conservative finite difference Weighted Essentially Non-Oscillatory (WENO) scheme (Jiang and Shu, 1996). The Hamilton-Jacobi formulation of the WENO scheme (Jiang and Peng, 2000) is used to discretize the level set function ϕ, turbulent kinetic energy k and the specific turbulent dissipation rate ω. The WENO scheme is a minimum third-order accurate in the presence of large gradients and provides the accuracy required to model complex free surface flows. The time advancement of the momentum equation, the level set function and the reinitialisation equation is treated with a Total Variation Diminishing (TVD) third-order Runge-Kutta explicit time scheme (Shu and Osher, 1988). The Courant-Frederick-Lewis (CFL) criterion is maintained at a constant value throughout the simulation using an adaptive time stepping strategy to determine the time steps. A first-order implicit scheme for the time advancement of k and ω removes the large source term contributions from these variables for the evaluation of the CFL criterion. This is reasonable, as these variables are largely driven by source terms and have a low influence from the convective terms. The diffusion terms of the velocities are also handled using an implicit scheme, removing them from the CFL criterion and the maximum velocities in the domain are used to determine the time steps to maintain the numerical stability of the simulation.

The model uses a Cartesian grid for spatial discretization and high-order finite difference schemes can be implemented in a straight forward manner. A ghost cell immersed boundary method (GCIBM) (Berthelsen and Faltinsen, 2008) is used to account for the complex geometric solid-fluid boundaries. The code is fully parallelised using the MPI library and the numerical model can be executed on high performance computing systems with very good scaling.

2.1. Level Set Method

The level set method (Osher and Sethian, 1988) is an interface capturing method in which the the zero level set of a signed distance function, $\phi(\vec{x},t)$ represents the interface between two phases. For the rest of the domain, $\phi(\vec{x},t)$ gives the closest distance of each point in the domain from the interface and the sign distinguishes the two phases across the interface. The

level set function is continuous across the interface and is defined as:

$$\phi(\vec{x},t)\begin{cases} > 0 & if\ \vec{x}\ is\ in\ phase\ 1 \\ = 0 & if\ \vec{x}\ is\ at\ the\ interface \\ < 0 & if\ \vec{x}\ is\ in\ phase\ 2 \end{cases} \tag{7}$$

The level set function provides a sharp representation of the interface. A partial differential equation based reinitialisation procedure presented by Peng et al. (1999) is used to maintain the signed distance property of the function, which can be lost on convecting the function under an external velocity field.

2.2. Numerical Wave Tank

The two-dimensional numerical wave tank has symmetry conditions on the side walls and the top of the tank. The bottom wall of the tank and boundaries of objects placed in the tank are treated with a no-slip or wall boundary condition. In a three-dimensional wave tank, the side walls are also subjected to wall boundary conditions. Wave generation is handled using the relaxation method (Larsen and Dancy, 1983), with the relaxation function presented by Jacobsen et al. (2012):

$$\Gamma(x) = 1 - \frac{e^{(1-x)^{3.5}} - 1}{e - 1} \tag{8}$$

where $\Gamma(x)$ is the relaxation function and $x \in [0,1]$ is the length scale along the relaxation zone and ensures a smooth transition of the still water to a wave. The relaxation function also absorbs any waves reflected from the objects placed in the wave tank, travelling towards the wave generation zone. This prevents the reflected waves from affecting the wave generation and simulates a wave generator with active absorption. The numerical beach is implemented using the active absorbing beach formulated by Schäffer and Klopman (2000).

3. Results and Discussion

3.1. Setup for the numerical simulations

The experiments (Irschik et al., 2002) at the Large Wave Channel (GWK), Hannover are carried out in a wave channel 309 m long, 5 m wide and 7 m high with a 23 m long 1 : 10 slope reaching a height of 2.3 m placed at 180 m from the wavemaker. A flat bed extends from the end of slope with a height of 2.3 m. A vertical cylinder of diameter $D = 0.7$ m is placed with its central axis at the top of the slope and incident waves with heights H between

$1.15 - 1.60$ m and periods T between $4.0 - 9.0$ s are generated. In the current study, the case with incident wave period $T = 4.0$ s, wave height $H_B = 1.30$ m and water depth $d = 3.8$ m presented in Choi et al. (2015) is chosen for comparison with the numerical results. The three-dimensional numerical wave tank is 54 m long, 5 m wide and 7 m high with a grid size of $dx = 0.05$ m resulting a total of 15.12 million cells. In order to study the wave breaking process for the different cases simulated in the study, a two-dimensional wave tank with the same dimensions is used as illustrated in Fig. (1). Waves with incident wave steepnesses $H_0/L_0 = 0.070, 0.063, 0.059$, corresponding to wave heights of $H_A = 1.44$ m, $H_B = 1.30$ m and $H_C = 1.23$ m are generated to study the breaking wave forces on a vertical cylinder.

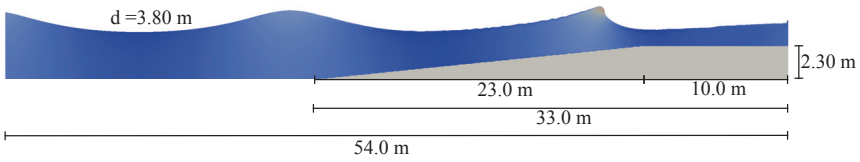

Figure 1: Dimensions of the two-dimensional numerical wave tank to determine breaking wave characteristics

3.2. Breaking wave characteristics

The process of wave breaking for incident waves with period $T = 4.0$ s, wavelength $L = 20.5$ m and heights $H_A = 1.44$ m $H_B = 1.30$ m and $H_C = 1.23$ m is studied in a two-dimensional wave tank to identify the various stages of wave breaking. The results are used to select the locations to place the cylinder in order to analyse the effect of the wave breaker location on the wave force acting on the cylinder.

Figure (2) depicts the free surface deformation and the evolution of the overturning wave crest of the plunging breaking waves produced over the slope along with the horizontal velocity contours for $H_B = 1.30$ m. As a result of wave shoaling over the slope, the wave crest becomes steeper and the wave crest approaches a near-vertical profile in Fig. (2a). Due to increasing water particle velocities at the wave crest and reducing particle velocities towards the bed, the wave becomes asymmetrical and a part of the wave crest develops into an overturning crest seen in Fig. (2b). On further propagation, the overturning crest develops into a plunging jet which impinges the preceding wave trough, creating an air pocket, splash-up and secondary waves shorewards. The breaking characteristics vary depending on the incident wave characteristics, which determine the size and flow features of the overturning wave crest

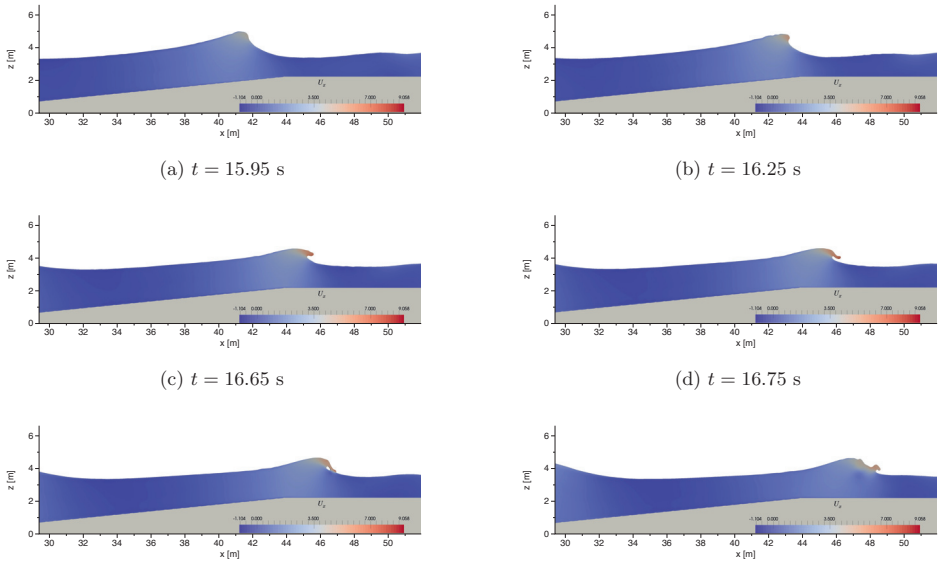

(a) $t = 15.95$ s (b) $t = 16.25$ s

(c) $t = 16.65$ s (d) $t = 16.75$ s

(e) $t = 16.90$ s (f) $t = 17.25$ s

Figure 2: Evolution of the breaking wave for $H_B = 1.30$ m with horizontal velocity contours

as seen in Figs. (2d-2f).

Similarly, simulations are carried out for incident waves with $H_A = 1.44$ m and $H_C = 1.23$ m and $T = 4.0$ s. It is observed that the breaker location moves shorewards as the incident wave height is reduced. The breaking locations for H_A, H_B and H_C are identified to be $x_b = 42.10$m, 43.65 m and 43.85 m with breaking heights of $h_b = 1.55$ m, 1.44 m and 1.32 m respectively. The information regarding the breaking process obtained from the two-dimensional simulations is used in further sections to determine the cylinder placement location to investigate various wave loading scenarios.

3.3. Validation of the numerical model for breaking wave force calculation

The numerical results for breaking wave forces and the free surface elevation along the frontline of the cylinder ($x = 43.65$ m) near the tank wall for $H_B = 1.30$ m are compared to the experimental data to validate the numerical model. The cylinder is placed with its axis at the top of the slope ($x = 44.00$ m), such that the front surface of the cylinder is directly at the breaking point and the vertical breaking wave crest impacts the cylinder front surface. A grid size of $dx = 0.05$ m is used. The filtered and Empirical Mode Decomposition (EMD)-treated experimental data from the experiments carried out at GWK, Hannover (Irschik et al., 2002),

presented by Choi et al. (2015) is used for the comparison with the numerical results for the wave force. Figure (3a) shows that the numerical model provides a good prediction of the breaking wave force and the calculated wave force is consistent over several wave periods. Since the wave impact is very sensitive to the wave breaking location, the consistent results indicate that the model simulates successive breaking waves at the same location consistently. The numerically calculated free surface elevation along the frontline of the cylinder at $x = 43.65$ m also presents a good agreement with the experimental data in Fig. (3b) showing that the model provides a good representation of the wave propagation in the wave tank.

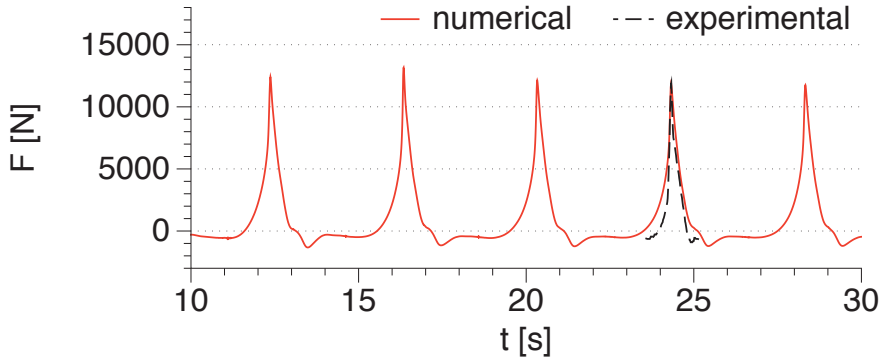

(a) wave force on the cylinder

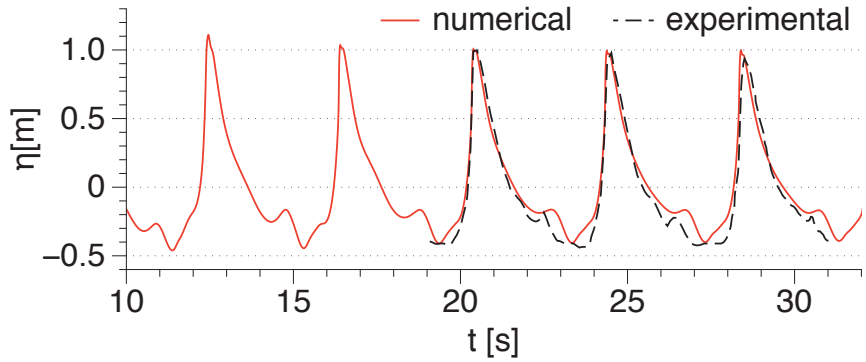

(b) free surface elevation at the tank wall, along the frontline of the cylinder

Figure 3: Comparison of numerical results with experimental data

A grid convergence study is carried out by repeating the above simulation with grid sizes of $dx = 0.20$ m, 0.15 m, 0.10 m and compared to the results at $dx = 0.05$ m and experimental

data for the wave force in Fig. (4). The results in Fig. (4a) show that the numerical values for the wave force converge to the experimental value at $dx = 0.05$ m, confirming the choice of the grid for the study. Figure (4b) shows the free surface elevation evaluated for the different grid sizes and for $dx = 0.15$ m and 0.20 m, neither the breaking location nor the vertical breaking crest is represented with sufficient accuracy. The wave forces calculated at these grid sizes is subsequently much lower as seen in Fig. (4a). At a grid size of $dx = 0.10$ m, the free surface differs slightly with regards to the breaking wave height but the corresponding difference in the calculated wave force is large. The vertical profile of the wave crest at breaking and the breaker location at $t = 24.2$ s is best represented by $dx = 0.05$ m. From the grid convergence studies, the grid size $dx = 0.05$ m is selected for all the simulations in this study.

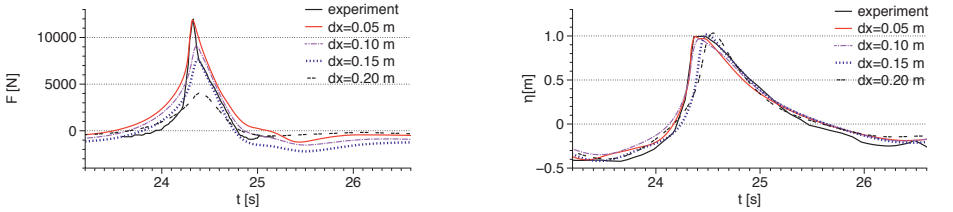

(a) calculated wave force

(b) calculated free surface elevation at $x = 43.65$ m

Figure 4: Grid convergence study for wave forces and free surface elevation near the wall along the frontline of the cylinder

3.4. Influence of cylinder location with respect to the breaker location

From the study about the breaking wave process for the three incident waves in section 3.2, five different locations at different stages of wave breaking are selected, similar to the loading cases identified in Irschik et al. (2002), as follows:

1. the wave breaks behind the cylinder, the crest is not yet vertical at impact.
2. the wave breaks exactly on the cylinder, the crest is vertical at impact.
3. the wave breaks just in front of the cylinder, the breaker tongue impacts the cylinder at crest level
4. the wave breaks in front of the cylinder, the breaker tongue impacts the cylinder slightly below the crest level
5. the wave breaks much before the cylinder, the breaker tongue impacts the cylinder much below the crest level.

The different scenarios are illustrated in Fig. (5) using case A with incident height $H_A = 1.44$ m as an example. An overview of the simulations carried out for the three different incident heights and the five different wave impact scenarios is listed in Table (1).

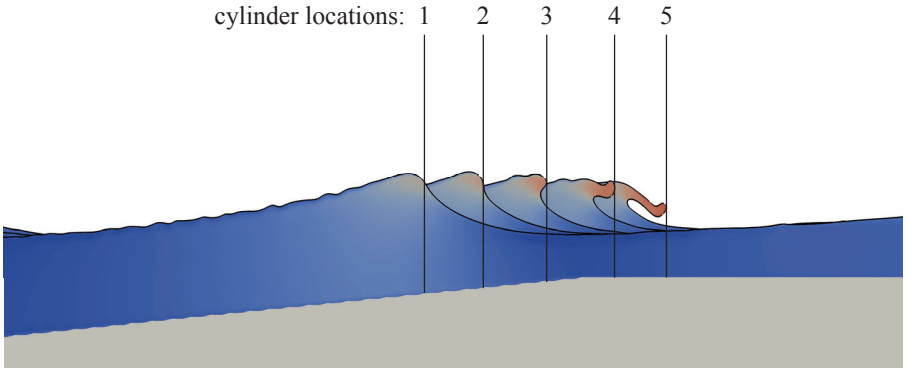

Figure 5: Location of the cylinder front surface for various wave loading cases

No.	H (m)	h_b (m)	x_b (m)	Cylinder axis (m)	Impact scenario
A1	1.44	1.55	42.10	40.95	before breaking
A2				42.45	vertical wave crest impact
A3				42.75	breaker tongue at crest level
A4				44.85	breaker tongue just below crest level
A5				46.25	breaker tongue much below crest level
B1	1.30	1.44	43.65	42.70	before breaking
B2				44.00	vertical wave crest impact
B3				44.60	breaker tongue at crest level
B4				46.35	breaker tongue just below crest level
B5				47.35	breaker tongue much below crest level
C1	1.23	1.32	43.85	42.85	before breaking
C2				44.20	vertical wave crest impact
C3				45.15	breaker tongue at crest level
C4				46.60	breaker tongue just below crest level
C5				47.85	breaker tongue much below crest level

Table 1: Overview of the simulations carried out to investigate the effect of different breaking wave impact scenarios

The calculated wave force on the cylinder in the different wave impact scenarios A1-A5 is presented in Fig. (6). The highest wave force $F = 16400$ N is calculated for scenario A4, where the breaker tongue impacts the cylinder just below the wave crest level. The lowest wave force $F = 11000$ N is calculated in scenario A1, where the wave breaks behind the cylinder. A small secondary force peak appears in scenario A5 representing the second impact from the wave crest behind the breaker tongue. Due to the small change of 0.3 m in the cylinder location between scenarios A2 and A3 and forces peaks in these two cases appear very close to each other and a slight difference is seen in the force magnitudes. The lowest force in this case in scenario A1 is about 33% lower than the highest force calculated in A4.

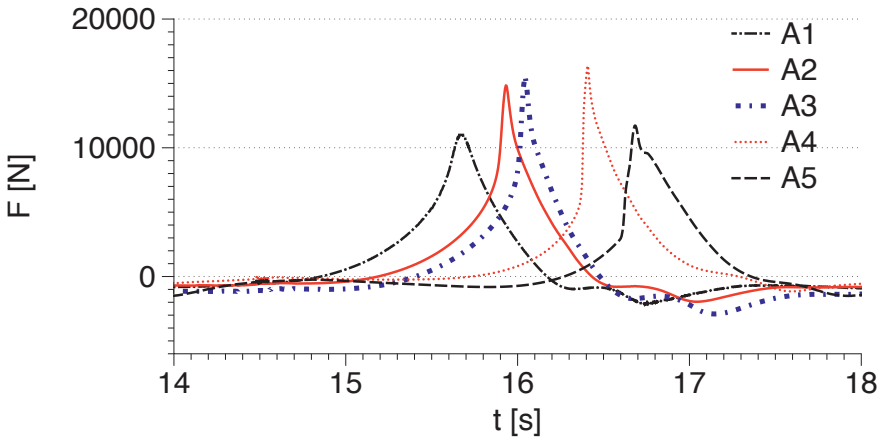

Figure 6: Calculated wave forces for $H_A = 1.44$ m for different wave impact scenarios

The wave forces calculated in scenarios B1-B5 is presented in Fig. (7) and the highest wave force is calculated for scenario B4 with $F = 14000$ N. The lowest force in this scenario is calculated for scenario B5 where the breaker tongue impacts the cylinder much below the wave crest level. A double peak in the force due to the first impact of the breaker tongue and the second impact of the wave crest is also clearly recognised for scenario B5. The wave forces calculated in scenarios B2 and B3 are similar, with a slightly higher force for B3. The wave force in scenario B1 with $F = 9800$ N is similar to scenario B5 with $F = 9400$ N. The lowest force calculated in B5 is about 33% lower than the highest force calculated in B4.

Figure (8) presents the wave forces calculated in scenarios C1-C5 with the highest force calculated in scenario C4 with $F = 12350$ N and the lowest force $F = 8380$ N for scenario C1. The difference between the highest and the lowest wave forces is 3970 N with about

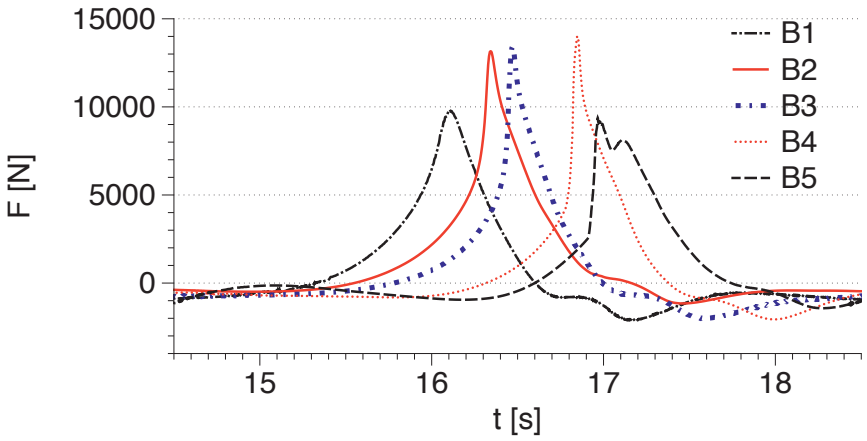

Figure 7: Calculated wave forces for $H_B = 1.30$ m for different wave impact scenarios

32% lower force in C1 compared to C4. The wave forces in the other scenarios simulated show a similar trend to that seen in the other two cases, where the wave force reduces as the cylinder is moved towards the wavemaker or towards the beach from the location resulting in the maximum wave force.

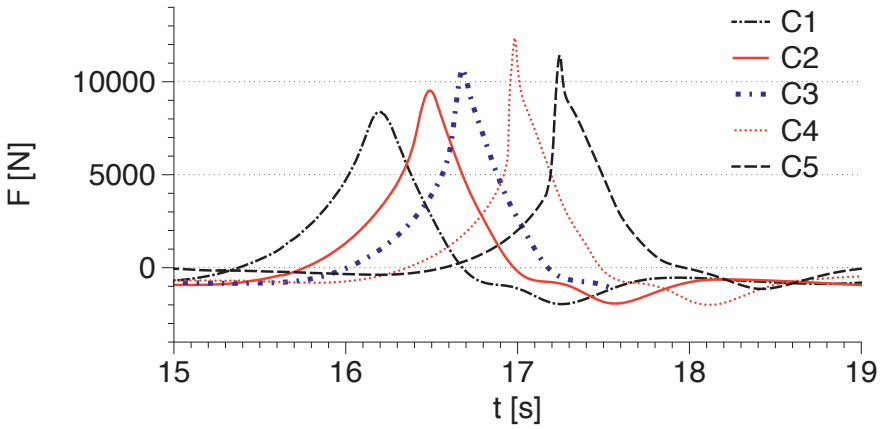

Figure 8: Calculated wave forces for $H_C = 1.23$ m for different wave impact scenarios

The results for the wave forces on the cylinder in the different scenarios for different wave heights show that the maximum force is obtained in wave impact scenario 4, where the breaker tongue impacts the cylinder just below the wave crest. The lowest breaking wave

force is generally obtained when the wave impacts the cylinder before its breaking point in scenario 1. These findings are in agreement with previous studies for focussed waves and periodic waves (Wienke et al., 2000; Irschik et al., 2002).

In order to obtain more insight into the difference in the physical free surface features in two varying wave impact scenarios, the breaking wave interaction with the cylinder in B2 and B5 are presented and the free surface features are discussed. Figure (9) presents the interaction process for scenario B2, where the wave impacts the cylinder at the breaker location with both isometric view of the tank and the top view around the cylinder. The vertical wave crest profile incident on the cylinder front surface is seen in Fig. (9a). The wave crest begins to overturn as it passes the cylinder in Figs. (9c). The separation of the incident wavefront by the cylinder and the generation of semi-circular waves meeting in the shadow zone behind the cylinder is seen in Fig. (9d). The meeting of the semi-circular wavefronts behind the cylinder and the formation of a chute-like jet is seen in Fig. (9f). The chute-like jet originates in the region of low horizontal velocities behind the cylinder and has a maximum horizontal velocities at the tip, where it meets the broken wave crest. Figure (9g) shows the fully developed chute-like jet and is seen to extend up to just behind the broken wave crest in Fig. (9h). The chute-like jet appears after the peak force is observed for the cylinder and thus may not have a significant effect on the forces experienced by the cylinder. The importance of the chute-like jet may be more apparent in the case of neighboring cylinders placed in the zone of influence of the chute-like jet behind the first cylinder. The chute-like jet can lead to a large wave run-up on the downstream cylinder. It can also result in interaction effects between the cylinders based on the distance between the two cylinders, influencing the wave forces on both cylinders.

Wave impact scenario B5 presented in Fig. (10) shows the interaction of a broken wave with the cylinder. The highly curled breaker tongue impacts the cylinder much below the wave crest level in Fig. (10a). Figure (10c) shows the separation of the incident wavefront. The formation of semi-circular wavefronts meeting behind the cylinder is absent in Fig. (10d). The broken wave separated around the cylinder propagates further with a region of low velocity in the shadow region behind the cylinder in Fig. (10e). There are no major free surface features at this stage in Fig. (10f). A mildly developed chute-like jet is seen in Fig. (10g) which is close to its collapse state and this weakly developed chute wave is seen to rejoin the free surface at some distance behind the broken wave crest in Fig. (10h).

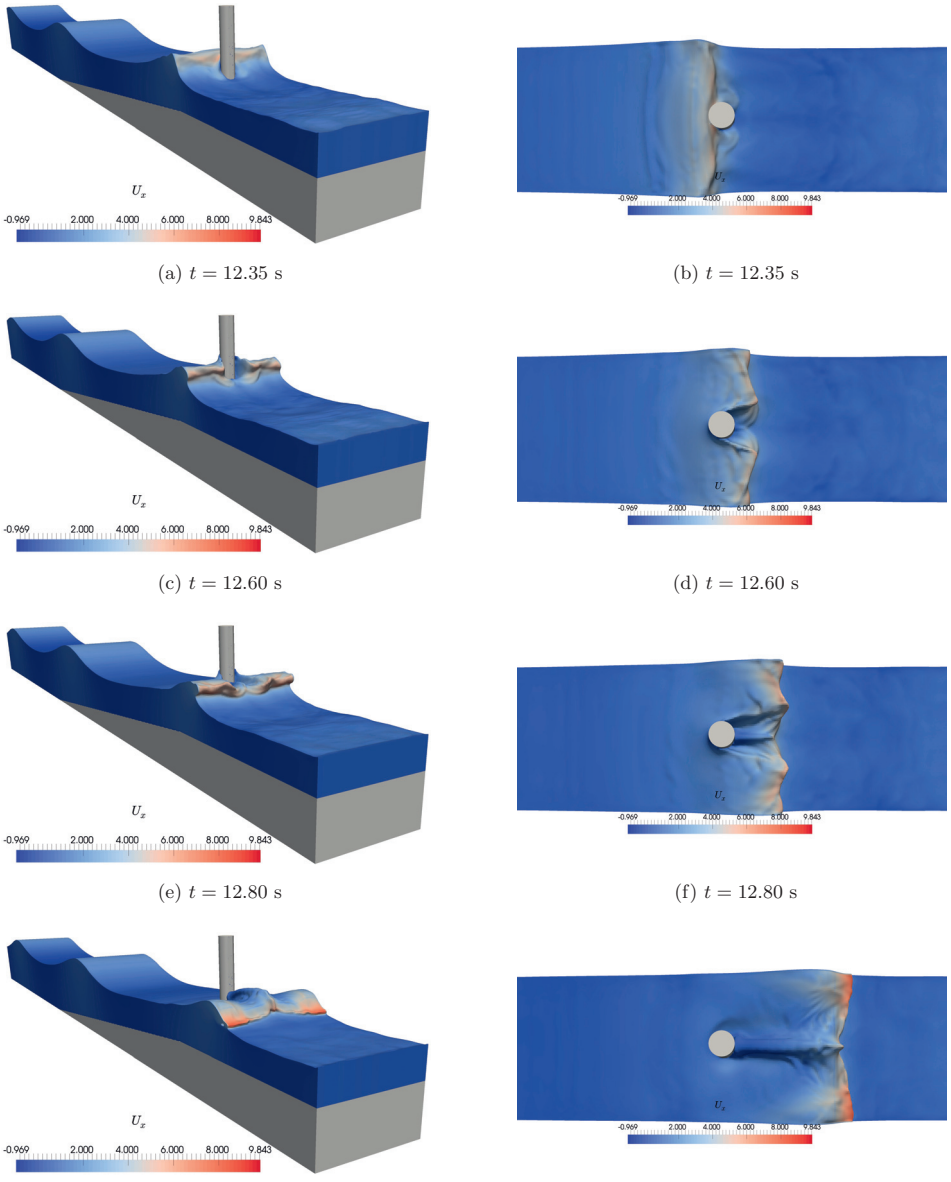

(a) $t = 12.35$ s (b) $t = 12.35$ s

(c) $t = 12.60$ s (d) $t = 12.60$ s

(e) $t = 12.80$ s (f) $t = 12.80$ s

(g) $t = 13.25$ s (h) $t = 13.25$ s

Figure 9: Isometric and corresponding top views of breaking wave interaction with the cylinder for $H_B = 1.30$ m for scenario B2

From the two different wave impact scenarios presented, the wave interaction process with the cylinder varies for the two cases in terms of free surface features and the velocities around

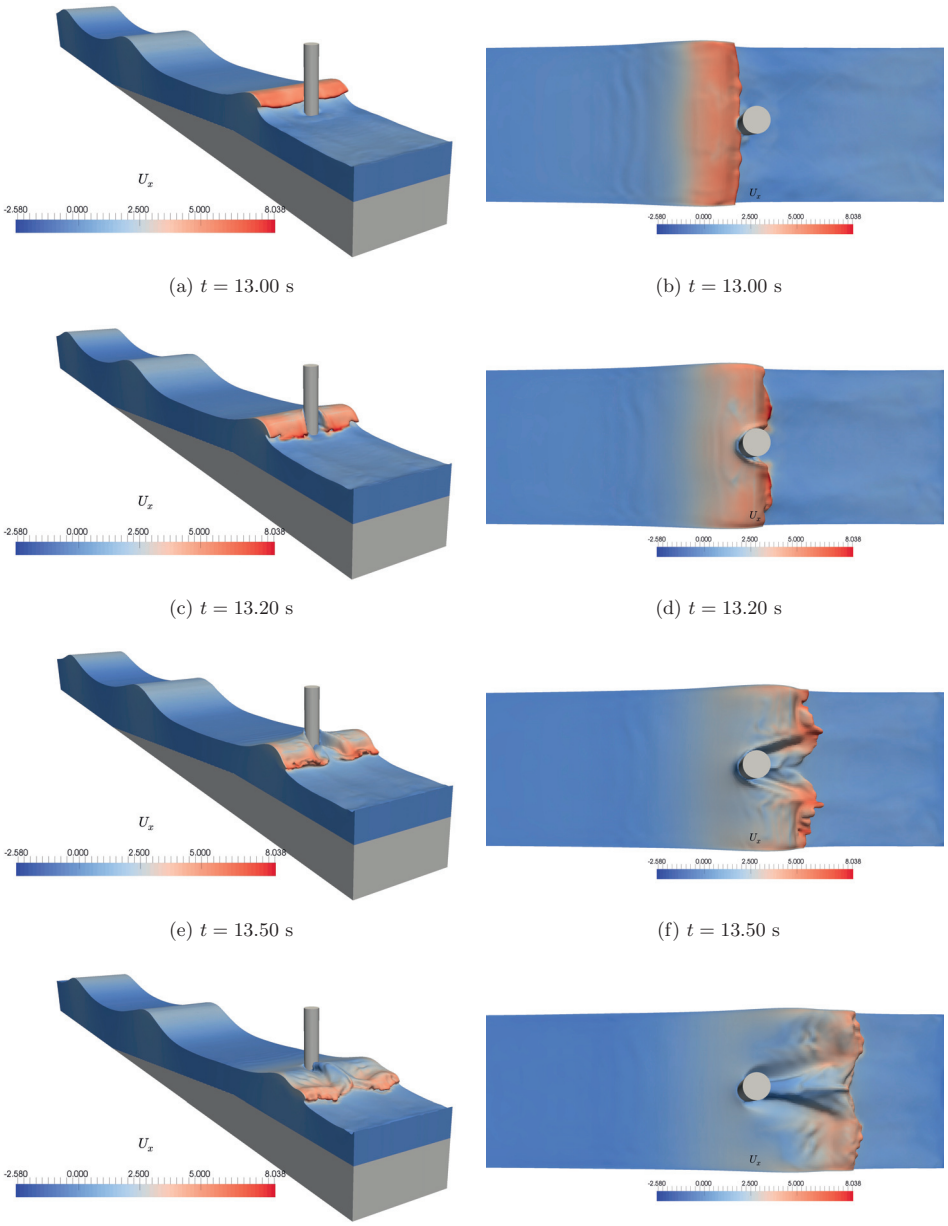

(a) $t = 13.00$ s (b) $t = 13.00$ s

(c) $t = 13.20$ s (d) $t = 13.20$ s

(e) $t = 13.50$ s (f) $t = 13.50$ s

(g) $t = 13.85$ s (h) $t = 13.85$ s

Figure 10: Isometric and corresponding top views of breaking wave interaction with the cylinder for $H_B = 1.30$ m for scenario B5

the cylinder. When the wave impacts the cylinder at its breaking point, in scenario B2, major free surface features are noticed in the shadow region behind the cylinder, with the development of a strong chute-like jet which extends up to the broken wave crest. Semi-circular waves are formed in front of the breaking wavefront around the cylinder, which meet in the shadow region and result in the chute-like jet. When the overturning wave impacts the cylinder with the breaker tongue much below the wave crest in scenario B5, the separation of the wavefront occurs without major free surface features in the region behind the cylinder. The chute-like jet is developed at a late stage is also seen to be weaker than in the previous scenario with regards to both the velocity of the chute tip and the length of extension.

4. Conclusions

The open-source CFD model REEF3D is used to simulate breaking wave interaction with a vertical cylinder. The effect of different incident wave heights and different wave impact scenarios for each incident wave height is studied by changing the location of the cylinder. The process of wave breaking is first studied using two-dimensional simulations. The cylinder locations for different wave impact scenarios are identified from these simulations. The numerical results for the wave force and the free surface elevation are compared to experimental data from large scale tests carried out at the Large Wave Channel, Hannover, Germany and a good agreement is obtained. The following conclusions can be drawn from the studies carried out in this study:

- Cylinder location with respect to the wave breaking location has a large influence on the wave forces exerted on the vertical cylinder. The highest force is seen in the case where the breaker tongue impacts the cylinder just below the wave crest level and the lowest force obtained when the wave breaks behind the cylinder.

- The difference between the highest and the lowest forces among the different scenarios evaluated for each incident wave is about $30\% - 33\%$.

- Different free surface features are observed in the different scenarios presented. The formation of a chute-like jet is seen in the shadow region behind the cylinder, where the wavefront split by the cylinder partly reunites. The chute-like jet is less developed and extends to a smaller distance when the wave impacts the cylinder at a later stage of breaking.

Acknowledgements

This study has been carried out under the OWCBW project (No. 217622/E20) and the authors are grateful to the grants provided by the Research Council of Norway. This study was supported in part with computational resources at the Norwegian University of Science and Technology (NTNU) provided by NOTUR, http://www.notur.no (NN2620K).

References

Alagan Chella, M., Bihs, H., Myrhaug, D., 2015a. Characteristics and profile asymmetry properties of waves breaking over an impermeable submerged reef. Coastal Engineering 100, 26–36.

Alagan Chella, M., Bihs, H., Myrhaug, D., Muskulus, M., 2015b. Breaking characteristics and geometric properties of spilling breakers over slopes. Coastal Engineering 95, 4–19.

Arntsen, Ø.A., Ros, X., Tørum, A., 2011. Impact forces on a vertical pile from plunging breaking waves, in: Coastal Structures.

Berthelsen, P.A., Faltinsen, O.M., 2008. A local directional ghost cell approach for incompressible viscous flow problems with irregular boundaries. Journal of Computational Physics 227, 4354–4397.

Bradshaw, P., Ferriss, D.H., Atwell, N.P., 1967. Calculation of boundary layer development using the turbulent energy equation. Journal of Fluid Mechanics 28, 593–616.

Bredmose, H., Jacobsen, N.G., 2010. Breaking wave impacts on offshore wind turbine foundations: focused wave groups and CFD. Proc., 29th International Conference on Ocean, Offshore and Arctic Engineering, Shanghai, China .

Bullock, G.N., Obhrai, C., Peregrine, D.H., Bredmose, H., 2007. Violent breaking wave impacts. part 1: Results from large-scale regular wave tests on vertical and sloping walls. Coastal Engineering 54, 602–617.

Chan, E.S., Melville, W.K., 1988. Deep-water plunging wave pressures on a vertical plane wall, in: Proc. of the Royal Society of London. A. Mathematical and Physical Sciences, pp. 95–131.

Choi, S.J., Lee, K.H., Gudmestad, O.T., 2015. The effect of dynamic amplification due to a structure s vibration on breaking wave impact. Ocean Engineering 96, 8–20.

Chorin, A., 1968. Numerical solution of the Navier-Stokes equations. Mathematics of Computation 22, 745–762.

Durbin, P.A., 2009. Limiters and wall treatments in applied turbulence modeling. Fluid Dynamics Research 41, 1–18.

Goda, Y., Haranaka, S., Kitahata, M., 1966. Study on impulsive breaking wave forces on piles. Report Port and Harbour Technical Research Institute 6, 1–30.

Irschik, K., Sparboom, U., Oumeraci, H., 2002. Breaking wave characteristics for the loading of a slender pile, in: Proc. 28*th* International Conference on Coastal Engineering.

Jacobsen, N.G., Fuhrman, D.R., Fredsøe, J., 2012. A wave generation toolbox for the open-source CFD library: OpenFOAM. International Journal for Numerical Methods in Fluids 70, 1073–1088.

Jiang, G.S., Peng, D., 2000. Weighted ENO schemes for Hamilton-Jacobi equations. SIAM Journal on Scientific Computing 21, 2126–2143.

Jiang, G.S., Shu, C.W., 1996. Efficient implementation of weighted ENO schemes. Journal of Computational Physics 126, 202–228.

Larsen, J., Dancy, H., 1983. Open boundaries in short wave simulations - a new approach. Coastal Engineering 7, 285–297.

Lin, P., Liu, P.L.F., 1998. A numerical study of breaking waves in the surf zone. Journal of Fluid Mechanics 359, 239–264.

Mo, W., Jensen, A., Liu, P.L.F., 2013. Plunging solitary wave and its interaction with a slender cylinder on a sloping beach. Ocean Engineering 74, 48–60.

Morison, J.R., O'Brien, M.P., Johnson, J.W., Schaaf, S.A., 1950. Force exerted by surface waves on piles. Journal of Petroleum Technology 2, 149–154.

Naot, D., Rodi, W., 1982. Calculation of secondary currents in channel flow. Journal of the Hydraulic Division, ASCE 108, 948–968.

NOTUR, 2012. The Norwegian Metacenter for Computational Science. http://www.notur.no/hardware/vilje .

Osher, S., Sethian, J.A., 1988. Fronts propagating with curvature- dependent speed: algorithms based on Hamilton-Jacobi formulations. Journal of Computational Physics 79, 12–49.

Peng, D., Merriman, B., Osher, S., Zhao, H., Kang, M., 1999. A PDE-based fast local level set method. Journal of Computational Physics 155, 410–438.

Schäffer, H.A., Klopman, G., 2000. Review of multidirectional active wave absorption methods. Journal of Waterway, Port, Coastal, and Ocean Engineering 126, 88–97.

Shu, C.W., Osher, S., 1988. Efficient implementation of essentially non-oscillatory shock capturing schemes. Journal of Computational Physics 77, 439–471.

van der Vorst, H., 1992. BiCGStab: A fast and smoothly converging variant of Bi-CG for the solution of nonsymmetric linear systems. SIAM Journal on Scientific and Statistical Computing 13, 631–644.

Wienke, J., Oumeraci, H., 2005. Breaking wave impact force on a vertical and inclined slender piletheoretical and large-scale model investigations. Coastal Engineering 52, 435–462.

Wienke, J., Sparboom, U., Oumeraci, H., 2000. Breaking wave impact on a slender cylinder, in: Coastal Engineering Conference, pp. 1787–1798.

Wilcox, D.C., 1994. Turbulence modeling for CFD. DCW Industries Inc., La Canada, California.

Zhao, Q., Armfield, S., Tanimoto, K., 2004. Numerical simulation of breaking waves by a multi-scale turbulence model. Coastal Engineering 51, 53–80.

Paper 6

Breaking Wave Interaction with Tandem Cylinders under Different Impact Scenarios

Bihs H., Kamath A., Alagan Chella M. and Arntsen Ø.A.
Submitted to *Journal of Waterway, Port, Coastal, and Ocean Engineering* 2015

Breaking wave interaction with tandem cylinders under different impact scenarios

Hans Bihs [1], Arun Kamath[1], Mayilvahanan Alagan Chella[1], and Øivind A. Arntsen[1]

ABSTRACT

The interaction of plunging breaking waves with a pair of cylinders placed in tandem is investigated using the open-source computational fluid dynamics (CFD) model REEF3D. The model is validated using experimental data for total wave forces and free surface for breaking wave interaction with a single cylinder. The wave interaction with the tandem cylinders is investigated for three different wave impact scenarios and three different distances between the cylinders in each scenario. The wave forces on the upstream cylinder are generally found to be equal to or less than the force on a single cylinder for the particular scenario. The force on the downstream cylinder is lower than the force on the upstream cylinder when the breaker tongue impacts the first cylinder. Under conditions where the breaker tongue impacts the downstream cylinder around the wave crest level, the wave force on the downstream cylinder is higher than the force on the upstream cylinder and also higher than the force on a single cylinder. The wave forces experienced by the tandem cylinders is highly influenced by the location of the breaking point with respect to the cylinders and the distance between the cylinders.

Keywords: breaking wave forces, vertical cylinder, CFD, computational fluid dynamics

INTRODUCTION

The evaluation of breaking wave forces on structures poses several challenges due to the complex air-water interaction, rapid free surface deformations and the impulsive nature of the force, with the peak impact force acting over a short duration of time. The

[1]Dept. of Civil and Transport Engineering., Norwegian University of Science and Technology, Trondheim, 7491, Norway. E-mail: hans.bihs@ntnu.no

Morison formula (Morison et al., 1950) which is generally used to evaluate wave forces on a cylinder for higher Keulegan-Carpenter numbers (KC$>$ 2) cannot be directly applied to evaluate breaking wave forces. Goda et al. (1966) proposed the use of an impact force term in addition to the quasi-static forces predicted by the Morison formula to evaluate breaking wave forces. The impact force depends on several breaking wave geometric and kinematic properties such as the shape of the wave and the distribution of water particle velocities under the wave (Wienke and Oumeraci, 2005). These properties are in turn influenced by parameters like the bottom slope and the incident wave height, making evaluation of breaking wave forces a challenging task.

Theoretical description of breaking waves is not possible without major simplifying assumptions (Cokelet, 1977). The current knowledge on breaking wave properties are mainly based on experimental investigations such as for deep water breaking waves by Kjeldsen and Myrhaug (1978), for wave breaking on a slope by Ting and Kirby (1996) and for wave breaking on a reef by Gourlay (1994), Blenkinsopp and Chaplin (2008). According to Christensen (1998), numerical modeling for breaking waves requires the evaluation of the physics with few assumptions like in computational fluid dynamics (CFD) models. Several authors have presented results for breaking wave kinematics using single-phase CFD models (Lin and Liu, 1998; Zhao et al., 2004). But a two-phase CFD model better resolves the breaking wave kinematics as shown by Jacobsen et al. (2012). In addition, results from Alagan Chella et al. (2015b) and Alagan Chella et al. (2015a) show that higher order discretization schemes for time and convection discretization, a tight velocity-pressure coupling and sharp representation of the free surface provide a realistic description of the breaking wave properties. These studies have advanced the knowledge in current literature regarding breaking wave properties.

In spite of the advances in the numerical modeling of breaking waves, the breaking wave forces have so far been studied mainly through experimental investigations such as Irschik et al. (2002), Irschik et al. (2004), Wienke and Oumeraci (2005), Arntsen et al. (2011). The measurement of the various parameters such as velocity and acceleration

during breaking is a challenging task. In addition, the breaking wave force depends on the location of the cylinder with respect to the breaking point (Chan and Melville, 1988; Bullock et al., 2007; Wienke and Oumeraci, 2005). The wave impact scenario for different distances of the cylinder surface from the breaking point is different and the assumption of instantaneous impact of the wave over the entire cylinder can also lead to errors in the evaluation of the wave force (Wienke et al., 2000). Apelt and Piorewicz (1986) carried out experiments to study the interference effects on breaking waves forces on groups of vertical cylinders and determined that the gap between the cylinders is important when the cylinders are placed along the direction of wave propagation.Sparboom et al. (2005) studied breaking wave forces on cylinder arrays due to freak waves and found that the breaking wave forces are reduced significantly along the array due to the sheltering effect of the upstream cylinders. In terms of numerical investigations into breaking wave forces, studies by Bredmose and Jacobsen (2010) using focussed waves with incident waves defined by the Jonswap spectrum and Mo et al. (2013) for solitary wave breaking using large eddy simulation (LES) turbulence modeling are notable works. Choi et al. (2015) presented results for breaking wave impact on a single cylinder in vertical and inclined configurations. There are no numerical studies in current literature investigating breaking wave forces on tandem cylinders, the effect of neighboring cylinders on the breaking wave forces on the cylinders along with the complex free surface deformations associated with the interaction.

The interaction of breaking waves with a cylinder involves several important free surface features such as run-up on the cylinder, the separation of the breaking wavefront around the cylinder and the meeting of the separated wavefront behind the cylinder leading to the formation of a water jet. The scenario is further interesting in the presence of neighboring cylinders, as is the case in coastal and offshore constructions. In this study, the open-source CFD model REEF3D (Alagan Chella et al., 2015b) is used to simulate breaking wave interaction with tandem cylinders placed at different distances from each other to study the influence of the clear distance between the cylinders on

the wave forces. In addition, three different wave impact scenarios on the first cylinder are also studied for each distance of separation. The numerical model is validated using experimental results from the Large Wave Flume (GWK) (Irschik et al., 2002) for breaking wave interaction with a single cylinder.

NUMERICAL MODEL

Governing equations

In the numerical wave tank REEF3D, the incompressible three-dimensional Reynolds-Averaged Navier-Stokes (RANS) equations are solved in conjunction with the continuity equation:

$$\frac{\partial u_i}{\partial x_i} = 0 \tag{1}$$

$$\frac{\partial u_i}{\partial t} + u_j \frac{\partial u_i}{\partial x_j} = -\frac{1}{\rho}\frac{\partial p}{\partial x_i} + \frac{\partial}{\partial x_j}\left[(\nu + \nu_t)\left(\frac{\partial u_i}{\partial x_j} + \frac{\partial u_j}{\partial x_i}\right)\right] + g_i \tag{2}$$

where u is the velocity, ρ is the density of the fluid, p is the pressure, ν is the kinematic viscosity, ν_t is the eddy viscosity and g the acceleration due to gravity.

The fifth-order conservative finite difference Weighted Essentially Non-Oscillatory (WENO) scheme proposed by Jiang and Shu (1996) is applied for the discretization of the convective terms of the RANS equation. Time advancement is carried out using a Total Variation Diminishing (TVD) third-order Runge-Kutta explicit time scheme (Shu and Osher, 1988). The time step size is controlled with adaptive time stepping based on the CFL criterion. This results in an optimal time step value for numerical stability and accuracy. The diffusion is treated with an implicit time scheme in order to remove it from the CFL criterion. The pressure is modeled with the projection method (Chorin, 1968). The Poisson equation for the pressure is solved with the preconditioned BiCGStab solver (van der Vorst, 1992). The domain decomposition strategy and MPI (Message Passing Interface) is used for parallelization. A Cartesian grid with

a staggered arrangement is used in the numerical model. Complex geometries are taken into account with the ghost cell immersed boundary method (Berthelsen and Faltinsen, 2008).

The k-ω model is employed for turbulence closure (Wilcox, 1994). Eddy viscosity limiters (Durbin, 2009) are used to control the overproduction of turbulence, often occurring in highly unsteady free surface flows. In addition, the fact that the turbulence length scales cannot pass the interface between water and air is considered with a free surface turbulence damping scheme (Naot and Rodi, 1982).

Free Surface

The complex wave hydrodynamics are modeled with a two-phase flow approach, calculating the flow for water and air. The interface between the two fluids is captured with the level set method (Osher and Sethian, 1988). The zero level set of the signed distance function $\phi(\vec{x}, t)$ represents the location of the free surface. With its signed distance property, it gives the shortest distance from the interface to all the points in the flow domain. Based on the sign of the level set function, the phases can be distinguished as follows:

$$\phi(\vec{x}, t) \begin{cases} > 0 & if\ \vec{x}\ is\ in\ phase\ 1 \\ = 0 & if\ \vec{x}\ is\ at\ the\ interface \\ < 0 & if\ \vec{x}\ is\ in\ phase\ 2 \end{cases} \tag{3}$$

The flow velocities calculated from Eq. (2) are used to convect the level set function:

$$\frac{\partial \phi}{\partial t} + u_j \frac{\partial \phi}{\partial x_j} = 0 \tag{4}$$

During the computation, reinitialization is carried out after every iteration using a partial differential equation Peng et al. (1999) in order to maintain the signed distance property of the level set function. The level set function is discretized with the

Hamilton-Jacobi formulation of the WENO scheme by Jiang and Peng (2000)

Wave generation and absorption

The numerical wave tank uses the relaxation method (Larsen and Dancy, 1983) for the wave generation. A relaxation function is used to moderate the velocity and the free surface using a wave theory in the relaxation zones with Eq. (5):

$$\begin{aligned} u_{relaxed} &= \Gamma(x) u_{analytical} + (1 - \Gamma(x)) u_{computational} \\ \phi_{relaxed} &= \Gamma(x) \phi_{analytical} + (1 - \Gamma(x)) \phi_{computational} \end{aligned} \tag{5}$$

where $\Gamma(x)$ is the relaxation function and $x \in [0, 1]$ is the x-coordinate scaled to the length of the relaxation zone. The relaxation function shown in Eq. (6) is used in the current numerical model (Jacobsen et al., 2012):

$$\Gamma(x) = 1 - \frac{e^{(1-x)^{3.5}} - 1}{e - 1} \tag{6}$$

In order to avoid reflections from the downstream boundary, an active wave absorption method is employed. Here, waves opposite to the reflected ones are generated, canceling out the reflections. Based on shallow water theory (Schäffer and Klopman, 2000), the following horizontal velocity is prescribed on the downstream boundary:

$$U(t) = -\sqrt{\frac{g}{h}}\, \xi(t) \tag{7}$$

where

$$\xi(t) = \eta(t) - h \tag{8}$$

Here, $\eta(t)$ is the actual free surface location along the downstream boundary and h the still water level. The method is applied in vertical strips along the downstream boundary, which are one grid cell wide. This way, different free surface elevations along the boundary can be taken into account (Higuera et al., 2013). Also, the handling of oblique waves is also implemented in the current model.

Numerical evaluation of wave forces

The breaking wave forces on the cylinders are calculated by integrating the pressure p and the surface normal component of the viscous shear stress tensor τ on the surface of the solid objects:

$$F = \int_{\Omega} (-\mathbf{n}p + \mathbf{n} \cdot \tau) d\Omega \tag{9}$$

where $\mathbf{n}$ is the unit normal vector pointing into the fluid and Ω is the surface of the object.

RESULTS AND DISCUSSION

Validation of the numerical model

The breaking wave force on a single vertical cylinder are calculated numerically and compared to experimental data to validate the numerical model. The experiments were carried out at the Large Wave Flume (GWK), Hannover, Germany (Irschik et al., 2002) on a vertical cylinder of diameter $D = 0.7$ m in a water depth of 3.80 m with incident waves of period $T = 4.0$ s. The cylinder is placed at the top of a 23 m long 1 : 10 slope, such that the still water depth at the cylinder is 1.50 m. In the numerical setup, the wave tank is 56 m long, 5 m wide and 7 m high with a grid size of $dx = 0.05$ m resulting in a total of 15.68 million cells. A cylinder with $D = 0.7$ m is placed with its center at 44.0 m and the incident waves of period $T = 4.0$ s break exactly on the front surface of the cylinder. The numerical setup is illustrated in Fig. (1). The numerically calculated wave force is compared to the EMD (Empirical

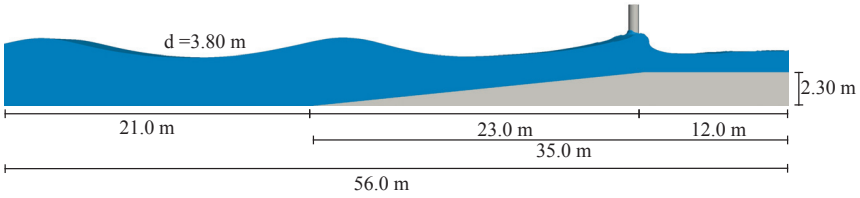

Fig. 1. Numerical wave tank setup used in the study

Mode Decomposition) treated experimental data from Choi et al. (2015) to filter out the dynamic amplification of the wave forces due to the vibration of the cylinder in Fig. (2a). A good agreement is seen between the numerical and experimental wave forces. The numerical results are also similar over several wave periods, showing that the numerical model predicts the the wave breaking location and consequently the breaking wave forces consistently. The free surface elevation near the wall along the frontline of the cylinder provides a representation of the wave incident on the cylinder. The comparison between numerical and experimental free surface shows a good agreement in Fig. (2b). The vertical wavefront in the figure shows that the wave breaks on the front surface of the cylinder.

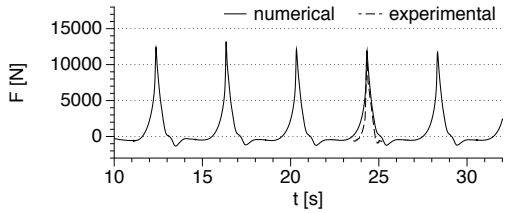

(a) wave force on the cylinder

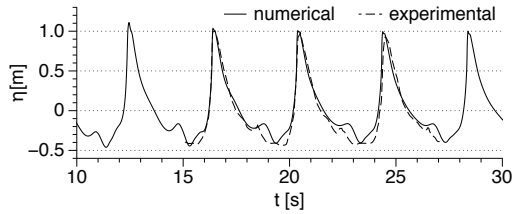

(b) free surface near the wall along the frontline of the cylinder

Fig. 2. Comparison of the numerical and experimental results

Effect of wave impact scenario and distance between tandem cylinders on the wave forces

The wave forces on tandem cylinders placed at different distances from each other are studied for different wave breaking scenarios. The different scenarios are determined

based on the location of the wave breaking point with respect to the front surface of the first cylinder. The scenarios considered in this study are:

- scenario A: breaker tongue impacts cylinder 1 just below the wave crest level
- scenario B: wave breaks exactly at cylinder 1 with a vertical wavefront
- scenario C: wave breaks behind cylinder 1

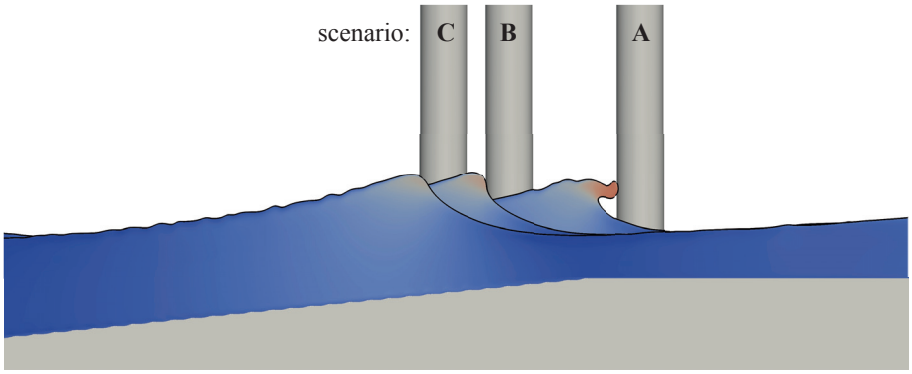

Fig. 3. Three different locations of cylinder 1 with respect to the wave breaking point considered in the study

The various scenarios are illustrated in Fig. (3). According to Irschik et al. (2002), scenario A and B result in the highest and the second highest total wave forces on a single cylinder respectively. The lowest wave forces are obtained in scenario C. The second cylinder is then placed with clear distances of $S = 1D$, $S = 2D$ and $S = 3D$ from the first cylinder. The resulting 9 different cases are listed in Table (1) along with the numerical force calculated for a single cylinder for each of the wave breaking scenarios, F_0.

The breaking wave forces calculated in scenario A, where the breaker tongue impacts cylinder 1 just below the wave crest level for the different distances S are presented in Fig. (4). In cases A1 and A2 with $S = 1D$ and $S = 2D$ respectively, cylinder 1 experiences the same force as that on a single cylinder, $F_0 = 14000$ N. In case 3, as S is increased to $3D$, cylinder 1 experiences a slightly reduced force of $0.92F_0$. The wave

Table 1. Details of the setups used in the different simulations

Case	H (m)	T (s)	clear distance (S)	scenario	F_0 (N)
A1			1D	breaker tongue impact	
A2	1.30	4.00	2D	on cylinder 1 just below	14000
A3			3D	the wave crest	
B1			1D		
B2	1.30	4.00	2D	breaking at cylinder 1	11850
B3			3D		
C1			1D	wave breaking behind	
C2	1.30	4.00	2D	cylinder 1	9800
C3			3D		

forces on the second cylinder are $0.63F_0$, $0.61F_0$ and $0.49F_0$ in cases A1, A2 and A3 respectively. Thus, the wave forces on the second cylinder are reduced as the distance between the cylinders is increased. The wave forces on cylinder 2 are reduced with increasing S because the cylinder moves farther away from the breaking point.

Further insight into the wave interaction problem is obtained from the free surface around the cylinders for case A1, where the cylinders are separated by a distance of $1D$, presented in Fig. (5) with horizontal velocity contours. The incident wave impacts cylinder 1 with the breaker tongue just below the wave crest level in Fig. (5a). The overturned wavefront is separated around cylinder 1 in Fig. (5b). Figure (5c) shows the separated broken wavefront incident on cylinder 2 and reconnecting with the free surface. As the broken wave crest propagates past cylinder 2, the runup in between the cylinders and the secondary breaking wave behind cylinder 2 is seen. The wave incident on cylinder 2 is at the final stage of the wave breaking process and the cylinder experiences low wave forces. When the separation between the cylinders is increased to $S = 2D$ and $S = 3D$, the wave incident on cylinder 2 has already rejoined the free surface and the wave does not produce the same impact as on the upstream cylinder.

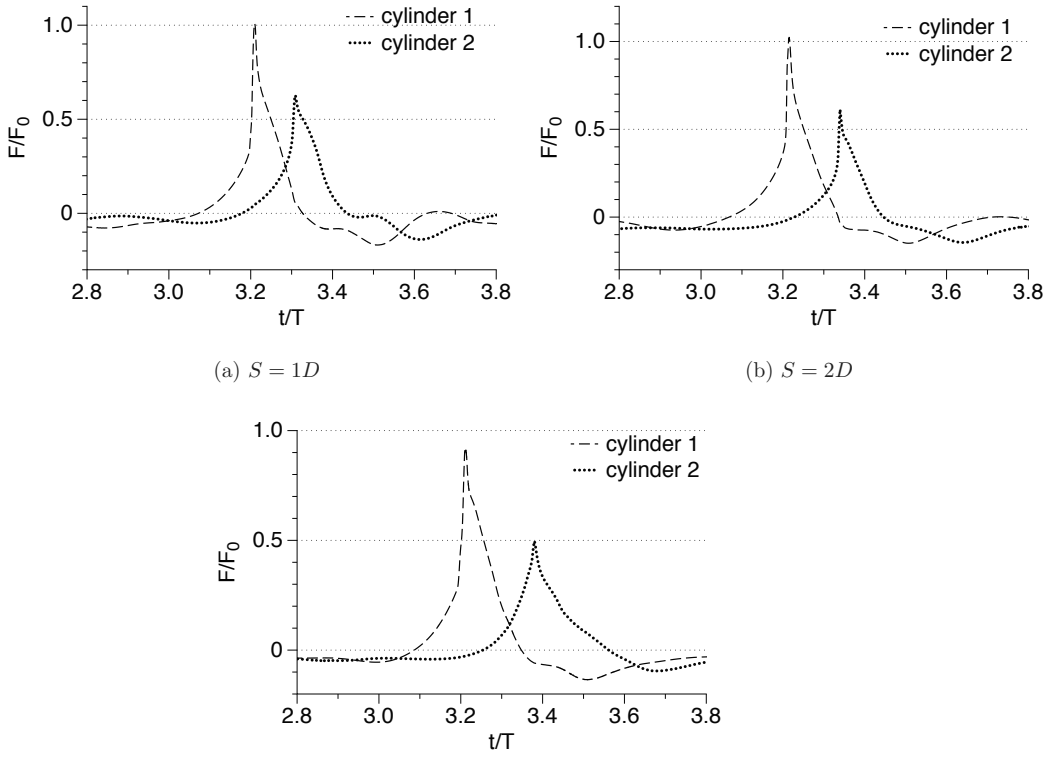

(a) $S = 1D$

(b) $S = 2D$

(c) $S = 3D$

Fig. 4. Wave forces on the cylinders for scenario A: breaker tongue impacting cylinder just below wave crest level

Also, the incident wavefront is completely separated around cylinder 1, producing a sheltering effect on the downstream cylinder. As a result, the water mass impacting cylinder 2 mainly consists of a partially-developed water jet formed due to the meeting of the separated wavefront behind cylinder 1. This leads to even lower forces on cylinder 2 in cases A2 and A3, whereas the wave forces on cylinder 1 do not change significantly when the breaker tongue impacts cylinder 1 just below the wave crest level.

The breaking wave forces on the two cylinders in scenario B, where cylinder 1 is placed at the breaking point of the wave and the force on a single cylinder $F_0 = 11850$ N are presented in Fig. (6). Cylinder 1 experiences slightly higher wave forces as the

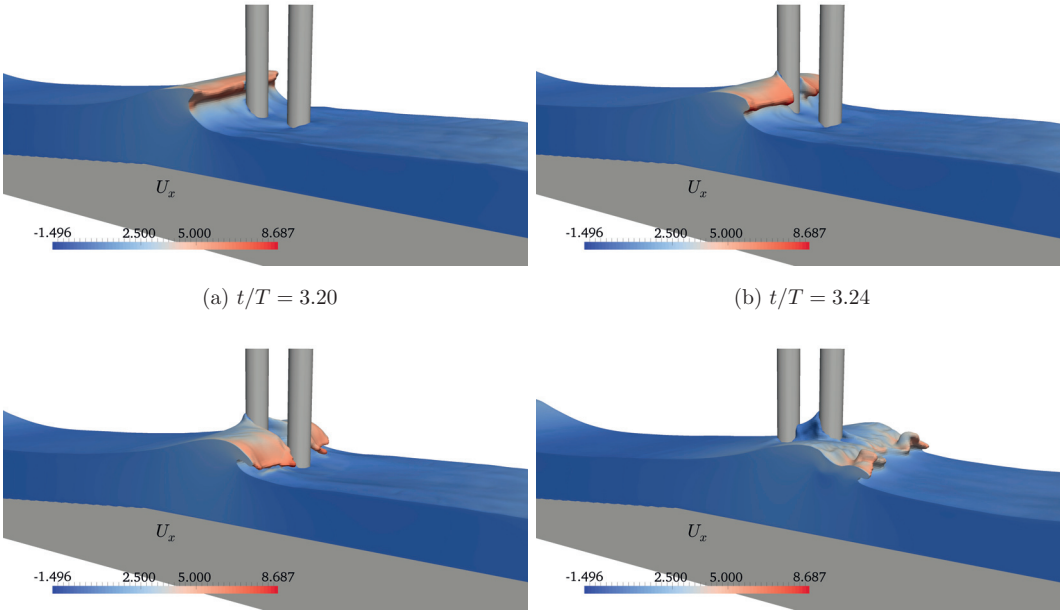

(a) $t/T = 3.20$ (b) $t/T = 3.24$

(c) $t/T = 3.29$ (d) $t/T = 3.40$

Fig. 5. Free surface around the cylinders in scenario A1 ($S = 1D$) with horizontal velocity contours

distance between the cylinders is increased with $0.89F_0$, $0.90F_0$ and $0.93F_0$ for $S = 1D$, $2D$ and $3D$ respectively. The wave forces on cylinder 2 increase significantly with increase in S with $0.67F_0$ for $S = 1D$ and $1.06F_0$ for $S = 3D$. Thus, in this scenario the wave force on the second cylinder can be higher than the force on a single cylinder, whereas the force on cylinder 1 is almost the same in all cases.

The wave interaction in this scenario is further studied using the free surface around the cylinders for case B2 ($S = 2D$) with horizontal velocity contours in Fig. (7). The incident wave crest is vertical at the point of impact with cylinder 1 in Fig. (7a), as it is placed at the breaking point of the wave. Figure (7b) shows the separation of the incident wavefront around cylinder 1, leading to a region of low velocities behind the cylinder. The separated wavefront meets behind the cylinder and a water jet is formed which impacts cylinder 2 along with the overturning wavefront that impacts

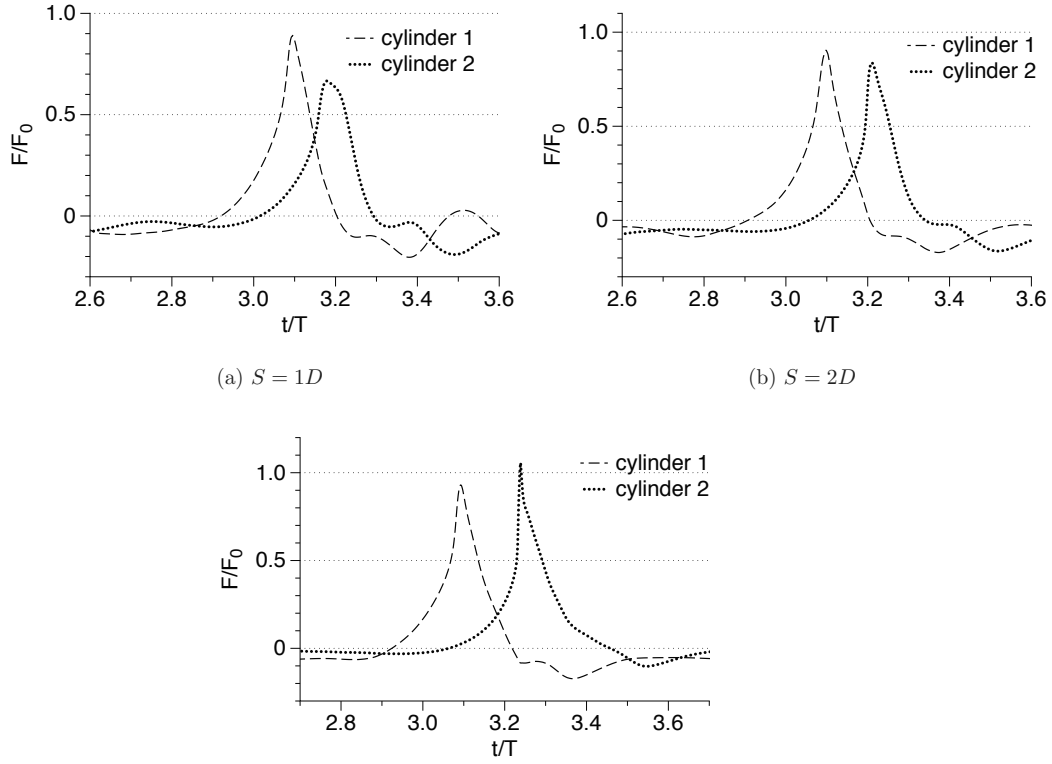

(a) $S = 1D$

(b) $S = 2D$

(c) $S = 3D$

Fig. 6. Wave forces on the cylinders for scenario B: wave breaking at cylinder 1

the cylinder at the wave crest level. Figure (7c) shows the runup on cylinder 2 due to the water jet originating behind cylinder 1 and the overturning wave crest separating around cylinder 2 after impact at wave crest level. The overturning wave crest rejoins the free surface behind cylinder 2 and the runup on cylinder 2 due to the water jet from behind cylinder 1 and a smaller water jet behind cylinder 2 is seen in Fig. (7d). In this case, the overturning wave crest impacts cylinder 2 at around the wave crest level. This impact scenario results in the second highest force in previous studies (Irschik et al., 2002; Wienke et al., 2000) with a single cylinder. The total wave force on cylinder 2 is only 6% lower than on cylinder 1 in case B2 due to this wave impact scenario. In

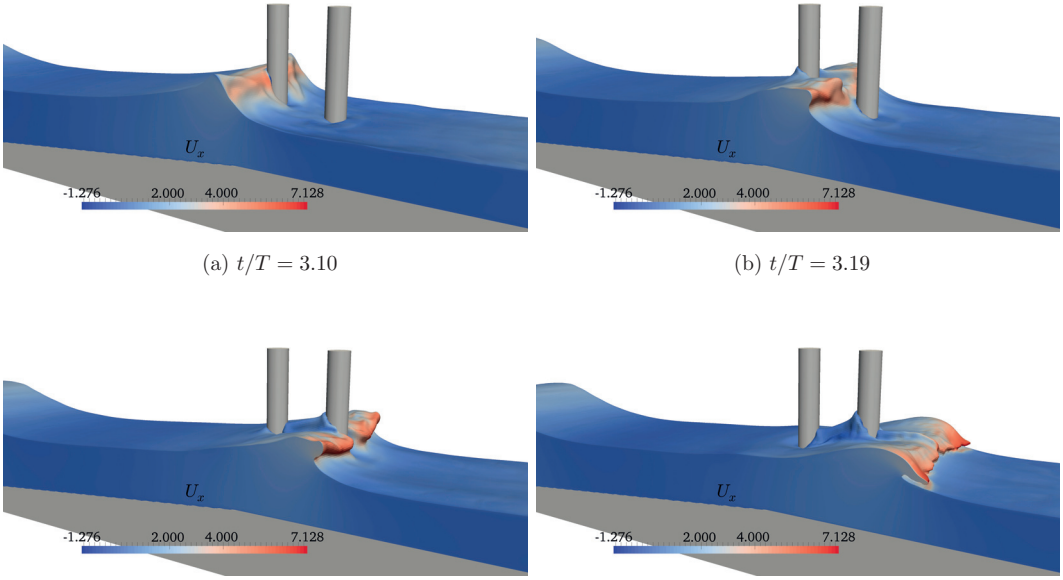

(a) $t/T = 3.10$ (b) $t/T = 3.19$

(c) $t/T = 3.25$ (d) $t/T = 3.34$

Fig. 7. Free surface around the cylinders for wave scenario B2 ($S = 2D$) with horizontal velocity contours

case B1, with $S = 1D$, the overturning wave crest impacts cylinder 2 before the breaker tongue is just below the wave crest level and this explains the 20% lower force on cylinder 2 in case B1 compared to case B2. On further increasing the distance between the cylinders to $S = 3D$, the overturning wave crest impacts cylinder 2 just below the wave crest level along with a fully developed water jet originating behind cylinder 1. This results in a higher force on cylinder 2 than on cylinder 1. Thus, when the wave breaks at cylinder 1, the sheltering effect on cylinder 2 is reduced and the downstream cylinder can be exposed to higher forces than the upstream cylinder.

In scenario C, the incident wave breaks behind cylinder 1 and the breaking wave forces on the two cylinders for different distances of separation S are presented in Fig. (8). The wave impacting cylinder 1 has not yet attained a vertical profile and the resulting wave force on a single cylinder in this scenario is $F_0 = 9800$ N. The wave forces

on cylinder 1 do not change significantly when S is varied from $1D$ to $3D$ with $0.91F_0$, $0.91F_0$ and $0.92F_0$ in cases C1, C2 and C3 respectively. The wave forces on cylinder 2 are increased significantly with $0.81F_0$ for $S = 1D$, $0.99F_0$ for $S = 2D$ and $1.04F_0$ for $S = 3D$. Thus, in this scenario the wave forces on cylinder 2 increase with increasing S and for cases C2 and C3, cylinder 2 experiences $8 - 12\%$ higher forces than cylinder 1.

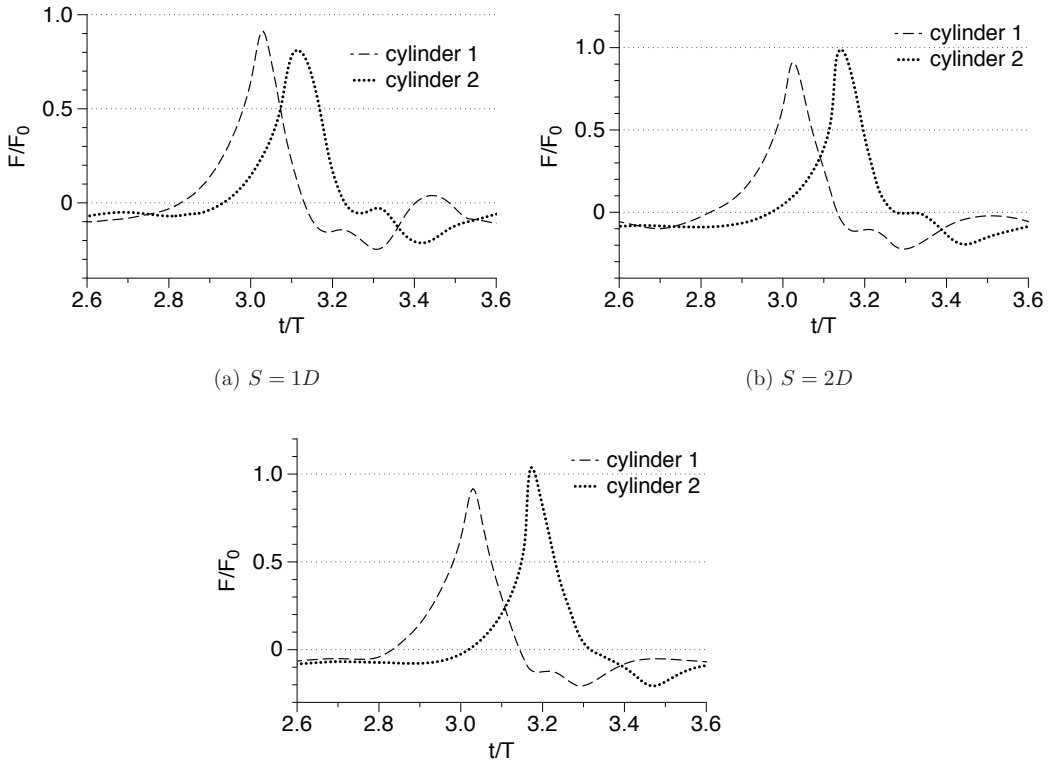

(a) $S = 1D$

(b) $S = 2D$

(c) $S = 3D$

Fig. 8. Wave forces on the cylinders for scenario C: wave breaking behind cylinder 1

The free surface around the cylinders in this scenario is investigated to correlate the wave breaking process with the wave forces experienced by the cylinders in Fig. (9) for case C3 with $S = 3D$. The incident wave on cylinder 1 in Fig. (9a) has not reached

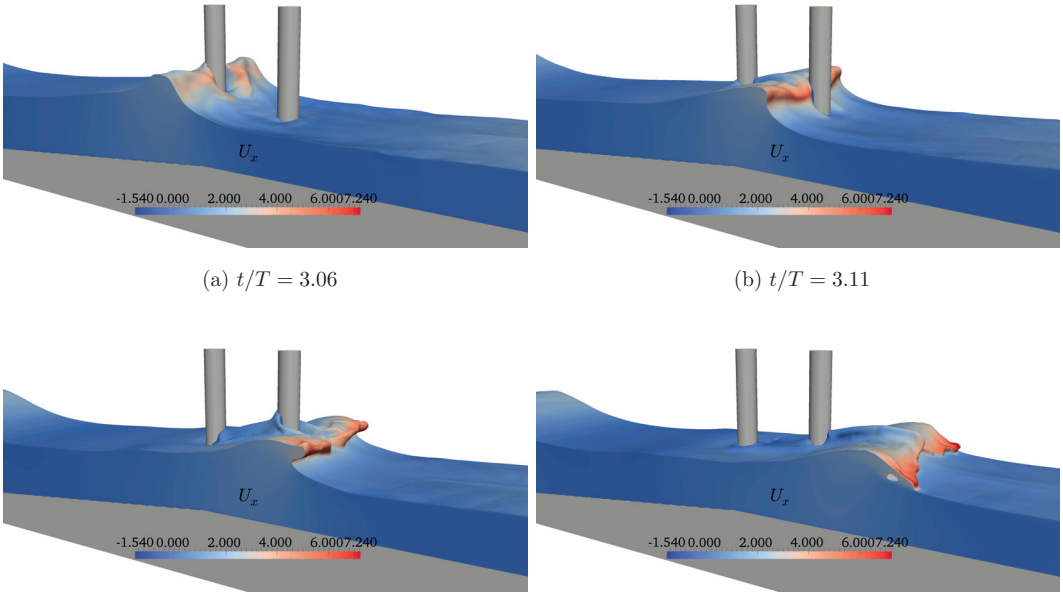

(a) $t/T = 3.06$ (b) $t/T = 3.11$

(c) $t/T = 3.18$ (d) $t/T = 3.63$

Fig. 9. Free surface around the cylinders for wave scenario C3 ($S = 3D$) with horizontal velocity contours

its breaking point and is yet to attain a vertical wavefront. The wavefront separates partially around cylinder 1 and the meets behind the cylinder. Figure (9b) shows that the overturning wave crest impacts cylinder 2 just below the wave crest level. A well-developed jet of water created by the meeting of the partially separated wavefront behind the upstream cylinder 1 is also observed. The broken wave crest propagates across cylinder 2 in Fig. (9c) and the run up in between the cylinders is seen. The reconnection of the overturning wave crest with the preceding trough behind cylinder 2 is shown in Figure (9d) along with the water jet developed behind the cylinder. Since the breaking wave impacts cylinder 2 just below the wave crest level, cylinder 2 experiences higher forces than cylinder 1 in case C3. This is similar to the findings in previous studies with a single cylinder (Wienke et al., 2000; Irschik et al., 2002), where the maximum force on the cylinder was obtained when the overturning wave

crest impacted the cylinder just below the wave crest level. In addition, the water mass impacting cylinder 2 consists of a well-developed water jet formed from the meeting of the partially separated wavefront behind cylinder 1, resulting in higher forces on cylinder 2 in comparison to the upstream cylinder.

From the results for wave forces on tandem cylinders, some similarities can be drawn between the breaking wave forces measured on a single cylinder in previous studies and the wave forces on a pair of tandem cylinders. In the case of a single cylinder, the maximum wave forces are obtained when the breaker tongue impacts the cylinder just below the wave crest level (Irschik et al., 2002). Regarding the results presented in this paper, the upstream cylinder 1 also experiences the highest forces in scenario A ($F = 14000 - 12880$ N), where the breaker tongue impacts the cylinder just below the wave crest level. In addition, in scenario C, where the breaking point of the wave is behind cylinder 1, the downstream cylinder 2 experiences higher forces ($F = 7938 - 10192$ N) compared to cylinder 1 ($F \approxeq 8920$ N) when the breaker tongue impacts the downstream cylinder 2 around the wave crest level. The second highest force on cylinder 1 in this study is computed for scenario B ($F = 10550 - 11020$ N), when the wave breaks exactly at cylinder 1. In the experiments by Irschik et al. (2002), this scenario resulted in one of the higher forces on a single cylinder. Cylinder 2 in scenario B experiences higher forces than cylinder 1 and on a single cylinder cylinder when the distance between the cylinders is such that the overturning wave crest impacts the cylinder 2 around wave crest level for case B3 ($F = 12561$ N). Thus, the wave forces on both cylinders in a tandem arrangement are highly influenced by the distance between the breaker location and the cylinder and the distance between the cylinders. It is seen that the trend observed for the single cylinder in previous studies (Irschik et al., 2002; Wienke et al., 2000) is also followed in the case of the tandem cylinders in this study.

CONCLUSION

The open-source CFD model REEF3D is used to simulate wave interaction with a pair of cylinders placed in tandem at different distances of separation for different wave

impact scenarios. The model was validated by comparing the numerical results for wave force and the free surface elevation with the experiments carried out on a single cylinder at the Large Wave Flume, Hannover, Germany by Irschik et al. (2002). The following conclusions can be drawn from the results:

- The total breaking wave force on the upstream cylinder is equal to or slightly lower than the force on a single cylinder for all distances of separation in every scenario simulated.
- The location of the breaking location with respect to the cylinders and the distance between the tandem cylinders have significant effects on the total breaking wave forces on tandem cylinders and associated free surface deformations.
- The downstream cylinder is effectively in the shadow region and the wave force on it is lower than the force on the upstream cylinder when the breaker tongue impacts the upstream cylinder just below the wave crest level.
- The force on the downstream cylinder is higher than the force on the upstream cylinder when the wave breaks at or behind the upstream cylinder and the breaker tongue impacts the downstream cylinder around wave crest level. The formation of a water jet behind the upstream cylinder overcomes the sheltering effect on the downstream cylinder.
- Under certain conditions, the total breaking wave force on the downstream cylinder is higher than the force on a single cylinder.
- The trend observed for the total breaking wave force on the cylinders is similar to that seen in the case of a single cylinder in previous studies.

This study provides insight into a simple case of two cylinders exposed to breaking waves and can be further extended to investigate breaking wave interaction with substructures of coastal constructions, consisting of multiple supporting cylinders.

ACKNOWLEDGEMENTS

This study has been carried out under the OWCBW project (No. 217622/E20) and the authors are grateful to the grants provided by the Research Council of Norway. This research was supported in part with computational resources at the Norwegian University of Science and Technology (NTNU) provided by NOTUR, http://www.notur.no (NN2620K).

REFERENCES

Alagan Chella, M., Bihs, H., and Myrhaug, D. (2015a). "Characteristics and profile asymmetry properties of waves breaking over an impermeable submerged reef." *Coastal Engineering*, 100, 26–36.

Alagan Chella, M., Bihs, H., Myrhaug, D., and Muskulus, M. (2015b). "Breaking characteristics and geometric properties of spilling breakers over slopes." *Coastal Engineering*, 95, 4–19.

Apelt, C. J. and Piorewicz, J. (1986). "Interference effects on breaking wave forces on rows of vertical cylinders." *Proc. 1st Australasian Port, Harbour and Offshore Engineering Conference, Sydney, Australia*.

Arntsen, Ø. A., Ros, X., and Tørum, A. (2011). "Impact forces on a vertical pile from plunging breaking waves." *Coastal Structures*.

Berthelsen, P. A. and Faltinsen, O. M. (2008). "A local directional ghost cell approach for incompressible viscous flow problems with irregular boundaries." *Journal of Computational Physics*, 227, 4354–4397.

Blenkinsopp, C. E. and Chaplin, J. R. (2008). "The effect of crest submergence on wave breaking over submerged slopes." *Coastal Engineering*, 55, 967–974.

Bredmose, H. and Jacobsen, N. G. (2010). "Breaking wave impacts on offshore wind turbine foundations: focused wave groups and CFD." *Proc., 29th International Conference on Ocean, Offshore and Arctic Engineering, Shanghai, China.*

Bullock, G. N., Obhrai, C., Peregrine, D. H., and Bredmose, H. (2007). "Violent breaking wave impacts. part 1: Results from large-scale regular wave tests on vertical and sloping walls." *Coastal Engineering*, 54(8), 602–617.

Chan, E. S. and Melville, W. K. (1988). "Deep-water plunging wave pressures on a vertical plane wall." *Proc. of the Royal Society of London. A. Mathematical and Physical Sciences*, Vol. 417, 95–131.

Choi, S.-J., Lee, K.-H., and Gudmestad, O. T. (2015). "The effect of dynamic amplification due to a structure s vibration on breaking wave impact." *Ocean Engineering*, 96, 8–20.

Chorin, A. (1968). "Numerical solution of the Navier-Stokes equations." *Mathematics of Computation*, 22, 745–762.

Christensen, E. D. (1998). "Turbulence in braking waves – a numerical investigation." *PhD thesis.*

Cokelet, E. D. (1977). "Breaking waves." *Nature*, 267, 769–774.

Durbin, P. A. (2009). "Limiters and wall treatments in applied turbulence modeling." *Fluid Dynamics Research*, 41, 1–18.

Goda, Y., Haranaka, S., and Kitahata, M. (1966). "Study on impulsive breaking wave forces on piles." *Report Port and Harbour Technical Research Institute*, 6(5), 1–30.

Gourlay, M. R. (1994). "Wave transformation on a coral reef." *Coastal Engineering*, 23, 17–42.

Higuera, P., Lara, L. J., and Losada, I. J. (2013). "Realistic wave generation and active wave absorption for Navier-Stokes models application to OpenFOAM." *Coastal Engineering*, 71, 102–118.

Irschik, K., Sparboom, U., and Oumeraci, H. (2002). "Breaking wave characteristics for the loading of a slender pile." *Proc. 28th International Conference on Coastal Engineering, Cardiff, Wales.*

Irschik, K., Sparboom, U., and Oumeraci, H. (2004). "Breaking wave loads on a slender pile in shallow water." *Proc. 29th International Conference on Coastal Engineering, Lisbon, Portugal.*

Jacobsen, N. G., Fuhrman, D. R., and Fredsøe, J. (2012). "A wave generation toolbox for the open-source CFD library: OpenFOAM." *International Journal for Numerical Methods in Fluids*, 70(9), 1073–1088.

Jiang, G. S. and Peng, D. (2000). "Weighted ENO schemes for Hamilton-Jacobi equations." *SIAM Journal on Scientific Computing*, 21, 2126–2143.

Jiang, G. S. and Shu, C. W. (1996). "Efficient implementation of weighted ENO schemes." *Journal of Computational Physics*, 126, 202–228.

Kjeldsen, S. and Myrhaug, D. (1978). *Kinematics and dynamics of breaking waves.* River and Harbour Laboratory (NHL) The Norwegian Institute of Technology.

Larsen, J. and Dancy, H. (1983). "Open boundaries in short wave simulations - a new approach." *Coastal Engineering*, 7, 285–297.

Lin, P. and Liu, P. L. F. (1998). "A numerical study of breaking waves in the surf zone." *Journal of Fluid Mechanics*, 359, 239–264.

Mo, W., Jensen, A., and Liu, P. L. F. (2013). "Plunging solitary wave and its interaction with a slender cylinder on a sloping beach." *Ocean Engineering*, 74, 48–60.

Morison, J. R., O'Brien, M. P., Johnson, J. W., and Schaaf, S. A. (1950). "Force exerted by surface waves on piles." *Journal of Petroleum Technology*, 2, 149–154.

Naot, D. and Rodi, W. (1982). "Calculation of secondary currents in channel flow." *Journal of the Hydraulic Division, ASCE*, 108(8), 948–968.

Osher, S. and Sethian, J. A. (1988). "Fronts propagating with curvature- dependent speed: algorithms based on Hamilton-Jacobi formulations." *Journal of Computational Physics*, 79, 12–49.

Peng, D., Merriman, B., Osher, S., Zhao, H., and Kang, M. (1999). "A PDE-based fast local level set method." *Journal of Computational Physics*, 155, 410–438.

Schäffer, H. A. and Klopman, G. (2000). "Review of multidirectional active wave absorption methods." *Journal of Waterway, Port, Coastal, and Ocean Engineering*, 126(2), 88–97.

Shu, C. W. and Osher, S. (1988). "Efficient implementation of essentially non-oscillatory shock capturing schemes." *Journal of Computational Physics*, 77, 439–471.

Sparboom, U., Oumeraci, H., Schmidt-Koppenhagen, R., and Grüne, J. (2005). "Large-scale model study on cylinder groups subject to breaking and nonbreaking waves." *Proc. 5th International Symposium WAVES 2005 Ocean Waves Measurement and Analysis, Madrid, Spain.*

Ting, F. C. K. and Kirby, J. T. (1996). "Dynamics of surf-zone turbulence in a spilling breaker." *Coastal Engineering*, 27, 131–160.

van der Vorst, H. (1992). "BiCGStab: A fast and smoothly converging variant of Bi-CG for the solution of nonsymmetric linear systems." *SIAM Journal on Scientific and Statistical Computing*, 13, 631–644.

Wienke, J. and Oumeraci, H. (2005). "Breaking wave impact force on a vertical and inclined slender piletheoretical and large-scale model investigations." *Coastal Engineering*, 52, 435–462.

Wienke, J., Sparboom, U., and Oumeraci, H. (2000). "Breaking wave impact on a slender cylinder." *Coastal Engineering Conference*, Vol. 2, 1787–1798.

Wilcox, D. C. (1994). *Turbulence modeling for CFD*. DCW Industries Inc., La Canada, California.

Zhao, Q., Armfield, S., and Tanimoto, K. (2004). "Numerical simulation of breaking waves by a multi-scale turbulence model." *Coastal Engineering*, 51(1), 53–80.

Paper 7

Numerical Investigations of the Hydrodynamics of an Oscillating Water Column Device

Kamath A., Bihs H. and Arntsen Ø.A. (2015)
Ocean Engineering 102, 40-50.

Ocean Engineering 102 (2015) 40–50

Contents lists available at ScienceDirect

Ocean Engineering

journal homepage: www.elsevier.com/locate/oceaneng

Numerical investigations of the hydrodynamics of an oscillating water column device

Arun Kamath *, Hans Bihs, Øivind A. Arntsen

Department of Civil and Transport Engineering, Norwegian University of Science and Technology, 7491 Trondheim, Norway

ARTICLE INFO

Article history:
Received 22 May 2014
Accepted 13 April 2015

Keywords:
Oscillating water column
Computational fluid dynamics
Wave energy
Porous media
REEF3D

ABSTRACT

An oscillating water column (OWC) device is a renewable energy device that is used to extract ocean wave energy through the action of waves on a partially submerged chamber consisting of an air and a water column. The operation of an OWC device involves complex hydrodynamic interactions between the waves and the device and a good understanding of these interactions is essential for the design of hydrodynamically efficient and structurally stable devices.

In this paper, a two-dimensional numerical wave tank is utilized to simulate the interaction of an OWC device with waves of different wavelengths and steepnesses. The chamber pressure, provided by a turbine in a prototype, is simulated using porous media flow theory in the numerical model. The pressure in the chamber and the velocity of the free surface are calculated to evaluate the efficiency of the device and the model is validated by comparing the numerical results with experimental data. The performance of the device under a range of wavelengths for different wave steepnesses is evaluated. The effect of wave steepness on the device efficiency at a lower wave steepness was found to be low, but a large reduction in performance was found in the presence of steep non-linear waves.

1. Introduction

An oscillating water column (OWC) device is a renewable energy device that is used to capture ocean wave energy and convert it to electrical energy. An OWC device consists of a chamber that is partially submerged in water and has an air column trapped above the water column. The water column in the chamber is excited by the incoming waves and the motion of the water column is transferred to the air column which is forced through a vent at the roof of the chamber. The pressurized air flows through the vent and drives a turbine to generate electrical energy. A good understanding of the hydrodynamics around an OWC device is essential in order to efficiently harness wave energy and to develop stable and economical OWC devices.

Several researchers have mathematically analyzed the hydrodynamics of an OWC device and devised formulae to evaluate the hydrodynamic efficiency. Evans (1978) calculated the efficiency of a wave energy converter modeled as a pair of parallel vertical plates, with a float connected to a spring-dashpot on the free surface as the wave energy absorber. This model considered the length of the chamber to be small compared to the waves and the water column moves like a weightless piston, resulting in a one-dimensional rigid motion of the free surface. Evans (1982) further studied the OWC device, including the spatial variation of the free surface and related the hydrodynamics to the dynamic air pressure developed in the chamber. This is considered to be a better representation of the system, as the free surface motion does not need to be piston-like under all operating conditions. Sarmento and Falcao (1985) developed a theory to evaluate the hydrodynamic efficiency of an OWC device with both linear and non-linear power take-off (PTO) systems. The authors concluded that the non-linear PTO was only marginally lower in efficiency compared to the linear system. They also noted that the device efficiency could be improved by introducing phase control, where the volume flow of air is controlled independently of the pressure by varying the external damping on the chamber. Sarmento (1992) carried out wave flume experiments of an OWC device using a small amplitude-to-wavelength ratio, A_0/λ and validated the theory presented by Sarmento and Falcao (1985). The external damping from a power take-off device was modeled using porous filter material and orifice plates to represent linear and non-linear PTO mechanisms respectively. The importance of external damping was presented by Thiruvenkatasamy and Neelamani (1997), who studied the effect of the nozzle area on the efficiency of an OWC device through wave flume experiments. In their experiments, the air pressure in the chamber was lowered for nozzle cross-sectional areas greater than 0.81% of the free surface,

* Corresponding author. Tel.: +47 73 59 46 40; fax: +47 73 59 70 21.
E-mail address: arun.kamath@ntnu.no (A. Kamath).

http://dx.doi.org/10.1016/j.oceaneng.2015.04.043
0029-8018/

resulting in a lower device efficiency. This implies that an optimal damping on the chamber is required under prevalent wave conditions in order to efficiently extract the incident wave energy. Morris-Thomas et al. (2007) carried out experiments to determine the influence of wall thickness, shape of the front wall and draught of the front wall for various wave parameters on the hydrodynamic efficiency of an OWC device. They reported a peak efficiency of about 0.7 and that the shape parameters of the device affect the bandwidth of the hydrodynamic efficiency curve. They concluded that a hydrodynamically smooth front wall slightly reduced the entrance losses, resulting in a slightly larger amount of wave energy available in the device chamber. Zhang et al. (2012) simulated the experiments presented by Morris-Thomas et al. (2007) with a two-dimensional computational fluid dynamics (CFD) based numerical model and presented the variation of the pressure and the free surface elevation inside the chamber, however without comparison to the experimental data. They reported reasonable agreement with experimental data for the hydrodynamic efficiency of the device with a slight over prediction of the efficiency in the model due to the complex pressure changes in the chamber around resonance. Teixeira et al. (2013) used a numerical model based on the semi-implicit Taylor–Galerkin method to simulate regular wave interaction with an OWC device including the aerodynamics in the chamber using the first law of thermodynamics and ideal gas transformation and compared their results with numerical results from the commercial CFD code Fluent. López et al. (2014) validated a CFD model using experimental results and studied the importance of external damping on the performance of an OWC device under regular and irregular waves to determine the optimum turbine-induced damping on an OWC device.

The OWC device absorbs wave energy through the motion of the air column that is pressurized due to the damping provided by the air vent and the power take-off device. This external damping on the device chamber is represented by a nozzle or vent in the roof of the chamber in experimental studies by Thiruvenkatasamy and Neelamani (1997) and Morris-Thomas et al. (2007). Sarmento (1992) used orifice plates and porous filter material. The use of a porous filter material in model testing is one of the methods to represent a linear power take-off device. This is justified by the fact that a Wells turbine is approximately linear and this simple method provides a good representation of the linear pressure-versus-flow rate characteristics (Falcao and Henriques, 2014). In a numerical model, the effect of a power take-off device can be simulated by considering the air flow in the vent as a flow through a porous medium. In the case of a linear power take-off device, the pressure drop across the vent due the presence of the porous medium can be governed by a linear pressure drop law. It is also possible to numerically implement a quadratic pressure drop law to simulate the effect of a self-rectifying impulse turbine. This method provides a good representation of the external damping on the device chamber to study the device hydrodynamics without difficulties in numerical computations due to the high air velocities in an air vent of a small width.

In current literature, there are not many numerical studies which control external damping in an explicit manner without changing the size of the air vent. Didier et al. (2011) used the porous media theory to define external damping on an OWC device modeled as a cylinder of small diameter. The application of the porous media flow theory to model the pressure drop across the vent on model scale OWC devices would help in understanding the hydrodynamics of the device in combination with the effect from the PTO device. The use of porous media flow theory to model the external damping provides the means to control the variation of the chamber pressure. The control over the chamber pressure variation is part of a strategy to improve the performance of the device, called phase control. This concept has been presented by several authors, for example Hoskin et al. (1986), Falcao and Justino (1999) and Lopes et al. (2009). A combined approach to model the variation of the free surface and the chamber pressure and control the pressure drop across the vent in the numerical model will provide useful insights into the operation of the device.

The objective of this study is to investigate the hydrodynamics of an OWC device including the variation of the free surface and pressure inside the chamber and represent the external damping provided by the PTO device using the porous media flow theory. The study uses a CFD model to carry out two-dimensional simulations of an OWC device placed in a numerical wave tank. The experimental data from Morris-Thomas et al. (2007) is used to validate the numerical model. The pressure drop in the experiments is quantified using the porous media flow theory and the external damping on the chamber is defined independent of the air vent width in the numerical model. The numerical model assumes incompressible air in the device chamber because the effect of air compressibility is negligible in the small scale model considered in this study as the ratio between the chamber volume and the OWC free surface is relatively small and much smaller than in a full-scale prototype. The variation of the free surface, chamber pressure and the velocity of the vertical free surface motion in the numerical model are compared to the experimental observations. The efficiency of the device over a range of wavelengths is calculated for a fixed wave amplitude. In real sea states, the incident wave amplitude may change over time. In order to investigate the performance of the device under changing conditions in the sea states, the effect of wave steepness on the device efficiency and performance under steep non-linear waves is evaluated. The knowledge gained from these studies using regular waves can help in obtaining a better understanding of the device performance under different wave steepnesses and amplitudes that are encountered in real sea states.

2. Numerical model

The open-source CFD model REEF3D solves the fluid flow problem using the incompressible Reynolds-averaged Navier–Stokes (RANS) equations along with the continuity equation:

$$\frac{\partial U_i}{\partial x_i} = 0 \tag{1}$$

$$\frac{\partial U_i}{\partial t} + U_j \frac{\partial U_i}{\partial x_j} = -\frac{1}{\rho}\frac{\partial P}{\partial x_i} + \frac{\partial}{\partial x_j}\left[(\nu + \nu_t)\left(\frac{\partial U_i}{\partial x_j} + \frac{\partial U_j}{\partial x_i}\right)\right] + g_i \tag{2}$$

where U is the velocity averaged over time t, ρ is the fluid density, P is the pressure, ν is the kinematic viscosity, ν_t is the eddy viscosity and g is the acceleration due to gravity.

Chorin's projection method (Chorin, 1968) is used to determine the pressure and a preconditioned BiCGStab solver (van der Vorst, 1992) is used to solve the resulting Poisson pressure equation. Turbulence modeling is handled using the two-equation k–ω model proposed by Wilcox (1994), where the transport equations for the turbulent kinetic energy, k, and the specific turbulent dissipation rate, ω, are

$$\frac{\partial k}{\partial t} + U_j \frac{\partial k}{\partial x_j} = \frac{\partial}{\partial x_j}\left[\left(\nu + \frac{\nu_t}{\sigma_k}\right)\frac{\partial k}{\partial x_j}\right] + P_k - \beta_k k\omega \tag{3}$$

$$\frac{\partial \omega}{\partial t} + U_j \frac{\partial \omega}{\partial x_j} = \frac{\partial}{\partial x_j}\left[\left(\nu + \frac{\nu_t}{\sigma_\omega}\right)\frac{\partial \omega}{\partial x_j}\right] + \frac{\omega}{k}\alpha P_k - \beta\omega^2 \tag{4}$$

$$\nu_t = \frac{k}{\omega} \tag{5}$$

where P_k is the production rate and closure coefficients $\sigma_k = 2,\ \sigma_\omega = 2,\ \alpha = 5/9,\ \beta_k = 9/100,\ \beta = 3/40$.

The highly strained flow due to the waves results in an overproduction of turbulence in the numerical wave tank. This is avoided by modifying the eddy viscosity formulation to introduce a stress limiter formula based on the Bradshaw et al. (1967) assumption as shown by Durbin (2009):

$$\nu_t \leq \sqrt{\frac{2}{3}}\frac{k}{|\mathbf{S}|} \tag{6}$$

where **S** stands for the source terms in the transport equations. The large difference between the density of air and water leads to a large strain at the interface in a two-phase CFD model. In reality, the free surface is a boundary at which eddy viscosity damping occurs. This effect is not accounted for in the $k-\omega$ model. The overproduction of turbulence due to the additional strain in this case is reduced using free surface turbulence damping using a source term in the specific turbulent dissipation equation as shown by Egorov (2004):

$$S_n = \left(\frac{6\ B\ \nu}{\beta\ dx^2}\right)^2 \beta\ dx\ \delta(\phi) \tag{7}$$

where model parameter B is set to 100.0 and dx is the grid size. The Dirac delta function, $\delta(\phi)$, is used to apply the limiter only at the free surface.

The fifth-order conservative finite difference weighted essentially non-oscillatory (WENO) scheme proposed by Jiang and Shu (1996) is used for the discretization of the convective terms of the RANS equations. The Hamilton–Jacobi formulation of the WENO scheme (Jiang and Peng, 2000) is used to discretize the level set function ϕ, turbulent kinetic energy k and the specific turbulent dissipation rate ω. The WENO scheme provides the accuracy required to model complex free surface flows and is a minimum third-order accurate in the presence of large gradients and shocks. A total variation diminishing (TVD) third-order Runge–Kutta explicit time scheme by Shu and Osher (1988) is employed for the time treatment of the momentum equation, the level set function and the reinitialization equation. An adaptive time stepping strategy is employed in the model to determine the time step size in the simulation using the Courant–Frederick–Lewis (CFL) criterion. The time advancement of k and ω is carried out with a first-order implicit scheme. These variables are largely driven by source terms and have a low influence from the convective terms. An explicit treatment of these variables would result in very small time steps due to the large source terms and this is avoided by the implicit treatment of the variables. In addition, the diffusion terms of the velocities are also handled using an implicit scheme, removing them from the CFL criterion.

The model uses a Cartesian grid for spatial discretization, which facilitates a straight forward implementation of the finite difference schemes. The boundary conditions for complex geometries are handled using an adaptation of the immersed boundary method (IBM), where the values from the fluid region are extrapolated into the solid region using ghost cells (Berthelsen and Faltinsen, 2008). The computational performance of the model is improved using the MPI library. The domain is decomposed into smaller parts and a processor is assigned to each part. The numerical model is completely parallelized and can be executed on high performance computing systems.

2.1. Level set method

The free surface is obtained using the level set method. In this method, the zero level set of a signed distance function, $\phi(\vec{x},t)$ called the level set function, represents the interface between water and air. For the rest of the domain, the level set function represents the closest distance of each point in the domain from the interface and the sign distinguishes the two fluids across the interface. The level set function is defined as:

$$\phi(\vec{x},t)\begin{cases} >0 & \text{if } \vec{x} \text{ is in phase 1} \\ =0 & \text{if } \vec{x} \text{ is at the interface} \\ <0 & \text{if } \vec{x} \text{ is in phase 2} \end{cases} \tag{8}$$

The level set function is smooth across the interface and provides a sharp description of the free surface. The signed distance property of the level set function is lost when the interface moves. A partial differential equation based reinitialization procedure presented by Peng et al. (1999) is then used to restore the signed distance property of the function.

2.2. Numerical wave tank

In a two dimensional numerical wave tank, symmetry conditions are enforced on the side walls and the top of the tank. The bottom wall of the tank and boundaries of objects placed in the tank are treated with a no-slip or wall boundary condition. A relaxation method is used for wave generation and absorption. In this method, an analytical solution obtained from wave theory is used to moderate the computational values in the relaxation zones. Implementation of the relaxation method has been demonstrated by Mayer et al. (1998), Engsig-Karup (2006) and Jacobsen et al. (2011). The values of the velocity and the free surface are moderated in the relaxation zones for wave generation and absorption zones using the following equations:

$$\begin{aligned} U_{relaxed} &= \Gamma(x)U_{analytical} + (1-\Gamma(x))U_{computational} \\ \phi_{relaxed} &= \Gamma(x)\phi_{analytical} + (1-\Gamma(x))\phi_{computational} \end{aligned} \tag{9}$$

where $\Gamma(x)$ is called the relaxation function and $x \in [0,1]$ is the length scale along the relaxation zone.

The relaxation function is a smooth function with a range $[0,1]$ and it facilitates the smooth transition between the computational and analytical values in the relaxation zones. In this study, the set of relaxation functions presented by Engsig-Karup (2006) for wave generation and absorption is used, where three relaxation zones are defined in the numerical wave tank. First, in the wave generation zone, the computational values of velocity and free surface are taken from zero to the analytical values expected using the appropriate wave theory using Eq. (9). The relaxation function transitions the values of velocity and free surface to the values prescribed by the wave theory and waves are generated and released into the wave tank. The second relaxation zone is adjacent to the wave generation zone and ensures that the waves propagating in the opposite direction to the generated waves, produced by reflection from the objects placed in the wave tank, do not affect the wave generation. This simulates a wave generator with active absorption. The last relaxation zone is the numerical beach, where the values for the free surface and velocity are brought to zero and pressure to its hydrostatic distribution to numerically dissipate the waves from the wave tank. In this way, the energy in the wave tank is removed by reducing the computational values smoothly without generating waves propagating in the opposite direction.

3. Hydrodynamic efficiency

The hydrodynamic efficiency of an OWC device is a measure of the wave energy that is available at the turbine for conversion to electrical energy. The power available at the turbine, p_{out}, is measured as the time average of the product of the chamber

pressure, P_c, and the volume flow rate of air across the turbine, q, as shown in the following equation:

$$p_{out} = \frac{1}{T}\int_0^T P_c(t) \cdot q(t)\, dt \tag{10}$$

In the numerical model, the value for the chamber pressure is available at every time step from the solution of the Poisson equation. The volume flow of air is calculated as the product of the velocity of the free surface and the cross-sectional area of the chamber as air is considered to be incompressible in this scenario. This method can be used to analyze the power absorption by the device from incident regular waves.

The incident wave energy flux is calculated using wave theory as shown in the following equation:

$$p_{in} = \frac{1}{4}\rho g A_0^2 \frac{\omega_i}{k_i}\left(1 + \frac{2k_i d}{\sinh 2k_i d}\right) \tag{11}$$

where A_0, ω_i, k_i are the amplitude, angular frequency and the wave number of the incident wave respectively and d is the water depth. The equation provides the wave power available per unit width and the wave power available at the mouth of the device is measured by multiplying the width of the device, l. The incident wave power for the fifth-order Stokes waves is calculated using Fenton's theory (Fenton, 1988). Thus, the hydrodynamic efficiency of the device η is calculated as the ratio of the power available at the turbine to the power incident at the mouth of the device:

$$\eta = \frac{p_{out}}{p_{in}.l} \tag{12}$$

To investigate the performance of the device over different incident wavelengths, the variation of the hydrodynamic efficiency is studied over various values of a dimensionless parameter κd, where $\kappa = \omega_i^2/g$, as in Evans and Porter (1995) and Morris-Thomas et al. (2007)

4. Porous media flow relation

The porous media flow equation is used to represent the external damping provided by a power take-off device on the OWC chamber. A linear pressure drop law is implemented in the model as

$$\Delta P = -\frac{\mu}{k_p} U_i \tag{13}$$

where μ is the dynamic viscosity of the fluid, ΔP is the pressure drop across the vent and $1/k_p$ is the permeability coefficient. For a given pressure drop, the permeability coefficient can be determined using Darcy's law for flow through porous media

$$q = \frac{-k_p A}{\mu}\frac{\Delta P}{L} \tag{14}$$

where q is the flow rate, A is the cross-sectional area, and L is the length along the direction of flow.

In a practical scenario, the pressure drop and flow across a turbine are known from the device characteristics supplied by the manufacturer. In this study, the values for the pressure drop and the flow rate across the vent under conditions close to resonance, in the experiments by Morris-Thomas et al. (2007), are used. Using $\Delta P = 500$ Pa and $q = 0.11\ \mathrm{m^3/s}$, to simulate the pressure drop from a vent of $V = 0.005$ m in Eq. (14), results in $1/k_p = 5 \times 10^8\ \mathrm{m^{-2}}$. This value of $1/k_p$ is used in all the numerical simulations in this study.

5. Results and discussion

A grid refinement study is carried out to ensure accurate wave generation and propagation in the numerical wave tank. Linear waves of wavelength $\lambda = 2.90$ m and wave height of $H = 0.12$ m are generated in the wave tank with a water depth of $d = 0.92$ m at grid sizes (dx) of 0.1 m, 0.05 m, 0.025 m and 0.01 m. The results are presented in Fig. 1. It is observed that the wave amplitudes are slightly higher at a grid size of $dx = 0.1$ m and $dx = 0.05$ m. This effect reduces on further refinement of the grid and the wave amplitude converges to the desired value from $dx = 0.025$ m. The improvement in the results on refinement from $dx = 0.025$ m to $dx = 0.01$ m is small. So, a grid size of $dx = 0.025$ m can be used for simulations with linear waves. Waves of higher steepness are generated using the fifth-order Stokes wave theory. Grid convergence study is carried out with fifth-order Stokes waves of wavelength $\lambda = 3.53$ m and a wave height of $H = 0.2$ m in a water depth of 0.92 m. The results are shown in Fig. 2 and it is seen that the wave amplitudes converge to the desired value from a grid size of $dx = 0.025$ m. There is no further improvement in the results on decreasing the grid size to $dx = 0.01$ m. Thus, a grid size of 0.025 m can be used for the simulation of fifth-order Stokes waves. The CFL number is set to 0.1 for all the simulations in this study.

5.1. Validation

In the first set of simulations, the experimental setup in Morris-Thomas et al. (2007) is used as illustrated in Fig. 3. The experiments were conducted at the University of Western Australia on a 1:12.5 scale model of an OWC prototype device. The numerical model is validated by comparing the numerically obtained free surface and pressure to the experimental observations. The OWC device is placed 20 m from the wave generation zone in a two-dimensional numerical wave tank of height 2.20 m. A grid size of $dx = 0.025$ m is used, following the grid convergence study. The wave generation zone is varied according to the incident wavelength in the case and is kept one wavelength long in both in zone 1 and zone 2. The numerical beach behind the device is 1 m long. The beach does not have an important effect on the simulation as the device covers the entire width of the tank. The wavelengths used in the experiments with an amplitude $A_0 = 0.06$ m are generated in a water depth of $d = 0.92$m. The OWC device has a front wall draught $a = 0.15$ m, chamber length $b = 0.64$ m, with wall thickness $\delta = 0.04$ m and a chamber height of 1.275 m. A vent of width $V = 0.05$ m is provided and the permeability factor needed to provide the damping from the $V = 0.005$ m used in the experiments is determined. The permeability factor required for this is

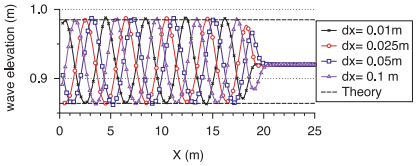

Fig. 1. Grid convergence for linear waves.

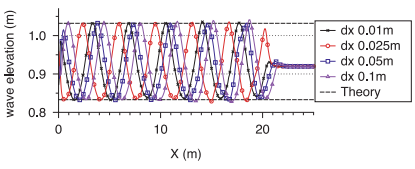

Fig. 2. Grid convergence for fifth-order Stokes waves.

determined to be $1/k_p = 5 \times 10^8$ m^{-2} and applied at the vent located at the roof of the device chamber.

A simulation is carried out using linear waves with a wavelength of $\lambda = 4.07$ m and amplitude $A_0 = 0.06$ m resulting in a wave steepness of $\xi = 0.029$ and $\kappa d = 1.26$. The variation of the free surface $A(t)$ and the chamber pressure $P_c(t)$ is calculated. The numerical results show a good match with the experimental data for the relative free surface elevation $A(t)/A_0$ and the chamber pressure in Fig. 4a and b respectively.

The free surface variation at two points along the center of the model was measured in the experiments and these values used for further analysis. Following the same approach, the free surface elevation is measured in the center of the device chamber in this study in order to replicate the experimental results and to validate the numerical model. The vertical velocity of the free surface w_{fs} is calculated using the time-series data of the free surface variation at the center of the chamber. The velocity of the vertical motion of the free surface in the chamber obtained from the numerical model matches the velocity determined from the experimental data in Fig. 4c. The chamber pressure and the free surface velocity are the two variables that determine the efficiency of the device. The numerical model provides a good representation of these

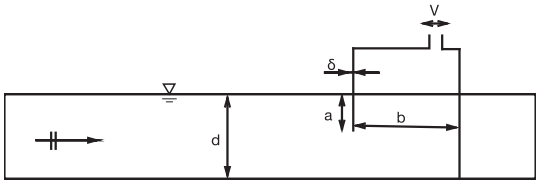

Fig. 3. Schematic of the OWC device used in the simulations.

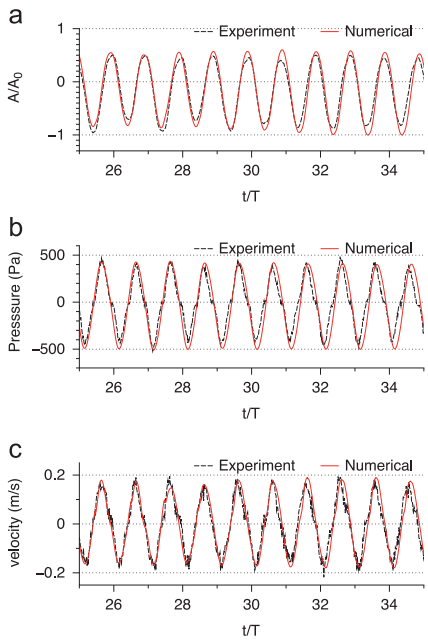

Fig. 4. Comparison of relative free surface elevation, velocity of the free surface and pressure inside the chamber for $\kappa d = 1.26$ and $\xi = 0.029$. (a) Relative free surface elevation at the center of the chamber. (b) Variation of chamber pressure. (c) Velocity of the free surface.

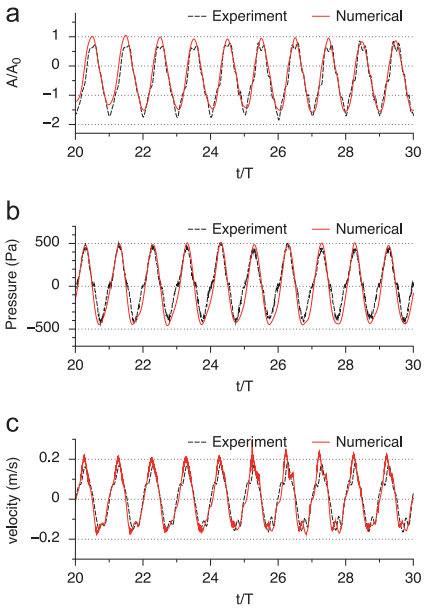

Fig. 5. Comparison of relative free surface elevation, velocity of the free surface and pressure inside the chamber for $\kappa d = 0.52$ and $\xi = 0.016$. (a) Relative free surface elevation at the centre of the chamber. (b) Variation of chamber pressure. (c) Velocity of the free surface.

parameters, which is essential for the accurate evaluation of the hydrodynamic efficiency.

Further, simulations are carried out to validate the numerical model for wavelengths on both sides of the resonant wavelength from the experiments. Linear waves of wavelength $\lambda = 7.36$ m ($\kappa d = 0.52$) and $\lambda = 2.29$ m ($\kappa d = 2.5$) with an amplitude $A_0 = 0.06$ m incident on the device. The numerically obtained values for the motion of the free surface, the pressure and the velocity of the free surface inside the chamber are seen to match the experimental observations in Figs. 5 and 6 respectively. From the three cases simulated with $\kappa d = 0.52, 1.26$ and 2.5, it is seen that the numerical model provides a good representation of the free surface motion and the pressure in the chamber over a range of wavelengths.

5.2. Effect of incident wavelength

Further, simulations with $\kappa d = 0.93, 1.12, 1.52, 1.92$ and 2.93 are carried out with a wave amplitude of $A_0 = 0.06$ m. The hydrodynamic efficiency of the device is calculated for each case using Eq. (12) and presented in Fig. 7. The variation of the hydrodynamic efficiency over κd from the numerical model largely agrees with the values obtained through experiments by Morris-Thomas et al. (2007) with a peak efficiency of $\eta_{max} = 0.76$ at $\kappa d = 1.26$ slightly higher than the peak efficiency of 0.74 observed in the experiments.

The device efficiency initially increases with increasing κd until it reaches resonance at $\kappa d = 1.26$ and then reduces with further increase in κd. According to Evans and Porter (1995), resonance occurs at $\kappa d = 2$ for small values of b/d and b/a and the fluid motion inside the chamber can be considered similar to the motion of a rigid piston. This uniform motion breaks down with an increase in b/d as the water particles have to travel a longer distance and the resonance occurs at a lower value of κd. In this study, $b/d = 0.7$ and the resonance occurs at $\kappa d = 1.26$ signifying a large difference in the device hydrodynamics at model scale in

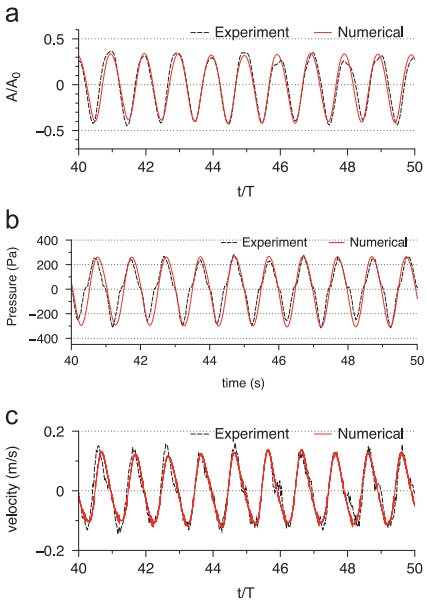

Fig. 6. Comparison of relative free surface elevation, velocity of the free surface and pressure inside the chamber for $\kappa d = 2.5$ and $\xi = 0.052$. (a) Relative free surface elevation at the centre of the chamber. (b) Variation of chamber pressure. (c) Velocity of the free surface.

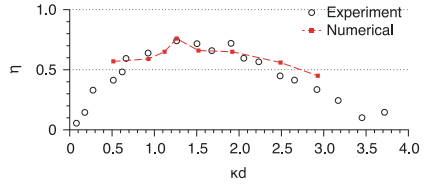

Fig. 7. Hydrodynamic efficiency of the device vs. κd.

comparison to the ideal scenario. This can be physically explained using the fluid particle excursions around the device calculated in the simulations. The water particles have a smaller orbital motion under a wave of length $\lambda = 1.96$ m ($\kappa d = 2.93$) and a larger orbital motion under a wave of length $\lambda = 4.07$ m ($\kappa d = 1.26$). The front wall of the device also interferes more with the shorter particle excursion under a lower wavelength of $\lambda = 1.96$ m leading to vortex formation behind the front wall. This leads to a break down of the rigid-piston like motion of the free surface resulting in lower volume flow rate $q(t)$ and a lower device efficiency.

The variation of the free surface relative to the incident amplitude $A(t)/A_0$ has a maximum of $A(t)_{\max}/A_0 = 1.0$ and the chamber pressure $P_c = 500$ Pa for $\kappa d = 0.52$ in Fig. 5. In the case with maximum efficiency, at $\kappa d = 1.26, A(t)_{\max}/A_0 = 0.57$ and $P_c = 460$ Pa in Fig. 4. In order to understand the lower efficiency of the device under a higher relative oscillation and chamber pressure, the phase of the vertical free surface velocity w_{fs} and the chamber pressure P_c variation for these two cases are studied. The phase difference between P_c and w_{fs} is related to the power absorption by the device as shown in Eq. (15). It arises from the time-average of the product of P_c, w_{fs} and the cross-sectional area of the device which gives a cosine term in the equation:

$$p_{out} = \frac{1}{T}\int_0^T P_c(t)\cdot q(t)\,dt = \frac{1}{2}|P_c|\cdot|w_{fs}|\;b.l\;\cos(\theta) \qquad (15)$$

where θ is the phase difference between P_c and w_{fs}. This equation leads to a reduction in the power absorbed by the device when the variation of P_c and w_{fs} is out of phase. The variation of the vertical velocity of the free surface w_{fs} and the chamber pressure P_c for $\kappa d = 0.52$ is slightly skewed and with a time shift of 0.07 T or phase difference $\theta = 0.44$ rad between w_{fs} and P_c in Fig. 8a. In the case with $\kappa d = 1.26$, w_{fs} and P_c are almost in-phase with a time shift of 0.02 T or a phase difference of $\theta = 0.125$ rad in Fig. 8b. The phase difference can be justified by the fact that the water particle excursions are very large under the longer wavelength at $\kappa d = 0.52$ compared to the particle excursion at $\kappa d = 1.26$. Extending the previously presented argument from Evans and Porter (1995), the large particle excursion leads to significant local particle motion and the free surface motion is no longer uniform along the length of the device for $\kappa d = 0.52$. Consequently, the variation of P_c and w_{fs} for $\kappa d = 0.52$ is irregular compared to the variation for $\kappa d = 1.26$. The phase difference between the variables and the reduced volume flow rate in result in a reduced efficiency at $\kappa d = 0.52$ compared to $\kappa d = 1.26$.

5.3. Effect of wave steepness

At first, linear waves with a wave steepness $\xi = H/\lambda = 0.03$ are generated in the numerical wave tank for $\kappa d = 0.52, 0.93, 1.12, 1.26, 1.52, 1.92$ and 2.93. The free surface variation inside the device chamber calculated for different incident wavelengths is presented in Fig. 9a. Since the wave steepness of $\xi = 0.03$ is a constant for all the cases simulated here, the longer incident waves have a proportionally higher incident amplitude. It is observed that the amplitude of the free surface motion in the chamber is directly related to the incident amplitude and the highest relative oscillation $A(t)_{max}/A_0$ is seen for $\kappa d = 0.52$ and it is the least for $\kappa d = 2.93$. Incident waves of longer wavelength and amplitude also induce the largest chamber pressure as they carry a higher amount of wave energy. The instantaneous power absorbed $p_{abs} = p_c \cdot w_{fs} \cdot b$ is calculated for three representative cases, $\kappa d = 0.52$, 1.26 and 2.93. In the case of $\kappa d = 1.26$, the device is close to resonance and almost the same amount of power is absorbed every half wave cycle, seen from the peaks of almost equal amplitude at every 0.5 t/T in Fig. 9b. The instantaneous power absorbed for $\kappa d = 0.52$ and 2.93, which are away from the resonant frequency of the device, is uneven and has lower peaks signifying lower energy absorption in these cases. Under resonant conditions, P_c and q are in phase, resulting in a positive value of

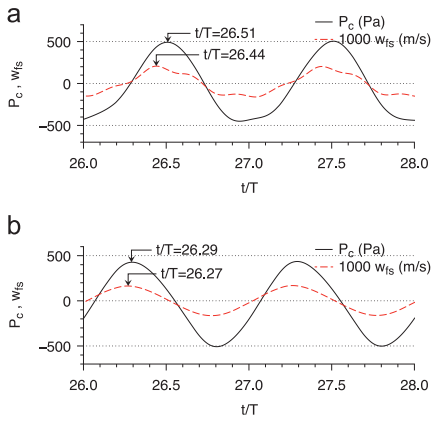

Fig. 8. Comparison of phase difference between vertical free surface velocity and chamber pressure for $\kappa d = 0.52$ and 1.26. (a) Variation of P_c and w_{fs} for $\kappa d = 0.52$. (b) Variation of P_c and w_{fs} for $\kappa d = 1.26$.

power absorbed. This is the power delivered by the device chamber to the turbine that produces electrical energy. In the case of $\kappa d = 2.93$, small parts of the instantaneous power curve cross the positive x-axis in Fig. 9b and result in negative values. This occurs when the chamber pressure and the volume flux are slightly out of phase. The negative values of p_{abs} signify work done by the device to produce outgoing waves due to the phase difference between the chamber pressure and the volume flux.

Next, fifth-order Stokes waves with a wave steepness of $\xi = 0.1$ are generated for $\kappa d = 0.93, 1.26, 1.52, 1.93, 2.49$ and 2.93 to study the hydrodynamic performance of the device under steep non-linear waves. It is not possible to simulate a wave with a steepness of $\xi = 0.1$ with $\kappa d = 0.52$ as the wave amplitude exceeds the height of the device chamber. The relative amplitude motion of the free surface in the chamber $A(t)/A_0$ for a wave steepness of $\xi = 0.1$ is larger for longer waves which have larger amplitudes. This trend is similar to that seen in the case with a wave steepness of $\xi = 0.03$, but the relative amplitudes for all the waves are lower and $A(t)_{max}/A_0 = 0.6$ for $\kappa d = 0.93$ in Fig. 10a. This implies that the steep non-linear waves do not excite the motion of the free surface as much as the waves with lower steepness. The instantaneous power absorbed at $\kappa d = 0.93, 1.26$ and 2.93 in Fig. 10b shows a region where the value for power absorbed is negative, meaning the device spends energy on producing waves radiating away from it. Thus, in spite of a peak of $p_{abs}/p_{in} \cong 0.68$, the total power absorbed over a wave period at $\kappa d = 1.26$ is low. In the case of $\kappa d = 0.93$ and 2.93, the peak value of p_{abs}/p_{in} is less than 0.5 and the power absorbed in these two cases is also low. Therefore, the hydrodynamic efficiency of the device in the presence of the steep, non-linear waves is low for all the simulated cases.

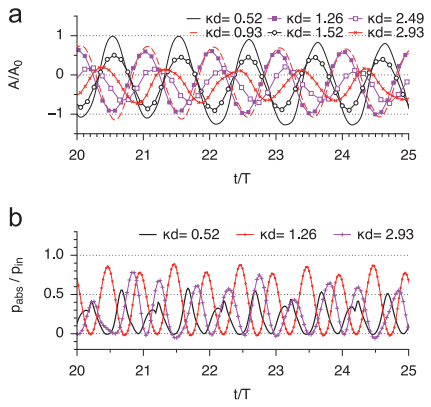

Fig. 9. Variation of free surface in the device chamber and instantaneous power absorbed for different κd at $\xi = 0.03$. (a) Variation of the relative free surface at the center of the chamber. (b) Instantaneous power absorption ratio for $\kappa d = 0.52, 1.26$ and 2.93 at $\xi = 0.03$.

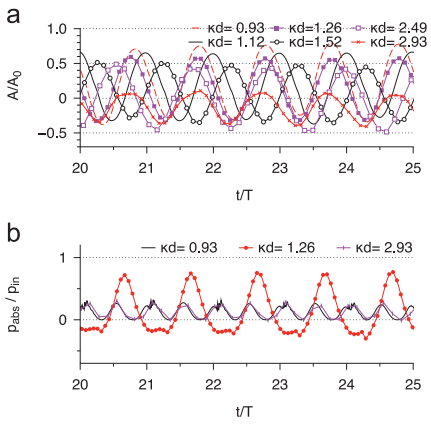

Fig. 10. Variation of free surface in the device chamber and instantaneous power absorbed for different κd at $\xi = 0.1$ using fifth-order Stokes waves. (a) Variation of the relative free surface at the center of the chamber. (b) Instantaneous power absorption ratio for $\kappa d = 0.93, 1.26$ and 2.93 at $\xi = 0.1$ using fifth-order Stokes waves.

The hydrodynamic efficiency of the device is calculated for each of the cases simulated using Eq. (12) and presented in Fig. 11. It is seen that the efficiency curve for $\xi = 0.03$ is similar to the efficiency curve obtained from the previous simulations with a constant incident amplitude of $A_0 = 0.06$ m. This shows that the wave steepness does not have a large influence on the device efficiency when linear waves of low steepness are incident. Whereas in the case of non-linear waves of steepness $\xi = 0.1$, the device efficiency is reduced considerably and is of the order $\eta \cong 0.35$. This is in agreement with the analysis of the variation of the free surface, chamber pressure and the instantaneous power absorption above.

The motion of the water particles in front of the device and the variation of the free surface in the chamber are further investigated at the resonant condition, $\kappa d = 1.26$, to obtain a better understanding of the difference in efficiency of the device for waves of different steepnesses. The streamlines in front of the device are studied over the duration of a wave period, along with the free surface motion inside the chamber of the device, during which the device completes one cycle of exhalation and inhalation of air through the vent in the roof of the chamber.

Fig. 12 shows the motion of the free surface in the chamber and the streamlines around the device for $\kappa d = 1.26$ at a wave steepness of $\xi = 0.03$. In Fig. 12a, the process of inhalation has just been completed and the free surface is correspondingly at its lowest elevation. The process of exhalation of air begins in Fig. 12b and the free surface is seen uniformly moving upwards. A recirculation zone starts to form behind the front wall as the water moves into the chamber (Fig. 12c) and moves towards the back wall and is then dissipated. The motion of the free surface is at its maximum in Fig. 12d at the end of the exhalation phase and the water column is horizontal due to the rigid piston-like motion of the water column at resonance. The inhalation phase is seen in Fig. 12e and f and the free surface moves downwards uniformly. There is no major disturbance of the water column or the free surface as the chamber inhales air through the vent in the roof. The recirculation zones seen in Fig. 12c behind the front wall and near the bottom at the back wall in Fig. 12d disintegrate in a very short time, under 0.04 t/T and the loss of wave energy due to flow separation behind the front wall and recirculation at the bottom of the chamber can be said to be low. Thus, $\kappa d = 1.26$ produces a resonant, rigid piston-like motion in the chamber of the device and most of the incident wave energy is delivered at the vent for

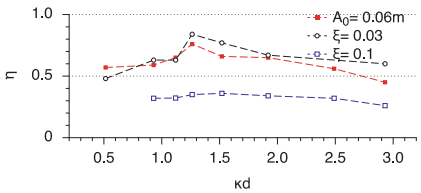

Fig. 11. Hydrodynamic efficiency of the device vs. κd for $\xi = 0.03$, $\xi = 0.1$ and $A_0 = 0.06$ m.

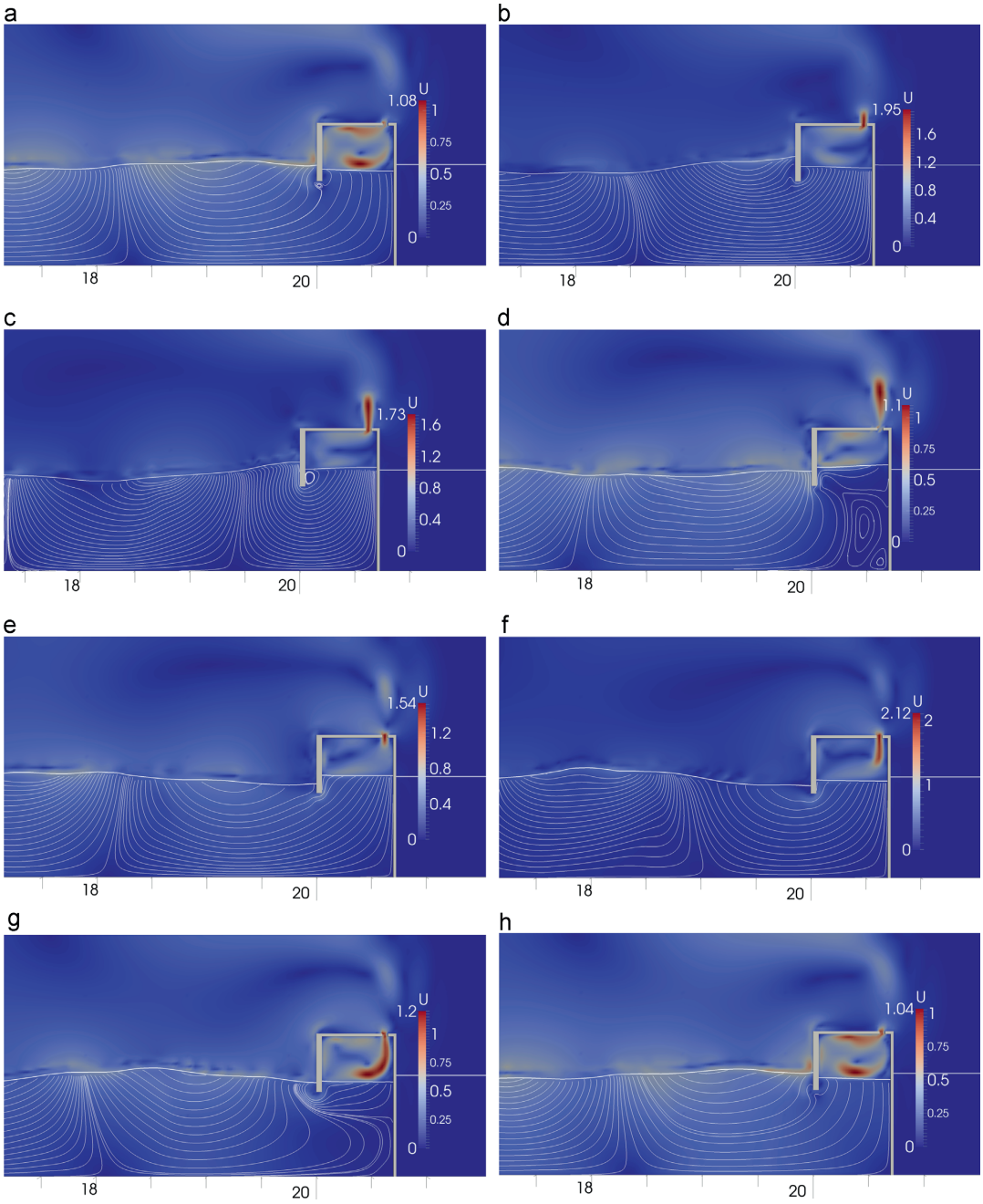

Fig. 12. Streamlines in front of the device and free surface in the chamber for $\kappa d = 1.26$ at $\xi = 0.03$ over half a wave period. (a) $t/T = 59.57$. (b) $t/T = 59.72$. (c) $t/T = 59.86$. (d) $t/T = 60.01$. (e) $t/T = 60.15$. (f) $t/T = 60.30$. (g) $t/T = 60.44$. (h) $t/T = 60.59$.

conversion into electrical energy by the turbine. The free surface just outside the chamber is almost horizontal indicating that the device absorbs most of the incident waves and wave reflection from the device is low.

The behavior of the OWC device over one wave period, when fifth-order Stokes waves with $\kappa d = 1.26$ and a steepness of $\xi = 0.1$ are incident on it, is seen in Fig. 13. The device has just completed the inhalation phase in Fig. 13a and the free surface is at its lowest elevation and a crest is approaching the device. The approaching crest is seen to build up against the front wall of the device in Fig. 13a even as the device just begins its exhalation phase. The formation of recirculation zones is seen behind the front wall in

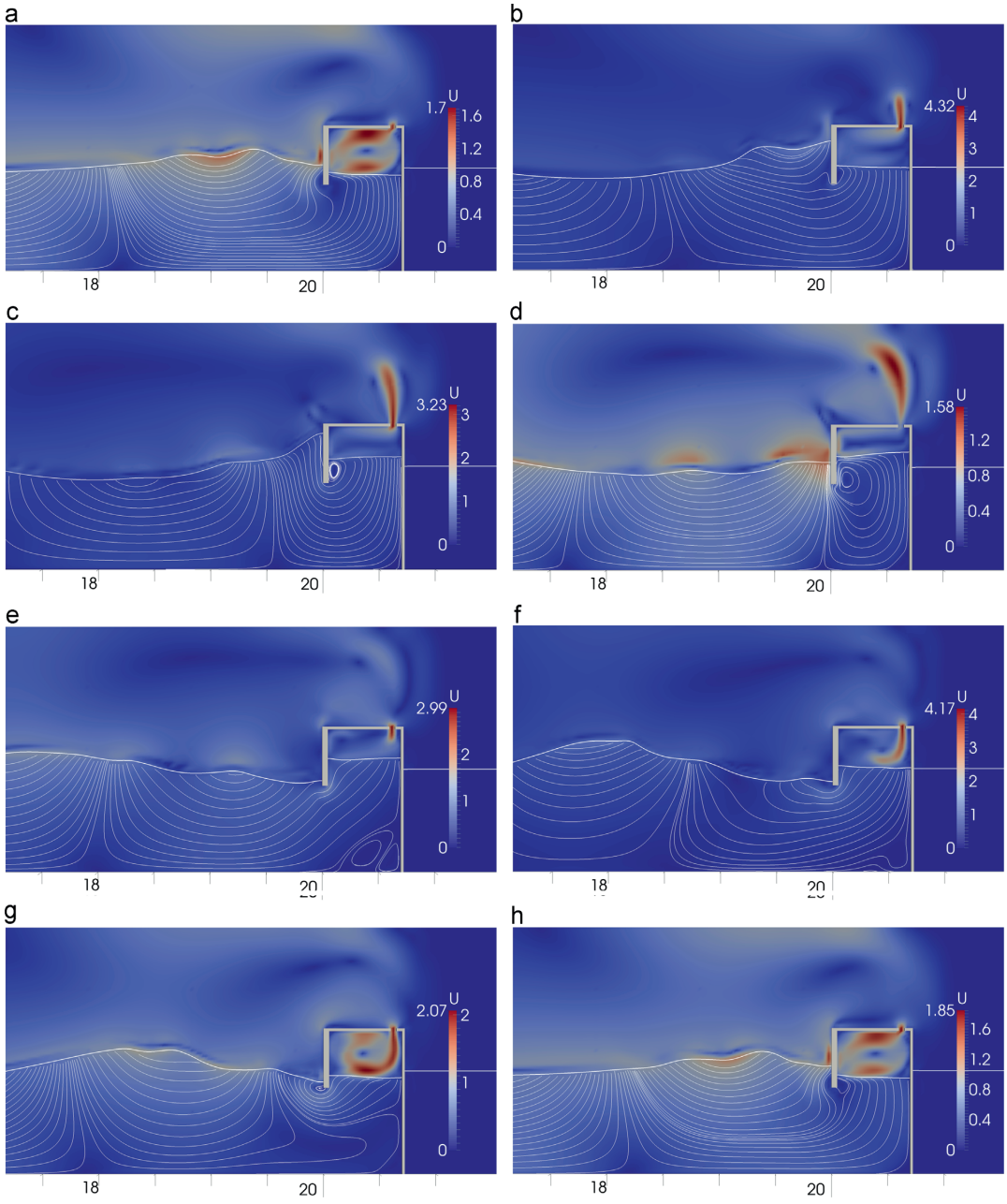

Fig. 13. Streamlines in front of the device and free surface in the chamber for $\kappa d = 1.26$ at $\xi = 0.1$ over the duration of a wave period. (a) $t/T = 21.32$. (b) $t/T = 21.46$. (c) $t/T = 21.61$. (d) $t/T = 21.76$. (e) $t/T = 21.90$. (f) $t/T = 22.05$. (g) $t/T = 22.19$. (h) $t/T = 22.34$.

Fig. 13c and d and is more prominent than in the case with $\xi = 0.1$. The vortices are also seen to form in front of the back wall towards the bottom of the device in Fig. 13e and f. The water elevation outside the chamber is at a minimum in Fig. 13f and g, when the device has started its inhalation phase and is in the process of pushing the water out of the chamber. This shows that the motion of the water around the device and the motion inside the device chamber are very much out of phase and the device is not absorbing all the incident wave energy. The free surface is not uniform in this case and there is a break down of the resonance that is seen at the same value of κd with $\xi = 0.03$. The motion of the water column is less uniform with the formation of eddies and prominent recirculation zones inside the chamber, behind the front wall and in front of the back wall towards the bottom of the

chamber. The disturbance in the flow due to the flow separation behind the front wall and the recirculation zone at the bottom of the chamber near the back wall is sustained for a longer period of time, about 0.44 t/T in this case, compared to when $\xi = 0.03$. This sustained disturbance in the flow is one of the contributors to the larger phase difference between the variation of the chamber pressure and the motion of the water column seen in this case. The energy lost due to the vortex formation and the larger phase difference between the chamber pressure and the volume flux of air through the chamber result in a lower power absorption by the device. Thus, the efficiency of the device with $\kappa d = 1.26$ at a higher wave steepness of $\xi = 0.1$ is low.

6. Conclusion

A CFD based two-dimensional numerical wave tank was used to study the hydrodynamics of an OWC device with incident regular waves. The numerical model was validated by comparing the variation of the free surface, the pressure and the vertical velocity of the free surface inside the device chamber for different wavelengths. The numerical results agreed well with the experimental data and the model produced a realistic representation of the flow physics involved. The pressure drop on the device chamber from a PTO device was modeled using the porous media flow theory. The permeability constant required was determined using the experimental data.

The variation of the hydrodynamic efficiency with the incident wavelength was studied. The occurrence of resonance at lower values of the relative depth κd for values of b/d closer to 1 than in the ideal scenario with $b/d \ll 1$ is discussed. The longer particle excursion required at higher values of b/d and the higher influence of the front wall on the particle excursion cause a break down of the rigid piston-like motion of the free surface inside the device chamber at wavelengths away from resonance. The variation of the pressure and free surface inside the chamber at various incident wavelengths was studied. The phase difference between the variation of the chamber pressure and the vertical velocity of the free surface resulting from local motion of the free surface contributed to the lowering of the device efficiency, in spite of large oscillations of the free surface and chamber pressure.

Simulations using linear waves of wave steepnesses $\xi = 0.03$ and non-linear waves of wave steepness $\xi = 0.1$ were carried out to study the influence of wave steepness and non-linear waves on the hydrodynamics of the device. The efficiency curve for $\xi = 0.03$ was found to be similar to the curve obtained from experiments and simulations using a range of wavelengths of linear waves with a constant amplitude of 0.06 m. On the other hand, the efficiency of the device was very poor, when exposed to fifth-order Stokes waves of a higher wave steepness. The wavelength, which produced resonant response at a steepness of $\xi = 0.03$, did not produce resonance in the device at a steepness of $\xi = 0.1$. The free surface motion and streamlines around the device at $\kappa d = 1.26$ for steepnesses $\xi = 0.03$ and $\xi = 0.1$ were studied and rigid piston-like motion was seen in the simulation with the lower wave steepness. The motion of the free surface was non-uniform at the higher wave steepness of $\xi = 0.1$. Thus, in addition to the wavelength of the incident waves, the wave steepness also has a significance impact on the hydrodynamic efficiency of an OWC device.

The numerical model provides a large amount of information regarding the flow physics in and around an OWC device and the behavior of the device under various conditions of incident waves and geometric configurations can be investigated using the chamber pressure and the motion of the free surface. The external damping is defined explicitly using the porous media theory and can be used to explore phase control methods to improve the performance of the device by controlling the damping on the device chamber. Further studies can be carried out to investigate the use of phase control to improve the device efficiency, formation, propagation and dissipation of vortices in the device chamber, and their influence on the hydrodynamic efficiency and also evaluate the wave forces acting on the device in order to design efficient and stable OWC devices for commercial deployment.

Acknowledgments

The authors are thankful to Michael Morris-Thomas, Principal Naval Architect, Worley Parsons, Perth, Australia for the experimental data and helpful discussions. This study has been carried out under the OWCBW project (No. 217622/E20) and the authors are grateful to the grants provided by the Research Council of Norway. This study was supported in part with computational resources at the Norwegian University of Science and Technology (NTNU) provided by NOTUR (No. NN2620K), http://www.notur.no.

References

Berthelsen, P.A., Faltinsen, O.M., 2008. A local directional ghost cell approach for incompressible viscous flow problems with irregular boundaries. J. Comput. Phys. 227, 4354–4397.
Bradshaw, P., Ferriss, D.H., Atwell, N.P., 1967. Calculation of boundary layer development using the turbulent energy equation. J. Fluid Mech. 28, 593–616.
Chorin, A., 1968. Numerical solution of the Navier–Stokes equations. Math. Comput. 22, 745–762.
Didier, E., Paixão Conde, J.M., Teixeira, P.R.F., 2011. Numerical simulation of an oscillating water column wave energy convertor with and without damping. In: Proceedings, International Conference on Computational Methods in Marine Engineering.
Durbin, P.A., 2009. Limiters and wall treatments in applied turbulence modeling. Fluid Dyn. Res. 41, 1–18.
Egorov, Y., 2004. Validation of CFD Codes with PTS-Relevant Test Cases. Technical Report Fifth Euratom Framework Programme ECORA Project, EVOL-ECORA D07.
Engsig-Karup, A.P., 2006. Unstructured Nodal DG-FEM Solution of High-Order Boussinesq-Type Equations (Ph.D. thesis). Technical University of Denmark, Lyngby.
Evans, D.V., 1978. Oscillating water column wave energy convertors. IMA J. Appl. Math. 22, 423–433.
Evans, D.V., 1982. Wave power absorption by systems of oscillating surface pressure distributions. J. Fluid Mech. 114, 481–499.
Evans, D.V., Porter, R., 1995. Hydrodynamic characteristics of an oscillating water column device. Appl. Ocean Res. 17, 155–164.
Falcão, A.F.O., Henriques, J.C.C., 2014. Model prototype similarity of oscillating-water-column wave energy converters. Int. J. Mar. Energy 6, 18–34.
Fălcao, A.F.O., Justino, P.A.P., 1999. OWC wave energy devices with air flow control. Ocean Eng. 26, 1275–1295.
Fenton, J.D., 1988. The numerical solution of steady water wave problems. Comput. Geosci. 14, 357–368.
Hoskin, R.E., Count, B.M., Nichols, N.K., Nicol, D.A.C., 1986. Phase control for the oscillating water column. In: Evans, D.V., Falcão, A.F.O. (Eds.), Hydrodynamics of Ocean Wave-Energy Utilization. Springer, Berlin, Heidelberg, pp. 257–268.
Jacobsen, N.G., Fuhrman, D.R., Fredsøe, J., 2011. A wave generation toolbox for the open-source CFD library: OpenFOAM. Int. J. Numer. Methods Fluids 70, 1073–1088.
Jiang, G.S., Peng, D., 2000. Weighted eno schemes for Hamilton–Jacobi equations. SIAM J. Sci. Comput. 21, 2126–2143.
Jiang, G.S., Shu, C.W., 1996. Efficient implementation of weighted ENO schemes. J. Comput. Phys. 126, 202–228.
Lopes, M.F.P., Hals, J., Gomes, R.P.F., Moan, T., Gato, L.M.C., Fălcao, A.F.O., 2009. Experimental and numerical investigation of non-predictive phase-control strategies for a point-absorbing wave energy converter. Ocean Eng. 36, 386–402.
López, I., Pereiras, B., Castro, F., Iglesias, G., 2014. Optimisation of turbine-induced damping for an OWC wave energy converter using a RANS-VOF numerical model. Appl. Energy 127, 105–114.
Mayer, S., Garapon, A., Sørensen, L.S., 1998. A fractional step method for unsteady free surface flow with applications to non-linear wave dynamics. Int. J. Numer. Methods Fluids 28, 293–315.
Morris-Thomas, M.T., Irvin, R.J., Thiagarajan, K.P., 2007. An investigation into the hydrodynamic efficiency of an oscillating water column. J. Offshore Mech. Arct. Eng. 129, 273–278.
Peng, D., Merriman, B., Osher, S., Zhao, H., Kang, M., 1999. A PDE-based fast local level set method. J. Comput. Phys. 155, 410–438.

Sarmento, A.J.N.A., 1992. Wave flume experiments on two-dimensional oscillating water column wave energy devices. Exp. Fluids 12, 286–292.
Sarmento, A.J.N.A., Falcão, A.F.O., 1985. Wave generation by an oscillating surface pressure and its application in wave energy extraction. J. Fluid Mech. 150, 467–485.
Shu, C.W., Osher, S., 1988. Efficient implementation of essentially non-oscillatory shock capturing schemes. J. Comput. Phys. 77, 439–471.
Teixeira, P.R.F., Davyt, D.P., Didier, E., Ramalhais, R., 2013. Numerical simulation of an oscillating water column device using a code based on Navier–Stokes equations. Energy 61, 513–530.
Thiruvenkatasamy, K., Neelamani, S., 1997. On the efficiency of wave energy Caissons in array. Appl. Ocean Res. 19, 61–72.
van der Vorst, H., 1992. BiCGStab: a fast and smoothly converging variant of bi-cg for the solution of nonsymmetric linear systems. SIAM J. Sci. Stat. Comput. 13, 631–644.
Wilcox, D.C., 1994. Turbulence Modeling for CFD. DCW Industries Inc., La Canada, CA.
Zhang, Y., Zou, Q.P., Greaves, D., 2012. Air–water two phase flow modelling of hydrodynamic performance of an oscillating water column device. Renew. Energy 41, 159–170.

Paper 8

Numerical Modeling of Power Take-off Damping in an Oscillating Water Column Device

Kamath A, Bihs H. and Arntsen Ø.A. (2015)
International Journal of Marine Energy 10, 1-16.

International Journal of Marine Energy 10 (2015) 1–16

Contents lists available at ScienceDirect

International Journal of Marine Energy

journal homepage: www.elsevier.com/locate/ijome

Numerical modeling of power take-off damping in an Oscillating Water Column device

Arun Kamath *, Hans Bihs, Øivind A. Arntsen

Department of Civil and Transport Engineering, Norwegian University of Science and Technology, 7491 Trondheim, Norway

ARTICLE INFO

Article history:
Received 15 September 2014
Revised 28 December 2014
Accepted 5 January 2015
Available online 10 January 2015

Keywords:
Oscillating Water Column
Computational Fluid Dynamics
Wave energy
Porous media
PTO damping
REEF3D

ABSTRACT

An Oscillating Water Column (OWC) is a wave energy converter consisting of a partially submerged chamber with an air column over the water column. The work done by the air column under excitation by the incident waves is used to generate electrical energy through a power take-off (PTO) device. The air column is under pressure due to the damping from the PTO device and this pressure is essential for the extraction of wave energy using the OWC. The relationship between the PTO damping and the hydrodynamic efficiency of the OWC provides more insight into the wave energy extraction using an OWC.

In this paper, two-dimensional Computational Fluid Dynamics (CFD) simulations are used to investigate the response of the OWC under different values of damping from the PTO device. The PTO damping on the chamber is represented using a linear pressure drop law with the permeability coefficient derived from Darcy's equation for flow through porous media. The model is validated by comparing the numerical results to experimental data. The influence of the PTO damping on the chamber pressure, the free surface motion, the velocity of the vertical motion of the free surface and the hydrodynamic efficiency of the OWC is studied. The hydrodynamic efficiency is calculated as the ratio of the power delivered at the vent of the OWC to the incident wave power. It is found that the PTO damping needed to attain the maximum OWC hydrodynamic efficiency increases with increasing incident wavelength. The formation of stagnation zones in the water due to high velocities for lower values of PTO damping is found to reduce the hydrodynamic efficiency.

* Corresponding author. Tel.: +47 73 59 46 40; fax: +47 73 59 70 21.
E-mail address: arun.kamath@ntnu.no (A. Kamath).

http://dx.doi.org/10.1016/j.ijome.2015.01.001
2214-1669/

Nomenclature

i, j, k	indices representing directions along the x-, y- and z-axis
u	velocity
t	time
ρ	density
p	pressure
ν	kinematic viscosity
ν_t	eddy viscosity
g	acceleration due to gravity
k	turbulent kinetic energy
ω	specific turbulent dissipation
P_k	turbulence production rate
$\sigma_k, \sigma_\omega, \alpha, \beta, \beta_k$	turbulence model closure coefficients
B	model parameter for free surface turbulence damping
dx	grid size
$\phi(\vec{x}, t)$	level set function
$\Gamma(x)$	relaxation function
P_{out}	power available at the vent
T	wave period
p_c	OWC chamber pressure
q	volume of air flowing through the vent
E_{in}	incident wave energy flux
a_0	incident wave amplitude
c_g	group velocity
η_{owc}	hydrodynamic efficiency of the OWC
l	width of the OWC device
L	length along the direction of flow through porous media
C	permeability coefficient
μ	absolute viscosity
k_p	intrinsic permeability of a porous medium
A_{cs}	cross-sectional area of the vent
η	variation of the free surface
w_{fs}	vertical velocity of the free surface motion
a	wave amplitude inside the OWC chamber
λ	incident wavelength
H	incident wave height
ξ	incident wave steepness (H/λ)

1. Introduction

An Oscillating Water Column (OWC) device is a renewable energy device used to convert incident wave energy into electrical energy. The device consists of a partially submerged chamber with an air column standing over the water column. The incident waves cause an oscillatory motion of the free surface of the water column, which transfers the motion to the air column. The air is then exhaled and inhaled through a vent in the chamber. A turbine which is the power take-off (PTO) device, is placed over the vent and the motion of the air column across the turbine is used to produce electrical energy. The vent opens to the atmosphere through the PTO device and this results in a pressure drop over the device chamber.

Evans [1] used a pair of parallel vertical plates to represent an OWC device to obtain a mathematical description of the working principles. A float connected to a spring-dashpot system on the free surface inside the device chamber was used to calculate the efficiency of the device under the

assumption of a rigid piston-like motion of the free surface in this work. In practice, the spatial variation of the free surface motion has an effect on the device efficiency. Evans [2] included the spatial variation of the free surface and derived expressions to calculate power absorption by the device using the volume flow of air and the chamber pressure. It was assumed that the air is incompressible in this scenario and the volume flow of air is equal to the product of the vertical velocity of the free surface and the surface area of the free surface. The hydrodynamic efficiency of the device is then calculated to evaluate the power available at the PTO device in comparison to the incident wave power. So, the device efficiency depends on the chamber pressure and the motion of the free surface. The damping on the OWC chamber due to the PTO device affects the chamber pressure, the free surface motion and consequently, the performance of the OWC.

In experimental investigations, the PTO damping is represented by porous membranes or vents of small dimensions. A study on the PTO device accounting for its linear and non-linear characteristics was presented by Sarmento and Falcão [3]. They presented analytical expressions for power absorbed by an OWC and the hydrodynamic efficiency considering two-dimensional variation in the free surface. They found that the power take-off was only marginally lesser for a PTO device with non-linear characteristics compared to a device with linear characteristics. Further, Sarmento [4] carried out experimental investigations on OWC devices in a wave flume and used filter membranes to represent the pressure drop from a linear PTO device and circular orifice plates to represent non-linear PTO devices to validate the theory presented in Sarmento and Falcão [3]. The importance of PTO damping on the device performance was also seen in experimental investigations by Thiruvenkatasamy and Neelamani [5], where the device efficiency was found to be very low when the area of the vent in the device was increased beyond 0.81% of the free surface area.

The relationship between the PTO damping and the OWC hydrodynamics can be used to improve the efficiency of the OWC. Numerical modeling of an OWC including the PTO damping can provide useful insight into the change in the OWC hydrodynamics under different values of PTO damping for different incident wavelengths. This provides the knowledge required to effectively tune the PTO damping with respect to the incident wavelength to obtain the maximum hydrodynamic efficiency. In this direction, Didier et al. [6] explored the use of porous media theory to model the PTO damping numerically with a linear pressure drop law on a simplified representation of the OWC device as a thin cylinder. López et al. [7] studied the optimization of turbine induced damping on an OWC device using a CFD model after validating the model with data from physical model tests. They concluded that each incident wavelength has an optimal damping condition. They varied the PTO damping in the numerical model by changing the dimensions of the OWC vent. The high air velocities resulting from small vent sizes make a simulation very expensive without adding much detail to the hydrodynamics of the OWC. Thus, a different approach that is computationally efficient and represents the hydrodynamics accurately can help to further investigate of the hydrodynamics of an OWC device including the PTO characteristics.

The objective of this study is to investigate the influence of PTO damping on the OWC chamber and on the hydrodynamics in and around the OWC under different incident wave conditions. An open-source CFD model is used to simulate an OWC in a two-dimensional numerical wave tank. First, the numerical model is validated by comparing the chamber pressure, variation of the free surface inside the chamber and the vertical velocity of the free surface with experimental data from Morris-Thomas et al. [8]. Then, the variation of the chamber pressure and the free surface inside the chamber is calculated numerically for different wavelengths, wave heights and PTO damping. The effect of the PTO damping on the chamber pressure, free surface and power absorption under different values of incident wavelengths and wave heights on the OWC is studied.

2. Numerical model

2.1. Governing equations

The open-source CFD model, REEF3D [9] uses the incompressible Reynolds-averaged Navier–Stokes (RANS) equations along with the continuity equation to solve the fluid flow problem:

$$\frac{\partial u_i}{\partial x_i} = 0 \tag{1}$$

$$\frac{\partial u_i}{\partial t} + u_j \frac{\partial u_i}{\partial x_j} = -\frac{1}{\rho}\frac{\partial p}{\partial x_i} + \frac{\partial}{\partial x_j}\left[(\nu + \nu_t)\left(\frac{\partial u_i}{\partial x_j} + \frac{\partial u_j}{\partial x_i}\right)\right] + g_i \tag{2}$$

where u is the velocity averaged over time t, ρ is the fluid density, p is the pressure, ν is the kinematic viscosity, ν_t is the eddy viscosity and g is the acceleration due to gravity.

The pressure is determined using Chorin's projection method [10] and the resulting Poisson pressure equation is solved using a preconditioned BiCGStab solver [11]. Turbulence modeling is carried out by the two-equation k-ω model proposed by Wilcox [12]. The transport equations for the turbulent kinetic energy, k and the specific turbulent dissipation rate, ω are given by:

$$\frac{\partial k}{\partial t} + u_j \frac{\partial k}{\partial x_j} = \frac{\partial}{\partial x_j}\left[\left(\nu + \frac{\nu_t}{\sigma_k}\right)\frac{\partial k}{\partial x_j}\right] + P_k - \beta_k k\omega \tag{3}$$

$$\frac{\partial \omega}{\partial t} + u_j \frac{\partial \omega}{\partial x_j} = \frac{\partial}{\partial x_j}\left[\left(\nu + \frac{\nu_t}{\sigma_\omega}\right)\frac{\partial \omega}{\partial x_j}\right] + \frac{\omega}{k}\alpha P_k - \beta\omega^2 \tag{4}$$

$$\nu_t = \frac{k}{\omega} \tag{5}$$

where, P_k is the production rate, ν_t is the eddy viscosity and closure coefficients $\sigma_k = 2,\ \sigma_\omega = 2,\ \alpha = 5/9,\ \beta_k = 9/100,\ \beta = 3/40$. The oscillatory nature of wave propagation results in large gradients or strain in the flow. The production terms in the turbulence model are directly dependent on the strain. This results in an unphysical overproduction of turbulence in the case of wave propagation. This is avoided by introducing a stress limiter in the definition of eddy viscosity based on the Bradshaw et al. [13] assumption and as demonstrated by Durbin [14]:

$$\nu_t \leqslant \sqrt{\frac{2}{3}}\frac{k}{|\mathbf{S}|} \tag{6}$$

where $\mathbf{S}$ represents the source terms in the transport equations.

In a two-phase numerical model, the large difference between the density of air and water results in a large strain at the free surface. The free surface in reality is a natural boundary which dampens the eddy viscosity but this effect is not accounted for by the k–ω model. The overproduction of turbulence in this case is reduced using free surface turbulence damping using a source term in the specific turbulent dissipation equation as shown by Egorov [15]:

$$S_n = \left(\frac{6B\nu}{\beta dx^2}\right)^2 \beta\ dx\ \delta(\phi) \tag{7}$$

where, model parameter B is set to 100.0 and dx is the grid size. The damping is carried out only at the free surface using the Dirac delta function, $\delta(\phi)$.

2.2. Discretization schemes

Discretization of the convective terms in the RANS equations is carried out using the fifth-order finite difference Weighted Essentially Non-Oscillatory (WENO) scheme proposed by Jiang and Shu [16] and the Hamilton–Jacobi formulation of the WENO scheme Jiang and Peng [17] is used to discretize the level set function ϕ, turbulent kinetic energy k and the specific turbulent dissipation rate ω. The scheme is a minimum third-order accurate in the presence of large gradients and shocks and provides the accuracy required to model complex free surface flows. A Total Variation Diminishing (TVD) third-order Runge–Kutta scheme [18] is used for time advancement of the momentum equation, the level set function and the reinitialisation equation. The time steps in the simulation are determined using an adaptive time stepping strategy satisfying the Courant–Frederick–Lewy (CFL) criterion. The time advancement of k and ω is carried out using a first-order implicit scheme as these terms are mainly source term driven with a low influence from convective terms. The implicit treatment of these

terms avoids small time steps resulting from large source terms in the turbulence model. The diffusion terms of the velocities are also removed from the CFL criterion by using an implicit scheme to handle these terms.

The numerical model uses a uniform Cartesian grid for spatial discretization and the implementation of higher-order finite difference schemes is straight-forward. The Immersed Boundary Method (IBM) [19] is used to handle the boundary conditions for complex geometries. This method extrapolates values from the fluid into the solid region using ghost cells. The numerical model is completely parallelised using the MPI library and can be executed on high performance computing systems.

2.3. Free surface

The free surface in the numerical wave tank is obtained using the level set method, where the interface between two fluids is represented by the zero level set of the level set function, $\phi(\vec{x}, t)$. The level set function gives the closest distance of each point in the domain from the interface and the two fluids are distinguished by the sign of the function. This signed distance function is defined as:

$$\phi(\vec{x},t)\begin{cases} > 0 & \text{if } \vec{x} \text{ is in phase 1} \\ = 0 & \text{if } \vec{x} \text{ is at the interface} \\ < 0 & \text{if } \vec{x} \text{ is in phase 2} \end{cases} \tag{8}$$

The definition of the level set function makes it continuous across the interface and provides a sharp representation of the free surface. The level set function is convected under the velocity field in the wave tank. The signed distance property of the function is lost by the motion of the free surface and it is restored by reinitializing the function after every iteration using the partial differential equation based procedure by Peng et al. [20].

2.4. Numerical wave tank

Wave generation and absorption in the numerical wave tank is carried out using the relaxation method [21]. In this method, relaxation functions are used to moderate the computational values with an analytical solution from wave theory in specific parts of the numerical wave tank reserved for wave generation and absorption, called relaxation zones. The relaxation method has been implemented by several authors like Mayer et al. [22], Engsig-Karup [23], and Jacobsen et al. [24]. The relaxation functions presented by Engsig-Karup [23] listed in Eq. (9) are implemented in the numerical model using three relaxation zones as illustrated in Fig. 1.

$$\Gamma(x)\begin{cases} = -2x^3 + 3x^2 & \text{for relaxation zone 1} \\ = -2(1-x)^3 + 3(1-x)^2 & \text{for relaxation zone 2} \\ = (1-x)^6 & \text{for wave absorption zone} \end{cases} \tag{9}$$

where $\Gamma(x)$ is called the relaxation function and $x \in [0, 1]$ is the length scale along the relaxation zone.

The waves are generated in the first relaxation zone, where the analytical values for velocity and free surface elevation from wave theory are gradually prescribed into the numerical wave tank. The second zone, placed right after the first zone, prevents reflections from the working zone of the wave tank from affecting the wave generation. The working zone of the wave tank is next to the second

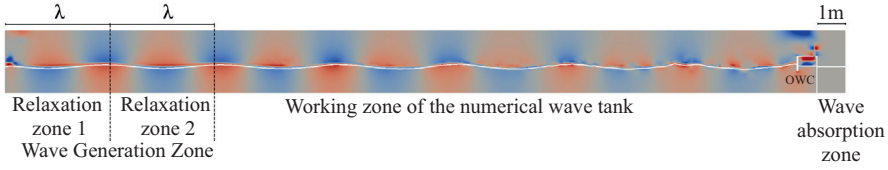

Fig. 1. Numerical wave tank showing the relaxation zones and the OWC.

relaxation zone and the objects to be studied are placed here. The third relaxation zone is placed at the far end of the numerical wave tank and is responsible for wave absorption. In this zone, the computational value of the velocity is smoothly brought to zero, the free surface elevation returned to the still water level and the pressure to its hydrostatic value. In this way, the wave energy is smoothly removed from the numerical wave tank without reflections from the boundary affecting the results in the working zone. The relaxation functions prescribe the values for the velocity and the free surface elevation in the relaxation zones using Eq. (10) with the corresponding relaxation functions.

$$\begin{aligned} u_{\text{relaxed}} &= \Gamma(x)u_{\text{analytical}} + (1-\Gamma(x))u_{\text{computational}} \\ \phi_{\text{relaxed}} &= \Gamma(x)\phi_{\text{analytical}} + (1-\Gamma(x))\phi_{\text{computational}} \end{aligned} \tag{10}$$

In this way, the required values are introduced into the numerical wave tank gradually, ensuring smooth wave generation and absorption.

3. Hydrodynamic efficiency of an OWC device

Hydrodynamic efficiency of an OWC provides a measure of the wave power available at the OWC chamber vent for the production of electrical energy by the PTO device. The hydrodynamic efficiency is used to investigate the effect of the OWC geometric configuration and PTO characteristics on the wave power absorption. The wave energy incident on the device chamber causes the free surface inside the chamber to oscillate and this energy is transferred to the air column above it. The presence of a PTO device results in a pressure in the chamber and the wave power absorbed is calculated as the work done by the air column under this pressure. The power available at the turbine P_{out}, per wave cycle of period T is measured as the time average of the product of the chamber pressure, p_c and the volume of air flowing through the vent q [2]:

$$P_{\text{out}} = \frac{1}{T}\int_0^T p_c(t)q(t)dt \tag{11}$$

Due to the small scale of the device and the chamber pressures developed, the air in the chamber is considered to be incompressible and the volume of air flowing through the vent is calculated as the product of the velocity of the free surface and the cross-sectional area of the chamber. The value for pressure is available at every point in the chamber for every time step from the Poisson pressure equation. So, the power available at the vent can be easily calculated. The incident wave energy flux, E_{in} is calculated as the product of energy content of the wave and the group velocity of the wave:

$$E_{\text{in}} = \frac{1}{2}\rho g a_0^2 c_g \tag{12}$$

where a_0 is the incident wave amplitude and c_g is the group velocity.

This provides the wave power incident per meter width of the device and the wave power incident on the device is calculated by multiplying the width of the device, l. The hydrodynamic efficiency of the device is then calculated as the ratio between the wave power available at the vent to the incident wave power:

$$\eta_{\text{owc}} = \frac{P_{\text{out}}}{E_{\text{in}}\, l} \tag{13}$$

4. Modeling the PTO damping

The PTO damping on the device chamber from the PTO device is modeled using the porous media flow relation. A PTO device such as the Wells turbine which has linear pressure drop characteristics can be effectively represented by a linear pressure drop law in model testing [3,25]. The porous media in the vent models the PTO damping, accounting for the pressure and free surface motion in the OWC chamber in the numerical model. A linear pressure drop law is implemented in the numerical model as:

$$\frac{\Delta p}{L} = -C\mu q \tag{14}$$

where μ is the dynamic viscosity of the fluid, Δp is the pressure drop across the vent, C is the permeability coefficient and L is the length along the direction of the flow. The permeability coefficient $C = 1/k_p$ is determined using Darcy's law for flow through porous media:

$$q = \frac{-k_p A_{cs}}{\mu} \frac{\Delta p}{L} \tag{15}$$

where k_p is the intrinsic permeability, q is the flow rate and A_{cs} is the cross-sectional area.

In this study, the flow rate q and the pressure drop across the vent Δp are known from the experimental data [8]. The values for the pressure drop and for the volume flow of air across the vent from the experiments under conditions close to resonance are used. The variables A_{cs} and L are known from the device configuration and μ is a known constant. Thus, the value of intrinsic permeability can be determined by solving Eq. (15) for k_p, which is used to determine the permeability coefficient C. In a practical scenario, the pressure drop and air flow across the turbine is known from the turbine characteristics and those values can be used to investigate the performance of the device. The porous media relation is then used at the vent to model PTO damping. In this way, the PTO damping in the numerical model is represented independent of the dimensions of the vent size and the influence of PTO damping on the device can be studied by varying the value of C.

5. Results and discussion

At first, the grid size for accurate wave generation and propagation in the numerical wave tank is determined using a grid refinement study. Linear waves of wavelength $\lambda = 4.0$ m and height $H = 0.12$ m with wave steepness $\xi = H/\lambda = 0.03$ are generated in a two-dimensional numerical wave tank 20 m long, 2.20 m high and with a water depth $d = 0.92$ m. The grid sizes are varied between $dx = 0.1$ m, $dx = 0.05$ m, $dx = 0.025$ m and $dx = 0.01$ m. It is seen from Fig. 2 that the waveform converges to the analytical envelope expected from the linear wave theory at a grid size of 0.025 m. This grid size is then used for all the numerical simulations carried out in the study.

5.1. Validation

The experimental setup used in Morris-Thomas et al. [8] is simulated to validate the numerical model. The experiments were carried out at the University of Western Australia in a wave tank of length 50 m and width 1.5 m. The model OWC was placed 37.5 m from the wavemaker. The PTO device was represented by a rectangular vent of width $b_v = 0.005$ m in the roof of the chamber 0.05 m from the rear wall. The same geometry is replicated in the numerical simulations with a minor change in the representation of the PTO device, where the vent width b_v is set to 0.05 m. The pressure drop equation (Eq. (14)) is to determine the value of C required to obtain the same pressure drop across a vent of width $b_v = 0.05$ m as that across a vent of width $b_v = 0.005$ m in the experiments. Using the experimental data for $\lambda = 4.07$ m, where $\Delta p = 500$ Pa, $q = 0.11$ m^3/s in Eq. (14), results in $C_{exp} = 5 \times 10^8$ m^{-2} for providing the same pressure drop and volume flux across a vent of width $b_v = 0.05$ m in the numerical model. A schematic diagram of the setup is shown in Fig. 3. The porous media in the numerical model is validated by simulating different incident wavelengths on the OWC with $C_{exp} = 5 \times 10^8$ m^{-2} used for the porous layer in the vent.

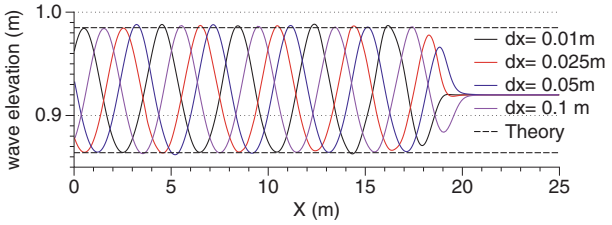

Fig. 2. Grid convergence for incident waves with $\lambda = 4.07$ m and $H = 0.12$ m.

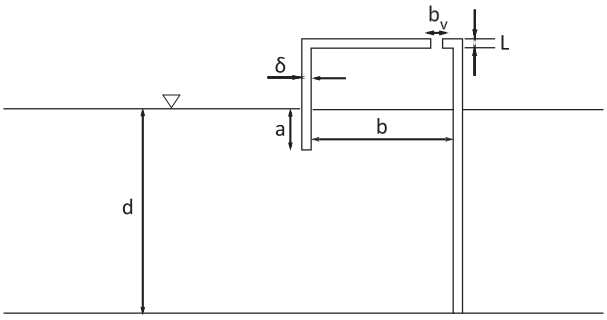

Fig. 3. Configuration of the OWC device.

In the first case, waves of wavelength $\lambda = 4.07$ m and height $H = 0.12$ m are incident on the OWC device in a water depth of $d = 0.92$ m. The device shows resonant response and has the maximum efficiency in the experiments for this wavelength. The device has a front wall draught $c = 0.15$ m and front wall thickness $\delta = 0.05$ m, a chamber length $b = 0.64$ m and a chamber height of 1.275 m. The first and the second relaxation zones are kept one wavelength long and the wave absorption zone is 1 m long. The device covers the entire width of the tank and the wave absorption zone does not have an important influence on the simulation.

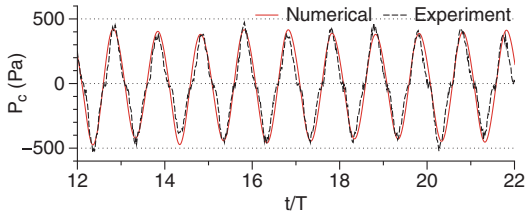

(a) variation of chamber pressure

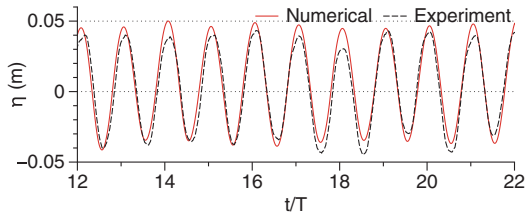

(b) relative free surface elevation at the centre of the chamber

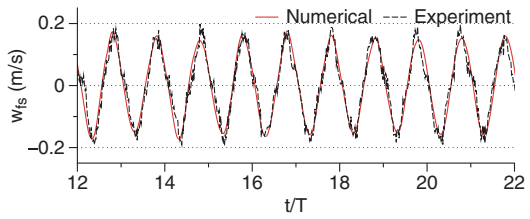

(c) velocity of the free surface

Fig. 4. Comparison experimental and numerical results for chamber pressure, free surface elevation and velocity of the free surface inside the chamber for $\lambda = 4.07$ m.

The variation of the chamber pressure $p_c(t)$ and the free surface at the center of the chamber $\eta(t)$ is calculated and compared with the experimental observations in Fig. 4a and b, respectively. The velocity of the free surface motion, w_{fs} is calculated using the free surface motion in the numerical simulations and experimental data and presented in Fig. 4c. A good agreement is seen between the numerical results and the experimental observations in these figures. This wavelength of $\lambda = 4.07$ m corresponds to the resonant frequency of the OWC chamber and the maximum efficiency was observed in the experiments for this incident wavelength. In spite of being the resonant condition, the free surface oscillations are not amplified (Fig. 4b) due to the PTO damping on the chamber but a large part of the incident wave energy is transferred from the water column to the air column resulting in a maximum efficiency at this incident wavelength.

Next, simulations are carried out with incident wavelengths of $\lambda = 5.07$ m and $\lambda = 2.90$ m with a wave height of $H = 0.12$ m. These wavelengths lie on either sides of the resonant wavelength and are used to study the device performance away from resonance. The variation of the chamber pressure p_c, free surface at the center of the chamber η and the velocity of the free surface w_{fs} for $\lambda = 5.07$ m is presented in Fig. 5 and a good agreement is seen between the numerical and experimental results. Similarly, a good agreement is seen between the numerical results and the experimental observations for the variation of the chamber pressure p_c, the free surface in the chamber η and the velocity of the free surface w_{fs} for $\lambda = 2.90$ m in Fig. 6. The free surface motion in these cases is further damped compared to the free surface motion in the resonant case.

It seen that a good representation of the fluid dynamics in the device chamber is obtained from the numerical model. It is also confirmed that a value of $C_{exp} = 5 \times 10^8$ m^{-2} provides the same pressure

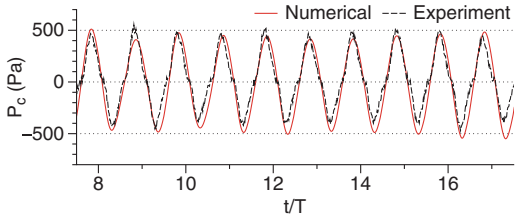

(a) variation of chamber pressure

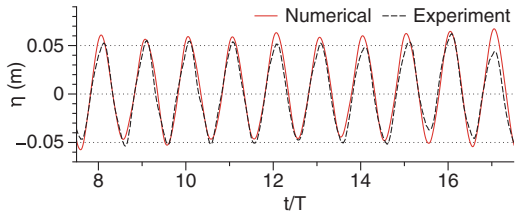

(b) relative free surface elevation at the centre of the chamber

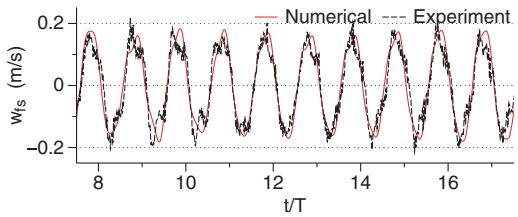

(c) velocity of the free surface

Fig. 5. Comparison experimental and numerical results for chamber pressure, free surface elevation and velocity of the free surface inside the chamber for $\lambda = 5.07$ m.

drop on a vent of width $b_v = 0.05$ m as that provided by a vent of width $b_v = 0.005$ m in the experiments. Thus, C_{exp} is taken to be the standard value of damping and then varied to study the influence of the PTO damping on the performance of the device. The cross-sectional area of the vent in the numerical model is larger than in the experiments and is higher than 0.81% of the free surface area. The damping provided by the vent is insufficient to develop the chamber pressure necessary for energy extraction from the device [5] and the porous media in the vent is responsible for the PTO damping.

5.2. Effect of PTO damping

In order to study the effect of PTO damping on the performance of the OWC device, the permeability coefficient C in Eq. (14) is varied. Simulations are carried out with values of $C_0, C_1, C_2, C_3, C_4, C_6$ and C_{10} with values listed in Table 1 to investigate the effect of PTO damping. The case without PTO damping (C_0) represents an OWC with a pressure drop from a vent of width $b_v = 0.05$ m. A total of 72 simulations with the 8 different values of the permeability coefficient C, for three different incident wavelengths λ are carried out for wave heights $H = 0.06$ m, $H = 0.12$ m and a constant wave steepness $\xi = 0.03$.

First, simulations are carried out with an incident wave height of $H = 0.06$ m for wavelengths $\lambda = 2.90$ m, 4.07 m and 5.07 m with permeability coefficients C_0 to C_{10}. The amplitudes of the chamber pressure p_c, the relative free surface in the chamber a/a_0, the vertical velocity of the free surface motion inside the chamber w_{fs} and the hydrodynamic efficiency of the OWC η_{owc} for the different incident wavelengths simulated are presented in Fig. 7. The chamber pressure is seen to increase as the

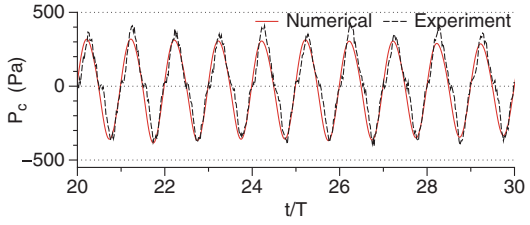

(a) variation of chamber pressure

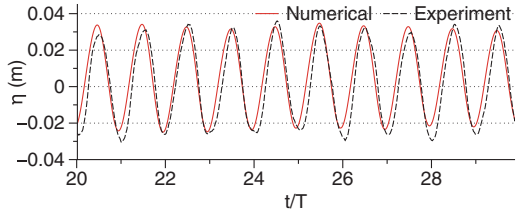

(b) relative free surface elevation at the centre of the chamber

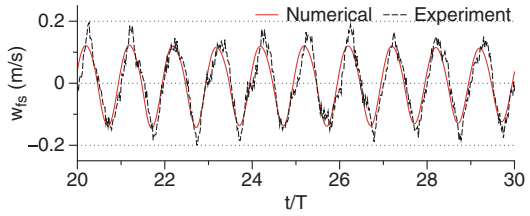

(c) velocity of the free surface

Fig. 6. Comparison experimental and numerical results for chamber pressure, free surface elevation and velocity of the free surface inside the chamber for $\lambda = 2.90$ m.

Table 1
List of damping values used in the simulations.

C	Value	Implication
C_0	0	No damping
C_1	1×10^8	Low damping
C_2	2×10^8	Low damping
C_3	3×10^8	Moderate damping
C_4	4×10^8	Moderate damping
C_{exp}	5×10^8	From experimental data
C_6	6×10^8	High damping
C_{10}	10×10^8	High damping

value of C is increased from C_0 to C_{10} in Fig. 7a. The longest wavelength simulated, $\lambda = 5.07$ m results in the largest chamber pressure for all values of C. The damping of the free surface motion inside the OWC chamber is seen in Fig. 7b. The relative free surface motion is about two times the incident amplitude for $\lambda = 5.07$ m under zero damping (C_0) and reduces to about 0.4 times the incident amplitude under high damping of C_{10}. For an incident wavelength of $\lambda = 4.07$, the maximum free surface elevation is $1.5a_0$ at C_0 and reduces to $0.35a_0$ at C_{10}. The free surface elevation inside the chamber reduces from $1.35a_0$ at C_0 to $0.2a_0$ at C_{10} for an incident wavelength of $\lambda = 2.90$ m. Thus, the free surface oscillations reduce with decreasing incident wavelength and increasing values of PTO damping.

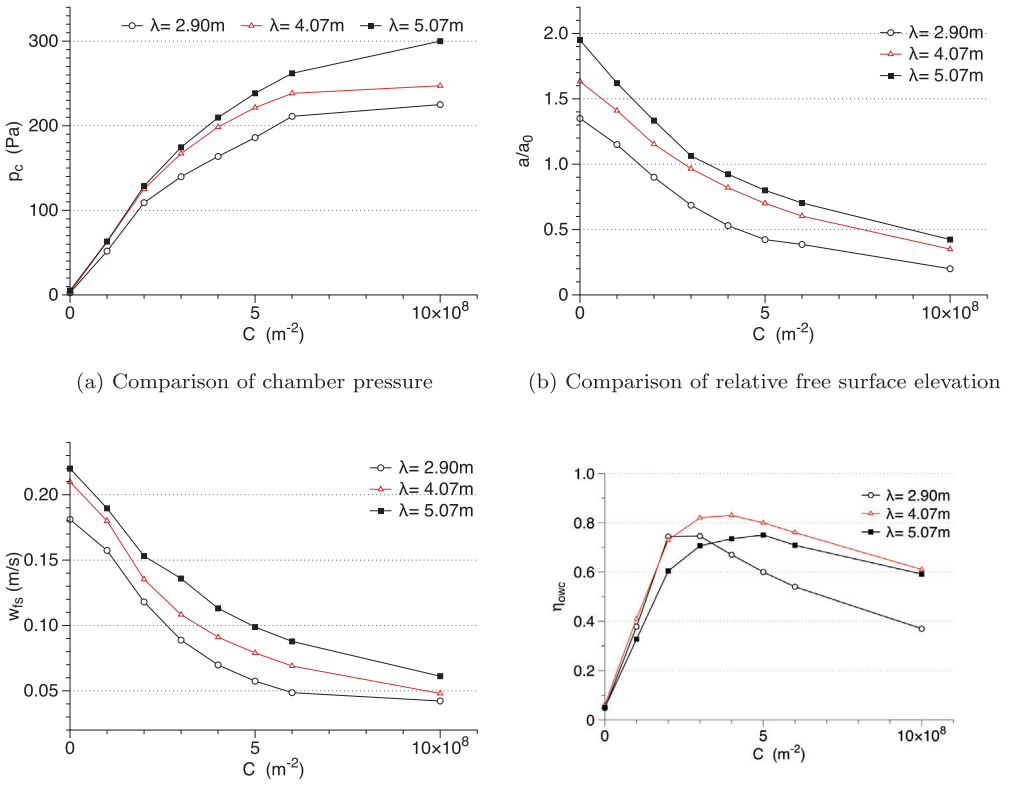

(a) Comparison of chamber pressure

(b) Comparison of relative free surface elevation

(c) Comparison of free surface velocity

(d) Comparison of OWC hydrodynamic efficiency

Fig. 7. Variation of chamber pressure, relative free surface amplitude, free surface velocity and OWC hydrodynamic efficiency for different wavelengths under different values of C for a constant wave height $H = 0.06$.

The vertical velocity of the free surface motion shows a similar trend where the velocity w_{fs} decreases with a decrease in wavelength and an increase in the PTO damping.

The hydrodynamic efficiency of the OWC initially increases with increasing PTO damping and then reduces after attaining a maximum value. In the case of the shortest wavelength simulated, $\lambda = 2.90$ m, η_{owc} reaches a maximum of 0.745 at C_3 and then reduces to 0.37 at C_{10}. The hydrodynamic efficiency for an incident wavelength of $\lambda = 4.07$ m reaches a maximum of 0.83 at C_4 and reduces to 0.61 at C_{10}. For an incident wavelength of $\lambda = 5.07$ m, a maximum value of 0.75 is seen for C_5 and the hydrodynamic efficiency reduces to 0.59 for C_{10}. Thus, it is seen that an increase in PTO damping results in an increase in the chamber pressure p_c and a decrease in the free surface elevation and the velocity of the free surface motion inside the OWC chamber. The hydrodynamic efficiency η_{owc} increases with increasing PTO damping, reaches a maximum and then reduces with further increase in the PTO damping for all the wavelengths. It is also observed that the PTO damping resulting in the maximum efficiency for a given wavelength increases with increasing incident wavelength.

Next, simulations are carried out with an incident wave height of $H = 0.12$ m. The chamber pressure increases with increasing PTO damping in Fig. 8a. The free surface amplitude and the velocity of the free surface in the OWC chamber reduce with an increase in the PTO damping in Figs. 8b and c. This variation of the chamber pressure, the relative free surface and the vertical velocity of the free surface with the PTO damping is similar to that seen for an incident wave height of $H = 0.06$ m. The variation in the hydrodynamic efficiency of the OWC with the PTO damping for the different wavelengths in Fig. 8d is similar but with certain differences to that seen for $H = 0.06$ m. The hydrodynamic efficiency increases with increase in PTO damping, reaches a maximum and reduces with

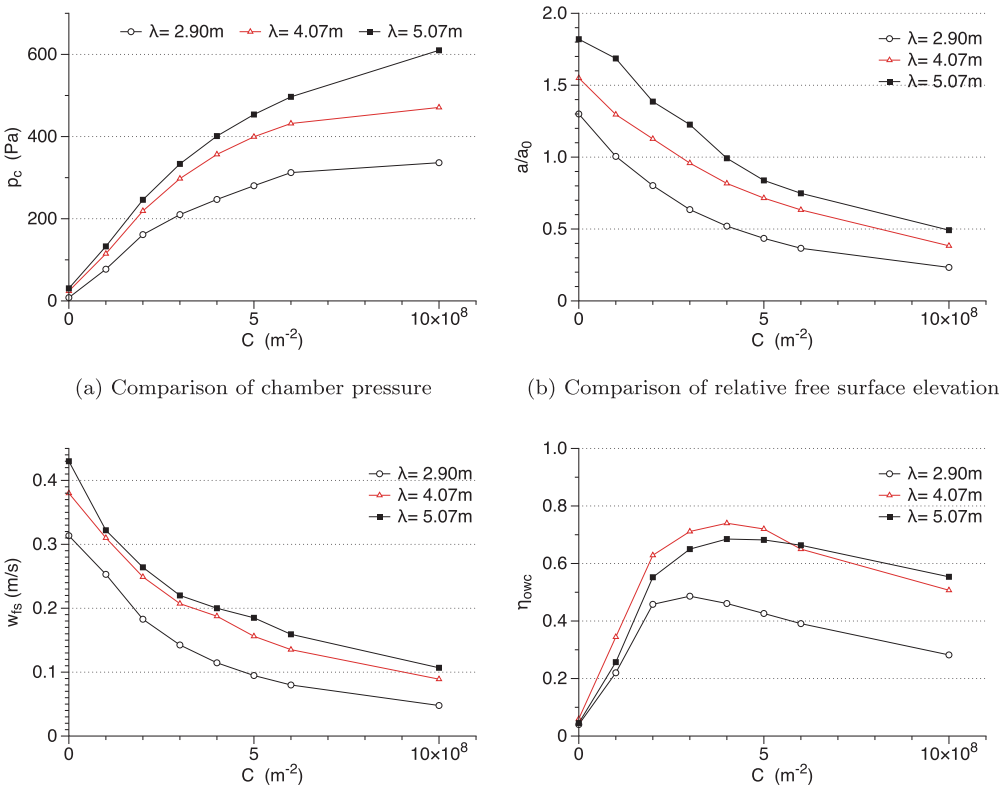

(a) Comparison of chamber pressure

(b) Comparison of relative free surface elevation

(c) Comparison of free surface velocity

(d) Comparison of OWC hydrodynamic efficiency

Fig. 8. Variation of chamber pressure, relative free surface amplitude, free surface velocity and OWC hydrodynamic efficiency for different wavelengths under different values of C for a constant wave height $H = 0.12$.

further increase in the PTO damping as seen for $H = 0.06$ m previously. Also, the maximum efficiencies are attained at the same values of C for each of the wavelengths. The difference is that the maximum efficiencies for every wavelength at every value of PTO damping is lower than that seen for $H = 0.06$ m. Thus, it is seen that the hydrodynamic efficiency of the device reduces with increasing wave amplitude for the same wavelength and damping conditions.

The investigations with a constant wave height for different wavelengths results in different wave steepnesses for the different cases. The wave steepness can influence the wave interaction with the OWC device. So, the influence of the PTO damping over various wavelengths for a constant wave steepness of $\xi = 0.03$ is investigated. The variation of $p_c, a/a_0$ and w_{fs} presented in Fig. 9 are similar to that seen previously for both $H = 0.06$ and $H = 0.12$ m. The curves for $\lambda = 4.07$ m and $\lambda = 5.07$ m lie close to each other and away from the curve for $\lambda = 2.90$ m because the incident wave heights are proportional to the wavelengths in these cases.

The hydrodynamic efficiency of the OWC for different wavelengths is shown in Fig. 9d. The efficiency for $\lambda = 2.90$ m in this case is lower than that computed for $H = 0.06$ m but higher than in the case of $H = 0.06$ m. The incident wave steepness $\xi = 0.03$ for $\lambda = 2.90$ m results in a wave height of $H = 0.087$ m in this case. Thus, the decrease in hydrodynamic efficiency with an increase in incident wave height is further affirmed. In the case of $\lambda = 4.07$, the wave height is $H = 0.122$ m resulting in an efficiency curve similar to that for $H = 0.12$ m and lower than the efficiency for $H = 0.06$ m. The efficiency in the case of $\lambda = 5.07$ m is the lower than that seen for $H = 0.06$ m and $H = 0.12$ m, as the wave height in this case is 0.152 m.

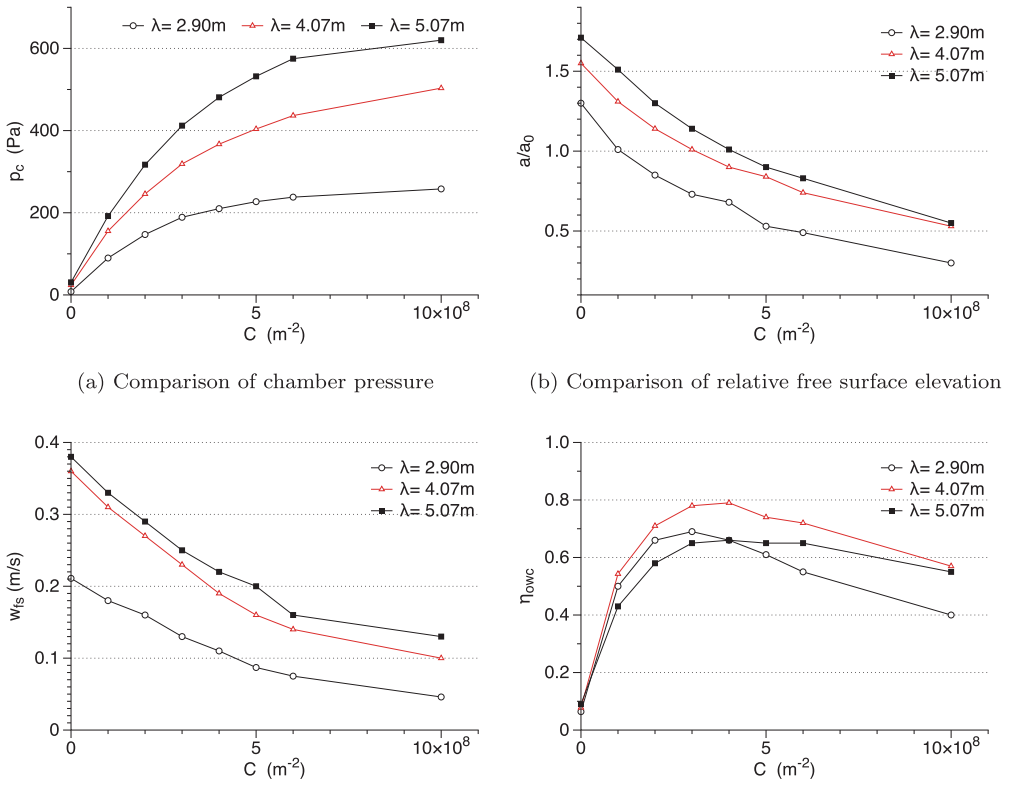

(a) Comparison of chamber pressure

(b) Comparison of relative free surface elevation

(c) Comparison of free surface velocity

(d) Comparison of OWC hydrodynamic efficiency

Fig. 9. Variation of chamber pressure, relative free surface amplitude, free surface velocity and OWC hydrodynamic efficiency for different wavelengths under different values of C for a constant steepness $\xi = 0.03$.

It is also observed that the maximum efficiency for $\lambda = 2.90$ m, 4.07 m and 5.07 m are computed at C_3, C_4 and C_5, respectively. These values remain the same for $H = 0.06$ m, $H = 0.12$ m and $\xi = 0.03$. Thus, the maximum hydrodynamic efficiency at a particular incident wavelength is obtained at a particular value of PTO damping. The wavelength resulting in the maximum efficiency also remains the same under different values of PTO damping for a given geometry of the OWC. The OWC attains the maximum efficiency for shorter wavelengths at lower PTO damping and at a higher PTO damping for longer wavelengths. In the absence of PTO damping (C_0), the OWC fails to effectively deliver the incident wave energy to the vent. In this case, there is a large motion of the water column motion but the air column is not under sufficient pressure to result in meaningful work though its motion. The efficiency is also lowered in the case of very high PTO damping (C_{10}). This is justified by the fact that in a highly damped OWC chamber, the motion of the water column is extremely damped and the volume flux of air through the vent is reduced.

From the results presented above, the PTO damping has an influence on the chamber pressure, motion of the free surface in the chamber and the hydrodynamic efficiency of the device. The influence of the PTO damping on the hydrodynamics of the device is further investigated by studying the streamlines in and around the OWC device for the incident wavelength of $\lambda = 4.07$ m for different

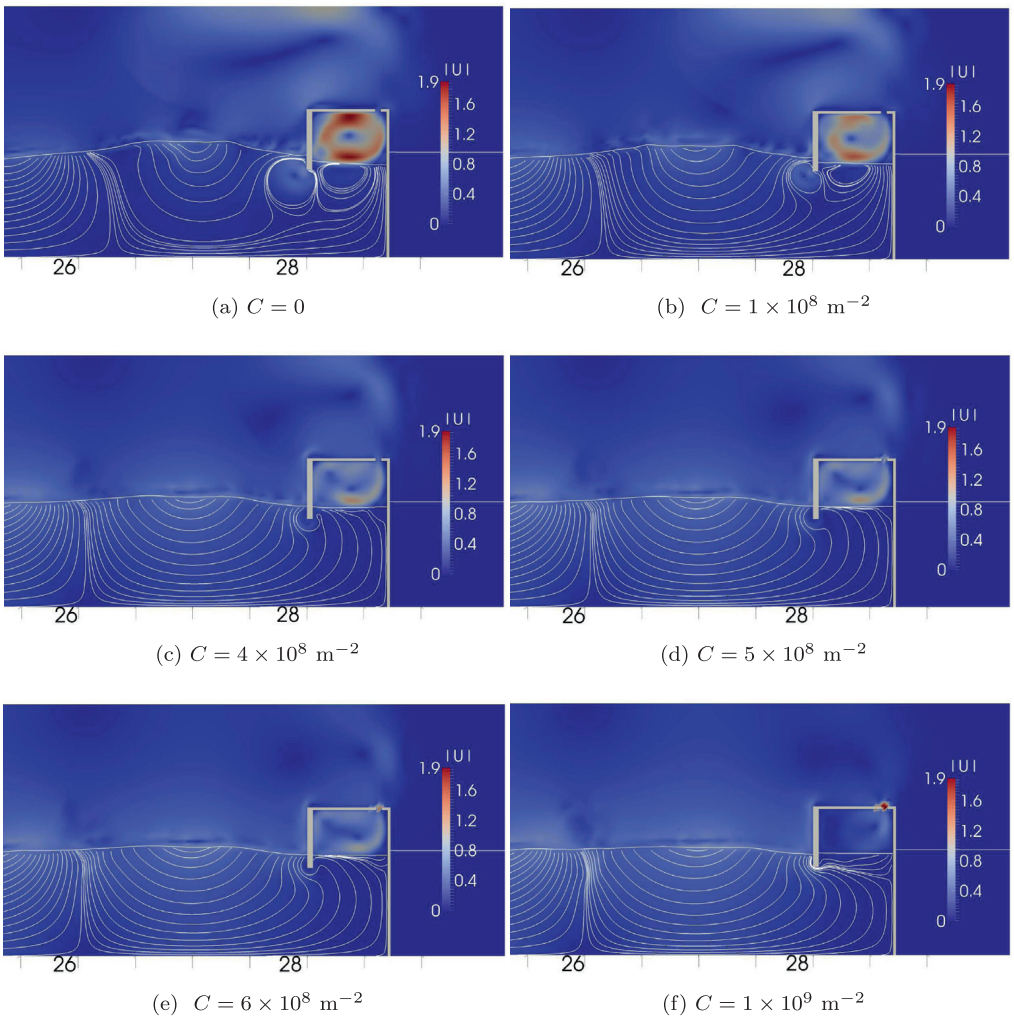

(a) $C = 0$ (b) $C = 1 \times 10^8$ m^{-2}

(c) $C = 4 \times 10^8$ m^{-2} (d) $C = 5 \times 10^8$ m^{-2}

(e) $C = 6 \times 10^8$ m^{-2} (f) $C = 1 \times 10^9$ m^{-2}

Fig. 10. Streamlines in front of the device and free surface in the chamber for $\lambda = 4.07$ m for different values of C at $t/T = 12.56$.

values of C at the same time during the simulation. The development of large stagnation zones in the water is seen in Fig. 10a and b for C_0 and C_1. A low PTO damping results in a low chamber pressure, a large amplitude of free surface oscillation and a high free surface velocity. Under these conditions, most of the wave energy is trapped in the large stagnation zones formed in and around the device. The size of the stagnation zones is reduced as the PTO damping on the chamber is increased in Fig. 10f. The increased PTO damping reduces the velocity of the free surface and a higher chamber pressure is developed. The optimum PTO damping creates conditions under which the hydrodynamic losses from stagnation zones and vortex formation in the water is reduced. Thus, a higher amount of the incident wave energy is available at the vent. This shows that the PTO damping on the device not only affects the conditions inside the chamber, but has significant effects on the hydrodynamics of the device and its interaction with the surrounding environment.

Thus, in the modeling, design and optimization of an OWC wave energy converter, the effect of the PTO damping should be taken into consideration as it affects the prevalent conditions inside the chamber and the hydrodynamics around the device. Also, the PTO damping could be adjusted according to the wave climate to tune the device for maximum hydrodynamic efficiency under the incident wave conditions.

6. Conclusions

A CFD model is used to study the effect of PTO damping on the OWC chamber in a two-dimensional numerical wave tank. Darcy's law for flow through porous media is used to model the PTO damping on the device chamber. The numerical model is validated by comparing the variation of the pressure, the free surface and the velocity of the free surface in the device chamber with experimental data from Morris-Thomas et al. [8]. It is seen from the results that the selected modeling approach represents the OWC hydrodynamics in a realistic manner. The size of the vent in the OWC device in the numerical model is kept large enough so that the damping provided by it is extremely low. So, the PTO damping is solely represented using the porous media in the vent of the OWC while preserving the geometry of the device used in the experiments. The influence of PTO damping on the chamber pressure, free surface motion inside the chamber and the efficiency of the device for different incident wave heights and wavelengths is investigated and the following conclusions are drawn:

- The hydrodynamic efficiency of an OWC decreases with increasing incident wave height.
- Increasing the PTO damping leads to a higher chamber pressure, lower free surface motion and lower velocity of the free surface motion for all the incident wavelengths.
- Hydrodynamic efficiency increases with increasing PTO damping, reaches a maximum value and reduces on a further increase in PTO damping.
- Maximum hydrodynamic efficiency for a given wavelength is seen to occur at a certain fixed value of PTO damping.
- The PTO damping resulting in maximum efficiency increases with increasing wavelength.
- Maximum hydrodynamic efficiency of an OWC can be achieved by tuning the PTO damping with respect to the incident waves. This increases the efficiency at incident wavelengths away from the resonant wavelength.
- Large stagnation zones are formed in front of the OWC and inside the chamber at lower PTO damping, which trap the wave energy and reduce the hydrodynamic efficiency of the OWC.
- An optimum value of PTO damping results in a reduction in the size of the stagnation zones and allows for sufficient motion of the pressurized air column in the OWC chamber, producing the maximum hydrodynamic efficiency.

Thus, the hydrodynamic efficiency of an OWC depends not only on the incident wavelength, but also on the wave height and the PTO damping. The PTO damping has a large influence on the hydrodynamics of an OWC and this can be used to attain the maximum possible hydrodynamic efficiency for a given incident wavelength. These results at a model scale do not include the effects of air compressibility. Further studies can be carried out at a large scale to account for air compressibility and also develop a formal relationship between the PTO damping and the OWC hydrodynamic efficiency.

Acknowledgements

The authors thank Michael Morris-Thomas, Principal Naval Architect, Worley Parsons, Perth, Australia for the experimental data and helpful discussions. This study has been carried out under the OWCBW project (No. 217622/E20) and the authors are grateful to the grants provided by the Research Council of Norway. This study was supported in part with computational resources at the Norwegian University of Science and Technology (NTNU) provided by NOTUR, http://www.notur.no.

References

[1] D.V. Evans, Oscillating water column wave energy convertors, IMA J. Appl. Math. 22 (1978) 423–433.
[2] D.V. Evans, Wave power absorption by systems of oscillating surface pressure distributions, J. Fluid Mech. 114 (1982) 481–499.
[3] A.J.N.A. Sarmento, A.F.O. Falcão, Wave generation by an oscillating surface pressure and its application in wave energy extraction, J. Fluid Mech. 150 (1985) 467–485.
[4] A.J.N.A. Sarmento, Wave flume experiments on two-dimensional oscillating water column wave energy devices, Exp. Fluids 12 (1992) 286–292.
[5] K. Thiruvenkatasamy, S. Neelamani, On the efficiency of wave energy caissons in array, Appl. Ocean Res. 19 (1997) 61–72.
[6] E. Didier, J.M. Paixão Conde, P.R.F. Teixeira, Numerical simulation of an oscillating water column wave energy convertor with and without damping, in: Proc., International Conference on Computational Methods in Marine Engineering, 2011, pp. 206–217.
[7] I. López, B. Pereiras, F. Castro, G. Iglesias, Optimisation of turbine-induced damping for an OWC wave energy converter using a RANS-VOF numerical model, Appl. Energy 127 (2014) 105–114.
[8] M.T. Morris-Thomas, R.J. Irvin, K.P. Thiagarajan, An investigation into the hydrodynamic efficiency of an oscillating water column, J. Offshore Mech. Arct. Eng. 129 (2007) 273–278.
[9] M. Alagan Chella, H. Bihs, D. Myrhaug, M. Muskulus, Breaking characteristics and geometric properties of spilling breakers over slopes, Coast. Eng. 95 (2015) 4–19.
[10] A. Chorin, Numerical solution of the Navier–Stokes equations, Math. Comput. 22 (1968) 745–762.
[11] H. van der Vorst, BiCGStab: a fast and smoothly converging variant of Bi-CG for the solution of nonsymmetric linear systems, SIAM J. Sci. Stat. Comput. 13 (1992) 631–644.
[12] D.C. Wilcox, Turbulence modeling for CFD, DCW Industries Inc., La Canada, California, 1994.
[13] P. Bradshaw, D.H. Ferriss, N.P. Atwell, Calculation of Boundary Layer Development using the turbulent energy equation, J. Fluid Mech. 28 (1967) 593–616.
[14] P.A. Durbin, Limiters and wall treatments in applied turbulence modeling, Fluid Dyn. Res. 41 (2009) 1–18.
[15] Y. Egorov, Validation of CFD codes with PTS-relevant test cases, Tech. Rep. 5th Euratom Framework Programme ECORA project, EVOL-ECORA D07, European Commission, 2004.
[16] G.S. Jiang, C.W. Shu, Efficient implementation of weighted ENO schemes, J. Comput. Phys. 126 (1996) 202–228.
[17] G.S. Jiang, D. Peng, Weighted ENO schemes for Hamilton–Jacobi equations, SIAM J. Sci. Comput. 21 (2000) 2126–2143.
[18] C.W. Shu, S. Osher, Efficient implementation of essentially non-oscillatory shock capturing schemes, J. Comput. Phys. 77 (1988) 439–471.
[19] P.A. Berthelsen, O.M. Faltinsen, A local directional ghost cell approach for incompressible viscous flow problems with irregular boundaries, J. Comput. Phys. 227 (2008) 4354–4397.
[20] D. Peng, B. Merriman, S. Osher, H. Zhao, M. Kang, A PDE-based fast local level set method, J. Comput. Phys. 155 (1999) 410–438.
[21] J. Larsen, H. Dancy, Open boundaries in short wave simulations – a new approach, Coast. Eng. 7 (1983) 285–297.
[22] S. Mayer, A. Garapon, L.S. Sørensen, A fractional step method for unsteady free surface flow with applications to non linear wave dynamics, Int. J. Numer. Meth. Fluids 28 (1998) 293–315.
[23] A.P. Engsig-Karup, Unstructured nodal DG-FEM solution of high-order Boussinesq-type equations (Ph.D. thesis), Technical University of Denmark, Lyngby, 2006.
[24] N.G. Jacobsen, D.R. Fuhrman, J. Fredsøe, A wave generation toolbox for the open-source CFD library: OpenFOAM, Int. J. Numer. Meth. Fluids 70 (9) (2011) 1073–1088.
[25] A.F.O. Falcão, J.C.C. Henriques, Model prototype similarity of oscillating-water-column wave energy converters, Int. J. Mar. Energy 6 (2014) 18–34.

Paper 9

Study of Air Chamber Volume and Compressibility Effects in an Oscillating Water Column Wave Energy Device

Kamath A, Bihs H. and Arntsen Ø.A.
Submitted to *International Journal of Marine Energy* 2015

Study of air chamber volume and compressibility effects in an oscillating water column wave energy device

Arun Kamath[1], Hans Bihs, Øivind A. Arntsen

Department of Civil and Transport Engineering, Norwegian University of Science and Technology, 7491 Trondheim, Norway

Abstract

The hydrodynamics of an oscillating water column (OWC) device can be studied in detail using computational fluid dynamics (CFD) simulations as it provides a large amount of detail regarding the flow field in and around the device. This is essential in order to understand the hydrodynamics of the device and produce an efficient and stable design. Water is generally modeled as an incompressible fluid in CFD simulations relating to coastal and marine civil engineering problems. In the case of an OWC device, the compressibility of air can have an influence on the efficiency of the device. CFD simulations with compressible air using the ideal gas law and incompressible water are carried out in a two-phase model to investigate the influence of air compressibility. This is compared with simulations with air modeled as an incompressible fluid. Simulations are carried out for a 1 : 12.5 model scale device in 2D and 3D and for an enlarged air chamber such that ratio of the chamber air volume to the water free surface area is 3.2 m, to investigate the effect of a higher air chamber. The results show that the effect of air compressibility on the free surface and pressure variation in the chamber of the device at the scales tested in this study is negligible, but an increase in the air volume changes the coupled dynamics in the system resulting in reduced chamber pressures, like in a device with lower than optimal damping.

Keywords: Oscillating Water Column, wave energy, air chamber, compressibility, Computational Fluid Dynamics, REEF3D

1. Introduction

An Oscillating Water Column (OWC) is a renewable energy device used to convert wave energy into electrical energy. It consists of a chamber partially submerged in water so that it encloses an air column over the water column. The water column in the chamber is excited by the incident waves and the motion of the water column is transferred to the air column. The air is inhaled into and exhaled out of the chamber. This drives a turbine that converts the kinetic energy from the motion of the air column into electrical energy. The ability of the device to transfer the incident wave energy to the air column is measured using the hydrodynamic efficiency. Several authors have analyzed OWC

[1]Corresponding Author, Email: arun.kamath@ntnu.no, Ph: (+47) 73 59 46 40, Fax: (+47) 73 59 70 21

devices and presented a mathematical description of the oscillation of the water column assuming incompressible air and a simplified representation of the device and the motion of the free surface such as [1] [2]. Sarmento and Falcão [3] considered air compressibility effects and their analysis indicated that air compressibility could be a factor for smaller values of relative water depth, that is ratio of water depth to incident wavelength (d/λ).

Previous experimental investigations [4], [5] have dealt with linear and non-linear power take-off devices and the effect of power take-off damping. Morris-Thomas et al. [6] experimentally determined the influence of the front wall shape, draught and thickness over various wavelengths on the hydrodynamic efficiency the OWC. Hong et al. [7] and Koo and Kim [8] used boundary element methods to numerically study the effects of air duct width, chamber length, skirt thickness and variation of bottom slope and compared it with experiments without considering the effects of air compressibility. Zhang et al. [9] simulated the experiments from [6] with a computational fluid dynamics (CFD) model considering incompressible air and found slight over prediction of the chamber pressure in the simulations. López et al. [10] carried out extensive studies to optimize power take-off damping through both experimental and numerical investigations assuming incompressible air. Kamath et al. [11] validated a CFD model to simulate model scale OWC devices in two dimensions using porous media theory to represent the power take-off damping and Kamath et al. [12] determined the effect of the power take-off damping on the OWC. Both these studies considered incompressible air in the presented results.

In current literature, the various numerical studies involving the OWC device chamber and the chamber pressure variation have assumed air to be an incompressible fluid. Compressibility of the air phase affects the volume of air in the chamber and consequently can influence the pressure developed in the chamber, the oscillation and the velocity of the free surface. The amplitudes of pressure developed in the chamber and the air velocities in a model scale OWC device are comparatively small compared to the atmospheric pressure and the speed of sound, justifying the assumption of incompressible air. Falcão and Henriques [13] proposed that the effects from compressibility are a function of the air volume in the chamber and in order to correctly represent the effects of compressibility in a model scale device, the ratio of the air chamber volume to the water free surface area in the model should be similar to that in a prototype.

In this study, the open source CFD model REEF3D [14] is used to simulate an OWC device in a two and three dimensional wave flume to investigate the difference between the free surface oscillation and the variation of chamber pressure with and without the assumption of air compressibility and the effect of an enlarged air chamber. The model has been validated using experimental data for simulation of an OWC device in two dimensions [11], [12] and in three dimensions [15] in previous studies. The ideal gas law is used to update the density of the air phase according to the chamber pressure developed in the device to account for compressibility. Simulations are carried out for a $1:12.5$ model scale device in two and three dimensional numerical wave tanks and similarly for an enlarged air chamber so that the ratio of the air volume to the water free surface area is 3.2 m.

2. Numerical Model

2.1. Governing Equations

The numerical model uses the Reynolds-averaged Navier Stokes (RANS) equations along with the continuity equation to solve the two-phase fluid flow problem:

$$\frac{\partial u_i}{\partial x_i} = 0 \tag{1}$$

$$\frac{\partial u_i}{\partial t} + u_j \frac{\partial u_i}{\partial x_j} = -\frac{1}{\rho}\frac{\partial p}{\partial x_i} + \frac{\partial}{\partial x_j}\left[(\nu + \nu_t)\left(\frac{\partial u_i}{\partial x_j} + \frac{\partial u_j}{\partial x_i}\right)\right] + g_i \tag{2}$$

where u is the velocity, ρ is the density of the fluid, p is the pressure, ν is the kinematic viscosity, ν_t is the eddy viscosity and g the acceleration due to gravity.

The projection method by [16] is used to determine the pressure and the Poisson pressure equation is solved using a preconditioned BiCGStab iterative solver developed by [17]. Turbulence modeling is handled using the two equation k-ω model proposed by [18]. The strain due to waves in the numerical wave tank leads to an unphysical over production of turbulence. This is avoided using eddy viscosity limiters as shown by [19]. In a two-phase model with air and water, the large difference in the density at the interface leads to an overproduction of turbulence at the interface. This is reduced by introducing free surface turbulence damping with a limiter around the interface based on the studies by [20]. The free surface is determined using the level set method by [21]. In this method, the zero level set of a signed distance function, $\phi(\vec{x}, t)$, represents the interface between water and air. For the rest of the domain, the level set function gives the closest distance to the interface and the sign distinguishes between the two fluids across the interface. The level set function is continuous across the interface and provides a sharp representation of the free surface. The signed distance property of the level set function is restored after convection using a partial differential equation based reinitialisation procedure presented by [22] after every time step.

The fifth-order conservative finite difference Weighted Essentially Non-Oscillatory (WENO) scheme proposed by [23] is used for discretization of convective terms of the RANS equations. The level set function, turbulent kinetic energy k and the specific turbulent dissipation rate ω are discretized using the Hamilton-Jacobi formulation of the WENO scheme [24]. The WENO scheme provides the accuracy required to model complex free surface flows and has numerical stability from its non-oscillatory property. The scheme considers the local smoothness of the stencils and can handle large gradients and provides a minimum of third-order accuracy. A TVD third order Runge-Kutta explicit time scheme developed by [25] is employed for time advancement of the level set function and the reinitialisation equation.

The time step size in the simulation is determined using an adaptive time stepping method. The maximum velocities in the domain during the current time step are used to evaluate the next time step size to satisfy the CFL criterion [26]. The time treatment for turbulent kinetic energy and dissipation are handled by a first-order implicit scheme as they have lower influence from the convective terms.

Explicit handling of the terms in the turbulence model can lead to very small time steps due to the large source terms involved. Due to the use of an implicit scheme to handle these terms and the diffusion, the CFL criterion is satisfied using only the maximum velocities in the domain. The model uses a Cartesian grid for spatial discretization facilitating a straight forward implementation of high order finite difference schemes. The boundary conditions for complex geometries are handled using a local directional ghost cell approach was presented by [27] extended to three dimensions. The code is run as a fully parallel program to increase the computational efficiency by using MPI (Message Passing Interface). The domain is decomposed into smaller pieces and a processor is assigned to each part to carry out the computations in parallel.

2.2. Numerical Wave Tank

Wave generation and wave absorption in the numerical wave tank is carried out using the relaxation method [28]. In this method, the analytical solution from wave theory is used to moderate the computationally generated waves in the wave tank. In the wave generation zone, the computational values of velocity and free surface are taken from zero to the analytical values expected by wave theory. The wave theory used to moderate the values is chosen based on the water depth and wave steepness in the simulation. At the numerical beach, the computational values for the velocity and free surface are brought to zero and all the energy is smoothly removed from the wave tank. The relaxation functions shown by [29] are implemented in the numerical model. This method of wave generation and absorption requires some part of the computational domain to be reserved for the relaxation zones. The relaxation zone for wave generation is generally one wavelength long and two times the generated wavelength for the numerical beach. Further details regarding the numerical model and its application to simulating OWC devices can be found in [12] and [11].

2.3. Inclusion of air compressibility in the model

The effect of air compressibility in the OWC chamber is included in the numerical model using the ideal gas law. The use of the ideal gas law is reasonable as the temperature and the pressure in the OWC chamber are within the range where air does not show significant deviation from the ideal gas law. The ideal gas law is implemented in the numerical model as follows:

$$\rho_{air} = \frac{P}{R_{specific} T} \tag{3}$$

where P is the pressure, R is the specific ideal gas constant for air and T is the absolute temperature. The pressure for every point in the domain at any given time step is available from the solution to the Poisson equation. The compressibility of the air phase is recalculated and updated for every time step taking into account the change in the density due to the change in pressure in the OWC chamber. The new value of the density of air is used to solve the RANS equations in the next time step. In this manner, the change in the properties of the air phase due to compressibility is accounted for and the effect of air compressibility on the efficiency of the OWC device can be analysed.

3. Results and Discussion

The OWC device used in the experiments by Morris-Thomas et al. [6] is simulated in the numerical wave tank 20 m long and 2.20 m high with a water depth of $d = 0.92$ m with a grid size of $dx = 0.025$ m. The front wall thickness is $\delta = 0.04$ m with a draught of $a = 0.15$ m. The total height of the device chamber is 1.275 m, with a 0.355 m high air column, the length of the chamber along the direction of wave propagation is $b = 0.64$ m and the power take-off damping from the turbine is represented by a vent of width $V = 0.05$ m. The setup is illustrated in Fig. (1a). In the experiments, the vent across the length of the chamber is 0.005 m wide, whereas the numerical model uses a vent of width 0.05 m, to avoid the large air velocities in the small vent which can make the simulation computationally inefficient. In order to provide the same pressure drop characteristics as the smaller vent in the experiments, the porous media flow relation is used to provide an equivalent damping as presented in [11] and [12]. The effect of compressibility on the OWC air chamber for different air chamber heights is studied for the incident wavelength $\lambda = 4.07$ m, wave height $H = 0.12$ m and wave period $T = 1.71$ s resulting in resonant response discovered from the experiments and the numerical simulations thereafter. An overview of the simulations carried out in the study is presented in Table (1) and Figs. (1b) and (1c) show the 2D and 3D numerical wave tanks used in the simulations.

No.	NWT	configuration	air treatment
1	2D	model scale	incompressible
2	2D	model scale	compressible
3	3D	model scale	incompressible
4	3D	model scale	compressible
5	2D	enlarged air chamber	incompressible
6	2D	enlarged air chamber	compressible

Table 1: List of simulations carried out in this study

The numerical results assuming incompressible air for the chamber pressure P_c and the free surface variation η inside the chamber are presented in Fig. (2) with comparison to the experimental data [6] for an incident wavelength $\lambda = 4.07$ m, period $T = 1.71$ s and wave height $H = 0.12$ m. The numerical results agree well with the experimental data and detailed results have been presented in previous studies by the authors [12, 11]. According to [11], the assumption of incompressibility is justified because the pressure amplitudes in the chamber are relatively small compared to the atmospheric pressure, the air velocities are low compared to the speed of sound and the volume of the air in the model scale simulations are small.

The effect of air compressibility for the setup presented in Fig. (1a) is investigated by carrying out simulations with and without including air compressibility. The pressure and the free surface inside the chamber calculated with compressible air are compared to the results obtained for the simulation

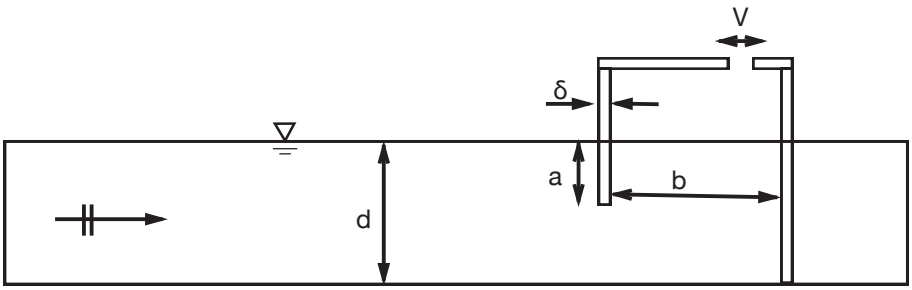

(a) schematic illustration of the OWC device used in the simulations

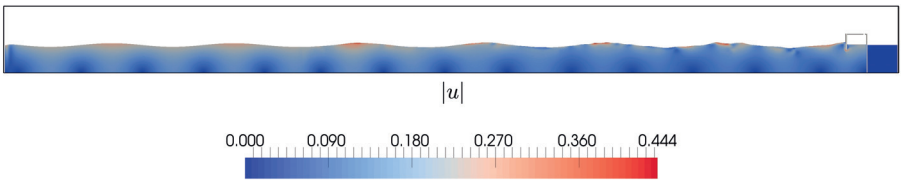

(b) 2D numerical wave tank with OWC device

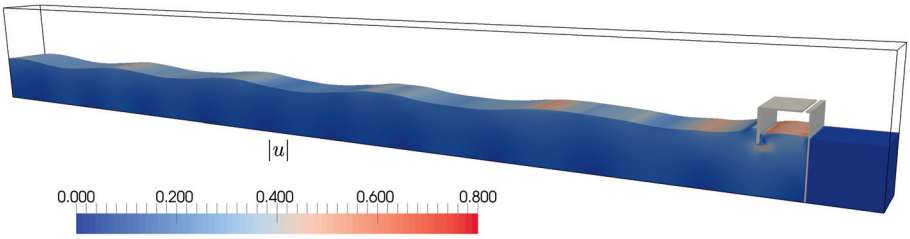

(c) 3D numerical wave tank with OWC device

Figure 1: OWC configuration and numerical wave tank setups for 2D and 3D simulations presented in the study

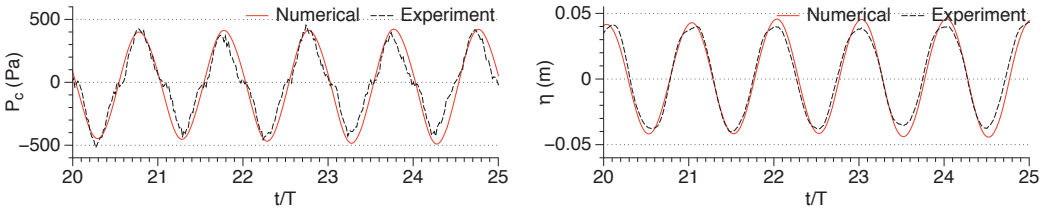

(a) comparison of chamber pressure variation

(b) comparison of free surface variation

Figure 2: Comparison of 2D numerical results with incompressible air with experimental data

considering incompressible air in Fig. (3). It is seen that the justification for assuming incompressible air holds true in this case, as the difference between the values calculated for the pressure and the free

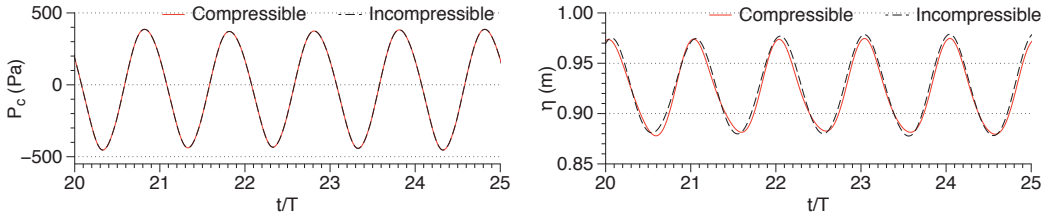

(a) comparison of chamber pressure variation

(b) comparison of free surface variation

Figure 3: Comparison of numerical results with incompressible and compressible air in a model scale 2D simulation

surface motion with and without air compressibility is negligible.

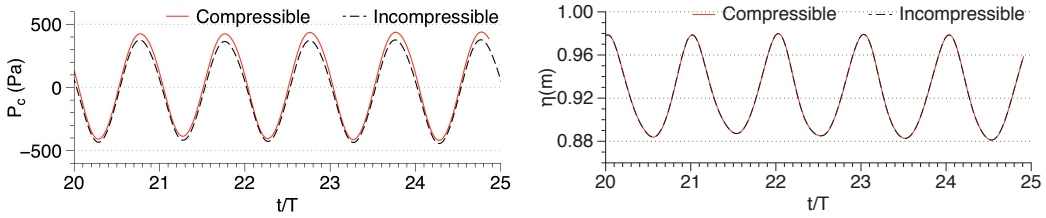

(a) comparison of chamber pressure variation

(b) comparison of free surface variation

Figure 4: Comparison of numerical results with incompressible and compressible air in a model scale 3D simulation

Further, the effect of air compressibility in a 3D numerical simulation is investigated by repeating the simulations in a 3D numerical wave tank 1 m wide, with the other dimensions of the tank and the device remaining the same. The OWC device extends all across the length of the tank (see Fig. 1c), with a slit across the complete width of the device, as in the experiments. The calculated pressure and the free surface variation inside the chamber with and without considering air compressibility are presented in Fig. (4). The calculated values in this configuration do not differ with and without the assumption of incompressible air. In addition, the values of pressure and the free surface calculated in the 3D case match with the values obtained in the 2D simulation in Fig. (5), showing that the 2D simulations can sufficiently account for the chamber hydrodynamics.

The results for 2D and 3D simulations with compressible and incompressible treatment of air in a $1:12.5$ scale model show that the effect of compressibility in the small model scale device is negligible. The good agreement between the results for the 2D and the 3D numerical results suggest that 2D simulations can be justifiably used to study the hydrodynamics of the OWC device. In order to further investigate the effect of compressibility in an OWC device with a larger air volume than in a $1:12.5$ model scale device, the height of the air chamber is increased to 3.2 m while maintaining other dimensions. The total height of the OWC chamber is increased to 4.12 m, so that the ratio of

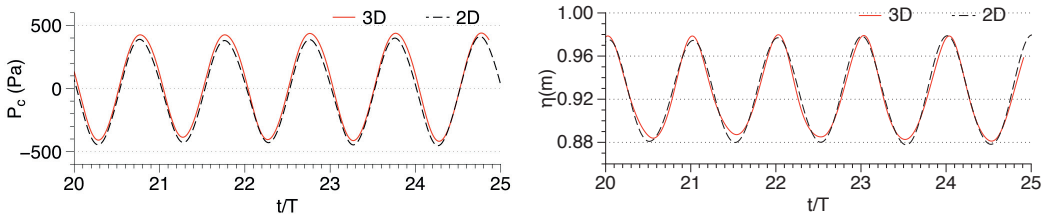

(a) comparison of chamber pressure variation

(b) comparison of free surface variation

Figure 5: Comparison of numerical results with incompressible air in model scale 2D and 3D simulations

the air volume per meter width to the water free surface area in the OWC is 3.2 m. Incident waves with wavelength $\lambda = 4.07$ m and height 0.12 m are generated in the two-dimensional numerical wave tank and the values for chamber pressure and free surface variation are calculated, with and without the ideal gas law governing the density of air phase in the chamber. The results presented in Fig. (6) show that the assumption of incompressible air is valid even in this configuration when the ratio of the air volume to the water free surface area in the device chamber is 3.2 m.

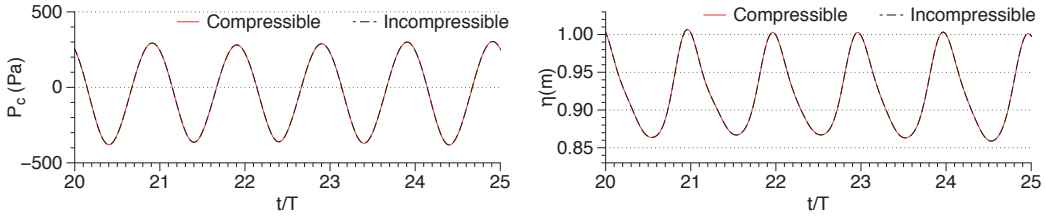

(a) comparison of chamber pressure variation

(b) comparison of free surface variation

Figure 6: Comparison of numerical results with incompressible and compressible air for the OWC device with enlarged air chamber

Figure (7) shows the comparison of the numerical values obtained assuming incompressible air, for the chamber pressure and the free surface variation in the chamber in the $1:12.5$ scale model and in the configuration with the enlarged air chamber, both measured below the vent. The pressure variation in the enlarged OWC chamber is seen to be lower with 280 Pa compared to the 400 Pa calculated at model scale. Correspondingly, the free surface variation in the chamber is increased in the enlarged device chamber with a crest elevation of 1.005 m compared to 0.975 in the model scale device. Thus, on increasing the volume of the air chamber by 800% so that the ratio of the air volume to the water free surface is 3.2 m, the chamber pressure is reduced by 30% and the free surface variation is increased by 31.8% compared to the values for the model scale simulation. It is also noticed that the simulations with inclusion of the ideal gas law to account for air compressibility provide the same results as the

simulations assuming incompressible.

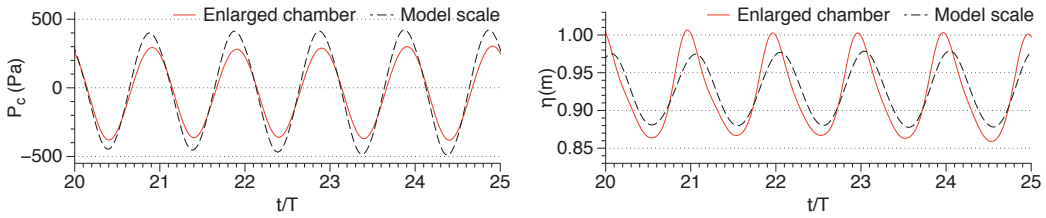

(a) comparison of chamber pressure variation

(b) comparison of free surface variation

Figure 7: Comparison of numerical results assuming incompressible air for the 1 : 12.5 model scale OWC and the configuration with enlarged air chamber

Further insight into the difference in the chamber hydrodynamics is obtained by studying the free surface variation inside the chamber, the phase difference between the pressure and the vertical velocity of the free surface inside the chamber for both the model scale and enlarged chamber devices. The free surface variations computed at three locations inside the chamber, 0.05 m from the front wall, center of the chamber and 0.05 m from the back wall, that is under the vent are presented in Fig. (8). The free surface variations at different locations inside the chamber are in phase with the largest oscillation height of 0.0905 m under the vent. The oscillations at the center are 11% lower than the oscillations under the vent. On the other hand, the free surface variations in the device with the enlarged chamber presented in Fig. (8b) show that there is a phase difference of $0.05T$ between the oscillations under the vent and the oscillations at the center and a phase difference of $0.08T$ between the oscillations near the front wall and the center of the device. Further, the oscillations under the vent are 15% higher than the oscillations at the center of the chamber. It can be said that the motion of the free surface inside the chamber is different for the model scale device and for the device with an enlarged chamber.

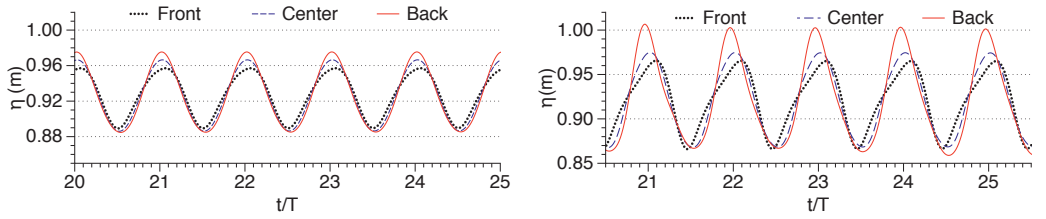

(a) free surface variations in the model scale device

(b) free surface variations in the enlarged chamber device

Figure 8: Free surface variations inside the chamber near the front wall, center and near the back wall, under the vent

The power absorbed by an OWC and delivered to the PTO device, (p_{out}) is calculated using the

chamber pressure P_c, vertical velocity of the free surface w_{fs} and the phase difference θ between them:

$$p_{out} = \frac{1}{T}\int_0^T P_c(t).\ q(t)dt = \frac{1}{2}|P_c|.\ |w_{fs}|\ A_{fs}\ cos(\theta) \tag{4}$$

where A_{fs} is the area of the water free surface in the chamber. Figure (9a) shows that the chamber pressure and the vertical velocity of the free surface inside the chamber (w_{fs}) for the model scale device are almost in phase. Whereas, a phase difference of $0.1T$ is seen between the chamber pressure and the velocity of the free surface under the vent for the device with the enlarged chamber in Fig. (9b). The difference in the free surface motion, introduces a phase difference between the chamber pressure and the vertical velocity of the free surface which is an indicator of the volume flux of air through the chamber. This results in a lower hydrodynamic efficiency of the OWC device with an enlarged chamber.

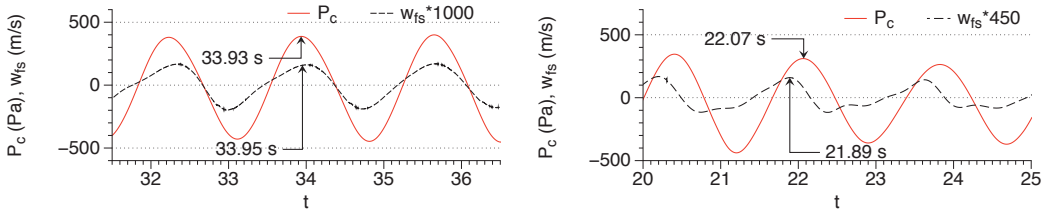

(a) pressure and free surface velocity in the model scale device (b) pressure and free surface velocity in the enlarged chamber device

Figure 9: Phase difference between the chamber pressure and the vertical velocity of the free surface in the chamber

Further insight into the chamber hydrodynamics is also obtained from the distribution of the air velocities inside the chamber in the model scale and enlarged chamber device during the lowest and highest positions of the free surface in the chamber presented in Fig. (10). The distribution of the inhalation velocities in Fig. (10a) shows that the stream of air inhaled in the chamber reaches down to the free surface with high velocities forcing an in-phase motion of most of the water column in the chamber. The exhalation velocities in Fig. (10b) show that the free surface under the vent extends slightly higher than the rest of the chamber due to the slightly higher suction velocities under the vent. In the case of the enlarged chamber, Figs. (10c) and (10d) show that the highest values of the inhalation and exhalation velocities are restricted to the top of the chamber and do not extend close to the free surface. Thus, the free surface in the enlarged chamber is affected to a lesser extent by the dynamic pressure forcing from the air and different parts of the free surface move out of phase with respect to each other and the pressure variation in the chamber. The coupled dynamics of the air and water column motion is broken down and the pressure in the chamber is lower even though each free surface motion is larger than in the case of the model scale device.

From the simulations carried out above, no major difference is seen between the simulations considering compressible air and the simulations assuming incompressible air for both 2D and 3D simulations

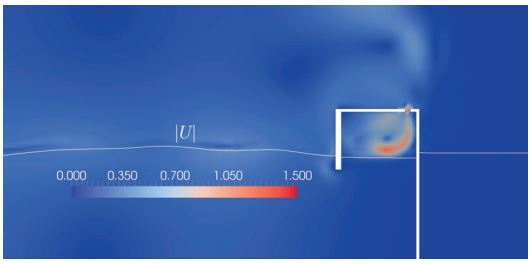

(a) model scale device at lowest position of the free surface

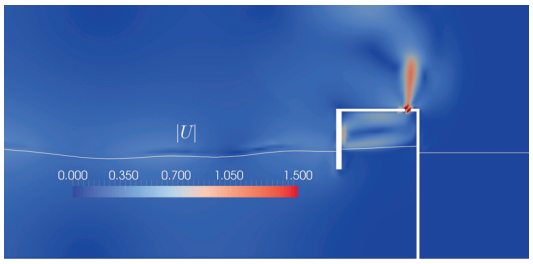

(b) model scale device at the highest position of the free surface

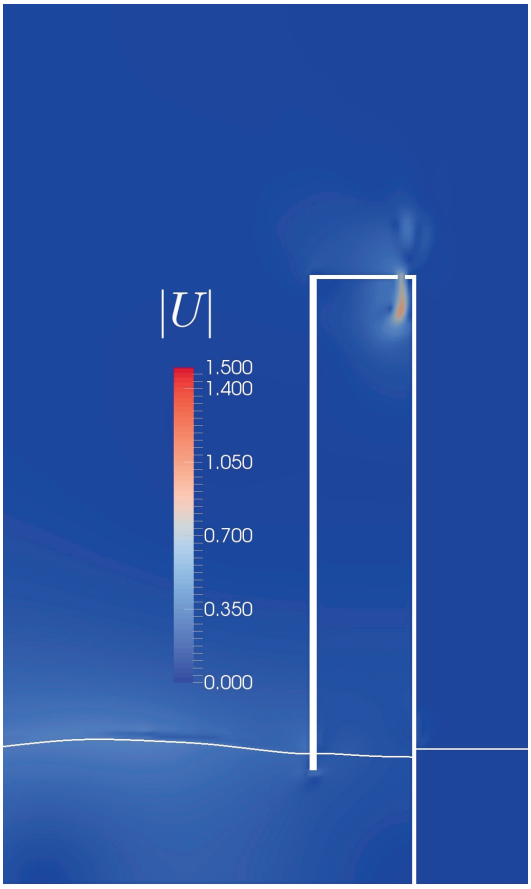

(c) enlarged chamber device at lowest position of the free surface

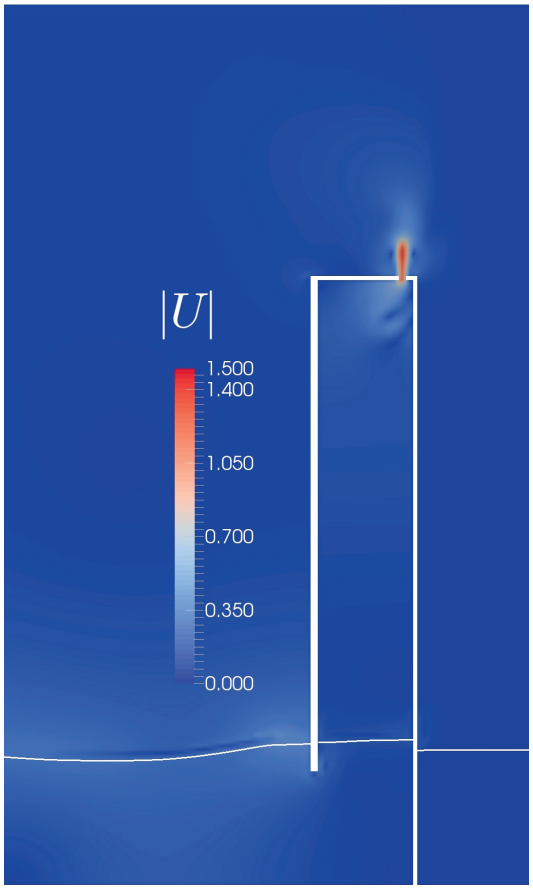

(d) enlarged chamber device at the highest position of the free surface

Figure 10: Velocity magnitude contours inside the OWC chamber showing the distribution of air velocities in the chamber at the lowest and highest positions of the free surface

in the numerical wave tank. Further, the amplitude of the chamber pressure oscillations in the device is found to reduce by 30% and the free surface oscillations increase by 31.8% on increasing the air volume by 800% such that the ratio of the air volume to the water free surface is 3.2 m. The decrease in the pressure oscillations and a corresponding increase in the free surface oscillations in the chamber are similar to the findings by [12] for the chamber response to less than optimal damping. This suggests that the volume of the air chamber in an OWC device has a significant impact on the hydrodynamic efficiency of the device. But this could be mainly because the the resonance motion of the water column for given device dimensions corresponds to a certain air volume in the chamber. This was seen through the differences in the air velocity distributions and the corresponding free surface motions in the chamber. As a result, the chamber pressure is reduced and the vertical velocity of the free surface is out of phase with the pressure variations. Since these parameters and the phase difference between their variation is used to calculate the hydrodynamic efficiency of the device, increasing the air volume in the chamber results in a lower hydrodynamic efficiency. The results also suggest that the effect of air compressibility in an OWC device is not be represented at model scale even by increasing the ratio of the air volume to the free water surface in the chamber.

4. Conclusions

- The numerical model simulated an OWC device considering air compressibility in the device chamber for 1 : 12.5 model scale device and no difference was found from results assuming incompressible air in a 2D numerical wave tank.
- The simulations with compressible and incompressible air in a 3D numerical wave tank produced the same results as in the 2D simulations at model scale and no effect due to air compressibility was found.
- The air volume in the chamber was increased by 800% so that the ratio between the air volume and the water free surface area is 3.2 m, but no difference was found between simulations considering compressible and incompressible air.
- The chamber pressure was reduced and the free surface variation was increased on increasing the air volume, similar to an OWC device with less than optimal damping.
- The influence of air compressibility is negligible but the the ratio of the air chamber volume to the water free surface area has a large influence on the chamber hydrodynamics.

Acknowledgements

This study has been carried out under the OWCBC project (No. 217622/E20) and the authors are grateful to the grants provided by the Research Council of Norway. This study was supported in

part with computational resources at the Norwegian University of Science and Technology (NTNU) provided by NOTUR, http://www.notur.no (NN2620K).

References

[1] D. V. Evans, Oscillating water column wave energy convertors, IMA Journal of Applied Mathematics 22 (1978) 423–433.

[2] D. V. Evans, Wave power absorption by systems of oscillating surface pressure distributions, Journal of Fluid Mechanics 114 (1982) 481–499.

[3] A. J. N. A. Sarmento, A. F. O. Falcão, Wave generation by an oscillating surface pressure and its application in wave energy extraction, Journal of Fluid Mechanics 150 (1985) 467–485.

[4] A. J. N. A. Sarmento, Wave flume experiments on two-dimensional oscillating water column wave energy devices, Experiments in Fluids 12 (1992) 286–292.

[5] K. Thiruvenkatasamy, S. Neelamani, On the efficiency of wave energy caissons in array, Applied Ocean Research 19 (1997) 61–72.

[6] M. T. Morris-Thomas, R. J. Irvin, K. P. Thiagarajan, An investigation into the hydrodynamic efficiency of an oscillating water column, Journal of Offshore Mechanics and Arctic Engineering 129 (2007) 273–278.

[7] K. Hong, S. H. Shin, D. C. Hong, H. S. Choi, S. W. Hong, Effects of shape parameters of OWC chamber in wave energy absorption, in: Proc., 17th International Offshore and Polar Engineering Conference, Lisbon, 2007.

[8] W. Koo, M. H. Kim, Nonlinear NWT simulation for oscillating water column wave energy convertor, in: Proc., 29th International Conference on Ocean, Offshore and Arctic Engineering, Shanghai, 2010.

[9] Y. Zhang, Q. P. Zou, D. Greaves, Air-water two phase flow modelling of hydrodynamic performance of an oscillating water column device, Renewable Energy 41 (2012) 159–170.

[10] I. López, B. Pereiras, F. Castro, G. Iglesias, Optimisation of turbine-induced damping for an OWC wave energy converter using a RANS-VOF numerical model, Applied Energy 127 (2014) 105–114.

[11] A. Kamath, H. Bihs, Ø. A. Arntsen, Numerical investigations of the hydrodynamics of an oscillating water column device, Ocean Engineering doi:10.1016/j.oceaneng.2015.04.043.

[12] A. Kamath, H. Bihs, Ø. A. Arntsen, Numerical modeling of power take-off damping in an oscillating water column device, International Journal of Marine Energy 10 (2015) 1–16.

[13] A. F. O. Falcão, J. C. . C. Henriques, Model-prototype similarity of oscillating-water-column wave energy converters, International Journal of Marine Energy 6 (2014) 18–34.

[14] M. Alagan Chella, H. Bihs, D. Myrhaug, M. Muskulus, Breaking Characteristics and Geometric Properties of Spilling Breakers over Slopes, Coastal Engineering 95 (2015) 4–19.

[15] A. Kamath, H. Bihs, Ø. A. Arntsen, Comparison of 2D and 3D simulations of an OWC device in different configurations, in: Proc. 34*th* International Conference on Coastal Engineering, Seoul, South Korea, 2014.

[16] A. Chorin, Numerical solution of the Navier-Stokes equations, Mathematics of Computation 22 (1968) 745–762.

[17] H. van der Vorst, BiCGStab: A fast and smoothly converging variant of Bi-CG for the solution of nonsymmetric linear systems, SIAM Journal on Scientific and Statistical Computing 13 (1992) 631–644.

[18] D. C. Wilcox, Turbulence modeling for CFD, DCW Industries Inc., La Canada, California., 1994.

[19] P. A. Durbin, Limiters and wall treatments in applied turbulence modeling, Fluid Dynamics Research 41 (2009) 1–18.

[20] D. Naot, W. Rodi, Calculation of secondary currents in channel flow, Journal of the Hydraulic Division, ASCE 108 (8) (1982) 948–968.

[21] S. Osher, J. A. Sethian, Fronts propagating with curvature- dependent speed: algorithms based on Hamilton-Jacobi formulations, Journal of Computational Physics 79 (1988) 12–49.

[22] D. Peng, B. Merriman, S. Osher, H. Zhao, M. Kang, A PDE-based fast local level set method, Journal of Computational Physics 155 (1999) 410–438.

[23] G. S. Jiang, C. W. Shu, Efficient implementation of weighted ENO schemes, Journal of Computational Physics 126 (1996) 202–228.

[24] G. S. Jiang, D. Peng, Weighted ENO schemes for Hamilton-Jacobi equations, SIAM Journal on Scientific Computing 21 (2000) 2126–2143.

[25] C. W. Shu, S. Osher, Efficient implementation of essentially non-oscillatory shock capturing schemes, Journal of Computational Physics 77 (1988) 439–471.

[26] M. Griebel, T. Dornseifer, T. Neunhoeffer, Numerical simulation in fluid dynamics: a practical introduction, SIAM, 1998.

[27] P. A. Berthelsen, O. M. Faltinsen, A local directional ghost cell approach for incompressible viscous flow problems with irregular boundaries, Journal of Computational Physics 227 (2008) 4354–4397.

[28] J. Larsen, H. Dancy, Open boundaries in short wave simulations - a new approach, Coastal Engineering 7 (1983) 285–297.

[29] N. G. Jacobsen, D. R. Fuhrman, J. Fredsøe, A wave generation toolbox for the open-source CFD library: OpenFOAM, International Journal for Numerical Methods in Fluids 70 (9) (2012) 1073–1088.